JCM
Scholarly, Peer-Reviewed and Fully
Refereed International Research
Journal
ISSN : 2583-9152

Journal of Condensed Matter

of
Condensed Matter Research Society

Vol. 03 No. 02 (2025)

Condensed Matter Research Society

Table of Contents

Polymer Electrolytes for Improving the Performance and Safety of Lithium-ion Batteries

Anjali[a], Monika, Ashish Kumar Mishra, Balbir Singh Patial[b,c]

Department of Physics, Himachal Pradesh University, Summerhill, Shimla-171005, Himachal Pradesh, India.

[a] anjali04aug@gmail.com
[b] bspatial@hpuniv.ac.in
[c] bspatial@gmail.com

Abstract

The growing global energy demand coupled with environmental protection measures is driving the need for advanced energy storage technologies capable of storing power generated from renewable sources such as wind, solar and hydropower. This enables broader integration of sustainable energy systems. Among various energy storage systems, batteries have proven to be the most efficient. In particular, Li-ion batteries (LIBs) have emerged as the most reliable and suitable energy storage devices because of their novel characteristics, including high energy density (Ed), high theoretical capacity, compact design and long-lasting performance compared to other storage systems. However, to enhance their energy and power densities and to address safety concerns caused by dendrite growth in the anodes, further optimization is required. Of the three key parts of a battery namely cathode, anode and electrolyte; electrolyte has a vital role, significantly influencing the electrochemical performance and overall operation. In high performance LIBs, solid polymer electrolytes have garnered significant interest because of their enhanced safety, lack of leakage, broad electrochemical stability window, mechanical flexibility and thermal-stability. This paper discusses various types of polymers including PMMA, PEO, PAN, PVDF, PVC, PS and PC, focusing on their synthesis methods and electrochemical performance. The aim is to provide insights into their potential for the advancement in LIB- technology.

Keywords: Energy Storage; Li-Ion Batteries; Polymer Electrolytes; Electrochemical Performance.
Received 30 January 2025; First Review 05 February 2025; Accepted 19 March 2025.

*** Address of correspondence**
Balbir Singh Patial
Department of Physics, Himachal Pradesh University, Summerhill, Shimla-171005, Himachal Pradesh, India.

Email: bspatial@gmail.com

How to cite this article
Anjali, Monika, Ashish Kumar Mishra, Balbir Singh Patial, Polymer Electrolytes for Improving the Performance and Safety of Lithium-ion Batteries, J. Cond. Matt. 2025; 03 (02): 1-8.

Available from:
https://doi.org/10.61343/jcm.v3i02.115

Introduction

As global energy demand continues to rise, many countries are increasingly turning to various renewable sources. It is projected that 50% of energy demand in the world is expected to be met by renewable sources, especially wind and solar, by 2050 [1]. Fossil fuel use will decrease to 31%, while renewables will account for 62% of energy production. This transition is expected to drive rapid growth in grid support and energy storage, with projections showing a more than 120-fold increase by 2040 according to Bloomberg New Energy Finance (BNEF) [2]. Consequently, the demand for energy storage devices to store power for extended use has become more critical. The demand for energy storage devices across various countries (figure 1) illustrates that the need for such devices can be increased with the expansion of renewable sources. Among different storage devices, lithium-ion batteries (LIBs) play a significant role in most commercially available batteries in the market. They have many advantages such as enhanced energy density (Ed), high operating voltages, long life cycle etc. and it is expected that its global shipments will reach 439.32 GWh by 2025 [3].

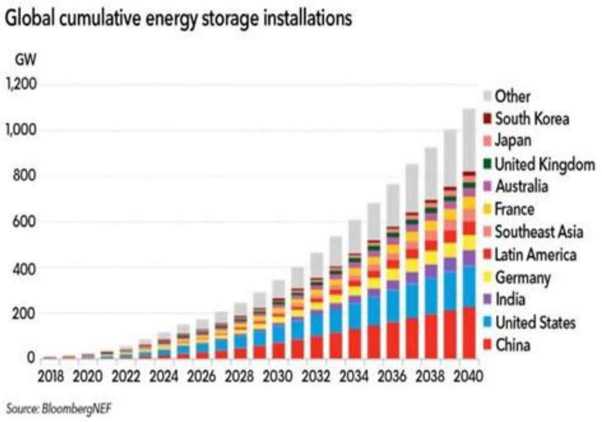

Figure 1: Forecasts for global energy storage installations by 2040 [2].

Among the major components of a battery, current research on anode and cathode materials of LIBs focuses on maximizing energy density and preventing dendrite formation [4]. Most of them, today rely on liquid electrolytes as Li^+ conductors, which offers high ionic conductivity and good electrode contact, but presents significant safety risks due to their low thermal stability and flashpoint. Additionally, during Li^+ deposition and stripping process, lithium dendrites can form spontaneously and hence, increasing the risk of short circuit. An ideal electrolyte must consider the factors such as conductivity, viscosity, melting point, toxicity and compatibility with electrodes. Altering the electrolyte's chemical or physical properties can significantly enhance safety and improve energy density in LIBs.

To address the challenges in commercial LIBs using liquid electrolyte, non-flammable solid-state electrolytes have been developed. These include inorganic and polymer electrolytes, as well as organic-inorganic hybrid composites. They offer advantages such as high mechanical strength, ionic conductivity exceeding 10^{-4} Scm^{-1}, negligible electronic conductivity and wide electrochemical stability windows. However, unlike liquid electrolytes, most solid-state electrolytes (SSEs) face difficulties in wetting and penetrating porous cathodes, limiting Li^+-conduction inside the cathode and across the electrode/electrolyte interface. Among SSEs, polymer-based variants show higher ability for improving interfacial contact with electrodes and techniques like in-situ polymerization or the insertion of a liquid component offer potential solutions to increase the wetting of thick cathodes [5]. This could lead to solid-state LIBs with higher energy density. This paper presents a comprehensive analysis of polymer-based SSEs, including the synthesis of polymer electrolyte films and the various polymer hosts utilized.

Synthesis of Polymer Electrolyte Films

Polymer electrolyte films represent an emerging technology with the potential to significantly influence various aspects of our lives, the environment, and the economy. The preparation of film requires the proper selection of polymer matrix, solvent and salt choice. The choice of polymer such as PEO, PVDF, etc. is critical because it is the backbone of the film, providing mechanical strength and flexibility. Selecting a suitable solvent is essential for dissolving the polymer and salts uniformly, whereas the salt provides the mobile ions, usually lithium ions in LIB applications. Some commonly used solvents and salts are acetonitrile (ACN), dimethylformamide (DMF), LiPF6, LITFSI, etc. The preparation of the polymer films can be done by various available methods as given below:

1. **Solution-casting Method:** Solution casting method is a simple and extensively used technique for the fabrication of polymer electrolyte films due to its versatility. It allows easy control over film thickness and is suitable for a wide range of polymers and salts. It follows the steps as mentioned below:
   - The desired amount of polymer is weighed and dissolved separately in the solvent by stirring the mixture for several hours. This process can be carried out at room temperature or at elevated temperatures depending on the polymer's solubility.
   - The required amount of the salt is weighed and then mixed with the dissolved polymer. The mixture is continuously stirred until homogeneous solution is obtained.
   - Formed homogeneous polymer-salt solution is placed in a vacuum chamber for a few minutes to remove any air bubbles.
   - For this, the prepared solution is cast into petri dish.
   - After drying, flexible and self-supporting film is produced.
   - The solvent should be compatible with both the polymer and the salt to produce a polymer film with a thickness ranging from micrometers to millimeters.

2. **Phase Inversion Method:** It is a versatile technique used to fabricate microporous polymer films or membranes. It can be categorized into the following forms:
   - Nonsolvent-induced Precipitation: In this method, a polymer solution is applied to a glass slide and then immersed in a nonsolvent. This causes the polymer to precipitate resulting in thin, porous polymer films. The different porosities formed during this process influence the ion-conductivity of these films. Films with smaller pores and a narrower pore distribution can prevent liquid leakage, while higher porosity is beneficial for achieving higher ionic conductivity.
   - Evaporation-induced Phase Separation: This method involves dissolving a copolymer in a mixed solution of volatile acetone as the solvent and ethanol as the nonsolvent. It is then cast onto a substrate to fabricate a film, which is then air-dried to produce a porous structure. This phase inversion method allows for easy control over the membrane structure enabling the creation of honeycomb or network-like structures.
   - Vapor-induced Precipitation: In this process, precipitation occurs by absorbing a nonsolvent from the vapor phase.
   - Thermally Induced Precipitation: This method involves precipitation by cooling, which causes the polymer to solidify and form a porous structure.

- Each phase separation method offers distinct advantages and allows for the tuning of membrane properties to meet specific requirements.

3. **Spin Coating Method:** This method is similar to the casting technique. Instead of spreading the film across the substrate as in casting, this method involves dropping the mixture onto the substrate and then placing it in a spin coater. The spin coater rotates at a variable speed, allowing precise control over the film's thickness by adjusting both the mixture's viscosity and the rotation speed. However, this technique is effective when the mixture's viscosity is relatively low. For gel-like mixtures, the spinning action alone is insufficient to spread the droplet into a thin-film.

4. **Hot Press Method:** In this method, polymer and salt are first combined in a mortar to form a fine powder through several minutes of mixing. This powder mixture is then placed between two Mylar sheets or similar materials and positioned in a heating chamber to set a temperature slightly above the polymer's melting point. The sample is pressed overnight using a weight-controlled pressure. After the pressing and heating process, it is gradually cooled to room temperature. Finally, it is removed from the Mylar sheets and transferred to a glove box.

Polymer Electrolytes

Polymer electrolytes consisting of a polymer host and a lithium salt with low lattice energy and large anions, function as electrolytes by dissolving within a polymer matrix. Ionic conduction in these materials is driven by the covalent interaction between the polymer and ionizing groups. Initially, polymer's electron-donating groups solvate the cation from the dopant salt, facilitating ion separation and ionic hopping, which generates conductivity. In conventional batteries, electrolytes and separators assist the ion movement between electrodes, but polymer electrolytes can replace both components in solid-state configurations. Polymer electrolytes are highly valued for their ability to accommodate electrode volume changes, improve current density, enhance safety, and reduce dendrite formation. However, their lithium-ion conductivity at room temperature remains low, though advancements like blending and modified derivatives have improved high performance. Key requirements for polymer electrolytes include ionic conductivity (> 10^{-4} $\mathrm{Scm^{-1}}$), electrical insulation, low activation energy, excellent thermal and chemical stability, high cation transference and compatibility with electrode materials. Additionally, they should be non-toxic, cost-effective, have a wide operational temperature range as well as both low melting point and high boiling point for optimal battery performance [6].

Ionic Conduction Mechanism in Polymer Electrolyte

Ionic conduction in polymer electrolytes is a complex process that depends on the structural dynamics of the polymer matrix and the interaction between lithium ions (Li^+) and polymer functional groups. The conduction mechanism is basically determined by the polymer's amorphous and crystalline phases, polymer-segment mobility and the formation of ion-conducting pathways.

1. **Polymer-Salt Complexation and Ion Dissociation** [7]: In polymer electrolytes, Li^+ ions coordinate with polar functional groups such as ether oxygens in poly (ethylene oxide) (PEO) or nitrile groups in polyacrylonitrile (PAN). The dissolution of lithium salts within the polymer matrix results in the formation of mobile charge carriers (Li^+ and anions), which are essential for ionic conduction.

2. **Segmental Motion and Ion Transport** [8]: The local movement of polymer chains greatly impacts the mobility of Li^+ ions. In the amorphous phase, polymer segments undergo dynamic relaxation, allowing Li^+ ions to hop between coordinating sites. This process is known as segmental-assisted transport and it involves the breaking and reforming of Li–polymer bonds in order to facilitate ion migration. Higher is the polymer flexibility, better is the ionic conductivity.

3. **Inter- and Intra-chain Hopping Mechanisms**: Ionic conduction occurs through three primary pathways [9]:
   - Intra-chain motion: Li^+ ions move along a polymer chain through weak coordination with functional groups.
   - Polymer-segment relaxation: The movement of polymer segments influences ion transport by modifying the polymer environment.
   - Inter-chain hopping: Li^+ ions jump from one polymer chain to another, enabling long-range ion diffusion.

4. **Crystalline vs. Amorphous Transport**: While it was assumed that only the amorphous phase contributes to ionic transport, recent studies have shown that crystalline polymer structures can also support ion migration. In crystalline PEO/$LiXF_6$ complexes [10], Li^+ ions move through cylindrical tunnels formed by folded polymer chains, offering a static pathway for conduction without requiring segmental motion. However, ionic transport is generally more efficient in the amorphous phase due to higher polymer flexibility.

5. **Glass Transition Temperature Dependence (T_g)**: Ionic conductivity is closely related to the polymer's

T_g. Below T_g, the polymer chains are rigid, restricting ion mobility and leading to poor conductivity. Above T_g, the polymer matrix transitions into a rubbery state, enhancing the flexibility of chains and facilitating faster ion transport [11].

Types of Polymer Electrolytes

These can be classified in the following types based on their physical state and composition:

1. **Gel Polymer Electrolytes (GPEs):** These consist of a polymer host swollen with liquid electrolyte. While maintaining a semi-solid form, GPEs exhibit higher ionic conductivity due to the liquid component, while still offering some mechanical strength. They are widely used in LIBs for balancing conductivity and safety.

2. **Composite Polymer Electrolytes (CPEs):** These are a hybrid form, combining a solid polymer electrolyte with ceramic or inorganic fillers to enhance mechanical properties and ionic conductivity. CPEs aim to improve conductivity, stability, and overall performance by leveraging both the polymer matrix and solid particles.

3. **Perovskite-type Polymer Electrolytes**: Perovskite-type polymer electrolytes combine the high ionic conductivity of perovskite ceramics, such as lithium lanthanum titanium oxide (LLTO), with the flexibility of polymers like poly (ethylene oxide) (PEO) and poly (vinylidene fluoride) (PVDF). Perovskite materials typically exhibit high lithium-ion conductivity, ranging from 10^{-3} to 10^{-4} S/cm at room temperature, while maintaining extremely low electronic conductivity, around 10^{-8} S/cm [12]. This balance makes them excellent candidates for solid-state electrolytes, as they efficiently transport lithium ions while minimizing electronic leakage, which is crucial for battery performance and safety. Blending perovskites with polymers enhances mechanical stability and interfacial compatibility, leading to improved performance in lithium batteries.

4. **Sulphide-type Polymer Electrolytes**: Sulphide-type polymer electrolytes combine highly conductive sulphide materials with flexible polymers to improve performance in solid-state lithium-ion batteries. Sulphide-based electrolytes, like lithium phosphorus sulphide (LPS) and lithium argyrodite (Li_6PS_5X, X = Cl, Br, I), are known for their excellent ionic conductivity and good electrochemical stability. However, they are brittle and highly sensitive to moisture, making them difficult to use on their own. Blending sulphide particles with polymers such as poly (ethylene oxide) (PEO) or polyacrylonitrile (PAN) improves mechanical flexibility and enhances compatibility with battery electrodes [13].

5. **Solid Polymer Electrolytes (SPEs):** These are composed of a polymer matrix with dispersed lithium salts and have been widely studied for applications in LIBs and other electrochemical systems. The ions are transported through the polymer structure, which remains in a solid state. Solid polymer electrolytes (SPEs) must provide good mechanical strength, safety, thermal stability, ionic conductivity, and electrochemical stability to prevent lithium dendrite growth. There are various host polymers are in use for the synthesis of polymer-electrolytes. Key properties of polymer hosts are [14]:
   - Electron donor groups (O, N, P, S) for coordinating with Li+-ions.
   - Fast segmental motion of polymer chains to enhance ionic conductivity.
   - Low Tg (glass transition temperature).
   - Elevated thermal decomposition temperature.
   - Larger molecular size.
   - Optimal spatial configuration for salt dissociation.
   - Appropriate distance between coordinating centres to avoid intra-polymer ion bonding.
   - Sufficient flexibility for enhanced performance.

Different Types of Polymer Host

Various types of polymer hosts are being researched for polymer electrolytes due to their ability to dissolve lithium salts and support ionic conduction (Table 1). Some of them are explained below:

1. **Polyethylene Oxide (PEO):** It is a leading candidate for SPEs in LIBs due to its ability to form complexes with metal salts, low cost and easy production. It is discovered in 1973 by Wright, PEO exhibits ionic conductivity with Li^+ salts, driven by its flexible ethylene oxide chains, high electrochemical stability and strong dielectric properties [15,16]. However, its semi-crystalline nature limits ionic-conductivity at room temperature and low Li^+ transference-number affect battery performance [17]. To address these issues, various strategies have been investigated to enhance ionic conductivity and interfacial properties. These include addition of plasticizer with high dielectric constant and incorporation of inorganic filler into PEO-based polymer-electrolyte to simultaneously improve ionic-conductivity and mechanical stability [5]. Additionally, blending with other polymers like PAN and PVDF, known for their favourable mechanical properties, to further strengthen the

mechanical stability of PEO-based electrolytes [18-19].

2. **Polyacrylonitrile (PAN):** PAN-based lithium salt complexes are known for their strong ionic conductivity, stable thermal property, mechanical strength and compatibility with electrode materials used in LIBs. PAN's semi-crystalline structure dissolves various lithium salts and effectively absorbs electrolytes. The addition of plasticizers enhances ion mobility, increasing conductivity to 1.7×10^{-3} Scm^{-1} at 20 °C and 1.1×10^{-3} Scm^{-1} at 10 °C [18]. The PAN based gel electrolyte has transference number more than 0.5, which can be increased to 0.7 by adding lithium bis (trifluoromethyl sulfonyl) imide (LiTFSI) and lithium bis (trifluoro methane sulfonyl) methide (LiTFSM) salts addition [20]. However, PAN's high electrolyte absorption can lead to swelling and passivation at the lithium electrode interface, impacting battery performance. Blending PAN with polymers like polyethylene oxide (PEO) improves ionic-conductivity, mechanical flexibility, and interfacial characteristics, making it more suitable for LIBs [21].

3. **Polymethylmethacrylate (PMMA):** It is a thermoplastic with good dimensional stability and high lithium-ion affinity, but its brittleness limits its use in flexible, solid-state devices. Initially used as a gelling agent, PMMA-based electrolytes exhibit moderate ionic conductivity with improvements observed when blended with other polymers or doped with lithium salts like LiTFSI [22]. It has been observed that combining PMMA with PVC enhances mechanical strength, while the addition of silica nanoparticles or ionic liquids to PMMA/LiTFSI further increases its conductivity to 2.44×10^{-6} S·cm^{-1} when prepared using the solution casting technique.[14]. Copolymerization and blending with materials like poly (vinylidene fluoride-hexafluoro propylene) and LLZN nanowires can also enhance performance making PMMA a versatile component in electrolyte formulations.

4. **Polyvinylidene Fluoride (PVDF):** It is a semi-crystalline polymer known for its high dielectric constant (~8.4) and anodic stability, attributed to its strong electron-withdrawing (–C–F) groups [6]. This characteristic enhances salt dissolution and increases charge carriers' concentration. PVDF-based electrolytes exhibit varying ionic conductivities, with improvements observed when plasticizers like propylene carbonate (PC) are added. For instance, PVDF with 30 mol% $LiClO_4$ and PC shows significant conductivity enhancement, reaching 1.74×10^{-3} S cm^{-1} at 30 °C [23]. Blending PVDF with lithium nitrate or phthaloyl starch can further improve ionic conductivity and electrochemical stability, though PVDF's interfacial stability with lithium remains a challenge.

5. **Polyvinyl Chloride (PVC):** PVC is another polymer host known for its chemical resistance, flexibility, and mechanical strength, making it suitable for creating durable electrolyte membranes. However, it often requires plasticizers to improve ion transport. Studies have shown that PVC complexes with LiTFSI, plasticized using dibutyl phthalate and dioctyl adipate, exhibit significantly enhanced ionic-conductivity as the PVC content decreases. These complexes also achieve an electrochemical stability window of ~ 4.0 V at 60°C [24]. Despite its advantages, PVC-based polymer electrolytes face challenges such as solvent exudation. This issue can be addressed by substituting PVC with a PVAC copolymer. Furthermore, instead of using auxiliary carrier solvents like tetrahydrofuran (THF) for PVC or PVAC, direct utilization of solvents has been suggested as a viable alternative [25].

6. **Polysiloxane (PS):** Polysiloxanes are known for their low temperature (T_g), significant free space, excellent electrochemical stability and flexibility [26]. Their amorphous nature allows for good ionic conductivity, especially when blended with other polymers or plasticizers.

7. **Polycarbonate (PC):** Polycarbonate polymers have gained attention as promising hosts in LIBs, especially for applications in solid-state and gel polymer electrolytes. These materials provide a balance of mechanical strength, ionic-conductivity and electrochemical robustness, making them ideal candidates for advanced energy storage technologies. Solid polymer electrolytes developed using aliphatic polycarbonates—such as poly (ethylene carbonate) and poly (propylene carbonate)-demonstrate enhanced ionic-conductivity, electrochemical stability and thermal resilience. This is attributed to their amorphous structure, high dielectric constant and flexible chain segments, which collectively contribute toward improved performance [6].

Each polymer host has its strengths and challenges and they are often modified or combined with other materials to enhance properties such as ionic conductivity, mechanical stability and thermal stability for use in LIBs.

Applications of Polymer Electrolytes in Lithium-based Batteries

Table 1: Comparison of Polymer Host for Solid State Electrolytes based on their associated challenges and applications.

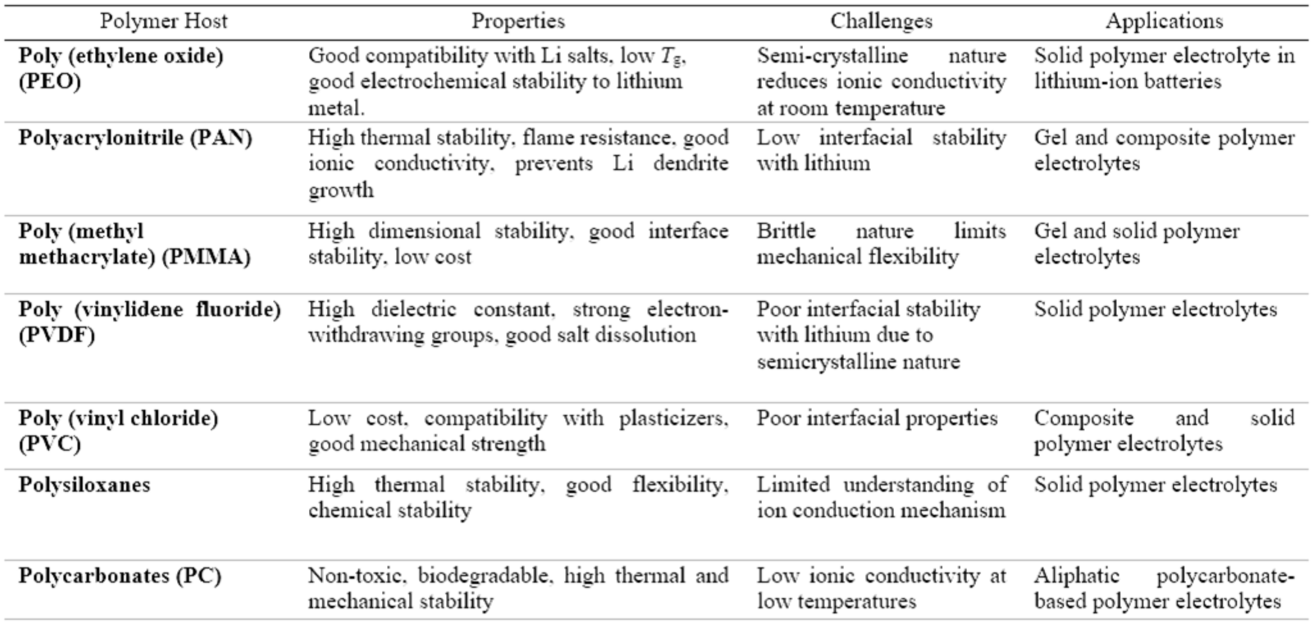

Polymer Host	Properties	Challenges	Applications
Poly (ethylene oxide) (PEO)	Good compatibility with Li salts, low T_g, good electrochemical stability to lithium metal.	Semi-crystalline nature reduces ionic conductivity at room temperature	Solid polymer electrolyte in lithium-ion batteries
Polyacrylonitrile (PAN)	High thermal stability, flame resistance, good ionic conductivity, prevents Li dendrite growth	Low interfacial stability with lithium	Gel and composite polymer electrolytes
Poly (methyl methacrylate) (PMMA)	High dimensional stability, good interface stability, low cost	Brittle nature limits mechanical flexibility	Gel and solid polymer electrolytes
Poly (vinylidene fluoride) (PVDF)	High dielectric constant, strong electron-withdrawing groups, good salt dissolution	Poor interfacial stability with lithium due to semicrystalline nature	Solid polymer electrolytes
Poly (vinyl chloride) (PVC)	Low cost, compatibility with plasticizers, good mechanical strength	Poor interfacial properties	Composite and solid polymer electrolytes
Polysiloxanes	High thermal stability, good flexibility, chemical stability	Limited understanding of ion conduction mechanism	Solid polymer electrolytes
Polycarbonates (PC)	Non-toxic, biodegradable, high thermal and mechanical stability	Low ionic conductivity at low temperatures	Aliphatic polycarbonate-based polymer electrolytes

Polymer electrolytes are emerging as a key solution for enhancing the performance, safety and longevity of lithium-based batteries. Their unique combination of flexibility, lightweight properties, and improved interfacial stability makes them ideal for next-generation energy storage systems. Some of the most promising applications include:

1. **Solid-state Lithium-ion Battery:** Solid-state lithium-ion batteries (SSBs) are gaining attention for their ability to replace traditional liquid electrolytes with solid polymer electrolytes, making them safer, more energy-dense and long-lasting. They are particularly promising for electric vehicles (EVs) and grid energy storage due to their stability and high energy capacity. Recent advancements have further improved their performance-Wang et al. [27] developed an electrospun solid polymer electrolyte (SPE) using a bio-polyamide (IBD) blended with PEO/Li bis(trifluoromethanesulfonyl)imide, achieving strong lithium-ion transport and an impressive ionic conductivity of 4.26×10^{-4} S/cm at 50°C. Meanwhile, Zhu et al. [28] introduced an inorganic-polymer gel electrolyte incorporating helical mesoporous silica nanofibers (HMSFs), leading to remarkable thermal stability (up to 372°C), a wide electrochemical window (5.30 V), and high ionic conductivity at room temperature (1.2×10^{-3} Scm^{-1}). These innovations bring us closer to safer, more efficient batteries that could revolutionize energy storage and transportation.

2. **Lithium-Metal Batteries (LMBs):** LMBs are a promising next-generation energy storage technology due to their high energy density, making them ideal for long-lasting applications. However, they face safety challenges, particularly dendrite formation, which can cause short circuits. To improve safety and performance, researchers are developing advanced electrolytes. A recent study by Xie et al. [29] introduced a gel polymer electrolyte (GPE) called AT11-GF, which uses a non-flammable material to enhance lithium-ion conduction. By adding a protective film-forming agent, they improved stability and compatibility with the lithium anode, achieving high ionic conductivity and long-lasting performance. These advancements bring us closer to safer and more efficient lithium-metal batteries.

3. **Lithium-air (Li-air) Batteries:** They are also known as lithium-oxygen batteries and are an emerging energy storage technology that uses oxygen from the air as the cathode material. They have the potential to achieve extremely high energy density, making them attractive for applications like electric vehicles and aerospace. Polymer electrolytes play a vital role in these batteries by providing a stable and efficient pathway for lithium-ion transport. Recent advancements, such as the gel polymer electrolyte (GPE) introduced by Yoon et al. [30], have significantly improved ionic conductivity, lithium stability and redox activity, leading to longer cycle life and higher capacity. Additionally, research by Song et al. [31] demonstrated that using a 3D garnet network composite polymer electrolyte enhances the performance of solid-state Li-air batteries, paving the way for more efficient and durable energy storage solutions.

4. **Lithium-Sulphur Battery:** Polymer electrolytes are being explored for lithium-sulphur (Li-S) batteries, which have a sulphur-based cathode and offer high

energy density, making them ideal for electric vehicles and renewable energy storage. One major challenge with Li-S batteries is stability, but recent research has led to significant improvements. For example, adding special polymers like poly(sulfur-1,3-diisopropenylbenzene) (PSD) into a P(VDF-HFP) polymer matrix has helped to improve ionic conductivity. Scientists have also developed flame-retardant polymer electrolytes to make these batteries safer. Another breakthrough involves using in situ electrochemical polymerization to create a non-flammable polyether electrolyte, which enhances lithium compatibility and improves battery performance. These innovations have led to higher capacity, faster charging, and longer battery life, making Li-S batteries a promising option for the future [32].

Fundamental Challenges in Lithium-ion Batteries

The development of next-generation lithium-ion (Li-ion) batteries faces several fundamental challenges that must be addressed to improve energy density, longevity and safety.

1. **Electrode-Electrolyte Interface Stability:** The formation of a stable solid electrolyte interphase (SEI) is crucial for battery performance, yet its composition and long-term stability remain poorly understood. Electrochemical side reactions with high-capacity cathodes can degrade electrolytes, reducing efficiency.

2. **Dendrite Formation and Safety Risks:** Lithium metal anodes can develop dendrites, which may lead to short circuits, overheating or even battery failure. Advanced solid-state electrolytes or protective coatings are needed to mitigate this issue.

3. **Limited Cycle Life:** High-capacity electrode materials, such as silicon and tin, suffer from significant volume expansion and contraction during charge-discharge cycles, causing mechanical stress and cracking, which reduces battery lifespan.

4. **Electrochemical-Mechanical Coupling:** Mechanical failure due to expansion, stress, and defects in solid-state electrolytes can hinder ion transport and overall battery performance. Understanding how electrochemical and mechanical properties interdepend is essential for improving battery durability.

5. **Fast Charging Limitations:** High charging rates can lead to lithium plating on the anode, reducing efficiency and increasing safety risks. New materials and electrolyte formulations are needed to enable safer and faster charging.

6. **Environmental and Cost Constraints:** The reliance on expensive and resource-limited materials like lithium, cobalt and nickel raises concerns about sustainability. Developing cost-effective recycling methods and alternative battery chemistries is crucial for large-scale adoption.

Addressing these challenges requires innovations in material science, interface engineering and electrolyte design to push Li-ion technology toward safer, more efficient and long-lasting energy storage solutions.

Summary and Future Prospective

In this paper, the critical role of polymer-based electrolytes in the advancement of LIB technology has been analysed. The increasing demand for renewable energy sources needs high-performance, safe and reliable energy storage solutions. Traditional liquid electrolytes have enabled LIBs to achieve significant energy densities, but these electrolytes come with safety constraints. Polymer electrolytes offer promising potential to improve the safety and efficiency of LIBs by reducing dendrite growth and enhancing stability. This paper analyses the properties and synthesis methods of various polymer hosts, highlighting how each material contributes to enhanced ionic conductivity and thermal stability are also analysed in detail.

Acknowledgement

The first author, Anjali, is grateful to the University Grants Commission (UGC), New Delhi, Government of India for UGC-JRF (Ref. ID: 231610057729).

References

1. BNEF, New Energy Outlook. Available online: https://www.powertechnology.com/news/bloomberg-new-energy-outlook-2019-2/.
2. BNEF, Electric Vehicle Outlook. Available online: https://about.bnef.com/electric-vehicle-outlook-2020/ (2020).
3. E Fan, L Li, Z Wang, J Lin, Y Huang, Y Yao & F Wu. Chemical Reviews, 120(14): 7020-7063, 2020.
4. Monika, AK Mishra & BS Patial. Journal of Condensed Matter, 1(02): 65-68, 2023.
5. X Lu, Y Wang, X Xu, B Yan, T Wu & L Lu. Advanced Energy Materials, 13(38): 2301746, 2023.
6. K Sashmitha & M Usha Rani. Polymer Bulletin 80: 89-135, 2023.
7. WS Young, WF Kuan & TH Epps III. Journal of Polymer Science Part B: Polymer Physics, 52(1): 1-16, 2014.

8. AM Stephan. European Polymer Journal, 42(1): 21-42, 2006.
9. A Maitra & A Heuer. Physical Review Letters, 98(22): 227802, 2007.
10. GS MacGlashan, YG Andreev & PG Bruce. Nature, 398: 792-794, 1999.
11. Z Li, J Fu, X Zhou, S Gui, L Wei, H Yang & X Guo. Advanced Science, 10(10): 2201718, 2023.
12. Y Meesala, A Jena, H Chang & RS Liu. ACS energy Letters, 2(12): 2734-2751, 2017.
13. W Zhao, J Yi, P He & H Zhou. Electrochemical Energy Reviews, 2: 574–605, 2019.
14. S Ramesh & Lu SC. Journal of Power Sources 185: 1439–1443, 2008.
15. F Deng, X Wang, D He, J Hu, C Gong, Y S Ye & Z Xue. Journal of Membrane Science, 491: 82-89, 2015.
16. AR Polu & HW Rhee. Journal of Industrial and Engineering Chemistry, 31: 323-329, 2015.
17. YL Ni'Mah, MY Cheng, JH Cheng, J Rick & BJ Hwang. Journal of Power Sources, 278: 375-381, 2015.
18. PL Kuo, CA Wu, CY Lu, CH Tsao, CH Hsu & SS Hou. ACS Applied Materials & Interfaces, 6(5): 3156-3162, 2014.
19. W Li, Y Wu, J Wang, D Huang, L Chen, & G Yang. European Polymer Journal, 67: 365-372, 2015.
20. H Yang & N Wu. Energy Science & Engineering, 10: 1643, 2022.
21. S Chai, Z Chang, Y Zhong, Q He, Y Wang, Y Wan, M Feng, Y Hu, W Li & W Wei. Advanced Functional Materials, 33: 2300425, 2023.
22. S Ramesh & Liew C-W. Measurement, 46: 1650–1656, 2013.
23. HS Choe, J Giaccai, M Alamgir & KM Abraham. Electrochimica Acta 40: 2289– 2293, 1995.
24. AM Sukeshini, A Nishimoto & M Watanabe. Solid State Ionics 86–88: 385–39, 1996.
25. H Sung; Y Wang & C Wan. Journal of the Electrochemical Society, 145: 1207–1211, 1998.
26. Z Zhang, D Sherlock, R West, K Amine & L Lyons. Journal of Macromolecules, 36(24): 9176-9180, 2003.
27. S Wang, J Li, T Li, W Huang, L Wang & S Tao. Chemical Engineering Journal, 461:141995, 2023.
28. Y Zhu, C Liu, Y Yang, Y Li & QH Wu. Electrochimica Acta, 446: 142097, 2023.
29. Y Xie, L Feng, D Li, Y Tang, C Zhu, M Wang & J Xu. Colloids and Surfaces A: Physicochemical and Engineering Aspects, 670: 131487, 2023.
30. Y Yoon & MW Shin. Electrochimica Acta, 462: 142763, 2023.
31. S Song, X Qin, Y Ruan, W Li, Y Xu, D Zhang & J Thokchom. Journal of Power Sources, 461: 228146, 2020.
32. J Chattopadhyay, TS Pathak & DM Santos. Polymers, 15(19): 3907, 2023.

A Review on Orthopaedic Biomaterials: Properties, Advances, and Future Directions

Shailja Singh[a], and Manvendra Singh Khatri[b]

Department of Physics, National Institute of Technology Uttarakhand, Srinagar (Garhwal), Uttarakhand- 246174, India.

[a] ds24phj003@nituk.ac.in
[b] mskhatri@nituk.ac.in

Abstract

Orthopaedic biomaterials play a pivotal role in advancing fracture fixation, joint replacement, and dynamic stabilization within orthopaedic applications. Primarily composed of metals, these biomaterials exhibit outstanding properties including high strength, ductility, fracture toughness, hardness, corrosion resistance, durability, and biocompatibility. Despite their versatility, the landscape of orthopaedic implant materials remains dominated by a limited range of metals, ceramics, composites and polymers. However, the durability of these implants is challenged by biological reactions and material degradation caused by wear and electrochemical corrosion. This article examines the developments that have taken place with respect to the biomaterials and their applications as implants in orthopaedic surgery. This encompasses history, types and properties of metals, polymers, ceramics, composite biomaterials, and processes of fabricating them. The characteristics like biocompatibility, mechanical properties, fluid stability, and the ability to induce osseointegration and the relevance of such materials for implants in orthopaedic surgery is also discussed in this article. Special attention is given to the development of novel bioactive metallic materials and their means of improving wear resistance and biocompatibility by changing the surface and applying coats. The scope of the review further covers advanced technologies including smart bio-materials, 3D/4D printing, use of nanotechnology, and prosthetics. Further, the review article discusses the current status and future trends concerning materials for orthopaedic surgery in greater detail.

Keywords: Biomaterials; Orthopaedics; Tissue Engineering; Osseointegration; Prosthetics; Scaffolds; Cytotoxicity.
Received 30 January 2025; First Review 07February 2025; Accepted 20March 2025.

*** Address of correspondence**
Shailja Singh
Department of Physics, National Institute of Technology Uttarakhand, Srinagar (Garhwal), Uttarakhand- 246174, India.

Email: ds24phj003@nituk.ac.in

How to cite this article
Shailja Singh, and Manvendra Singh Khatri, A Review on Orthopaedic Biomaterials: Properties, Advances, and Future Directions, J. Cond. Matt. 2025; 03 (02): 9-16.

Available from:
https://doi.org/10.61343/jcm.v3i02.126

Introduction

In today's rapidly evolving world, orthopaedic concerns are increasing due to accidents, advancing age, and congenital factors. To address orthopaedic fractures and other bone issues effectively, the use of orthopaedic implants and prosthetics are essential. Substance that has been engineered to interact with biological systems for medical purposes, whether therapeutic (e.g., implants, drug delivery systems) or diagnostic (e.g., biosensors) referred as Biomaterials. These materials are typically designed to be compatible with living tissues and can be derived from natural sources, synthetic polymers, metals, ceramics, or composites thereof [1]. As per the evolution there are 3 generations of biomaterials. The First-Generation Biomaterials (1950s-1980s) focused on inertness that did not interact extensively with biological systems. The Second-Generation Biomaterials (1980s-early2000s) focused on improving bioactivity and enhancing interactions with biological tissues. Lastly, the Third Generation Biomaterials (early 2000s-present) emphasizes advanced functionality, tissue regeneration and customization for specific medical applications [1,2]. The selection of biomaterials is based on the specific needs of medical treatments, like orthopaedic implants, dental work, or tissue engineering, to ensure safety, effectiveness, and compatibility [3].

Compatibility of orthopaedic implants with the human body is crucial for successful application in healing, correcting deformities, and restoring lost functions. While advancements in biomaterials and prosthetics have been made, challenges remain in diagnosing infections, and dealing with implant toxicity, corrosion, and wear-and-tear. The development of novel biomaterials and prosthetic devices, with the introduction of nanotechnology, is essential for advancing orthopaedic care, improving patient outcomes, and meeting the evolving healthcare needs of diverse patient populations.

This review offers an overview of diverse medical biomaterials, emphasizing the promising role of metal materials in orthopaedic implants. Methods to enhance the surface biocompatibility of metal materials, such as surface treatments and coating techniques, were reviewed. The discussion also addressed the current limitations of these approaches and outlined future research directions aimed at enhancing their overall effectiveness.

Properties of biomaterials

1. Biocompatibility: By definition, biocompatibility refers to the ability of biomaterials to meet their intended function in a certain clinical setting, particularly within the body of a patient, without inflicting any adverse effects [1]. This ensures that there is maximum success in treatment while protecting the patients as much as possible. Biocompatibility is, therefore, an imperative aspect for the faster placement of new, innovative devices to the healthcare market. The skin irritation and cytotoxicity were the first two testing protocols for material toxicity and skin irritability according to the American Standards and Test Methods International (ASTM) during late 1980s. These standards were later revised by the International Organization for Standards (ISO) [4]. Biocompatibility evaluation involves assessments such as: genotoxicity, cytotoxicity, irritation or intracutaneous reactivity and testing for implantation and hemocompatibility [5,6].

2. Mechanical properties: The mechanical characteristics of biomaterials are the contributing factors to their performance and appropriateness for particular biomedical applications. It includes Young's modulus, ultimate tensile strength, yield strength, ductility, fatigue resistance, corrosion resistance, and fracture toughness [1]. Corrosion resistance is the most crucial property owing to the extreme differences between the body environment and the atmosphere. Metals that withstand oxidation in air might be seen succumbing to internal corrosion within the human body due to body fluids which contain ions that facilitate corrosion. Thus, it is important to look for ways to reduce ion release from metals and at the same time protecting the metals for long lasting periods [6,7].

3. Tribological behaviour: Tribology is a field that examines surface interactions between hard materials in the context of relative motion, emphasizing friction, wear and lubrication [8]. Although rigid material, including brittle ceramic materials can endure external mechanical forces, they are unsuitable for joint implants due to their inefficiency under stress impacts. Therefore, metals and rigid plastics are used instead because of the advantageous properties they possess over time. Presently, regular materials for arthroplasties include blends such as Ceramic-on-UHMWPE, Metallic-on-UHMWPE, Ceramic-on-Ceramic, CoCrMo-on-CoCrMo and Al_2O_3-on-CoCrMo [1,9]. Inadequate friction characteristics can result in excessive wear to the surfaces of an implant causing metal debris shedding into the adjacent tissues. This can provoke unwanted reactions in the tissues and markedly shorten the lifespan of the implant [10].

4. Osseointegration: Osseointegration is a phenomenon where the living bone tissue grows on the implant surface forming a direct structural and functional interaction. It guarantees the stability, functionality, and longevity of the endoprosthesis, especially of orthopaedic and dental implants [11]. Surface is a key factor contributing to the process of osseointegration as it is clearly understood in the review by Geraldo Roberto Martins Matos [12] and Wennerberg [13]. They explained how the surface designs of dental implants affect their integration with the bone, with particular focus on the role of textures and finishes in the implants' performance.

Classification

Biomaterials comprise a varied range of materials [14]. We have categorized biomaterials based on the primary materials they are composed of, as shown in the Figure 1.

1. Metallic Biomaterials

Surgical implants rely heavily on metals and metallic alloys, because of their superior strength, resistance to fracture, interatomic bonding and ease of engineering processes. They are commonly used in orthopaedics, dentistry, peripheral cardiovascular devices, and neurovascular implants. Due to their good electrical conductivity, they are also used in cardiac pacemaker devices for neuromuscular stimulation. Prosthetic devices can be made from a range of metallic biomaterials as per requirements and properties [1,15,16].

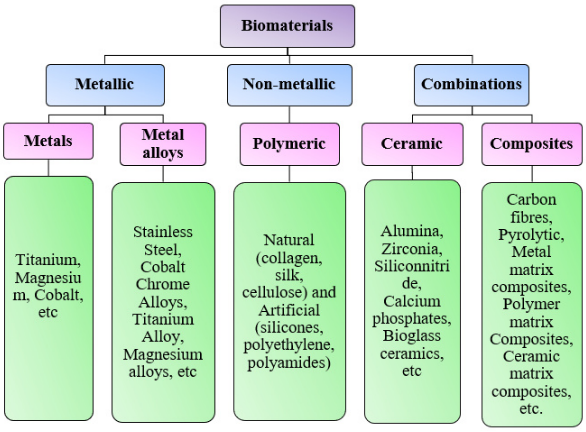

Figure 1: Classification of different types of biomaterials.

316L Stainless Steel: 316L stainless steel (SS) is widely used for the fabrication of implants due to its resistance to corrosion, ease of processing, good mechanical properties, and biocompatibility [14,17]. Due to lesser carbon content than the 316 standards, it reduces the chances of inter-granular corrosion after welding. Despite having many qualities of good biomaterial this stainless steel is prone to corrosion, especially due to chloride ions in blood. The elastic modulus of this SS ranges approximately from 200 to 210 GPa, while that of natural bones ranges from 3 to 20 GPa. Due to this significant difference, it leads to joint separation over a period of time [1,15,18].

Cobalt Chrome: Cobalt Chrome (CoCr) alloys are known for their excellent mechanical properties, corrosion resistance and biocompatibility. They often contain additional metals like nickel, molybdenum, to enhance the overall properties. These alloys are often cast because of their work-hardening tendencies above room temperature, which makes them ideal for hip implant components and dentures. However, these materials can leach toxic ions into the biological environment, potentially causing cancerous growths and other unwanted effects. The elastic modulus of these alloys' ranges up to 220-230 GPa. Due to the significant difference in the elastic modulus between bones and implants, stress shielding occurs, leading to bone atrophy. Altering the surface of cobalt-chromium alloys by direct laser interference patterning has been proved to be as biocompatible as commonplace stent materials. This leads to the possibility of using it for fast endothelialisation while preventing thrombosis in the cardiovascular system [1,17,19].

Titanium and titanium alloys: Since 1960s, titanium and its alloys have been utilized in biomedical fields, from dentistry, cardiovascular, orthopaedics, prosthetics, craniofacial surgeries to reconstructive joint procedures. Titanium and its alloys are valued for their non-reactive nature, biocompatibility, as well as stiffness, and performance reliability over time. Nitinol, a nickel-titanium alloy, enjoys thermal memory, shape recovery properties, and excellent absorption qualities. However, over time it releases nickel ions, which increases toxicity within the biological environment. The β-Titanium alloys have also been developed, which cause minimal stress shielding due to their lower modulus of elasticity as compared to its other states. However, at high temperatures they lose their structure and properties [1,20].

Magnesium and magnesium alloys: It is the most likely candidate material for bone implants and biomedical applications because of its antitoxic nature. Its Young's modulus is also comparable to that of bones, helping to reduce stress shielding effect. They have high cell compatibility with macrophages thus enhancing tissue healing and efficiency of implants performance. Their implants dissolve in physiological environment and are eventually replaced by bones tissues eliminating the need of secondary surgery procedures [21]. Magnesium, being a soft metal, suffers from low corrosion resistance and low mechanical integrity. The excessive bodily corrosion of magnesium and its alloys when implanted in the human body risks inciting pathological reactions discouraging the alloy due to excess loss of mechanical strength and failure of the implants. Surface treatment is a common method to enhance the bioactivity of magnesium alloys and control their degradation rate [22,23].

2. Polymeric biomaterials

Polymeric biomaterials can be natural or synthetic, offers tuneable physical, chemical and biological properties, making them suitable for a variety of medical applications. They exist as bulk materials, coatings and pharmaceutical nanoparticles in drug delivery systems. Natural polymers such as horn, hair and cellulose have been used in medicine for ages, especially in suturing. Some of the major polymeric biomaterials with significance in orthopaedics include polymethyl methacrylate (PMMA), polyether ether ketone (PEEK), polylactide (PLLA) and ultra-high molecular weight polyethylene (UHMWPE). PMMA bone cements are widely used for various purposes such as denture implants, prosthetic bone, skull bone replacements, eye tags and kidney treatment membranes etc. UHMWPE is found in the acetabular components of total hip replacement systems, in the knee joint prosthesis systems, and in polypropylene mesh used for finger joints replacements, intravenous cannulas, and non-absorbable sutures [24]. Besides the dental and orthopaedic implants, silicone and other polymeric biocompatible materials are also used extensively in plastic surgeries [25,26].

3. Ceramics

Ceramic biomaterials are compounds made from metals, non-metals, metal oxides, nitrides, sulphides and carbides. They have high mechanical strength, better corrosion resistance, electrical insulation and chemical stability. There are three categories of ceramic biomaterials based on their interactions with physiological environment: bioinert, bioactive, and bioresorbable [27]. Bioinert ceramics like $A1_2O_3$ (alumina), ZrO_2 (zirconia), Si_3N_4 (silicon nitride) are chemically inert, causing minimal tissue reaction making them safe for use in articular components. They have high wear and compressive strength. The first highly pure alumina, Biolox® was obtained from chemically purified and grounded corundum powders by Erhard Doerre in the beginning of 1974 [28]. Bioactive ceramics such as cellulose and bioactive glasses bond well with bone but are often used as coatings on metal implants due to their inferior mechanical properties. Bioresorbable ceramics include calcium sulphate, calcium phosphates, and porous hydroxyapatite etc. They dissolve in the body and are gradually substituted with new tissue over time. Such materials do not promote inflammation and are effective in treating the bone fracture. Due to similarities between, bioactive and biodegradable ceramics, they are often researched simultaneously [27,29].

Table 1: Comparison of different types of biomaterials.

	Metals and alloys	**Polymers**	**Composites**	**Ceramics**
Type	Cobalt and its alloys, Stainless steel, magnesium and its alloy, titanium and its alloys etc.	Natural (collagen, silk, cellulose) and Artificial (silicones, polyethylene, polyamides)	Metal matrix composite, Ceramic matrix composite and polymer matrix composite	Bioactive, bioresorbable and bioinert
Benefits	High tensile strength, thermally and electrically conductive	Radiolucency, high corrosion resistance, flexibility and adaptability	Customizability and enhanced properties according to the requirement	Excellent hardness, corrosion resistance, non-biodegradable and non-conductive
Issues	Less corrosion resistance, insufficient bio tolerance, material fatigue over time	Low wear resistance, tensile strength and mechanical strength	Complex processing	Brittle, low wear resistance, high stress shielding and less osseointegration
Uses	Joint replacement, spinal implants and bone fixation	Bone fixation, regeneration, and Cartilage, ligament and tendon repairs	Long bone (femur, tibia) fixation and artificial ligaments	Total hip replacement, total knee replacement, spinal implants and dental implants
e.g.	Ti-6Al-4V, Ti6Al7Nb, CoCrMo, 316L, 316LVM Stainless Steel etc.	PMMA, PLA, PVA, PCL, PEEK PVA–PVP co-polymers, UHMWPE etc.	Glass fiber composite, carbon fiber-reinforced polymers (CFRPs), bioactive ceramic composites etc.	Alumina (Al_2O_3), zirconia (ZrO_2), silicon nitride (Si_3N_4) and bioactive glasses etc.

4. Composites

Composites are the materials made up of two or more different constituents: the matrix and the dispersed phase. The matrix is normally ductile, weaker and ultimately surrounds the dispersed phase providing support to it. Together, these combinations climb the overall property of the material. The performance of composites relies on the shape, size and orientation of dispersed phase within the matrix. They offer great variety of mechanical and biological properties, effectively optimizing design and minimizing their impact on surrounding tissue [30]. They are considered beneficial due to their ability to vary elastic properties in order to provide better mechanical integration with bones or tissues but still possess high strength and endurance. For example, a more dynamic insulation system is provided through the use of carbon fibre reinforced epoxy plates. They are thinner and can be used where the support of broken bones is required to hasten their healing without introducing bulky interfaces. Composite biomaterials can be of the following variety of types: Ceramic Matrix Composite, Metal Matrix Composite, Polymer Matrix Composite and the materials known as advanced composites [14].

Methods of Preparation

Table 2: Comparison of methods for preparing biomedical materials.

Methods	**Advantages**	**Limitations**	**Ref.**
Electrodeposition	Cost-effective, protective, less reactive and biocompatible layers formation	Some materials can't be easily deposited and hard control over size	[23]
Solvent Casting with Particulate Leaching	Good control over porosity and cost-effective used in bone and cartilage tissue engineering	Requires optimization, potential toxicity from solvents and gives limited mechanical properties.	[31-33]
Electrospinning	Produces fine, uniform fibers that mimic ECM, high surface area	Scalability issues, complex setup	[33, 34]
3D Bioprinting	Enables complex tissue structures, personalized applications	Maintaining cell viability and functionality	[33,35]
Phase Separation	Good for creating porous structures	Difficult to control pore uniformity	[33,36]
Melt Processing	Suitable for high-strength applications, good for thermoplastics	Limited to thermoplastics, high processing temperatures	[32,33]
Gas Foaming	Environment friendly, suitable for porous structures used in drug delivery and tissue engineering.	Challenges in maintaining pore uniformity	[32,33]
Sol-Gel Process	Produces bioactive ceramic materials, good for coatings	Time-consuming, potential shrinkage during drying	[31]

In order to prepare biomaterials materials, several advanced engineering techniques are employed. These techniques are directed toward achieving certain properties, such as biocompatibility, mechanical strength, or porosity. These techniques can be utilized in designing scaffolds, implants, and drug delivery systems. List of methods employed for preparing biomedical materials are shown in table 2.

Methods of improving biomaterials

Improving biomaterial properties is very crucial for successful integration and functionality in medical applications. Two significant methods to enhance their properties are coating methods and surface treatments.

1) Coating method: Coating methods involve applying a layer of material onto the surface of a biomaterial to improve its properties. Various types of coatings can be employed, including:

a. Biopolymer coating and bioceramic coating: Biopolymers, such as chitosan, alginate, hyaluronic acid, and bioceramics, such as calcium phosphate like dicalcium phosphate dihydrate (DCPD), hydroxyapatite (HA) and fluorinated hydroxyapatite (FHA) are often used for coating biomaterials. This is due to their origin and favourable interactions with biological tissues. These coatings can facilitate cell adhesion, proliferation, and differentiation, thereby improving the overall biocompatibility of the underlying material [37]. For example, chitosan promotes osteoblast adhesion and proliferation, making it a suitable candidate for orthopaedic applications. Calcium phosphate coatings like DCPD helps in bone regeneration, HA and FHA are used to improve resistance to decay, improve biocompatibility and promote osteointegration [38].

b. Hydrogel Coating: Hydrogels are hydrophilic polymer networks that can absorb significant amounts of water. Their coatings can enhance the biocompatibility by providing a softer, more flexible surface that mimics the extracellular matrix (ECM). This mimicry can improve cellular interactions, reduce inflammation, and promote tissue integration [39]. Hydrogels have been particularly effective in promoting cellular behaviour and facilitating drug delivery in various biomedical applications [40].

c. Antibacterial Coating: To reduce the risk of infection associated with implanted biomaterials, antibacterial coatings can be applied. These coatings often incorporate antibacterial agents, such as silver nanoparticles, which release ions that inhibit bacterial growth. This method not only improves biocompatibility but also enhances the longevity and functionality of the implant [41]. Antibacterial coatings have been shown to effectively reduce microbial colonization on surfaces, thus minimizing the chances of implant-related infections [42].

d. Bioactive Glass Coating: Bioactive glasses are a class of biomaterials that can bond with bone and stimulate healing. Coating metallic implants with bioactive glass can enhance their integration with surrounding tissues and promote osteogenesis, making them suitable for orthopaedic applications [3,43]. These coatings can also release ions that stimulate biological responses, improving overall biocompatibility.

2) Surface Treatment: Surface treatment improves the biomaterial by altering the physical and chemical properties at the nano/microscale level. These treatments can affect surface roughness, charge, and chemical composition leading to enhanced biological responses [44]. Some common surface treatment methods include:

a. Plasma-immersion ion implantation: When high voltage is applied to gas, they get ionized producing plasma. These ions are directed to the target substrate. The substrate is provided with high voltage bias attracting positively charged ions from plasma toward itself. The high energy ions cause them to penetrate into the surface of the substrate and hence the surface is modified. This process enhances surface wettability, improves surface roughness, and introduces functional groups that promote cell adhesion and growth. The treated surfaces can interact better with proteins and cells, leading to improved biocompatibility [45].

b. Chemical Modification: Chemical treatments involve altering the surface chemistry of biomaterials by applying various chemicals to introduce specific functional groups. For instance, salinization can be used to create surfaces with amino or carboxyl groups, enhancing protein adsorption and cell attachment. This method is particularly effective for improving the performance of implants in contact with biological fluids [46].

c. Surface Roughening: Creating micro- or nanoscale roughness on the surface of biomaterials can significantly enhance cell adhesion and proliferation. Techniques such as sandblasting, etching, or using laser treatments can create a roughened surface that mimics the natural topography of bone, leading to better osseointegration in orthopaedic and dental implants [12].

d. Biomimetic Approaches: This method aims at developing biomaterials that closely mimic/resemble the structure and functions of biological systems. Mimicking the natural extracellular matrix (ECM) can lead to improve cell attachment, proliferation, and biocompatibility. Techniques such as electrospinning and 3D printing can create fibrous structures resembling the ECM protein, promoting better cellular interactions and tissue integration. Additionally, modifying surfaces to present specific bioactive molecules can guide cellular behaviour, improving healing and integration [44].

Complexities of Biomaterial Implants

I. Due to difference in elastic modulus of biomaterials and bones, stress shielding becomes the major issue related to biomaterials.
II. The loading phase in biomaterials involving cycles of bending, twisting and shearing stresses, presents challenges in fatigue resistance, material degradation, and performance under multi-axial loading conditions.

II. With time many biomaterials start to release ions into the body that are harmful for the organs as well as for blood circulation. Inflammation from surgery or traumatism can usually cause ion deposits, thus making the situation surrounding the implants more severe.

IV. Over time, some of the biomaterials need to be replaced due to the decay or degrade of their properties.

V. The internal body fractures of implants usually become compromised due to the ions deposited from inflammation associated with surgical or injury procedures.

Future Aspects of Biomedical Materials

With the advancements in biomedical materials, several future trends are apparent.

I. Smart Biomaterials: These biomaterials are able to react to external stimuli such as temperature, pH or mechanical stress without harming the internal environment, allowing for customized solutions in medication practices like shape memory polymers. These polymers can change their shapes inside a body using body temperature. The week, self-expanding borne stents and scaffold for tissue regeneration were made from these polymers. Such characteristics of shape memory polymers make them a relevant innovation for future biomedical material design [44,47].

II. Bioprinting and 4D Bioprinting: In spite of the fact that 3D bioprinting has gone a long way into tissue engineering, 4D bioprinting is a relatively new technology that incorporates the time dimension. Thus, the materials that are printed can transform in shape or perform different functions after a period of time. One recent example is 4D bioprinting of aortic valve models that can open and close in response to blood flow [48,49]. This technique can be very beneficial for the advancement of biomaterials.

III. Nanotechnology and nanocoating's: The mechanical strength, wear and tear resistance, corrosion resistance etc. of orthopaedic biomaterials can be increased with the incorporation of nanotechnologies in the biomaterials. For example, HA nanocoating's are done to improve the osseointegration of biomaterials [50,51,52].

IV. Personalized and Patient-Specific Biomaterials: The progress in 3D printing technology and computational modelling has made it possible to create tailored biomaterials for specific patient anatomy. 3D printed implants can be designed for a complicated case of bone reconstruction using the patients CT or MRI scans and other information. Customized biomaterials allow for better adjustment and working efficiency of the device in the patient's body, and consequently minimizing the chances of rejection risk of the implant and its complications. Additionally, utilizing genetic and molecular information in biomaterial design further increases their compatibility with human tissue [53,54].

Conclusion

I. There has been a continuous evolution in the betterment of biomaterials. Metallic biomaterials are still playing their authentic role in orthopaedic implants due to their mechanical stability. Furthermore polymeric, composite, ceramic biomaterials are also being utilised for their biocompatibility, osseointegration and corrosion resistance properties respectively.

II. Surface treatments and coating methods aimed to enhance implant functionality are being utilised for improving biomaterial properties as well as for their customize use. These treatments help to promote better integration with biological tissues, reduce infection risks, and increase the durability of implants.

III. With the advancements in biomedical materials, several future trends are apparent. These consist of the emergence of functional biomaterials or smart biomaterials, better development of bioprinting, and the use of nanotechnology across drug delivery systems and tissue engineering. It is also anticipated that customized and green materials will be integral in enhancing medical technologies of the future.

As ongoing research advances, orthopaedic implants will become increasingly safe, versatile, and tailored to meet the specific needs of patients, offering substantial improvements in both patient care and quality of life.

References

1. Q Chen and G A Thouas, *"Metallic implant biomaterials"*, Materials Science and Engineering: R: Reports, 87:1-57, 2015.
2. M Navarro, A Michiardi, O Castano and J A Planell. JR Soc. Interface, 5: 1137-1158, 2008.
3. M Niinomi, T Narushima and M Nakai, *"Advances in metallic biomaterials"*, Heidelberg, DE: Springer, 2015.
4. A Bruinink and R Luginbuehl, *"Evaluation of biocompatibility using in vitro methods: Interpretation and limitations"*, Tissue Engineering III: Cell-Surface Interactions for Tissue Culture, 117-152, 2012.
5. W H De Jong, J W Carraway and R E Geertsma, *"In vivo and in vitro testing for the biological safety*

evaluation of biomaterials and medical devices", In Biocompatibility and performance of medical devices. Woodhead Publishing, 123-166, 2020.

6. M N Helmus, D F Gibbons and D Cebon, *"Biocompatibility: meeting a key functional requirement of next-generation medical devices"*, Toxicologic pathology, 36(1): 70-80, 2008.
7. W Jin and P K Chu, *"Orthopedic implants"*, Encyclopedia of biomedical engineering, 1(3): 425-439, 2019.
8. F Findik, *"Latest progress on tribological properties of industrial materials"*, Materials & Design, 57: 218-244, 2014.
9. S Tkachenko, et al. *"Wear and friction properties of experimental Ti–Si–Zr alloys for biomedical applications"*, Journal of the mechanical behavior of biomedical materials, 39: 61-72, 2014.
10. H F Li, J Y Huang, G C Lin and P Y Wang, *"Recent advances in tribological and wear properties of biomedical metallic materials"*, Rare Metals, 40(11): 3091-3106, 2021.
11. S Parithimarkalaignan and T V Padmanabhan, *"Osseointegration: an update"*, The Journal of Indian Prosthodontic Society, 13(1): 2-6, 2013.
12. G R M Matos, *"Surface roughness of dental implant and osseointegration"*, Journal of maxillofacial and oral surgery, 20: 1-4, 2021.
13. T Albrektsson and A Wennerberg, *"On osseointegration in relation to implant surfaces"*, Clinical implant dentistry and related research, 21: 4-7, 2019.
14. A J Festas, A Ramos and J P Davim, *"Medical devices biomaterials–A review"*, Proceedings of the Institution of Mechanical Engineers, Part L: Journal of Materials: Design and Applications, 234(1): 218-228, 2020.
15. X Duan, et al. *"Research progress of metal biomaterials with potential applications as cardiovascular stents and their surface treatment methods to improve biocompatibility"*, Heliyon, 10(4), 2024.
16. G Szczęsny, et al. *"A review on biomaterials for orthopaedic surgery and traumatology: from past to present"*, Materials, 15(10): 3622, 2022.
17. D Pathote, D Jaiswal, V Singh and C K Behera, *"Optimization of electrochemical corrosion behavior of 316L stainless steel as an effective biomaterial for orthopedic applications"*, Materials today: proceedings, 57: 265-269, 2022.
18. C Morsiya, *"A review on parameters affecting properties of biomaterial SS 316L"*, Australian Journal of Mechanical Engineering, 20(3): 803-813, 2022.
19. P E Lushchik, et al. *"Co-Cr alloys for biocompatible medical products"*, In E3S web of conferences (Vol. 452, p. 05015). EDP Sciences, 2023.
20. P Pesode and S Barve, *"A review-metastable β titanium alloy for biomedical applications"*, Journal of Engineering and Applied Science, 70(1): 25, 2023.
21. Y Chen, J Dou, H Yuand C Chen, *"Degradable magnesium-based alloys for biomedical applications: The role of critical alloying elements"*, Journal of Biomaterials Applications, 33(10): 1348-1372, 2019.
22. S Virtanen, *"Biodegradable Mg and Mg alloys: Corrosion and biocompatibility"*, Materials Science and Engineering: B, 176(20): 1600-1608, 2011.
23. Y Song, S Zhang, J Li, C Zhao and X Zhang, *"Electrodeposition of Ca–P coatings on biodegradable Mg alloy: in vitro biomineralization behavior"*, Acta Biomaterialia, 6(5): 1736-1742, 2010.
24. M J Kasser, *"Regulation of UHMWPE biomaterials in total hip arthroplasty"*, Journal of Biomedical Materials Research Part B: Applied Biomaterials, 101(3): 400-406, 2013.
25. S M Kurtz and J N Devine, *"PEEK biomaterials in trauma, orthopaedic, and spinal implants"*, Biomaterials, 28(32): 4845-4869, 2007.
26. K L Ong, B M Yun and J B White, *"New biomaterials for orthopaedic implants"*,Orthopaedic Research and Reviews: 107-130, 2015.
27. S Punj, J Singh and K J C I Singh, *"Ceramic biomaterials: Properties, state of the art and future prospectives"*, Ceramics International, 47(20): 28059-28074, 2021.
28. P Dalla Pria, *"Evolution and new application of the alumina ceramics in joint replacement"*, European Journal of Orthopaedic Surgery & Traumatology, 17(3): 253-256, 2007.
29. M Bohner, *"Bioresorbable ceramics"*, Degradation rate of bioresorbable materials: 95-114, 2008.
30. M K Egbo, *"A fundamental review on composite materials and some of their applications in biomedical engineering"*, Journal of King Saud University-Engineering Sciences, 33(8): 557-568, 2021.
31. S Murugan and S R Parcha, *"Fabrication techniques involved in developing the composite scaffolds PCL/HA nanoparticles for bone tissue engineering applications"*, Journal of Materials Science: Materials in Medicine, 32(8): 93, 2023.
32. A Prasad, M R Sankar and V Katiyar, *"State of art on solvent casting particulate leaching method for orthopaedic scaffoldsfabrication"*, Materials Today: Proceedings, 4(2): 898-907, 2017.

33. E Babaie and S B Bhaduri,*"Fabrication aspects of porous biomaterials in orthopaedic applications: A review"*, ACS Biomaterials Science & Engineering, 4(1): 1-39, 2018.
34. Q Song, S Prabakaran, J Duan, M Jeyaraj, S Mickymaray, A Paramasivam and M Rajan, M,*"Enhanced bone tissue regeneration via bioactive electrospun fibrous composite coated titanium orthopaedic implant"*, International Journal of Pharmaceutics, 607: 120961, 2021.
35. M Meng, J Wang, H Huang, X Liu, J Zhang and Z Li. *"3D printing metal implants in orthopaedic surgery: methods, applications and future prospects"*, Journal of orthopaedic translation, 42: 94-112, 2023.
36. F Yang, X Qu, W Cui, J Bei, F Yu, S Lu and S Wang,*"Manufacturing and morphology structure of polylactide-type microtubules orientation-structured scaffolds"*, Biomaterials, 27 (28): 4923-4933, 2006.
37. J R Smith, D A Lamprou, C Larson and S J Upson,*"Biomedical applications of polymer and ceramic coatings: a review of recent developments"*, Transactions of the IMF, 100(1): 25-35, 2022.
38. R Maurya, A R Siddiqui and K Balani,*"In vitro degradation and biomineralization ability of hydroxyapatite coated Mg-9Li-7Al-1Sn and Mg-9Li-5Al-3Sn-1Zn alloys"*, Surface and Coatings Technology, 325: 65-74, 2017.
39. C Hachimi Alaoui and A Fatimi,*"A 20-year patent review and innovation trends on hydrogel-based coatings used for medical device bio fabrication",* Journal of Biomaterials Science, Polymer Edition, 34(9): 1255-1273, 2023.
40. H Chen, et al. *"Progress in surface modification of titanium implants by hydrogel coatings"*, Gels, 9(5): 423, 2023.
41. L Zhao, et al. *"Antibacterial nano-structured titania coating incorporated with silver nanoparticles"*, Biomaterials, 32(24): 5706-5716, 2011.
42. C L Romanò, et al. *"Antibacterial coating of implants in orthopaedics and trauma: a classification proposal in an evolving panorama"*, Journal of orthopaedic surgery and research, 10: 1-11, 2015.
43. S Lopez-Esteban, et al. *"Bioactive glass coatings for orthopedic metallic implants"*, Journal of the European Ceramic Society, 23(15): 2921-2930, 2003.
44. S Devgan and SS Sidhu,*"Evolution of surface modification trends in bone related biomaterials: A review"*, Materials Chemistry and Physics, 233: 68-78, 2019.
45. T Lu, Y Qiao and X Liu,*"Surface modification of biomaterials using plasma immersion ion implantation and deposition",* Interface focus, 2(3): 325-336, 2012.
46. W Sun, W Liu, Z Wu and H Chen,*"Chemical surface modification of polymeric biomaterials for biomedical applications"*, Macromolecular Rapid Communications, 41(8), p.1900430, 2020.
47. B K M B Alemu Reta and T Tesfaye,*"Smart and intelligent biomaterials for novel applications–a review"*, International Journal of Polymeric Materials and Polymeric Biomaterials, 74(2): 140-158, 2025.
48. C Shen and A Shen,*"4D printing: innovative solutions and technological advances in orthopedic repair and reconstruction, personalized treatment and drug delivery"*, BioMedical Engineering OnLine, 24(1): 5, 2025.
49. E Yarali, et al. *"4D printing for biomedical applications"*, Advanced Materials, 36(31): 2402301, 2024.
50. J Yazdani, et al. *"A short view on nanohydroxyapatite as coating of dental implants"*, Biomedicine & Pharmacotherapy, 105: 553-557, 2018.
51. S Kumar, et al. *"Nanotechnology-based biomaterials for orthopaedic applications: Recent advances and future prospects"*, Materials science and engineering: C, 106: 110154, 2020.
52. W Liang, et al. *"Current developments and future perspectives of nanotechnology in orthopaedic implants: an updated review",* Frontiers in Bioengineering and Biotechnology, 12: 1342340, 2024.
53. Y Lu. *"Toward fully automated personalized orthopedic treatments: innovations and interdisciplinary gaps"*, Bioengineering, 11(8): 817, 2024.
54. M Kouhi, et al. *"Recent advances in additive manufacturing of patient-specific devices for dental and maxillofacial rehabilitation"*, Dental Materials, 2024.

Review Study of Some Sillen Structure Chloride Phosphor Materials

Rashmi V. Pandey[1,a], Halim S. Ahamad[1,b], Supriya Kshetrapal[1,c], and Nilesh Ugemuge[2,d]

[1] *Saint Francis De Sales College Seminary Hills Nagpur, Maharashtra, India.*
[2] *Anand Niketan College of Science, Arts and Commerce, Warora, Maharashtra, India.*

[a] rashmipandey2021@gmail.com
[b] ngp2k10@gmail.com
[c] supriyaksh83@gmail.com
[d] nileshugemuge@gmail.com

Abstract

Silicates and halides have long been recognized as effective luminescent materials, each with distinct advantages and disadvantages. Silicates are stable but require higher synthesis temperatures, while halides are more suitable for applications like optically stimulated luminescence and scintillation due to their lower melting points and the importance of defects and colour centres. However, most halides, except for fluorides, are quite hygroscopic, which can affect their stability in ambient conditions and necessitate protective measures. Sillen structure lattices present a promising alternative, as they can be synthesized at significantly lower temperatures than silicates and are less hygroscopic than their halide counterparts. Despite their potential, research on sillen structure has not been as extensive as that on silicates and halides. This review aims to summarize existing studies on the synthesis, crystal structures, and luminescence of various Sillen structure chloride phases, encouraging further research in this area.

Keywords: Silicates, Halides, Sillen structure chloride, Synthesis, Crystal structures & Luminescence.
Received 31 January 2025; First Review 03 March 2025; Accepted 19 March 2025.

*** Address of correspondence**
Rashmi V. Pandey
Saint Francis De Sales College Seminary Hills
Nagpur, Maharashtra, India.

Email: rashmipandey2021@gmail.com

How to cite this article
Rashmi V. Pandey, Halim S. Ahamad, Supriya Kshetrapal, and Nilesh Ugemuge, Review Study of Some Sillen Structure Chloride Phosphor Materials, J. Cond. Matt. 2025; 03 (02): 17-20.

Available from:
https://doi.org/10.61343/jcm.v3i02.128

Introduction

Halides are extremely effective luminous materials that are commonly employed in optically stimulated luminescence (OSL), thermoluminescence (TL), and scintillation due to their ability to generate defects, colour centres, and excitons. Halides have a low melting point, which provides advantages; nonetheless, their hygroscopic nature, with the exception of fluorides, necessitates preventive measures for stability under ambient settings [1].

Chloride-based phosphors, which are a subgroup of halides, are gaining popularity due to their distinct optical features and versatility. They have uses in lighting, high-performance displays, radiation detection (for example, PET scans), dosimetry, and sophisticated technologies like quantum dots and nanophotonics. Their low synthesis temperatures enable devices that are both energy efficient and sustainable. However, their hygroscopic nature restricts their use in humid situations, prompting further study to increase stability and widen applications [1-3].

Sillen bismuth-based oxyhalides, first reported in 1941 [1], are renowned for their catalytic characteristics [2, 3, 11, 12], unusual crystal structures [13-18], and Bi^{3+} luminescence [4-10]. Compounds like $SrBiO_2Cl$, $BaBiO_2Cl$, and $CaBiO_2Cl$ display photoluminescence and radioluminescence, making them suitable for advanced applications. The Sillen X1 series ($ABi^{3+}O_2X$; A = Cd, Ca, Sr, Ba, Pb; X = Cl, Br, I) has three primary crystallographic forms: tetragonal (I4/mmm), orthorhombic (Cmcm), and monoclinic (P21/m) [19], making it valuable for efficient and creative luminous materials.

Sillen structures have various advantages, although they have not been investigated as thoroughly as silicates and halides. This lack of research has left gap in our understanding of their synthesis methods, crystal structures, and luminous characteristics. This review examines current knowledge on Sillen structure chloride phases, with a focus on their synthesis, crystal characteristics, and luminous activity. By summarizing these findings, the study aims to highlight the unexplored potential of these materials and

Table 1: Summarizes typical synthesis and Characterization for various Bismuth Oxychloride.

Parameters	BaBiO$_2$Cl	CaBiO$_2$Cl	SrBiO$_2$Cl
Synthesis Method	BaCO$_3$+BiOCl, 700-800°C	Varying reactants calcination 600-800°C	SrCO$_3$+BiOCl, 700-800°C
Crystal Structure	Orthorhombic (Cmcm)	Monoclinic (P2$_1$/m)	Orthorhombic (Cmcm)
Doping Effects	Maintains phase purity	Lattice distortion with Ag, Co, Ni doping	Bi^{3+} active in photocatalysis
Bandgap	2.53 eV-3.71 eV	2.5 eV – 3.4 eV	2.88 eV – 3.52 eV
Photocatalytic Activity	Enhanced by Doping	Improved with metal doping	Superior dye degradation, better charge separation
PL Characteristics	Strong emission, red up conversion (doped), reduced at high Temperature	Blue shift with calcination temperature	Blue shifted emission, stable luminescence.

stimulate future research to widen their applications in advanced luminous technologies.

Materials and Methods: Bismuth Based Oxyhalides

1. Barium Bismuth Oxychloride (BaBiO$_2$Cl)

Several researchers studied BaBiO$_2$Cl using solid-state methods, commonly heating BaCO$_3$ and BiOCl at temperatures ranging from 700-800 °C [20-25]. X-ray diffraction (XRD) investigation indicated that the compound had an orthorhombic structure with the Cmcm space group, and doping was discovered to maintain phase purity [21, 23, 25]. SEM images show that pure BaBiO$_2$Cl is made up of layer-stacked nanoplates, while doped samples have more irregular morphologies [21, 23]. Optical studies revealed bandgaps ranging from 2.53 eV to 3.71 eV, with doping improving light absorption and photocatalytic activity [21–25]. Photoluminescence (PL) studies revealed strong emissions and red upconversion luminescence in doped samples, while the intensity reduced with increasing temperature [20, 23, 24]. These findings demonstrate the potential of BaBiO$_2$Cl for photo catalytic and luminescent applications.

2. Calcium Bismuth Oxychloride (CaBiO$_2$Cl)

Several researchers studied of CaBiO$_2$Cl using multiple solid-state techniques, employing different reactants and calcination conditions [20, 22, 26, 29]. X-ray diffraction (XRD) study confirmed its monoclinic structure (P2$_1$/m). Doping with Ag, Co, and Ni caused lattice aberrations and enhanced light absorption. FESEM and SEM showed plate-like morphologies in pure CaBiO$_2$Cl, whereas doped samples had lower particle sizes [27-28]. Optical evaluation with UV-Vis DRS and FTIR revealed lower bandgaps ranging from 2.5 to 3.4 eV, resulting in increased photocatalytic performance, particularly in metal-doped samples under visible light [26–28]. Photoluminescence investigations revealed blue shift in emission spectra as calcination temperatures increased [26]. These findings emphasize the tunable photocatalytic capabilities of CaBiO$_2$Cl, particularly when doped with metals.

3. Strontium Bismuth Oxychloride (SrBiO$_2$Cl)

Several researchers studied of SrBiO$_2$Cl utilizing several solid-state techniques and conditions [21-22, 24, 29, 30]. Characterization studies revealed an orthorhombic structure (Cmcm space group) with high crystallinity and no detected impurities [20-30]. The Rietveld refinement analysis revealed a layered structure comprised of alternating [SrBiO$_2$]$^+$ and Cl$^-$ layers, with Bi^{3+} ions playing a substantial role in photocatalytic activity [20-22, 29-30]. SEM and FESEM images revealed a layered nanoplate morphology [21]. Optical studies using UV-Vis DRS revealed bandgaps ranging from 2.88 to 3.52 eV, allowing for photocatalysis driven by both UV and visible light. The photoluminescence investigation revealed blue-shifted emission, reduced charge recombination, and steady luminescence [20-21, 24, 30]. Photocatalytic tests showed that SrBiO$_2$Cl is more effective than BaBiO$_2$Cl for dye degradation due to better charge separation and enhanced hydroxyl radical production [21-22, 30]. These findings emphasize SrBiO$_2$Cl's potential for enhanced photocatalytic and optoelectronic applications [20, 24].

Conclusion

BaBiO$_2$Cl, CaBiO$_2$Cl, and SrBiO$_2$Cl are promising compounds for photocatalysis and luminescence applications, each with its own advantages and limitations. BaBiO$_2$Cl has stable photocatalytic activity under UV light for organic pollutant degradation and strong luminescent characteristics, with potential applications in anti-counterfeiting, bioimaging, and photodynamic treatment. CaBiO$_2$Cl's photocatalytic effectiveness is boosted via structural changes and doping techniques, resulting in improved pollutant degradation and light absorption. SrBiO$_2$Cl's improved hydroxyl radical production enhances photocatalytic performance under UV light and demonstrates promising luminous capabilities for light-emitting devices.

Together, these compounds provide a broad platform for environmental remediation, innovative materials, and energy applications. Future study on $BaBiO_2Cl$, $CaBiO_2Cl$, and $SrBiO_2Cl$ should focus on enhanced doping methods, hybrid structures, and composites to improve photocatalytic efficiency, light absorption, and charge separation. Furthermore, research into their potential applications in environmental remediation, optoelectronics, energy harvesting, and sustainable luminous devices is critical for large-scale, multifunctional utilization.

References

1. Sharma, K., & Moharil, S. V. (2023), *"Review of chlorosilicates as phosphor hosts"*, Crystal Research and Technology, 58(1), 2200272. https://doi.org/10.1002/crat.202200272.
2. Sillen, L. G. (1941), Rontgenuntersuchung von Calcium/Wismutoxychloriden und -oxybromiden. Zeitschrift für anorganische und allgemeine Chemie, 248(1), 121. https://doi.org/10.1002/zaac.19412480203.
3. Thomas, J. M., Ueda, W., Williams, J., & Harris, K. D. M. (1989), *"New families of catalysts for the selective oxidation of methane"*, Faraday Discussions of the Chemical Society, 87, 33. https://doi.org/10.1039/DC9898700033.
4. Burch, R., Chalker, S., Loader, P., Thomas, J. M., & Ueda, W. (1992), *"Investigation of ethene selectivity in the methane coupling reaction on chlorine-containing catalysts"*, Applied Catalysis A: General, 82(1), 77–90, https://doi.org/10.1016/0926-860X(92)80185-9.
5. Blasse, G., & Bril, A. (1968), *"Investigations on Bi^{3+}-activated phosphors"*, The Journal of Chemical Physics, 48(1), 217–222, https://doi.org/10.1063/1.1667890.
6. Dieguez, E., Arizmendi, L., & Cabrera, J. M. (1985), *"X-ray induced luminescence, photoluminescence, and thermoluminescence of $Bi_4Ge_3O_{12}$"*, Journal of Physics C: Solid State Physics, 18(24), 4777–4786. https://doi.org/10.1088/0022-3719/18/24/021.
7. Jacquier, B., Boulon, G., Sallavuard, G., & Gaume-Mahn, F. (1972), *"Bi^{3+} center in a lanthanum gallate phosphor"*, Journal of Solid-State Chemistry, 4(3), 374–378. https://doi.org/10.1016/0022-4596(72)90152-1.
8. Kim, C.-H., Pyun, C.-H., Choi, H., & Kim, S.-J. (1999). *"Luminescence of CaS:Bi"*, Bulletin of the Korean Chemical Society, 20(3), 337–340, https://doi.org/10.5012/bkcs.1999.20.3.337.
9. Moncorgé, R., Jacquier, B., & Boulon, G. (1976), *"Temperature dependent luminescence of $Bi_4Ge_3O_{12}$: Discussion of possible models"*, Journal of Luminescence, 14(5–6), 337–348. https://doi.org/10.1016/0022-2313(76)90003-X.
10. Shionoya, S., & Yen, W. M. (2000), *"The phosphor handbook (Vol. 1)"*, CRC Press. https://doi.org/10.1201/9781420041552.
11. Weber, M. J., & Monchamp, R. R. (1973), *"Luminescence of $Bi_4Ge_3O_{12}$: Spectral and decay properties"*, Journal of Applied Physics, 44(12), 5495–5499. https://doi.org/10.1063/1.1662183.
12. Burch, R., Chalker, S., Loader, P. K., Thomas, J. M., & Ueda, W. (1992), *"Investigation of ethene selectivity in the methane coupling reaction on chlorine-containing catalysts"*, Applied Catalysis A: General, 82(1), 77–90, https://doi.org/10.1016/0926-860X(92)80156-8.
13. Thomas, J. M., Ueda, W., Williams, J., & Harris, K. D. M. (1989), *"New families of catalysts for the selective oxidation of methane"*, Faraday Discussions of the Chemical Society, 87, 33–48. https://doi.org/10.1039/DC9898700033.
14. Charkin, D. O., Berdonosov, P. S., Dolgikh, V. A., & Lightfoot, P. (2003), *"A reinvestigation of quaternary layered bismuth oxyhalides of the Sillen X1 type"*, Journal of Solid-State Chemistry, 175(2), 316–321. https://doi.org/10.1016/S0022-4596(03)00297-4.
15. Dolgikh, V. A., & Kholodkovskaya, L. N. (1992), *"The crystal chemistry of layer metal oxide halides and oxide chalcogenides (Sillén phases)"*, Russian Journal of Inorganic Chemistry, 37(5), 488–496.
16. Fray, S. M., Milne, C. J., & Lightfoot, P. (1997). *"Synthesis and structure of $CaBiO_2Cl$ and $SrBiO_2Cl$: New distorted variants of the Sillén X1 structure"*, Journal of Solid-State Chemistry, 129(1), 115–120, https://doi.org/10.1006/jssc.1996.7245.
17. Kennard, M. A., Darriet, J., Grannec, J., & Tressaud, A. (1995), *"Cation ordering in the Sillén X1-type oxychloride, $BaBiO_2Cl$"*, Journal of Solid-State Chemistry, 117(1), 201–205, https://doi.org/10.1006/jssc.1995.1263.
18. Sillen, L. G. (1939), "*Uber die Struktur der Oxyhalogenide des dreiwertigen Bismuts"*, Zeitschrift für anorganische und allgemeine Chemie, 242(1), 41–62, https://doi.org/10.1002/zaac.19392420105.
19. Sillen, L. G. (1942), *"Uber die Kristallstruktur von BiOCl"*, Naturwissenschaften, 22(15), 318–319. *https://doi.org/10.1007/BF01475647*.
20. Olchowka, J., Kabbour, H., Colmont, M., Adlung, M., Wickleder, C., & Mentre, O. (2016), *"$ABiO_2X$ (A = Cd, Ca, Sr, Ba, Pb; X = Halogen) Sillen X1 series: Polymorphism versus optical properties"*, Inorganic Chemistry, 55(14), 7009–7018. https://doi.org/10.1021/acs.inorgchem.6b01024.
21. Huang, H., Wang, S., Zhang, Y., & Han, X. (2015), *"$MBiO_2Cl$ (M = Sr, Ba) as novel photocatalysts: Synthesis, optical property, and photocatalytic

activity", Materials Research Bulletin, 62, 206–211. https://doi.org/10.1016/j.materresbull.2014.11.032.

22. Lin, X.-P., Huang, F.-Q., Wang, W.-D., Shan, Z.-C., & Shi, J.-L. (2008), *"A series of Bi-based oxychlorides as efficient photocatalysts"*, Key Engineering Materials, 368–372, 1503–1506. https://doi.org/10.4028/www.scientific.net/KEM.368-372.1503.
23. Zhang, Z., & Liang, Y. (2022), *"Synthesis and upconversion luminescence properties of* $BaBiO_2Cl:Yb^{3+}$, Er^{3+} *phosphor"*, Crystals, 12(10), 1465. https://doi.org/10.3390/cryst12101465.
24. Porter-Chapman, Y., Bourret-Courchesne, E., & Derenzo, S. E. (2008), "Bi^{3+} luminescence in $ABiO_2Cl$ (A = Sr, Ba) and $BaBiO_2Br$", Journal of Luminescence, 128, 87–91, https://doi.org/10.1016/j.jlumin.2007.05.007.
25. Peng, J., Peng, Y., Wang, T., Wu, Z., Wang, Q., Li, Y., Yin, Z., Han, J., Qiu, J., Yang, Z., & Song, Z. (2022), *"Enhanced UV–Vis–NIR photocatalytic activity of La-doped* $BaBiO_2Cl$*: Role of oxygen vacancies"*, Journal of Solid-State Chemistry, 314, 123381, https://doi.org/10.1016/j.jssc.2022.123381.
26. Shi, R., Xu, T., Zhu, Y., & Zhou, J. (2012), *"High photocatalytic activity of oxychloride* $CaBiO_2Cl$ *under visible light irradiation"*, CrystEngComm, 14, 6257–6263, https://doi.org/10.1039/c2ce25672j.
27. Feng, Y., Huang, W., Hu, C., Zhao, W., Jiao, P., Zhong, Y., & Zhou, H. (2014), *"Preparation of Ag-modified* $CaBiO_2Cl$ *and its photocatalytic ability under visible light"*, Advanced Materials Research, 955–959, 120–126. https://doi.org/10.4028/www.scientific.net/AMR.955-959.120.
28. Zhu, B.-Q., Hu, C.-H., Feng, Y., Yin, X.-H., Zhong, Y., & Zhou, H.-Y. (2015), *"Synthesis and photocatalytic activity of M-doped* $CaBiO_2Cl$ *(M = Ag, Co, and Ni) under visible light"*, ICMSA 2015 Conference Proceedings, https://doi.org/10.2991/icmsa-15.2015.118.
29. Fray, S. M., Milne, C. J., & Lightfoot, P. (1997), *"Synthesis and structure of* $CaBiO_2Cl$ *and* $SrBiO_2Cl$*: New distorted variants of the Sillén X1 structure"*, Journal of Solid-State Chemistry, 128, 115–120, https://doi.org/10.1006/jssc.1996.7229.
30. Suzuki, H., Kunioku, H., Higashi, M., Tomita, O., Kato, D., Kageyama, H., & Abe, R. (2018), *"Photocatalytic water oxidation by a Sillén-related oxychloride* $PbBiO_2Cl$*"*, Chemistry of Materials, 30, 5862–5869, https://doi.org/10.1039/d3ta00906h.

A Review Study of Magnetic Nano-Particles Synthesis, Characterization Methods and Applications

Manoj Kumar[a], and Genius Walia[b]

Department of Physics, University College of Basic Sciences & Humanities Guru Kashi University, Bathinda, Punjab, India.

[a] manojjt977@gmail.com
[b] waliagenius@gmail.com

Abstract

Magnetic nanoparticles (MNPs) have drawn a lot of interest due to their special qualities, which include large surface area, super para magnetism, and ease of functionalization. These qualities make MNPs perfect for use in electronics, biomedicine, and environmental remediation. This article delivers a critical and nuanced overview, integrating diverse perspectives to advance a deeper understanding of MNP synthesis, characterization, and applications. Typical synthesis methods are covered, such as sol-gel, hydrothermal, thermal decomposition, and co-precipitation. This paper also covers important characterization methods for evaluating the structural and magnetic properties of MNPs, including vibrating sample magnetometry (VSM), X-ray diffraction (XRD), and transmission electron microscopy (TEM). The many uses of MNPs in areas such as environmental pollution control, bio-sensing, and biomedicine are also covered. In addition to offering mechanistic insight into the synthesis, functionalization, and use of MNPs, this thorough analysis also describes the limitations and future possibilities.

Keywords: Magnetic nanoparticles, Synthesis, Characterization, Applications.
Received 27 January 2025; First Review 23 February 2025; Accepted 24 March 2025.

*** Address of correspondence**
Manoj Kumar
Department of Physics, University College of Basic Sciences & Humanities Guru Kashi University, Talwandi Sabo, Bathinda, Punjab, India.
Email: manojjt977@gmail.com

How to cite this article
Manoj Kumar, and Genius Walia, A Review Study of Magnetic Nano-Particles Synthesis, Characterization Methods and Applications, J. Cond. Matt. 2025; 03 (02): 21-26.

Available from:
https://doi.org/10.61343/jcm.v3i02.61

Introduction

The science of manipulating or miniaturizing matter at the atomic and molecular levels and dealing with matter at the scale of one billionth of a meter (1 nm = 10^{-9} m), is known as nanotechnology. In general, the nanoparticle size ranges from 1nm to 100 nm [1]. The prefix "nano" is used to denote "one billionth" of something. Richard Phillips Feynman has been introduced first of all the idea of nanotechnology in the meeting of American Physical Society in December 1959 with his well-known speech, "There's plenty of room at the bottom" [2].

Magnetic nanoparticles (MNPs) are those nanoparticles which shows unique magnetic properties. These nanoparticles have size range from 1 to 200 nanometres and are prepared by the magnetic materials such as nickel, cobalt, iron etc. Today's theoretical foundation for the manufacture and use of magnetic nanoparticles (MNPs) is largely based on Néel's discoveries about the magnetic behaviour of tiny particles. His contributions to solid-state physics and magnetism won him the 1970 Nobel Prize in Physics. Due to unique properties MNPs are used widely in many applications such as biomedicine, data storage and environmental remediation.

In recent years, nanoparticles of magnetic nature have gained numerous attention due to their special qualities and uses. In this study the synthesis, characterization and applications of magnetic nano particles are briefly explained.

Synthesis Methods

Different synthesis methods are utilized to get magnetic nano particles of suitable size, morphology, stability and biocompatibility. All these methods are categorised into three different kinds: -

1. Chemical synthesis methods

2. Physical synthesis methods

3. Biological synthesis methods

Following figure (1) shows a pictorial representation of MNPs synthesis using chemical, physical and biological synthesis methods.

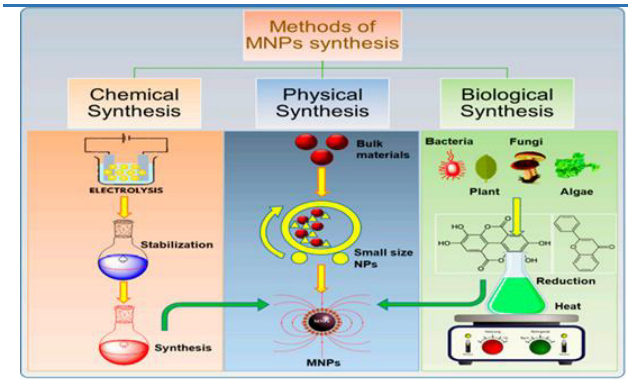

Figure 1: Shows chemical, physical and biological synthesis methods of synthesising magnetic nanoparticles [3].

1. Chemical Synthesis Methods

There are several bottom-up approaches to chemical synthesis for magnetic nano particles. The following are few popular methods typically used to synthesize magnetic nano particles.

1.1 Coprecipitation Synthesis Method

Coprecipitation is the mostly used method for preparing MNPs having controlled size and required magnetic properties [4]. With this method, a base is combined with an inert environment at ambient temperature to combine the Fe (II) ion and Fe (III) aqueous salt solution. Cost-effective, large quantities production and mild condition operation are the advantages of this method. Limited control over particle size and shape, aggregation of prepared nanoparticles and impurities are the disadvantages of coprecipitation method.

Following figure (2) represents the coprecipitation synthesis method for preparation of Fe_3O_4 nano-particles.

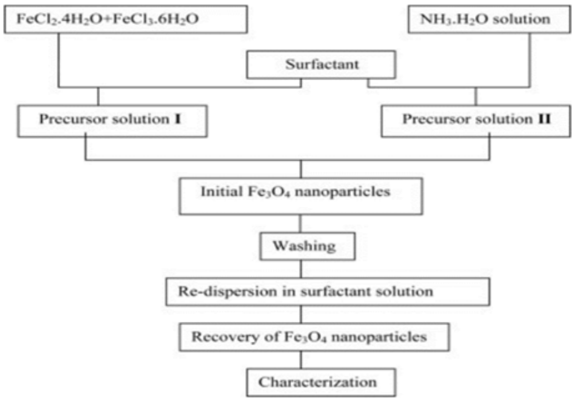

Figure 2: shows the coprecipitation method for preparation of Fe_3O_4 magnetic nano-particles [5].

1.2 Thermal Decomposition Synthesis Method

The thermal decomposition synthesis method is commonly used for synthesis of iron oxide magnetic nanoparticles, particularly Fe_3O_4 and Fe_2O_3, which have various applications. By break down iron precursors with the help of heated natural surfactants, magnetic iron oxide nanoparticle samples with excellent crystallinity and size control have been produced [6]. The iron precursor is dissolved in a suitable solvent with a stabilizing agent such as oleic acid or oleylamine.

This forms a homogeneous solution or suspension. Then the solution is heated under controlled conditions to a specific temperature range, typically between 200°C to 400°C. At high temperatures, the iron precursor undergoes decomposition and release components such as water and organic ligands (if present) and desired iron oxide MNPs formed [7]. This technique has been accounted for as one of the most mind-blowing techniques to create MNPs of uniform size and homogeneous shape in large scale [8]. Disadvantage of this technique are environmental unfriendly synthesis and costly in nature.

1.3 Micro-emulsion Synthesis Method

Hydrophilic and lipophilic phases, which include surfactants and co-surfactants are constituents of micro-emulsions. This fluid is transparent and isotropic and is made up of water, oil, and amphiphile. This method includes mixing of oil and a surfactant to water while stirring them with magnetic stirrer between 100 to 20¬0C.

There are three kinds of micro-emulsions: - a) The fluid stage of oil in water (O/W), which contains some oil drops, b) Water in oil (W/O), wherein water droplets are present but oil is the dominating phase, c) In this type there is equal quantity of oil and water are used. For example, in the micro-emulsion of W/O type, a surfactant was applied to water droplets in organic solvent for shrinking the size of the MNPs [9-10]. This method yields size and shape MNPs, also suitable for coating nanoparticles with surfactants. But low yield, high cost and toxic organic solvent requirement are the disadvantages of micro-emulsion method.

1.4 Hydrothermal Synthesis Method

Various wet-chemical technologies are used in the hydrothermal method to crystallize material in an airtight vessel from an aqueous solution at high temperatures (between 130°C and 250°C) and high vapour pressures of range 0.3 and 4 MPa [11]. The amount to which minerals are soluble in water affects the crystallisation process. This method was used to create uniformly sized particles of several magnetic nanomaterials [12].

Zheng and others used the hydrothermal technique for producing Fe3O4 nanoparticles with the use of Aerosol-OT (AOT) as surfactant [13]. Advantages of this method are pure nanoparticles synthesis, good control over morphology and size and environment friendly also. Time consumption, special equipment requirement are the disadvantages of this method.

1.5 Sol-Gel Synthesis Method

This process produces gels at room temperature by hydrolysing and polycondensing metal alkoxides. Water or another solvent is used to dissolve metallic salts in order to create sol [14]. Because of Van der Waals interactions between the particles, which become increased as the temperature is increased and the mixture is stirred. In the end, gel is produced after the mixture is heated till the solvent has vaporized and the solution is dried out [15-16]. By using the sol-gel method Akbar and others have effectively manufactured α-Fe_2O_3 nanoparticles, and have investigated their magnetic properties [17]. Low processing temperature, high purity and homogeneity and fine nanoparticles production are the advantages of this method. Disadvantages of this method are long processing time for synthesis and high cost of instrument.

2. Physical Synthesis Methods

There are two types of physical methods which are bottom-up and top-down. The present study will cover three physical processes: wire explosion, laser evaporation, and ball milling.

2.1 Ball Milling Method/Mechanical Synthesis Method

High-energy impact grinding, or mechanical milling, can be done in a variety of mills, usually planetary and shaker mills, using balls inside of containers. The components of planetary mills are several cylindrical containers positioned on a rotating platform as shown in following figure (3). Each of the two horizontal rotations around the container axis and the base centre are included in the planetary movements. Shaker mills are often more efficient, but planetary mills offer greater versatility for producing samples in larger quantities. It is an easy-to-understand interaction that produces fine-finished particles by mechanically crushing coarse-finished particles [18-19]. Benjamin and colleagues created this method for the first time in 1970, and it creates homogenous composite particles with a consistent, closely spaced interior structure [20].

Figure 3: contains pictures of planetary and shaker mills.

2.2 Laser Evaporation Synthesis Method

This bottom-up technique involves condensation to synthesize nanoparticles from fluid or vaporous stages [21]. It is also used to manufacture iron oxide MNPs [22]. The raw materials used in this process are selected as coarse finished particles, which are vaporized through with the help of laser light. It is positioned at the base of a cell that has been lowered in a fluid arrangement and identified by laser radiation. A beam of laser light is used for irradiating the substance in the liquid solution. The material's vapours cooled to the gaseous stage, which causes a rapid accumulation and nucleation that results to nanoparticles formation [23].

2.3 Wire Explosion Synthesis Method

The modern physiochemical method of wire explosion produces MNPs in a safe and hygienic manner. This method is really helpful because it eliminates the necessity for retreating results or separating nanoparticles from the arrangement. Iron oxide MNPs were recently designed utilizing this technique to remove arsenic from water [24]. It protects the environment and uses the least amount of energy to create nano powders that are less polluting [25].

3. Biological Synthesis Method

It is renowned method which is used for producing MNPs in green synthesis way, involves microorganisms and plants [26]. This technique produces MNPs that are bio-resorbable and which are widely used in industry of biomedical. This approach has the advantages as efficiency, sustainability, and also environment friendly. While the nanoparticles are poorly dispersed is its drawback [27]. Scientists currently have a lot of interest in developing nanoparticles from plant tissue, concentrates, exudates, and other plant parts [28]. Researchers may have different viewpoints on the method chosen depending on their findings and intended usage. Because of this, there isn't only one method that is thought to be the most effective for producing MNPs. There are drawbacks to each strategy, and the choice is influenced by a variety of factors as size of prepared nanoparticles, their yield, their shape, morphology and experiment's expense.

Characterization Techniques

Characterizing the synthesized magnetic nanoparticles is crucial for understanding their properties and potential applications. Following are few commonly used characterization techniques.

1. X-ray Diffraction (XRD) Technique

- **Purpose:** this technique is used to determine the structural information of synthesized nanoparticles and purity of phase of the nanoparticles.

- **Description:** The diffraction pattern tells information about the crystal lattice parameters and the size of the crystallites.

2. Transmission Electron Microscopy (TEM)

- **Purpose:** this is used to determine the size, shape, and morphology of the synthesized nanoparticles.

- **Description:** High-resolution TEM (HRTEM) can results lattice fringes, providing insight into the crystallinity of the nanoparticles.

3. Atomic Force Microscopy (AFM)

- **Purpose:** AFM is used to determine three-dimensional surface topology, also provide information about particle size & aggregation.

4. Fourier Transform Infrared Spectroscopy (FTIR)

- **Purpose:** FTIR is used to identify the surface functional groups and bonding interactions on the nanoparticles.

- **Description:** This information is essential for understanding the surface chemistry and potential functionalization of the nanoparticles.

5. Vibrating Sample Magnetometry (VSM)

- **Purpose:** To measure the magnetic properties of the nanoparticles.

- **Description:** Properties measured include saturation magnetization, coercivity, and remanence. These are critical for applications in magnetic storage, imaging, and hyperthermia.

6. Thermogravimetric Analysis (TGA)

- **Purpose:** TGA is used to determine thermal stability of prepared MNPs by measuring weight loss with respect to temperature.

The characterization techniques are used according to the desired application purposes. Following Table-1 shows the comparative study of all above discussed techniques with their purposes, advantages and limitations

Application of MNPs

The MNPs in last few years shows their importance on account of their outstanding results in different fields due to their unique properties. The use and applications of MNPs in a few prominent domains, including biomedicine, bio-detecting, climate, farming, and catalysis, have been compiled in this overview. The following is a brief overview of MNP's significant uses in these fields-

1. Biomedicine

Magnetic resonance imaging is improved because of ability of MNPs to interact with external fields and vary the magnetic fields in the surrounding area. Energy dissipation, translation and rotation caused by the many types of force and torque that the external applied magnetic field produces and generates at dipoles. There are numerous applications for such phenomena, such as separation of cells, biomarker development, and magnetic medication delivery, biomedical imaging, the detection of bacteria for theranostics, the induction of drug release, and hyperthermia.

Table 1: Comparative study of magnetic nanoparticle characterization techniques.

Characterization Technique	Purpose	Advantages	Limitations
X-ray Diffraction (XRD)	Structural analysis, phase identification	Non-destructive, provides crystal structure information	Limited for amorphous materials, requires pure samples
Transmission Electron Microscopy (TEM)	Morphology and size analysis	High-resolution imaging, nanoscale analysis	Expensive, requires complex sample preparation
Atomic Force Microscopy (AFM)	Surface topography and mechanical properties	High spatial resolution, non-destructive, works in ambient conditions	Small scan area, slow scanning speed, possible tip-sample interaction artifacts
Fourier Transform Infrared Spectroscopy (FTIR)	Surface chemistry and functional group analysis	Quick analysis, useful for organic coatings	Limited to functional group detection, not quantitative
Vibrating Sample Magnetometry (VSM)	Magnetic property evaluation	Provides precise magnetic measurements	Requires a uniform sample
Thermogravimetric Analysis (TGA)	Thermal stability and composition	Quantifies organic coatings and thermal stability	Cannot analyse individual nanoparticle properties

2. Bio-sensing

MNPs-based sensors have been used in many industries with outstanding results, including food industry, laboratory, medical diagnostics, and environmental observing [29-30]. The biomedical sector has anticipated a broad range of applications for MNP-based biosensors because of its sensitivity, compact size, and exciting non-invasive detecting feature [31].

3. Environment

Because the release of hazardous, chemicals and compounds, degradation and contamination are becoming serious environmental problems. Wastewater, drinking water, ocean, and groundwater all contain various organic contaminants that could have major negative effects on human health [32-33]. It could be necessary to use some more effective methods to improve water quality. Nanotechnology is now being recognized as one of the better and more reliable substitutes for ordinary treatments. Purification of water and air has been reported to use nanomaterials, carbon, and metal oxide [34].

4. Agriculture

Numerous studies have been done demonstrating the effective use of metallic nanoparticles for improving soil quality, germination of seeds, and plant protection [35-36]. Iron oxide magnetic nanoparticles are used as soil nourishment to enhance production with very few losses [37].

5. Energy Storage

Data storage, electrochemical storage, and thermal storage are only a few of the energy storage systems that use MNPs, especially those made of pure metallic elements, because of their large surface area and magnetic features, which improve the efficiency of these systems [38].

6. Catalysis

MNPs have important benefits in the realm of catalysis because of their magnetic characteristics, which make separation and reusability simple. They have been successfully used in a number of catalytic processes, such as photo-oxidation and hydrogenation reactions [39].

Conclusion

The production of magnetic nanoparticles is a difficult process influenced by various parameters. Understanding and optimizing these parameters is crucial for producing nanoparticles with the desired properties for specific applications. This chapter provides a comprehensive summary of different synthesis methods, characterization techniques, laying the foundation for further research and development in this exciting field.

References

1. S Horikoshi and N Serpone, Microwaves in Nanoparticle Synthesis 1st edn (Berlin: Wiley) 2013.
2. R P Feynman, "*There's plenty of room at the bottom"*, Engineering and Science 23, pages 22-36, 1960.
3. A Ali, T Shah, R Ullah, P Zhou, M Guo, M Ovais, Z Tan and Y Rui, "*Review on Recent Progress in Magnetic Nanoparticles: Synthesis, Characterization, and Diverse Applications"*, Front. Chem.9:629054, 2021.
4. S K Vashist, *"Magnetic Nanoparticles-Based Biomedical and Bioanalytical Applications"*, Journal of Nanomedicine & Nanotechnology 04(02) e130, 2013.
5. J Sun, S Zhou, P Hou, Y Yang, J Weng, X Li and M Li, *"Synthesis and characterization of biocompatible Fe_3O_4 nanoparticles"*, Journal of Biomedical Materials Research Part AVolume 80A, Issue 2 p. 333-341, 2007.
6. TK Indira and PK Lakshmi, *"Magnetic nanoparticles - A review"*, International Journal of Pharmaceutical Sciences and Nanotechnology 3, pages 1035–1042, 2010.
7. Y W Jun, J W Seo and J Cheon, *"Nano scaling laws of magnetic nanoparticles and their applicability's in biomedical sciences"*, Accounts of Chemical Research, 41(02), pages 179-189, 2008.
8. J Kudr, Y Haddad, L Richtera, Z Heger, M Cernak, V Adam and O Zitka, *"Magnetic Nanoparticles: From Design and Synthesis to Real World Applications"*, Nanomaterials (Basel), 7(9), 243, 2017.
9. J A L Pérez, M A L Quintela, J Mira, J Rivas and S W Charles, *"Advances in the Preparation of Magnetic Nanoparticles by the Microemulsion Method"*, The Journal of Physical Chemistry B, 101 (41), pages 8045-8047, 1997.
10. J Mosayebi, M Kiyasatfar and S Laurent, Synthesis, *"Functionalization, and Design of Magnetic Nanoparticles for Theranostic Applications"*, Advanced Healthcare Materials, 6(23), 2017.
11. W Wu, Q He and C Jiang C, *"Magnetic Iron Oxide Nanoparticles: Synthesis and Surface Functionalization Strategies"*, Nanoscale Research Letters. 3, pages 397–415, 2008.
12. X Wang, J Zhuang, Q Peng and Y Li, *"A general strategy for nanocrystal synthesis"*, Nature 437(7055), 121-4, 2005.
13. Y Zheng, C Yao, B Feng and Y Wang, *"Synthesis and magnetic properties of Fe_3O_4 nanoparticles"*. Materials Research Bulletin. 41(3), 2006.
14. S A M K Ansari, E Ficiarà, F A Ruffinatti, I Stura, M Argenziano, O Abollino, R Cavalli, C Guiot and F D'Agata, *"Magnetic Iron Oxide Nanoparticles: Synthesis, Characterization and Functionalization for Biomedical Applications in the Central Nervous System"*, Materials, 12(3), 2019.

15. S Hasany, I Ahmed, J Rajan and A Rehman, *"Systematic Review of the Preparation Techniques of Iron Oxide Magnetic Nanoparticles"*, Nanoscience & Nanotechnology. 2, pages 148-158, 2012.
16. M T Mohammed and S Mohammed, *"Synthesis and characterization of nanocoating's derived by sol–gel onto a new surgical titanium surface"*, Materials Research Express, 6(7), 2019.
17. S Akbar, S K Hasanain, N Azmat and M Nadeem, *"Synthesis of Fe_2O_3 nanoparticles by new Sol-Gel method and their structural and magnetic characterizations"*, arXiv preprint condensed matter/0408480, 2004.
18. H J Fecht, E Hellstern, Z Fu and W L Johnson, "Nanocrystalline Metals Prepared by High-Energy Ball Milling", Metallurgical and Materials Transactions A, 21, pages 2333-2337, 1990.
19. M S El-Eskandarany, *"Mechanical Alloying for Fabrication of Advanced Engineering Materials"*, William Andrew Publishing/Noyes, New York, 2001.
20. J S Benjamin, *"Dispersion strengthened superalloys by mechanical alloying, Metallurgical Transactions"*, 1, pages 2943-2951, 1970.
21. P Biehl, M Von der Lühe, S Dutz and FH Schacher, *"Synthesis, Characterization, and Applications of Magnetic Nanoparticles Featuring Polyzwitterionic Coatings"*, Polymers (Basel), 10(1), 91, 2018.
22. D N Shin, Y Matsuda and E R Bernstein, *"On the iron oxide neutral cluster distribution in the gas phase. II. Detection through 118 nm single photon ionization"*, The Journal of Chemical Physics, 120(9), pages 4157–4164, 2004.
23. H Kurland, J Grabow, G Staupendahl, W Andrä, S Dutz and M E Bellemann, *"Magnetic iron oxide nanopowders produced by CO_2 laser evaporation"*, Journal of Magnetism and Magnetic Materials, 311, 73-77, 2007.
24. K Song, W Kim, C Y Suh, D Shin, K S Ko, and K Ha, *"Magnetic Iron Oxide Nanoparticles Prepared by Electrical Wire Explosion for Arsenic Removal"*, Powder Technology, 246, pages 572-574, 2013.
25. Y A Kotov, *"Electric Explosion of Wires as a Method for Preparation of Nanopowders"*, Journal of Nanoparticle Research. 5, pages 539-550, 2003.
26. R Verma, S Pathak, A K Srivastava, S Prawer and S Tomljenovic-Hanic, *"ZnO Nanomaterials: Green Synthesis, Toxicity Evaluation and New Insights in Biomedical Applications"*, Journal of Alloys and Compounds. 876 160175, 2021.
27. A Komeili, *"Molecular Mechanisms of Compartmentalization and Biomineralization in Magnetotactic Bacteria"*, FEMS Microbiology Reviews. 36, pages 232-255, 2012.
28. S Gul, S B Khan, I U Rehman, M A Khan and M Khan, *"A Comprehensive Review of Magnetic Nanomaterials Modern Day Theranostics*", Frontiers in Materials. 6, 179, 2019.
29. J B Haun, T J Yoon, H Lee and R Weissleder, *"Magnetic Nanoparticle Biosensors"*, WIREs Nanomedicine and Nanobiotechnology. 2, pages 291-304, 2010.
30. T A P Rocha-Santos, *"Sensors and Biosensors Based on Magnetic Nanoparticles"*, TrAC Trends in Analytical Chemistry. 62, pages 28-36, 2014.
31. G Chen, I Roy, C Yang and P N Prasad, *"Nanochemistry and Nanomedicine for Nanoparticle-Based Diagnostics and Therapy"*, Chemical Reviews. 116, pages 2826-2885, 2016.
32. Y Jin, F Liu, C Shan, M Tong and Y Hou, *"Efficient Bacterial Capture with Amino Acid Modified Magnetic Nanoparticles"*, Water Research. 50, pages124-134, 2014.
33. J Govan, *"Recent Advances in Magnetic Nanoparticles and Nanocomposites for the Remediation of Water Resources"*, Magnetochemistry 6, 49, 2020.
34. R Baby, B Saifullah and M Z Hussein, *"Carbon Nanomaterials for the Treatment of Heavy Metal-Contaminated Water and Environmental Remediation"*, Nanoscale Research Letters. 14, 341, 2019.
35. Y S El-Temsah, A Sevcu, K Bobcikova, M Cernik and E J Joner, *"DDT Degradation Efficiency and Ecotoxicological Effects of Two Types of NanoSized Zero-Valent Iron (nZVI) in Water and Soil"*, Chemosphere 144, pages 2221-2228, 2016.
36. M Rui, C Ma, Y Hao, J Guo, Y Rui, X Tang, Q Zhao, X Fan, Z Zhang, T Hou and S Zhu, *"Iron Oxide Nanoparticles as a Potential Iron Fertilizer for Peanut (Arachis hypogaea)"*, Frontiers in Plant Science. 7, 815, 2016.
37. S Mishra, C Keswani, P Abhilash, L F Fraceto and H B Singh, *"Integrated Approach of Agri-Nanotechnology: Challenges and Future Trends"*, Frontiers in Plant Science. 8, 471, 2017.
38. N Suresh Kumar, R P Suvarna, K C B Naidu and B V S Reddy, *"Magnetic nanoparticles for high energy storage applications, Fundamentals and industrial applications of magnetic nanoparticles"*, Woodhead Publishing, pages 601–618, 2022.
39. J Govan and Y K Gun'ko, *"Recent Advances in the Application of Magnetic Nanoparticles as a Support for Homogeneous Catalysts"*, Nanomaterials, 4(2), pages 222 -241, 2014.

The Role of Chalcone Derivatives as Potential Antioxidant Additive for Biofuel Applications: A Critical Review

Sankaran Nampoothiri V[a], Sunil Raj R[b], Saji Chandran[c], Lynnette Joseph[d]

Centre for Advanced Functional Materials, Department of Physics, Bishop Moore College, Mavelikara-690110, Kerala, India.

[a] sankarann93@gmail.com
[b] sunilrajharipad@gmail.com
[c] sajichandran23@gmail.com
[d] lynnettejohn@gmail.com

Abstract

The world's energy demands have been rising to unprecedented levels due to the depletion of fossil resources and concerns about global warming. A potential remedy to these challenges is to investigate alternative bioenergy sources while also increasing the efficiency of existing biofuels. Biofuels are renewable energy sources since they are biodegradable fuels made from biomass. Notwithstanding the positive aspects of biofuels, their use can lead to issues such as poor oxidation, inherent stability, and limited energy supply, significantly impacting biofuel consumption, emissions, and energy efficiency. Small molecules, such as chalcone analogs, are good options for additive applications because they are versatile, easy to synthesize, inexpensive, integral materials across various applications, and provide energy for critical chemical reactions. Compounds with potential characteristics such as antioxidant activity and considerable energy availability are eligible to be used as fuel additives. The abundance of antioxidant properties of chalcone molecules is the most significant consideration in their use as additives for biofuels. Antioxidant additives offer numerous benefits, including the reduction of NOx emissions. The current review delves into the synthesis methods and performance of the chalcone molecule as an additive, including comprehensive information on antioxidant mechanisms, oxidation stability studies, antioxidant additives, and energy availability.

Keywords: Chalcone, Biofuels, Antioxidant property, Calorific value, Additive Application.
Received 31 January 2025; First Review 03 March 2025; Accepted 19 March 2025.

*** Address of correspondence**
Lynnette Joseph
Department of Physics, Bishop Moore College
Mavelikara, Kerala, India.

Email: lynnettejohn@gmail.com

How to cite this article
Sankaran Nampoothiri V, Sunil Raj R, Saji Chandran, Lynnette Joseph, The Role of Chalcone Derivatives as Potential Antioxidant Additive for Biofuel Applications: A Critical Review, J. Cond. Matt. 2025; 03 (02): 27-38.

Available from:
https://doi.org/10.61343/jcm.v3i02.139

Introduction

The Energy Institute (EI) published the 72nd edition of the statistical assessment of the global energy study, which found that the world continues to rely on fossil fuel usage, with coal, oil, and natural gas accounting for 80% of the total. In comparison, renewable sources contribute only 8.2% [1]. A few studies have reported on the production statistics of these fossil fuels with oils, coal, natural gas, nuclear energy, hydroelectricity, and others. According to the BP Statistical Review of World Energy, published in June 2009, it is found that 88% of primary energy production comes from fossil fuels, with oil (35%), coal (29%), and natural gas (24%). Nuclear energy accounts for 5% of total primary energy consumption, followed by hydroelectricity at 6% [2].

Fossil fuels are detrimental to the environment and are a major threat to the terrestrial ecosystem. Fuel combustion emits significant amounts of pollutants, including carbon dioxide and carbon monoxide, causing considerable environmental issues and compromising living conditions.

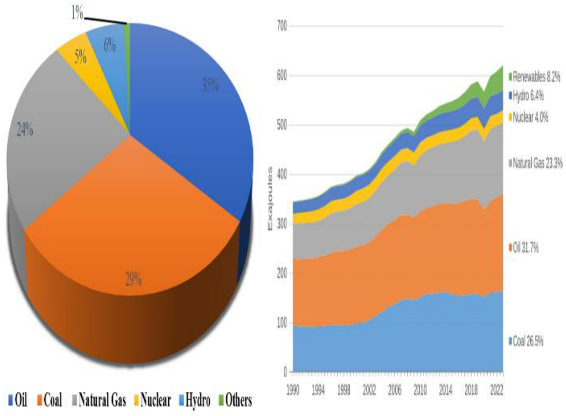

(a) (b)

Figure 1: (a) Production of world primary energy [2] from different sources in 2009 (b) Global primary energy consumption,1990-2023 (reported by the 72nd edition of Statistical Review of World Energy).

Another important consideration is the finite supply of these non-renewable energy sources. This raises a crucial question of how long we will be able to acquire petroleum goods [3], as their availability is a significant global concern. The nearly entire fatigue state of fossil fuels has boosted the scientific community's interest in alternative bioenergy sources with enhanced fuel efficiency [4]. Study findings and evaluations periodically warn of the declining availability of conventional energy sources, like petroleum, natural gas, coal, and massive volumes of environmentally innocuous biomass, which are recommended as viable options to meet energy needs [5].

Biofuels are considered renewable energy sources because they are biodegradable fuels made from biomass [6]. Though the method of producing biofuel from endurable biomass is complicated, extensive research in the area is going on constantly, as they are an excellent alternative to nonrenewable fuels [7]. Renewable fuel will reach 4.6 million barrels of equivalent oil per day in 2040, up from 1.3 million barrels of equivalent oil per day today. This will raise the percentage of biofuels in the global energy matrix [8,9]. The concern is that oxidation, intrinsic stability, and energy availability constraints affect the energetic performance of currently employed biofuels [10]. Furthermore, according to a 2010 study by Lelievald *et al.*, [11] air pollution causes approximately 3 million premature deaths globally. Hence, the need for other options in the case of bioenergy sources is critical, considering the increasing percentage of air pollution caused by motor vehicles, gases from industry, and other factors.

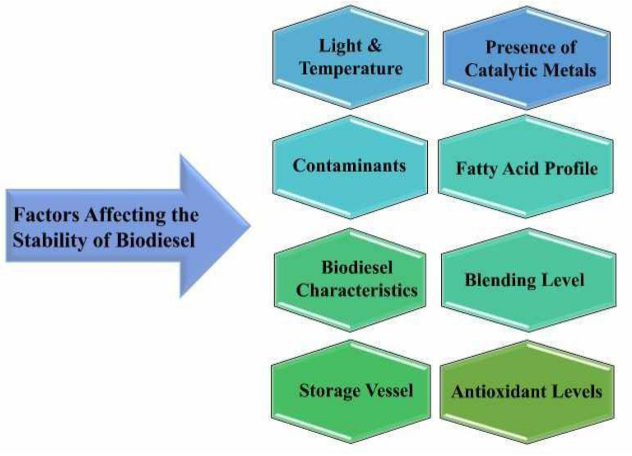

Figure 2: Primary Reasons that affect the efficiency of Biodiesel.

An early-generation biofuel that can be produced from plant or animal sources is biodiesel [12,13]. Biodiesel has caught experts' interest compared to other potential alternative resources due to its numerous benefits [14]. The essential truth is that biodiesel has a lower impact on global warming than fossil-based alternatives due to climate-friendly biogenic carbon dioxide in animal fat and vegetable oil. Biodiesel has more excellent biodegradability, intrinsic lubricity, combustion efficiency, lower aromatic and sulfur content, more remarkable flash point, and higher cetane number than petroleum diesel, which are significant technical and environmental benefits. According to a 2014 study by Oliveira and Coelho [15], ethanol and biodiesel are the primary renewable fuels utilized in land transportation worldwide. The global energy matrix [3] gets increased contribution from biodiesel and ethanol.

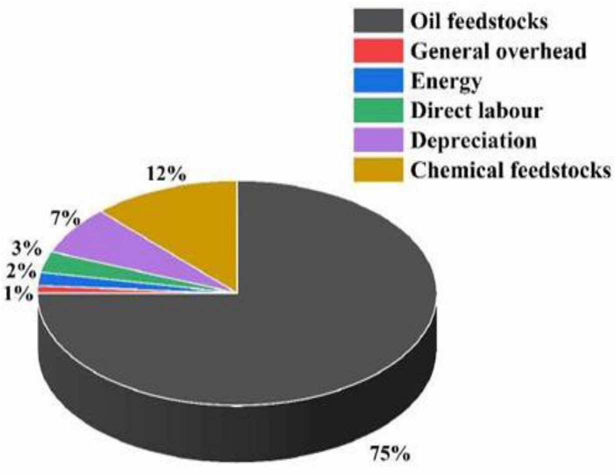

Figure 3: Average cost estimate for producing biodiesel [16–18].

However, a matter of concern lies in the fact that biodiesel's calorific value is 5% lower than that of mineral diesel, and biodiesel engines lose 1-8% of their power [19]. Furthermore, various factors influence biodiesel manufacturing costs, such as chemicals and catalysts, feedstock, etc. The feedstock is the most significant factor, accounting for over 75 percent of the entire production cost of biodiesel. Feedstock selection differs among countries based on agricultural techniques and geography. Type selection and cost-effective feedstock are crucial to reducing the total expense of biodiesel. Aside from the high cost of producing biodiesel fuel, other significant drawbacks exist.

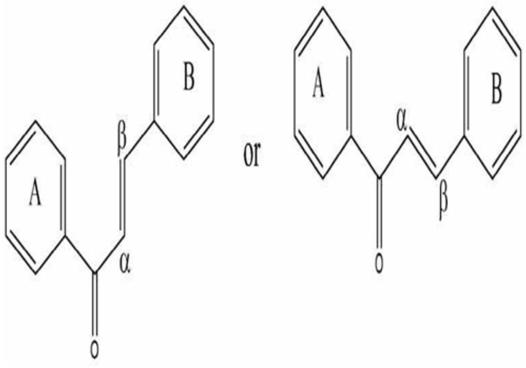

Figure 4: The general structure of chalcones [19].

Having one or more hydroxyl groups is regarded as a significant element in the antioxidant action of chalcones

[20]. It is critical to boost the efficiency of existing fuels while also seeking potential alternative bioenergy sources to meet the world's needs. Here, we emphasize the key elements of the chalcone molecule as a biofuel additive, revealing its potential as the next generation of efficient additives. Three key areas are addressed in the following:

1) Profile of the Chalcone molecule

2) Effects of Antioxidant additives on biofuels

3) Impact of chalcone as an antioxidant additive on biofuel

Basics of Chalcone Derivative

Chalcone's significant role in the synthesis of therapeutic substances, owing to its massive number of replaceable hydrogen atoms that allow for many derivatives, especially into the two aromatic rings, is a key attraction in the twenty-first century. Therapeutic substances such as deoxybenzoins and hydantoins, crucial in pharmacology, are derived from chalcone molecules. Chalcone molecules, also known as alpha beta-unsaturated ketones, contain reactive keto ethylene and are referred to as benzylidine acetophenones or benzalacetophenones. Kostanecki and Tambor deduced that these compounds are members of the chalcone family [21].

The nomenclature of chalcone compounds changes over time. The prime numbers are ascribed to the phenyl ring that wraps around the carbonyl system in the chemical abstract pattern, whereas the British Chemical Abstract pattern and the Journal of the Chemical Society assigned prime numbers to the phenyl ring that is situated away from the carbonyl system [22].

Antioxidant Additives

Several additives are used in biofuels, particularly biodiesel. These include Metal-based additives, Oxygenated additives, Antioxidant additives, Cold flow improver additives, Lubricity improver additives, and Cetane number improver additives [23].

Understanding the roles of these additives is crucial as they can prevent fuel instability and its subsequent outcomes, such as deterioration of appearance, darkening, and accumulation of gums and sediments, and they also affect combustion attributes [24–27]. The outcomes of Ashok et al. [28] Palash et al. [29] showed that adding an antioxidant additive to biodiesel effectively reduced NO_x emissions. Mechanically, these additives primarily block the formation of free radicals (hydroperoxyl (OOH), peroxyl (ROO), and alkoxyl (RO) in readily degradable fuels such as biodiesel, reducing the chances of these free radicals reacting with N_2 or N_2O during fuel storage or combustion and thus reducing NO_x emissions. Various factors, including the composition of the biodiesel, the unsaturation concentration, and the biodiesel blends, determine the additive's concentration. A combination of antioxidant additives can improve fuel stability to the standard specification.

Antioxidant Property of Chalcone Derivatives

The literature shows that numerous chalcone derivatives exhibit significant antioxidant activity. Many chalcones have been synthesized and found to have antioxidant properties due to their versatility in receiving a range of functional groups in their rings. Studies also found that hybrid derivatives had antioxidant characteristics. Yasukazu Ohkatsu et al. investigated chalcone derivatives' antioxidant and photo-antioxidant characteristics and the impacts of hydroxyl groups connected to the molecule's aromatic rings [30]. They synthesized the chalcone molecule using a 1:3 ratio of malonyl-coenzyme A and p-coumaroyl-coenzyme A molecules. The radical-scavenging activity of all chalcone molecules was assessed regarding the number (n) of peroxy radicals caught by a phenolic moiety and the radical-trapping rate constant. The study found that the examined chalcones have good antioxidation properties acquired from the precursor, p-coumaric acid.

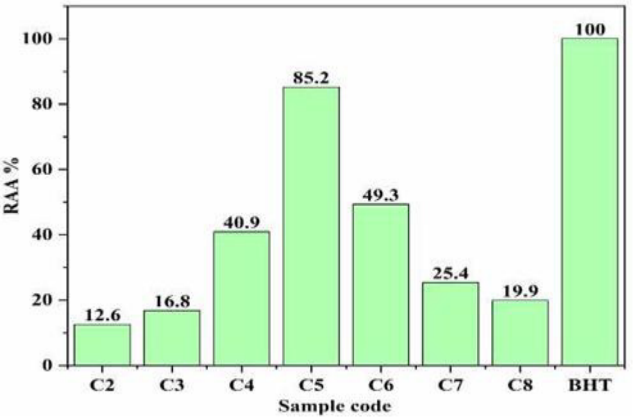

Figure 5: Relative antioxidant activity percentage (RAA %) employing β-carotene-linoleic acid assay.

Munevver Sokmen et al. [31] conducted antioxidant investigations on seven synthetic curcuminoids and one chalcone molecule. DPPH & β-carotene/linoleic acid tests evaluated the compound's antioxidant properties. In the β-carotene-linoleic acid assay, 2,4,6-trihydroxyphenolic chalcone (C5) inhibited the synthesis of conjugated dienes more effectively than all other curcuminoids (C1-7). The chalcone (C5) inhibited the production of conjugated dienes by 85.2%, indicating that the molecule has an increased antioxidant ability. While the synthetic curcuminoids C6 and C4 had the most significant values (49.3% and 40.9%, respectively), the rest had relatively low values, with all of them having a value of less than 30%. So, according to this antioxidant activity assay, the chalcone molecule has higher antioxidant activity than all other curcuminoid samples, with a comparable value of 85.2% to that of the synthetic antioxidant butylated hydroxytoluene (BHT), which inhibits the formation of conjugated dienes by 100 %. The chalcone (C5) has a higher antioxidant value due to its polyphenolic nature, which improves its water solubility and reaction with linoleic acid in the emulsion. This also protects it from oxidation and yields conjugated dienes [31].

The primary explanation for the potent antioxidant nature of chalcone derivatives is associated with the presence of functional groups of various kinds. Arene rings and conjugated double bond systems increase the possibility of electron transfer processes; low redox potentials and various intramolecular interactions contribute to chalcone's high antioxidant activity. The type and position of the substituents connected to a chalcone molecule determine its level of antioxidant capability. Shaifali Singh et al. [32] investigated the antioxidant properties of a series of chalcone derivatives by changing the substituents and measuring all samples using the DPPH method.

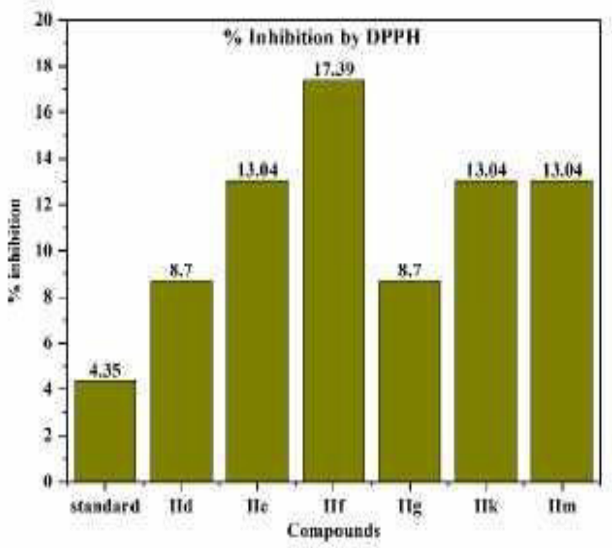

Figure 6: Results of Antioxidant Activity Study with the DPPH Method.

According to the findings, all chalcone derivatives displayed good antioxidant properties. Sample IIf displayed the most robust activity, whereas the IId, IIe, IIg, IIk, and IIm samples showed average antioxidant potential.

Free radical damage generates oxidative stress in the system, which the antioxidants help to regulate. In addition to the phenyl and hydroxyl groups, the presence of vinylene and reactive keto groups in chalcones and their derivatives shows good antioxidative potential. The research findings are given in table 1 [32]. The high degree of variability in the structure of chalcone and aurone molecules can be utilized to evolve novel antioxidants with improved efficacy and lower toxicity. Tamanna Narsinghani et al. [33] executed a comparison analysis to determine the antioxidant potential of chalcone and aurone derivatives.

Table 1: Name and Sample code of the chalcone molecules [32].

Chalcone	Sample Code
1-(2-hydroxyphenyl)-3-(2-methoxyphenyl) prop-2-en-1-one	IId
1-(2-hydroxyphenyl)-3-(4-methoxyphenyl) prop-2-en-1-one	IIe
1-(2-hydroxyphenyl)-3-(2,4-dimethoxyphenyl) prop-2-en-1-one	IIf
3-(2-chlorophenyl)-1-(2-hydroxyphenyl) prop-2-en-1-one	IIg
3-(2,6-dichlorophenyl)-1-(2-hydroxyphenyl)prop-2-en-1-one	IIk
1-(2-hydroxyphenyl)-3-(4-nitrophenyl) prop-2-en-1-one	IIm

All the chalcone compounds were synthesized following the Claisen- Schmidt condensation approach, and aurone was synthesized through oxidative cyclization. Four distinct in vitro investigations were used to assess the antioxidant activity of each sample. Among the chalcone molecules, SB7 (2’,5’-dihydroxy-4- dimethylamino chalcone) showed the most favorable antioxidative properties, especially in the DPPH free radical scavenging assay, iron chelating assay, and reducing power assay.

Similarly, the aurone sample SB8 (5-hydroxy-4’-dimethylamino aurone) demonstrated good antioxidant properties, particularly in iron chelating, hydrogen peroxide scavenging, and reduced power assays. The chalcone sample SB2 (2’,4’-dihydroxy-4-dimethylamino chalcone) and aurone sample SB8 (5-hydroxy-4’- dimethylamino aurone) demonstrated strong antioxidant properties in iron chelation and reducing power tests.

Table 2: Sample code and compound name of all the samples.

Sample Code	Compound
SB1	2’,5’ - Dihydroxy-3,4-dimethoxy chalcone
SB2	2’,4’ - Dihydroxy-4-dimethylamino chalcone
SB3	6 - Hydroxy-4’- dimethylamino aurone
SB4	6- Hydroxy-4’- chloro aurone
SB5	2’,4’- Dihydroxy- 4- chloro chalcone
SB6	5- Hydroxy-3’,4’-dimethoxy aurone
SB7	2’,5’- Dihydroxy-4-dimethylamino chalcone
SB8	5- Hydroxy-4’-dimethylamino aurone
SB9	6- Hydroxy-3’,4’-dimethoxy aurone
SB10	2’,4’- Dihydroxy-3,4-dimethoxy chalcone

The study ultimately found that a specific functional group in the molecule can increase or decrease the antioxidant mechanism. Adding a dimethylamino group to samples SB7 (chalcone) and SB8 (aurone) significantly increases antioxidant activity. Still, including a chloro group reduces activity for chalcone and aurone, specifically SB4 and SB5. The group's attachment to the A-ring (ideally at position 5/5’) gave higher antioxidant properties in the samples [33]. Lucas M. Berneira et al. studied the effect of functional groups in chalcone structures as substituents on antioxidant activity [34]. They synthesized a Chalcone analog using Claisen-Schmidt condensation with moderate to good yields.

Table 3: Antioxidant activity of all the samples using different assays [33].

Sample No.	DPPH scavenging ability IC_{50} µg/ml ± SD	H_2O_2 scavenging ability IC_{50} µg/ml ± SD	Iron chelating activity assay IC_{50} µg/ml ± SD	Reducing power IC_{50} µg/ml ± SD
SB1	132.22 ± 0.7	89.59 ± 1.8	159.22 ± 1.02	111.79 ± 0.69
SB2	65.8 ± 0.7	135.88 ± 0.53	140.16 ± 1.08	53.6 ± 1.1
SB3	109.92 ± 1.02	193.91 ± 0.36	179.33 ± 0.31	70.1 ± 2.2
SB4	266.12 ± 0.49	178.13 ± 0.36	179.18 ± 0.74	188.31 ± 0.31
SB5	264.95 ± 1.6	129.02 ± 0.85	159.97 ± 0.29	155.87 ± 0.68
SB6	222.19 ± 0.7	206.57 ± 0.19	185.05 ± 1.2	151.43 ± 0.25
SB7	24.32 ± 0.87	153.85 ± 2.1	90.81 ± 0.86	47.79 ± 1.3
SB8	243 ± 0.13	174.07 ± 1.9	149.98 ± 0.51	64.16 ± 1.2
SB9	173.29 ± 0.94	248.16 ± 0.76	213.83 ± 0.68	168.23 ± 0.83
SB10	35.2 ± 1.5	70.1 ± 0.92	166.73 ± 2.5	134.45 ± 0.34
Ascorbic acid	98.77 ± 0.53	445.92 ± 1.4	126.12 ± 0.5	53.24 ± 0.72

The presence of hydroxyl groups mainly contributes to an increase in the effect of compounds because these active hydroxyl substituents can delay the formation of hydroperoxides through the transfer of protons that stabilize free radicals in the oil. In contrast, A decreased antioxidant property was observed in chalcone molecules with methoxy groups, which restricts electron capture from the radical. Differential scanning calorimetry noted that hydroxychalcone molecules had antioxidant activity in biodiesel at concentrations of 1250 ppm or higher [34]. Visakh Prabhakar et al. [35] showed that the antioxidant capabilities of chalcones are affected by substituents. The Claisen-Schmidt reaction was used to generate nine monosubstituted chalcone derivatives. The percentage inhibition of the ten target chalcones, including the unsubstituted parent chalcone, was estimated, revealing that ortho derivatives are the most appropriate for antioxidant activity.

Impact of Chalcone as an Antioxidant Additive for Biofuel Applications

Compared to mineral diesel, the most significant difficulty for biodiesel is its higher oxidation tendency, and the risks of microorganism’s proliferation are very substantial in diesel-biodiesel blends [36]. The oxidation of biodiesel triggers a series of reactions in the system. It starts with developing hydroperoxides, which may generate impermeable gums and sediments, causing obstructions on fuel injector nozzles and fuel filters. The mere presence of germs exacerbates the condition by catalyzing the reaction. As a result of oxidation and bacterial products, the process results in increased fuel viscosity. Chalcone's prominent antioxidant properties can be used to mix with biodiesel to improve its oxidative stability. Since it is rarely recorded in the literature, chalcones are versatile compounds because of the aromatic rings in the structure, which allow for substituting numerous functional groups.

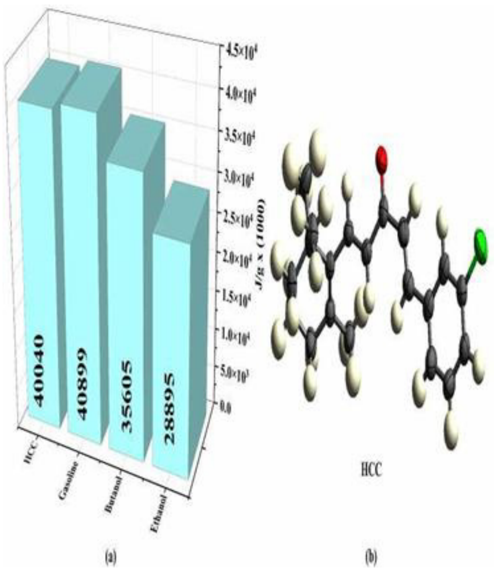

Figure 7: A comparison of the calorific powers of ethanol, butanol, petrol, and HCC. The fuels used were n-butanol, hydrated ethanol, and ordinary type C gasoline [37].

Eduardo Coelho da M. Faria et al. [37] reported the performance of a trimethoxy-chalcone ($C_{18}H_{18}O_4$) utilized as an antioxidant addition for diesel and biodiesel blends. They studied the efficacy of $C_{18}H_{18}O_4$ chalcone as a potential antioxidant addictive, for which it was blended with S10 B20 diesel. They conducted a 140-day storage stability test on S10 B20 diesel blended with $C_{18}H_{18}O_4$ chalcone. The oxidation stability before and after the test was assessed using the accelerated oxidation method (modified Rancimat Method). According to the findings, the accelerated oxidation stability time is enhanced by 50% for chalcone concentrations of 0.05 mg/mL, which is lower than 0.03 mg/mL chalcone concentration. Hence, the chalcone concentration directly influences the fuel's oxidation stability. The HOMO and LUMO energy also reveal the GAP value (241.7 kJ/mol), which shows the high reactional stability for $C_{18}H_{18}O_4$. Because of its remarkable antioxidant activity in diesel S10 B20, the study concluded that chalcone $C_{18}H_{18}O_4$ is a promising option for additive development. They also explored the possible additive application of a chalcone 4-(4-chlorophenyl)-1-[4-(2-oxo-2-phenylethoxy) phenyl]- butan-2-one (HCC), $C_{23}H_{17}ClO_3$. An adequate energy availability and antioxidant effect define a potential additive's performance. Eduardo Coelho da M. Faria et al. [37] compared the calorific energy availability of gasoline, butanol, ethanol, and HCC. The chalcone compound (HCC) showed a significant calorific power value of 40040 j/g, higher than butanol (35605 j/g) and ethanol (28895 j/h) [8], indicating a value comparable to gasoline fuel. There is just a 2.14% distinction between chalcone HCC and gasoline fuel. They found that for biofuels, chalcone HCC is a practical addition and also has a variety of uses, including chemical susceptibility, energy enhancement, and potential biological applications [8]. The calorific power measurement indicates a compound's ability to liberate energy during oxidation, and for fuels, higher calorific power values are related to more remarkable performance, perhaps allowing it to be used as a fuel additive.

Another chalcone compound, namely 1-[3-(2- oxo-2-phenyl-ethoxy)-phenyl]-3-phenyl-propenone (chalcone I) [38], had a calorific value of 12783 kcal/kg when compared to HCC chalcone (chalcone II) [8] molecules and some fuels. The experimental values for fuels such as gasoline, butanol, and ethanol are comparable to those found in the literature [39–41]. The calorific power of chalcone II was found to be 85% larger than that of ethanol (6906 kcal/kg) and around 30% more than that of gasoline (9775 kcal/kg). The value of E_{GAP} was calculated theoretically, showing similar kinetic stability for chalcones I and II, as reported by Eduardo Coelho da M. Faria et al [38]. The E_{GAP} values of chalcone I and chalcone II (599.51 kJ/mol and 602.34 kJ/mol, respectively) were compared to BHT (E_{GAP} = 546.1 kJ/mol) [42], toluene derivatives (E_{GAP} = 477.8 kJ/mol) [43], and thiazolidinone (E_{GAP} = 481.8 kJ/mol) [44]. From the comparison, these chalcones revealed comparable kinetic stability to other additives utilized. The comparison study suggests additional research on the use of chalcones as additives.

Igor D. Borges et al. [45] Performed structural alterations on chalcone molecules abbreviated as BCH and NCH, where the changes are associated with the third aromatic ring of both chalcones. Observations on oxidation stability results via the modified Rancimat method reveal that NCH chalcone performs better than BCH chalcone and S10 B15 without additives samples. Furthermore, the NCH functioned efficiently at lesser concentrations (109.0 ppm (BCH) & 100.7 ppm (NCH)). Both compounds delayed biofuel degradation and retained biofuel characteristics for 90 days without further processing.

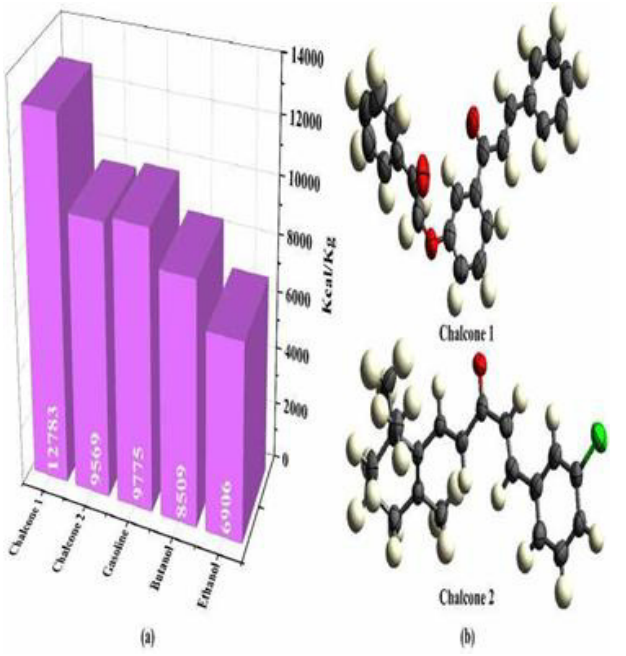

Figure 8: A comparison of the calorific power of chalcones I and II, familiar type C petrol, n-butanol, and hydrated ethanol [38].

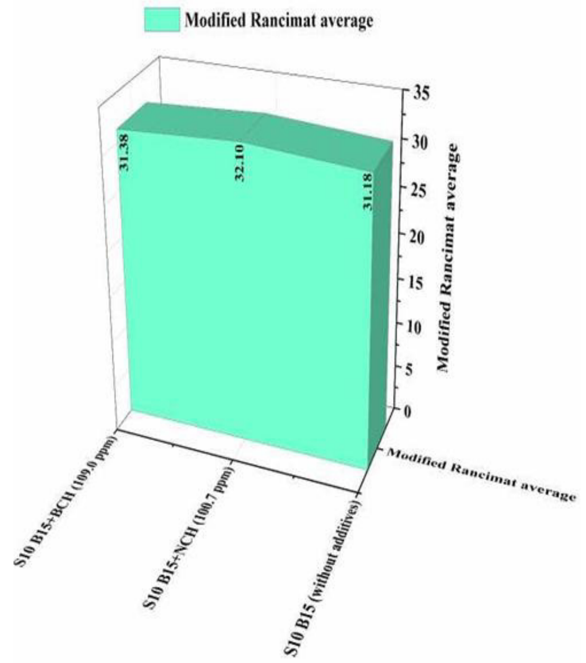

Figure 9: The modified Rancimat approach yields the measurement of oxidation stability of all the samples [45].

The amount of energy freed during the oxidation of a fuel commune to the heat of combustion. The total amount of energy delivered during fuel oxidation is often referred to as the heat of combustion[46].Its higher value indicates more extraordinary fuel performance. It is best to use additives with considerable energy availability.

Arylsulfonamide chalcones had outstanding heat of combustion values comparable to conventional fuels with high energy availability. The oxidative stability results from the Rancimat method showed a stability of roughly 27 hours in a diesel-biodiesel mix (B20) following 140 days of storage. It is superior to certain commercial additives, as reported by Duarte et al. in 2023 [47].

BCH and NCH chalcones have higher kinetic stability and are comparable to other additives. These findings unambiguously showed the practicality of the compounds stated previously (BCH, NCH) as antioxidant additives to diesel-biodiesel mixtures to maintain fuel properties' A. Moreira et al. [48] conducted an oxidative stability comparison study that included a synthetic chalcone TMC20 and a commercial additive after 140 days of stability, utilizing the Rancimat test.

Table 4: Sample identification [48].

Sample	Description (fuel + additive)	Additive concentration	Bottle filling percent
S1	S10 B11 diesel	Free	25 (±0.27) %v/ v
S2	S10 B11 diesel	Free	100 (± 0.07) % v/v
S3	S10 B11 diesel + TMC20	0.03 (±0.002) mg/ mL	25 (± 0.27) %v/ v
S4	S10 B11 diesel + TMC20	0.03 (±0.002) mg/ mL	50 (± 0.14) %v/ v
S5	S10 B11 diesel + TMC20	0.03 (±0.002) mg/ mL	100 (± 0.07) % v/v
S6	S10 B11 diesel + commercial additive	0.5 (±0.08) %v/v	25 (± 0.27) %v/ v
S7	S10 B11 diesel + commercial additive	0.5 (±0.08) %v/v	100 (± 0.07) % v/v
S8	S10 B11 diesel + commercial additive	0.8 (±0.08) %v/v	25 (± 0.27) %v/ v
S9	S10 B11 diesel + commercial additive	0.8 (±0.08) %v/v	100 (± 0.07) % v/v
S10	S10 B11 diesel + commercial additive	1.0 (±0.08) %v/v	25 (± 0.27) %v/ v
S11	S10 B11 diesel + commercial additive	1.0 (±0.08) %v/v	100 (± 0.07) % v/v

It was completed following the regulations provided in standard EN 1575168. The theoretical calculations reveal that the TMC20 has more kinetic stability than other additive compounds. Compared to commercial additives, the performance of TMC20 is inferior since chalcone molecules are used naturally at a relatively low concentration of 0.03 mg/mL without any other type of processing. The chalcone in the fuel+TMC2 mixture preserved the fuel's qualities over 140 days of preservation while postponing the fuel's degradation [48].

From figure 10, samples S3, S4, and S5 correspond to a fuel+ mixture of chalcone TMC20 with the same additive concentration and varying bottle filling percent. The additive does not stop fuel oxidation; rather, it simply postpones it.

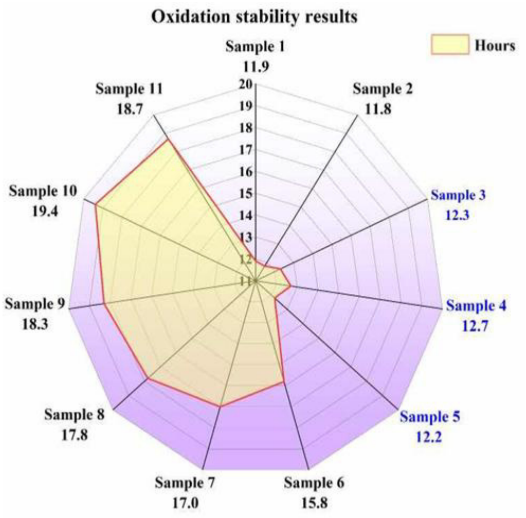

Figure 10: Results of the Rancmat test show oxidation stability following 140 days of stability. According to procedure EN 15751:2014, repeatability r = 0.22027 + 0.0434 (here x is the average of the two measurements that were made) was used to compute the measurement uncertainty represented by error bars [48,49].

The study recommends implementing additives to maintain the fuel's physical and chemical properties while enhancing its stability during storage and using chalcones as a comparable biofuel additive. Loide O Sallum et al. [45,50] reported that cyclohexanone-based chalcones are good alternatives in the field of fuel additives with the chalcones $C_{24}H_{26}O$, $C_{20}H_{14}OCl_4$, and $C_{20}H_{16}OCl_2$ with the sample codes BH I, BH II and, BH III respectively, showing good calorific value.

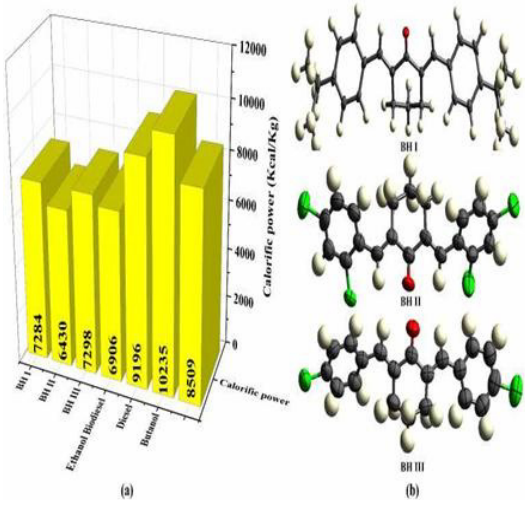

Figure 11: Values of calorific power for chalcone BH I, II, and III and n-butanol, diesel, biodiesel, and hydrated ethanol. The calorific value of biodiesel depends on its composition. (Performed with an average value) [50].

All three chalcones had a calorific value higher than ethanol and slightly lower than biodiesel. The study strongly recommends the additive application of chalcones with fuels.

Discussion

The current research world primarily focuses on methods to strengthen the oxidative stability of biodiesel, such as adding antioxidants to its composition [51]. The capacity of these compounds to prevent or reduce fuel oxidation makes them more widely accepted [52] .The antioxidant activity of chalcone has been noted, where its α, β-unsaturation aryl structure provides an advantage and might have substituents called hydroxyls, which are usually associated with its antioxidant activities. Despite its significant antioxidant properties, adding chalcones as a biodiesel blend has yet to be frequently reported in the literature. The literature characterized the chalcone compounds based on prospective features such as solid energy availability and antioxidant activity. The capacity of chalcones to interact in many different kinds of chemical and biological interactions suggests the usage of biofuels [8]. The compounds' antioxidant activity was assessed using different radical scavenging methods and antioxidant additive analysis, such as rancimat and modified raincoat tests, to analyze oxidation stability. Looking through the literature, it is recognizable that substitutions play a significant role in antioxidant activity in chalcones. Among the replacements, substituting specific functional groups contributes to higher antioxidant activity, with the substitution site being crucial. Diverse functional groups play diverse roles and contribute to antioxidant activity. The presence of double bonds also contributes significantly to the antioxidant properties of chalcones. The synthesis technique, environmental factors, fuel management and storage, and biodiesel components all have an impact on the antioxidant effect.

The energy GAP (E_{GAP}), the theoretically determined absolute difference between HOMO and LUMO applying the Density Functional Method (DFT) of chalcone compounds, exhibits significant antioxidant potential [53]. The antioxidant potential is directly correlated with the energy GAP value [37]. The comparison study of E_{GAP} performance of different chalcone molecules and commercial additives is shown in table 5. The E_{GAP} or GAP parameter determines molecular reactivity and chemical stability. GAP values in the high ranges signify substantial excitation energy, low chemical reactivity, and outstanding chemical stability. According to the results of the comparative study, the chalcone molecules have excellent or comparable E_{GAP} values to commercial additives such as BHT, thiazolidinone, toluene derivatives, which are widely employed to preclude or cut down oxidation processes in biodiesel. Thermodynamics of a compound depends on various factors. Accessibility of energy is directly proportional to molecular shape. As a result, characteristics such as chemical bonding structure, carbon content, and oxygenated compound content have a significant impact on the thermodynamic property of the compound [8].

Table 5: Comparison study of E_{GAP} performance of different chalcone molecules and commercial additives.

Chalcone & Sample Code	E_{GAP} Value (Kj/mol)	Ref	Commercial Additive	E_{GAP} Value (Kj/mol)	Ref
$C_{23}H_{18}O_3$ (I)	599.51	[38]	BHT	546.1	[42]
$C_{23}H_{17}BrO_3$ (BCH)	598.11	[45]	Toluene Derivative	477.8	[43]
$C_{23}H_{17}NO_5$ (NCH)	586.38		Thiazolidinone	481.8	[44]
$C_{18}H18O4$ (TMC20)	565.38	[37]	Ether Molecule	273.8 - 404.6	[54]
$C_{23}H_{17}ClO_3$ (HCC)	602.34	[8]	P-Phenylene Diamine	56.8 - 114.5	[55,56]

The calorific ability of the chalcone molecule as an additive has been assessed in terms of energy. The calorific value (CV) provides fuel characteristics such as intrinsic energy and is the quantity of heat transmitted into the burning chamber during the period of combustion [57].

Table 6: Calorific value of chalcones.

Chalcone Compound & Sample Code	Calorific Value (Kcal/kg)	Ref
$C_{23}H_{18}O_3$ (I)	12783	[38]
$C_{23}H_{17}ClO_3$ (HCC)	9569	[58]
$C_{24}H_{26}O$ (BH I)	7284	[50]
$C_{20}H_{14}OCl_4$ (BH II)	6430.2	
$C_{20}H_{16}OCl_2$ (BH III)	7298.7	

Table 7: Calorific values of fuels.

Fuels	Calorific Value (Kcal/kg)	Ref
Gasoline	9775	[50]
Butanol	8509	
Ethanol	6906	
BD-B100 (methyl palm)	8525.7	[59]
BD-B100 (Cynara carduncului)	8885.0	[50,60]
BD-B25 (Pomace Olive)	10399.3	

This pertains primarily to the compound's ability to release energy during the oxidation process, whereas high calorific power values are correlated with more outstanding performance in fuels [38]. Tables 6 and 7 show the calorific value of some chalcones and fuels, respectively. According to the comparison, chalcone molecules have a performance similar to or comparable to that of fuels. Some chalcone molecules show higher calorific values than some of the fuels reported here. The high calorific value of fuels is related to improved performance. As a result, the excellent energy availability and susceptibility of chalcone molecules strongly suggest that chalcones can be associated with fuels. Eventually, it will increase the stability and efficiency of the compound.

Conclusion and Future Prospective

In recent studies, scientists and researchers have expressed a strong interest in chalcones and their analogs. These molecules are versatile and suited for an extensive list of applications. The capability to make substitutions on aromatic rings results in notable features that can be employed in various fields. Chalcone analogs as fuel additives are a far superior answer to the current energy availability problem, despite their synthesis being less expensive and faster; also, the absence of chlorinated reagents makes them more environmentally friendly. This review examined the potential application of chalcone analogs as biofuel additives based on their antioxidation properties, factors influencing antioxidation properties, oxidation stability, and additive potential capabilities using experimental and theoretical methodologies. Based on the results;

- Most of the research showed that among all the different properties of chalcone, the antioxidative property is the most essential, favoring additive application. Several variables contribute to the improved antioxidative properties of chalcone analogs, including their structure, substitutions, substitution positions, and effects such as resonances.

- Chalcone analogs are highly effective materials for preserving biofuel characteristics. They have good oxidation stability properties comparable to some commercial additives.

- The more significant part of the studies has addressed the significance of additive compounds. These chemicals can improve the qualities of fuels, including diesel, biodiesel, petrol, and aviation oil, by combining them, resulting in increased fuel economy and efficiency.

- Particularly in biodiesel because NOx emissions are high due to higher oxygen content, higher in-cylinder gas temperature, fluctuations in fuel injection parameters, lower compressibility, and higher cetane numbers.

- Most of the studies recommended future studies on the additive application side of the chalcone molecule due to its beneficial blending capabilities compared to various fuels in terms of experimental studies (calorific) and theoretical studies (kinetic stability).

- Aside from its outstanding antioxidant properties and oxidation stability, chalcone's susceptibility and superior energy availability make it a suitable fuel additive.

Small molecules like chalcones are less expensive and easier to synthesize and have already received widespread acceptance in many technological fields. Yet, this review discovered that the potential of chalcones as a cheaper, more efficient alternative additive still needs to be fully explored. The results from the literature validate that chalcone molecules can be used as a possible candidate for additive application in the perspectives of antioxidant effectiveness, oxidative stability, and energy availability in the future. The lack of literature on this topic necessitates thoroughly examining this potential additive application of chalcone analogs, which has yet to receive the attention it deserves. This review suggests additional research on this topic. As a result, scientists can generate more energy-efficient biofuels while developing new, highly efficient fuel additives that will significantly solve the energy availability constraint of currently used biofuels.

Reference

1. *In Partnership with Statistical Review of World Energy 2023 | 72 Nd Edition*.
2. Bp *BP Statistical Review of World Energy June 2009*; 2009.
3. Nicoletti, G.; Arcuri, N.; Nicoletti, G.; Bruno, R. A Technical and Environmental Comparison between Hydrogen and Some Fossil Fuels. *Energy Convers Manag* 2015, *89*, 205–213, doi:10.1016/j.enconman.2014.09.057.
4. Vassilev, S. V.; Vassileva, C.G.; Vassilev, V.S. Advantages and Disadvantages of Composition and Properties of Biomass in Comparison with Coal: An Overview. *Fuel* 2015, *158*, 330–350.
5. Demirbas, A. Biofuels Sources, Biofuel Policy, Biofuel Economy and Global Biofuel Projections. *Energy Convers Manag* 2008, *49*, 2106–2116, doi:10.1016/j.enconman.2008.02.020.
6. Gaurav, N.; Sivasankari, S.; Kiran, G.S.; Ninawe, A.; Selvin, J. Utilization of Bioresources for Sustainable Biofuels: A Review. *Renewable and Sustainable Energy Reviews* 2017, *73*, 205–214.
7. Weldemichael, Y.; Assefa, G. Assessing the Energy Production and GHG (Greenhouse Gas) Emissions Mitigation Potential of Biomass Resources for Alberta. *J Clean Prod* 2016, *112*, 4257–4264, doi:10.1016/j.jclepro.2015.08.118.
8. Faria, E.C.M.; Duarte, V.S.; da Silva, A.M.; Fernandes, F.S.; de Paula, R.L.G.; Alonso, C.G.;

Oliveira, G.R.; Napolitano, H.B. New Halogen Chalcone with Potential for Application in Biofuels. *Energy & Fuels* 2020, *34*, 5958–5968, doi:10.1021/acs.energyfuels.0c00322.

9. Hosseinzadeh-Bandbafha, H.; Tabatabaei, M.; Aghbashlo, M.; Khanali, M.; Demirbas, A. A Comprehensive Review on the Environmental Impacts of Diesel/Biodiesel Additives. *Energy Convers Manag* 2018, *174*, 579–614, doi:10.1016/j.enconman.2018.08.050.10.
10. Pikula, K.; Zakharenko, A.; Stratidakis, A.; Razgonova, M.; Nosyrev, A.; Mezhuev, Y.; Tsatsakis, A.; Golokhvast, K. The Advances and Limitations in Biodiesel Production: Feedstocks, Oil Extraction Methods, Production, and Environmental Life Cycle Assessment. *Green Chem Lett Rev* 2020, *13*, 275–294, doi:10.1080/17518253.2020.1829099.
11. Lelieveld, J.; Evans, J.S.; Fnais, M.; Giannadaki, D.; Pozzer, A. The Contribution of Outdoor Air Pollution Sources to Premature Mortality on a Global Scale. *Nature* 2015, *525*, 367–371, doi:10.1038/nature15371.
12. Naqvi, M.; Yan, J. First-Generation Biofuels. In *Handbook of Clean Energy Systems*; Wiley, 2015; pp. 1–18.
13. Naik, S.N.; Goud, V. V.; Rout, P.K.; Dalai, A.K. Production of First- and Second-Generation Biofuels: A Comprehensive Review. *Renewable and Sustainable Energy Reviews* 2010, *14*, 578–597.
14. Aghbashlo, M.; Tabatabaei, M.; Rastegari, H.; Ghaziaskar, H.S.; Valijanian, E. Exergy-Based Optimization of a Continuous Reactor Applied to Produce Value-Added Chemicals from Glycerol through Esterification with Acetic Acid. *Energy* 2018, *150*, 351–362, doi:10.1016/j.energy.2018.02.151.
15. De Oliveira, F.C.; Coelho, S.T. History, Evolution, and Environmental Impact of Biodiesel in Brazil: A Review. *Renewable and Sustainable Energy Reviews* 2017, *75*, 168–179, doi:10.1016/j.rser.2016.10.060.
16. Lim, S.; Teong, L.K. Recent Trends, Opportunities and Challenges of Biodiesel in Malaysia: An Overview. *Renewable and Sustainable Energy Reviews* 2010, *14*, 938–954, doi:10.1016/j.rser.2009.10.027.
17. Atabani, A.E.; Silitonga, A.S.; Badruddin, I.A.; Mahlia, T.M.I.; Masjuki, H.H.; Mekhilef, S. A Comprehensive Review on Biodiesel as an Alternative Energy Resource and Its Characteristics. *Renewable and Sustainable Energy Reviews* 2012, *16*, 2070–2093, doi:10.1016/j.rser.2012.01.003.
18. Lin, L.; Cunshan, Z.; Vittayapadung, S.; Xiangqian, S.; Mingdong, D. Opportunities and Challenges for Biodiesel Fuel. *Appl Energy* 2011, *88*, 1020–1031, doi:10.1016/j.apenergy.2010.09.029.
19. Jasim, H.A.; Nahar, L.; Jasim, M.A.; Moore, S.A.; Ritchie, K.J.; Sarker, S.D. Chalcones: Synthetic Chemistry Follows Where Nature Leads. *Biomolecules* 2021, *11*, 1203, doi:10.3390/biom11081203.
20. Mathew, B.; Adeniyi, A.A.; Joy, M.; Mathew, G.E.; Singh-Pillay, A.; Sudarsanakumar, C.; Soliman, M.E.S.; Suresh, J. Anti-Oxidant Behavior of Functionalized Chalcone-a Combined Quantum Chemical and Crystallographic Structural Investigation. *J Mol Struct* 2017, *1146*, 301–308, doi:10.1016/j.molstruc.2017.05.100.
21. Kostanecki, S. and T., J Synthesis, Characterization and Biological Evaluation of Some Novel Chalcone Derivatives Containing Imidazo [1,2-a] Pyridine Moiety. *J Chem Ber* 1899, *32*, 1921–1926.
22. Patel, Dr.R. Basics of Chalcone and Related Novel Synthesis. 2015.
23. Çelik, M. Analysis of the Effect of N-Heptane and Organic Based Manganese Addition to Biodiesel on Engine Performance and Emission Characteristics. *Energy Reports* 2021, *7*, 1672–1696, doi:10.1016/j.egyr.2021.03.024.
24. Senthil, R.; Silambarasan, R. Environmental Effect of Antioxidant Additives on Exhaust Emission Reduction in Compression Ignition Engine Fuelled with Annona Methyl Ester. *Environ Technol* 2015, *36*, 2079–2085, doi:10.1080/09593330.2015.1021856.
25. Schober, S.; Mittelbach, M. The Impact of Antioxidants on Biodiesel Oxidation Stability. *European Journal of Lipid Science and Technology* 2004, *106*, 382–389, doi:10.1002/ejlt.200400954.
26. Karavalakis, G.; Hilari, D.; Givalou, L.; Karonis, D.; Stournas, S. Storage Stability and Ageing Effect of Biodiesel Blends Treated with Different Antioxidants. *Energy* 2011, *36*, 369–374, doi:10.1016/j.energy.2010.10.029.
27. Ramalingam, S.; Rajendran, S.; Ganesan, P. Improving the Performance Is Better and Emission Reductions from Annona Biodiesel Operated Diesel Engine Using 1,4-Dioxane Fuel Additive. *Fuel* 2016, *185*, 804–809, doi:10.1016/j.fuel.2016.08.049.
28. Ashok, B.; Nanthagopal, K.; Jeevanantham, A.K.; Bhowmick, P.; Malhotra, D.; Agarwal, P. An Assessment of Calophyllum Inophyllum Biodiesel Fuelled Diesel Engine Characteristics Using Novel Antioxidant Additives. *Energy Convers Manag* 2017, *148*, 935–943, doi:10.1016/j.enconman.2017.06.049.

29. Palash, S.M.; Kalam, M.A.; Masjuki, H.H.; Arbab, M.I.; Masum, B.M.; Sanjid, A. Impacts of NOx Reducing Antioxidant Additive on Performance and Emissions of a Multi-Cylinder Diesel Engine Fueled with Jatropha Biodiesel Blends. *Energy Convers Manag* 2014, *77*, 577–585, doi:10.1016/j.enconman.2013.10.016.
30. Kostopoulou, I.; Detsi, A. Recent Developments on Tyrosinase Inhibitors Based on the Chalcone and Aurone Scaffolds. *Curr Enzym Inhib* 2018, *14*, 3–17, doi:10.2174/1573408013666170208102614.
31. Sökmen, M.; Akram Khan, M. The Antioxidant Activity of Some Curcuminoids and Chalcones. *Inflammopharmacology* 2016, *24*, 81–86, doi:10.1007/s10787-016-0264-5.
32. Singh, S.; Sharma, P.K.; Kumar, N.; Dudhe, R. *Journal of Advanced Scientific Research Anti-Oxidant Activity of 2-Hydroxyacetophenone Chalcone*; 2011; Vol. 2.
33. Narsinghani, T.; Sharma, M.C.; Bhargav, S. Synthesis, Docking Studies and Antioxidant Activity of Some Chalcone and Aurone Derivatives. *Medicinal Chemistry Research* 2013, *22*, 4059–4068, doi:10.1007/s00044-012-0413-3.
34. Berneira, L.M.; Rockembach, C.T.; da Silva, C.C.; de Freitas, S.C.; Rosa, B.N.; Pinto, E.; Anjos, F.M.; dos Santos, M.A.Z.; de Pereira, C.M.P. Employment of Thermal Analysis Applied to the Oxidative Stability Evaluation of Biodiesel Using Chalcone Analogues. *J Therm Anal Calorim* 2021, *146*, 1473–1482, doi:10.1007/s10973-020-10189-w.
35. Prabhakar, V.; Iqbal, H.; Balasubramanian, R. *Antioxidant Studies on Monosubstituted Chalcone Derivatives-Understanding Substituent Effects*; 2016; Vol. 29.
36. Varatharajan, K.; Pushparani, D.S. Screening of Antioxidant Additives for Biodiesel Fuels. *Renewable and Sustainable Energy Reviews* 2018, *82*, 2017–2028, doi:10.1016/j.rser.2017.07.020.
37. Coelho, E.; Faria, M.; Duarte, V.S.; Oliveira, A.M.; De, E.H.; Cavalcanti, S.; Napolitano, H.B. A Trimethoxy-Chalcone Applied as Antioxidant and Antibacterial Additive for Diesel and Biodiesel Blend.
38. Faria, E.C.M.; Duarte, V.S.; De Paula, R.L.G.; Da Silva, A.M.; Fernandes, F.S.; Vaz, W.F.; Oliveira, G.R.; Napolitano, H.B. Comparative Study of Chalcones and Their Potential as Additives for Biofuels. *Energy and Fuels* 2021, *35*, 552–560, doi:10.1021/acs.energyfuels.0c03448.
39. Elfasakhany, A. Experimental Study on Emissions and Performance of an Internal Combustion Engine Fueled with Gasoline and Gasoline/n-Butanol Blends. *Energy Convers Manag* 2014, *88*, 277–283, doi:10.1016/j.enconman.2014.08.031.
40. Bayraktar, H. Experimental and Theoretical Investigation of Using Gasoline-Ethanol Blends in Spark-Ignition Engines. *Renew Energy* 2005, *30*, 1733–1747, doi:10.1016/j.renene.2005.01.006.
41. Yüksel, F.; Yüksel, B. The Use of Ethanol-Gasoline Blend as a Fuel in an SI Engine. *Renew Energy* 2004, *29*, 1181–1191, doi:10.1016/j.renene.2003.11.012.
42. Chinna Babu, P.; Sundaraganesan, N.; Dereli, Ö.; Türkkan, E. FT-IR, FT-Raman Spectra, Density Functional Computations of the Vibrational Spectra and Molecular Geometry of Butylated Hydroxy Toluene. *Spectrochim Acta A Mol Biomol Spectrosc* 2011, *79*, 562–569, doi:10.1016/j.saa.2011.03.034.
43. Krishna Kumar, V.; Suganya, S.; Mathammal, R. Molecular Structure, Vibrational Spectra, HOMO, LUMO and NMR Studies of 2,3,4,5,6-Penta Bromo Toluene and Bromo Durene Based on Density Functional Calculations. *Spectrochim Acta A Mol Biomol Spectrosc* 2014, *125*, 201–210, doi:10.1016/j.saa.2013.12.070.
44. Mohammed, H.A.; Attia, S.K.; Nessim, M.I.; Shaaban, M.E.; El-Bassoussi, A.A.M. Studies on Some Thiazolidinones as Antioxidants for Local Base Oil. *Egypt J Chem* 2019, *62*, 1619–1634, doi:10.21608/EJCHEM.2019.6662.1560.
45. Borges, I.D.; Faria, E.C.M.; Custódio, J.F.M.; Duarte, V.S.; Fernandes, F.S.; Alonso, C.G.; Sanches-Neto, F.O.; Carvalho-Silva, V.H.; Oliveira, G.R.; Napolitano, H.B. Insights into Chalcone Analogues with Potential as Antioxidant Additives in Diesel-Biodiesel Blends. *RSC Adv* 2022, *12*, 34746–34759, doi:10.1039/d2ra07300e.
46. Duarte, V.S. *chalconas e benzimidazóis: desenvolvimento de aditivos em misturas de biocombustíveis*; 2023,
47. Duarte, V.S.; D. Borges, I.; d'Oliveira, G.D.C.; Faria, E.C.M.; de Almeida, L.R.; Carvalho-Silva, V.H.; Noda-Pérez, C.; Napolitano, H.B. Arylsulfonamide Chalcones as Alternatives for Fuel Additives: Antioxidant Activity and Machine Learning Protocol Studies. *New Journal of Chemistry* 2023, *47*, 10003–10015, doi:10.1039/D3NJ00255A.
48. Moreira, C.A.; Faria, E.C.M.; Queiroz, J.E.; Duarte, V.S.; Gomes, M. do N.; da Silva, A.M.; de Paula, R.L.G.; Franco, C.H.J.; Cavalcanti, E.H. de S.; de Aquino, G.L.B.; et al. Structural Insights and Antioxidant Analysis of a Tri-Methoxy Chalcone with Potential as a Diesel-Biodiesel Blend Additive. *Fuel Processing Technology* 2022, *227*, 107122, doi:10.1016/j.fuproc.2021.107122.
49. British Standards Institute staff Automotive Fuels Blends of Fatty Acid Methyl Ester (FAME) with

Diesel Fuel. 1915.

50. Sallum, L.O.; Duarte, V.S.; Custodio, J.M.F.; Faria, E.C.M.; Da Silva, A.M.; Lima, R.S.; Camargo, A.J.; Napolitano, H.B. Cyclohexanone-Based Chalcones as Alternatives for Fuel Additives. *ACS Omega* 2022, *7*, 11871–11886, doi:10.1021/acsomega.1c07333.
51. Uğuz, G.; Atabani, A.E.; Mohammed, M.N.; Shobana, S.; Uğuz, S.; Kumar, G.; Al-Muhtaseb, A.H. Fuel Stability of Biodiesel from Waste Cooking Oil: A Comparative Evaluation with Various Antioxidants Using FT-IR and DSC Techniques. *Biocatal Agric Biotechnol* 2019, *21*, doi:10.1016/j.bcab.2019.101283.
52. Zuleta, E.C.; Baena, L.; Rios, L.A.; Calderón, J.A. *The Oxidative Stability of Biodiesel and Its Impact on the Deterioration of Metallic and Polymeric Materials: A Review*; 2012; Vol. 23.
53. Izgorodina, E.I.; Seeger, Z.L.; Scarborough, D.L.A.; Tan, S.Y.S. Quantum Chemical Methods for the Prediction of Energetic, Physical, and Spectroscopic Properties of Ionic Liquids. *Chem Rev* 2017, *117*, 6696–6754, doi:10.1021/acs.chemrev.6b00528.
54. Rad, A.S. Al-Doped Graphene as Modified Nanostructure Sensor for Some Ether Molecules: Ab-Initio Study. *Synth Met* 2015, *209*, 419–425, doi:10.1016/j.synthmet.2015.08.016.
55. Diab, M.A.; El-Sonbati, A.Z.; El-Ghamaz, N.A.; Morgan, S.M.; El-Shahat, O. Conducting Polymers X: Dielectric Constant, Conduction Mechanism and Correlation between Theoretical Parameters and Electrical Conductivity of Poly (N,N′-Bis-Sulphinyl p-Phenylenediamine-2,6-Diaminipyridine) and Poly (N,N′-Bis-Sulphinyl p-Phenylenediamine-3,5-Diamine-1,2,4-Trizole). *Eur Polym J* 2019, *115*, 268–281, doi:10.1016/j.eurpolymj.2019.03.036.
56. Yang, S.; Ye, C.; Song, X.; He, L.; Liao, F. ARTICLE TYPE Theoretical Calculations Based Synthesis of Poly(p-Phenylenediamine)-Fe_3O_4 Composite: A Magnetically Recyclable Photocatalyst with Highly Selectivity for Acid Dyes Received (in XXX, XXX) Xth XXXXXXXXX 20XX, Accepted Xth XXXXXXXXX 20XX., doi:10.1039/c0xx00000x.
57. Oliveira, L.E.; Da Silva M. L. C. P. Comparative Study of Calorific Value of Rapeseed, Soybean, Jatropha Curcas and Crambe Biodiesel. *RE&PQJ* 2024, *11*, 679–682, doi:10.24084/repqj11.411.
58. Faria, E.C.M.; Duarte, V.S.; Da Silva, A.M.; Fernandes, F.S.; De Paula, R.L.G.; Alonso, C.G.; Oliveira, G.R.; Napolitano, H.B. New Halogen Chalcone with Potential for Application in Biofuels. *Energy and Fuels* 2020, *34*, 5958–5968, doi:10.1021/acs.energyfuels.0c00322.
59. Covalcante, M. S. Conceicao, L. R. V. Bastos, R. R. C. Costa, A. C. G. Rocha F. N. Zamian,J. R. In 52nd Congresso Brasilerio de Quimica, Recife, Brazil. 2012, 14–18.
60. Antonio, M.; Nascimento, R.; Lora, E.S.; Venturini, O.J.; Maldonado, M.R.; Andrade, R.V.; Sérgio, P.; Corrêa, P.; Antônio, M.; Leite, H. *Utilização Do Biodiesel de Mamona Em Micro-Turbinas a Gás-Testes de Desempenho Térmico e Emissões*.

Harnessing Machine Learning for Comparative Analysis of Nanomaterials in Agro-Environmental Applications

Gunaram[1,a], Arjun Choudhary[2,b] and Gaurav Sharma[3,c]

[1] *Department of Physics, Government Engineering College, Ajmer, Rajasthan, India.*
[2] *Department of Computer Science, Government Engineering College, Ajmer, Rajasthan, India.*
[3] *Department of Physics, Rajendra College, JP University, Chappra, Bihar, India.*

[a] grphysics1974@gmail.com
[b] arjun116a@gmail.com
[c] gaurav.kmc891101@gmail.com

Abstract

This article explores the transformative potential of integrating nanomaterials (NM) and machine learning (ML) to address critical global challenges, particularly in agriculture sustainability and climate change mitigation. By conducting a comparative analysis of various nanomaterials and their applications in agriculture and environmental protection, we demonstrate how ML techniques can optimize the properties and functionalities of these materials. In agriculture, nanomaterials are used in developing nanofertilizers, nanopesticides, and nanosensors, which enhance crop yield, pest control, and soil health monitoring. In environmental applications, nanofilters help mitigate climate change-related issues. This research underscores the value of combining NM and ML to advance sustainable agro-environmental solutions, highlighting the role of interdisciplinary approaches in creating smarter, more efficient technologies. By leveraging advanced ML algorithms and AI, we can improve the specificity, sensitivity, and accuracy of nanomaterials, offering innovative solutions to challenges such as food security and environmental conservation.

Keywords: Machine Learning, Nanomaterial, Artificial Intelligence.
Received 29 January 2025; First Review 19 March 2025; Accepted 11 April 2025.

*** Address of correspondence**
Gunaram
Department of Physics, Government Engineering College, Ajmer, Rajasthan, India.

Email: grphysics1974@gmail.com

How to cite this article
Gunaram, Arjun Choudhary and Gaurav Sharma, Harnessing Machine Learning for Comparative Analysis of Nanomaterials in Agro-Environmental Applications, J. Cond. Matt. 2025; 03 (02): 39-43.

Available from:
https://doi.org/10.61343/jcm.v3i02.102

Introduction

Machine learning (ML) presents transformative opportunities in addressing NM insights and critical global challenges such as agriculture sustainability and climate change mitigation. This approach leverages the potential of ML algorithms for analyzing big datasets, identify patterns and make predictions, which can significantly boost the efficiency and capability of nanomaterials in agriculture. Therefore, the analysis of nanomaterial properties is crucial in agro-environmental applications where we can utilize the results in various disciplines few of those are discussed below in this section.

This work can be utilized to enhance Crop Productivity. Nanomaterials can improve nutrient delivery and uptake, leading to better crop growth and higher yields. Secondly, Nanotechnology can improve water retention and distribution in soil, leading to more efficient water use and better drought resistance [1]. Nanomaterials can also be used to detect and manage plant diseases, pests, and other stress factors, ensuring healthier crops [2].

More over by applying Predictive Analysis on historical data, ML can predict crop yields, pest outbreaks, and environmental impacts, allowing for proactive management. As in today Real-time monitoring becomes very important in sensing. This can be done with the help of ML algorithms which can process data from nanosensors in real-time, providing immediate insights into soil health, water usage, and plant stress.

The collaboration of ML with the nanomaterials can lead be phenomenal progress in the science. The nanomaterials are equally important with ML for steady progress. Nanomaterials are revolutionizing agro-environmental applications due to their unique properties and versatility. Here in this section, we have discussed some of the important key point about the nanomaterials. Nanomaterials have shown significantly better results in crop growth and yield compared to traditional fertilizers and pesticides. Hence, they are very significant in enhanced Crop Growth and Yield of the crop. Secondly as the nanomaterials have much higher surface area, they reduce the number of agricultural inputs needed, nanomaterials contribute to more sustainable farming practices. Nanotechnology with ML enables precise delivery of agrochemicals, ensuring that nutrients and pesticides are delivered directly to the target areas. This reduces waste, minimizes environmental impact, and lowers labor costs [1-2]. Nanomaterials can detect plant diseases, ensuring healthier crops and safer food production. Nanomaterials have emerged as crucial components in the field of biosensors owing to their exceptional electrical, chemical, and optical properties [2]. Hence, the nanomaterial plays a crucial role in plant health and food safety.

Literature Review

In a study by Shi Xuan Leongand Nguan Soon examines the capacity of machine learning techniques to enhance the effectiveness of nanosensors in agricultural and environmental contexts. It examines diverse machine learning approaches and their applications in enhancing the precision and efficacy of nanosensors [3]. In another study by Dania Tamayo Vera reviews the uses of machine learning methodologies for agro-climatic research, highlighting their potential to improve agricultural practices by analyzing climatic data. It provides important insights into how machine learning can be employed to forecast crop yields, control pest populations, and optimize resource efficiency [4]. The connection between nanotechnology and agricultural production systems pertains to the incorporation of nanotechnology within these frameworks were discussed in Lalita Rana et al. [5]. This discourse emphasizes the significance of innovative approaches, including machine learning, in advancing sustainable agricultural practices.

The latest progress in the interpretation of data obtained from nanosensors, utilizing machine learning methodologies for applications in agro-environmental settings are deeply demonstrated in [6] by Claudia Leslieet al. In another study Zhang Z et al. [7] discusses the advancement of machine-learning algorithms that are used to improve nanosensors, which have attracted significant attention for their predictive and adaptive capabilities. This innovation has the potential to significantly enhance the efficiency of data collection and processing applications. Makhlouf& Ali [8], they released a publication focused on Waste Recycling Technologies for the production of Nanomaterials.

Research gap

Nanomaterials hold immense promise for a wide range of applications in the agro-environmental sectors, offering the potential to revolutionize practices across various disciplines. Their diverse applications extend to improving soil quality, enhancing crop yield, and even addressing environmental challenges, making them an exciting area of study [3]. This review delves into the critical aspects of nanomaterials, focusing on the advancements in nanostructure design, their unique properties and their enhanced abilities in adsorption and catalysis. These improvements are significantly driven by the integration of machine learning, which optimizes their functional applications. However, despite these promising advancements, several key research gaps remain, hindering the full potential of nanomaterials in agro-environmental applications.

One of the primary concerns is the long-term environmental impact of nanomaterials, particularly in terms of their effects on soil health, water quality, and biodiversity. The persistent nature of these materials in the environment could lead to unforeseen ecological consequences, which remain inadequately understood. Another pressing issue is the lack of comprehensive regulations and uniform safety protocols governing the use of nanomaterials in agriculture. This gap creates challenges in ensuring the safe and responsible application of these materials, particularly when their effects on human health and the environment are still being studied. Establishing stringent guidelines for their safe usage is essential to promote their broader adoption in agricultural practices.

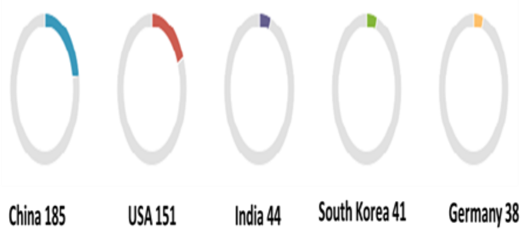

Figure 1: Distribution of Universities and Research Centers Conducting Research on Nanomaterials in Agro-environmental Applications, Categorized by Country.

Additionally, the economic viability of nanomaterials remains a significant barrier to their widespread implementation. The high costs associated with their production and application make them less accessible, especially to farmers in developing countries who may face financial constraints. There is a need for research focused on developing more cost-effective methods for the production and application of nanomaterials, which would help to democratize their use and ensure their benefits reach a broader population. Research is needed to develop cost-effective methods for their production and application to make them accessible to farmers, especially in developing countries as shown in Fig. 1-2. Addressing these critical research gaps is crucial for ensuring the sustainable and successful integration of nanomaterials into agricultural practices is shown in Fig.3. As illustrated in Fig 1-3, overcoming these challenges will be pivotal in unlocking the full potential of nanomaterials and ensuring their safe, effective, and equitable use in agro-environmental applications.

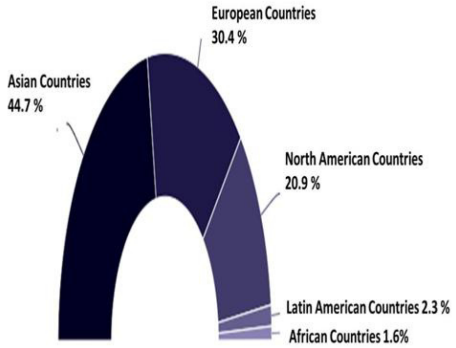

Figure 2: Regional Distribution of Universities and Research Centers Engaged in the Study and Development of Nanomaterial based Technologies.

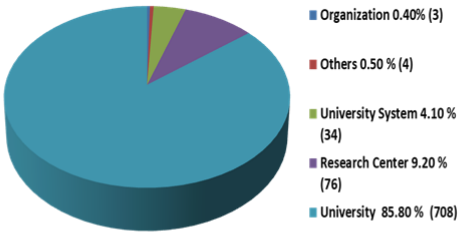

Figure 3: Categorization of Universities and Research Centers Based on Their Specialization in Nanotechnology Research and Development for Agro-environmental Applications.

Methodology

Harnessing machine learning for comparative analysis of nanomaterial properties involves using advanced algorithms to analyze and predict properties that aren't tangible or physical. Here's a high-level overview of how you can approach this:

1. Data Collection: Gather data of nonomaterials for various applications, products, companies and countries to analyze. This could include experimental data, literature values.

2. Data Preprocessing: Clean and preprocess the data for machine learning models. This may involve normalization, handling missing values, and feature engineering etc.

3. Model Selection: We have selected four machine learning models for our analysis. The chosen models are presented below and depicted in Figure 6 as Support Vector Regression (SVR), Random Forest Regression (RFR), Gradient Boosting Regression (GBR) & Artificial Neural Networks (ANN).

4. Model Training: The approach comprises splitting data into training and testing subsets, with the training subset used to train models on Google Colab.

5. Model Evaluation: We evaluated the effectiveness of these components in our models using the metrics Mean Absolute Error & Root Squared Error as demonstrated in fig. 6.

6. Comparative Analysis: We here compared the performance of different models to determine which one provides the best predictions for machine learning to analyze and compare the performance of nanomaterials in agro-environmental applications, leading to more informed decision-making and improved agricultural practices as shown in fig. 4-6.

Implications

The implications of using nanomaterials in agro-environmental applications are vast and multifaceted. Here are some key points discussed:

1) Enhanced Agricultural Productivity: Nanomaterials can significantly boost crop yields, improve plant health by enhancing nutrient delivery with providing better disease and pest management.

2) Environmental Sustainability: By reducing the chemical inputs and enabling targeted application of agrochemicals, nanomaterials contribute to more sustainable farming practices. This minimizes environmental pollution and conserving natural resources.

3) Soil and Water Quality Improvement: Nanomaterials can remediate contaminated soils and improve water retention, distribution, healthier soil and efficient water use.

4) Economic Benefits: The adoption of nanotechnology in agriculture can lead to increased food production, reduced input costs and improved food security.

5) Innovation and Research Opportunities: The field of nanotechnology in agriculture is still evolving, offering numerous opportunities for research and innovation to address current and future challenges in food production and environmental management.

Results and Discussion

Results

1) The machine learning models utilized in our analysis consist of Support Vector Regression (SVR), Random Forest Regression (RFR), Gradient Boosting Regression (GBR) and Artificial Neural Networks (ANN) producing the subsequent results.

2) Performance metrics: The ML models used for Applications Vs % of Products for Nonomaterials and compares the performance of different models to identify the most effective one as shown in fig. 4 & 5.

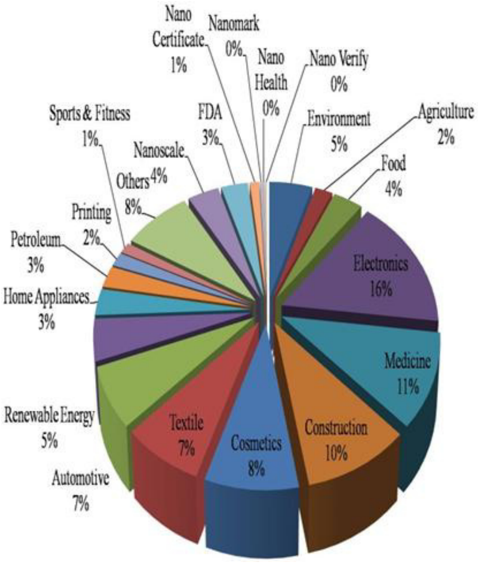

Figure 4: Comparative Analysis of Various Agricultural and Environmental Applications of Nanomaterials.

3) Comparative Analysis: Compares the performance of different applications vs. % of companies for nanomaterials agro-environmental applications. Highlight the strengths and weaknesses of each nonomaterials based on the ML analysis as shown in Fig. 5.

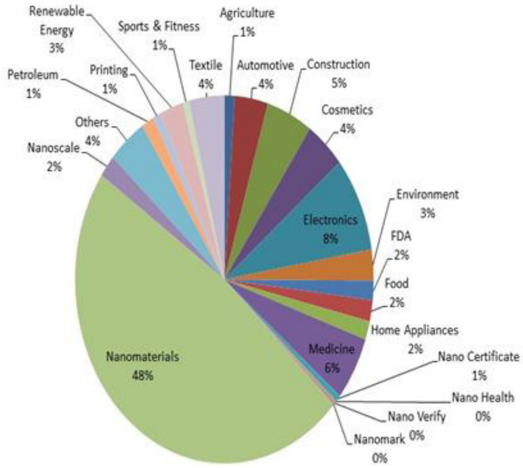

Figure 5: Companies Utilizing Nanomaterial-based Technologies in Agro-environmental Applications, Highlighting Key Industrial Adoption Trends and Sectoral Distribution.

4) Predictive Insights: The findings obtained from the machine learning models encompass a comparative analysis of different models and their performances, which is represented through the visualization of Mean Absolute Error (MAE) and R^2 values. A lower and positive MAE score, in conjunction with a higher and positive R^2 score, signifies enhanced model performance. This analysis details how these findings can be utilized for optimization in various applications, as illustrated in Figure 6. This study used various machine learning models, including Support Vector Regression (SVR), Random Forest Regression (RFR), Gradient Boosting Regression (GBR) & Artificial Neural Networks.

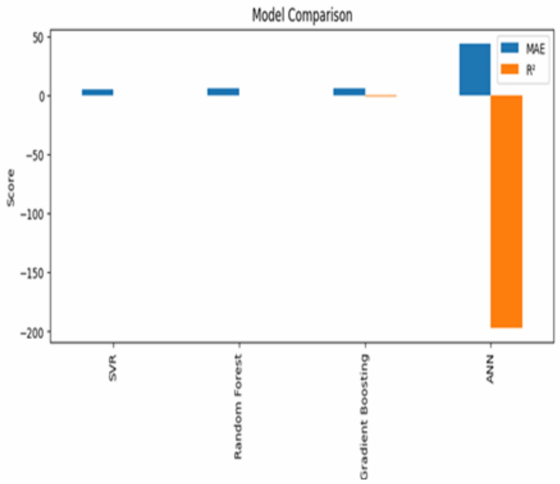

Figure 6: Visualization of Machine Learning Model Performance Metrics, Comparing Mean Absolute Error (MAE) and R^2 Scores for Different Predictive Models Used in the Analysis of Nanomaterials.

5) Feature Importance: Examine the various characteristics present in the models to determine which features exert the most substantial influence on the predictions, as illustrated in Figure 6 and table 1.

Discussion

In conclusion, this study underscores the significant potential of nanomaterials, enhanced by machine learning (ML), for advancing agricultural practices. The results of our ML analysis demonstrate the comparative performance of various nanomaterials in real-world agricultural settings, revealing their promising capabilities to improve efficiency and sustainability.

However, several challenges and limitations were encountered throughout the study. Issues such as data quality, the potential for model overfitting, and constraints related to computational resources must be addressed to ensure more accurate and generalizable findings in future research.

Table 1: Performance Evaluation of Various Machine Learning Model.

Models / Metric's	**Mean Absolute Errors** (MAE) **Positive score**	**R Squared Error (R^2) Positive score**	**ML Performance**	**Accuracy**
Support Vector Regression (SVR)	Lesser and positive score of MAE	Higher and positive score	Excellent	Good
Random Forest Regression (RFR)	Lesser and positive score of MAE	Higher and positive score	Good	Good
Gradient Boosting Regression (GBR)	Higher and positive score of MAE	Lower and Negative score	Bad	Bad
Artificial Neural Networks (ANN)	Higher and positive score of MAE	Lower and Negative score	Worse	Worse

Despite these challenges, the implications of our findings are clear. The integration of ML and nanomaterials offers a path toward more efficient, eco-friendly farming practices. By enhancing crop yields, reducing reliance on harmful chemicals, and minimizing environmental impact, nanomaterials, when coupled with advanced ML techniques, can contribute to more sustainable agricultural systems.

Moving forward, continued research and development are necessary to overcome the existing barriers and unlock the full potential of nanomaterials in agriculture, ensuring their safe, effective, and widespread use in addressing global food production challenges.

Conclusions

Machine learning presents significant opportunities for enhancing the comparative analysis of nanomaterials in agro-environmental contexts. The first two models Support Vector Regression (SVR) & Random Forest Regression (RFR) exhibited good performance as indicated by their advantageous and high Mean Absolute Error (MAE) scores, alongside a zero R-squared (R2) value. A brief conclusion summarizing the three key aspects (a) Enhanced Efficiency: ML enables precise and efficient analysis of large datasets, optimizing the use of nanomaterials for various agricultural applications. This leads to better crop yields, reduced chemical use, and improved resource management. (b) Informed Decision-making: By providing predictive insights, ML helps in making informed decisions regarding the selection of ML Models and application of nanomaterials. This can enhance plant protection, soil health, and overall agricultural productivity. (c) Future Research: There is ample scope for further research to address current limitations, such as data quality issues and model generalizability and to explore new applications of ML in agro-environment.

Reference

1. Makhlouf, A. S. H. Ali et al.: "*Waste Recycling Technologies for Nanomaterials Manufacturing*", Topics in Mining, Metallurgy and Materials Engineering, 2021, DOI: 10.1007/978-3-030-68031-2.
2. Sheikhzadeh, Elham et al.: *"Nanomaterial application in bio-sensors for the detection of infectious diseases"*, Talanta, 2020, 122026, doi: 10.1016/j.talanta.2020.122026.
3. Shi Xuan Leong, Nguan Soon et al.: The Royal Society of Chemistry 2022, 13, 11009-11029, DOI: 10.1039/D2SC02981B.
4. Dania Tamayo Vera, Xiuquan Wang et al.: *"A Review of Machine Learning Techniques in Agro climatic Studies"*, Agriculture 2024, 14(3), 481.
5. Lalita Rana, Manish Kumar et al.: *"Nexus between nanotechnology and agricultural production systems: challenges and future prospects"*, Review Discover Applied Sciences (2024) 6:555, https://doi.org/10.1007/s42452-024-06265-7.
6. Claudia Leslie, Arellano Vidal and Joseph Edward Govan: *"Machine Learning Techniques for Improving Nanosensors in Agro-environmental Applications"*, MDPI Journals /Agronomy / Volume 14 /Issue 2 /10.3390/Agronomy 2024, 14, 341.
7. Zhang, Z., Liu, X. et al.: *"Advances in Machine-Learning Enhanced Nanosensors"*, Small Struct. 2023, 2300325.
8. Adewale Adewuyi, Woei Jye Lau.: *"Nanomaterial development and its applications for emerging pollutant removal in water in Chapter-3"*, Handbook of Nanotechnology Applications, 2021, https://doi.org/10.1016/B978-0-12-821506-7.00003-X.

A Review on the Green Synthesis of Metal Oxide Nanoparticles for Antimicrobial Activity Using Different Plant Parts

Manimehala U[1], Sneha Asha[2], Merin Tomy[1], Anu M A[1], Xavier T S[1,a] and Binoy J[1,b]

[1] *Centre for Advanced Materials Research, Department of Physics, Govt. College for Women, Thiruvananthapuram-695014, Kerala, India.*
[2] *Department of Zoology, Government College for Women, Thiruvananthapuram-695014, Kerala, India.*

[a] xavierkattukulam@gmail.com
[b] binoyjohndas@gmail.com

Abstract

In recent years, green chemistry has witnessed a surge towards sustainable approaches for nanoparticle synthesis. Researchers are now exploring the potential of diverse plant extracts to produce ecological nanoparticles. Biomedical sciences increasingly focus on synthesizing various metal oxide nanoparticles (MONPs) mediated by plants due to their extensive biological applications. Plant-mediated biogenic synthesis of MONPs is a sustainable, less harmful, and low-cost method; additionally, it has advantages for biological analysis regarding antifungal and antibacterial activities. Plants contain diverse phytochemicals, including amino acids, terpenoids, polyphenols, and flavonoids, which can act as both reducing and stabilizing agents. This report focuses on the plant-mediated synthesis of nanoparticles (NPs), such as zinc oxide (ZnO), titanium dioxide (TiO_2), iron oxide (FeO), nickel oxide (NiO), and copper oxide (CuO), offering essential insights into their antimicrobial activity against various bacterial strains in different concentrations. It explores their structural properties, such as shape and size, analysed through advanced techniques and their antimicrobial effectiveness against various microbe strains.

Keywords: Green synthesis, Metal Oxide Nanoparticles, Plant extracts, Antimicrobial Activity.
Received 2 April 2025; First Review 18 April 2025; Accepted 18 April 2025.

*** Address of correspondence**
Xavier T S
Centre for Advanced Materials Research, Department of Physics, Govt. College for Women, Thiruvananthapuram-695014, Kerala, India.

Email: xavierkattukulam@gmail.com

How to cite this article
Manimehala U, Sneha Asha, Merin Tomy, Anu M A, Xavier T S, Binoy J, A Review on the Green Synthesis of Metal Oxide Nanoparticles for Antimicrobial Activity Using Different Plant Parts, J. Cond. Matt. 2025; 03 (02): 44-49.

Available from:
https://doi.org/10.61343/jcm.v3i02.153

Introduction

Microbial infections are disorders resulting from the invasion of harmful bacteria into the body's tissues. These infections can manifest in various forms, ranging from small, localized problems to severe, life-threatening diseases [1–3]. In addition, the efficacy of traditional pharmaceutical interventions for microbial disorders declines over time [4]. This scenario occurs due to antimicrobial resistance to conventional treatments and the high utilization or improper usage of these therapies [5]. Additionally, bacteria acquire resistance by employing genetic alterations or mobile genetic components that facilitate the transfer of resistance genes. There is an urgent need to explore novel methods for addressing antimicrobial issues [6–9]. Researchers have focused on establishing environmentally beneficial solutions using nanotechnology [10,11]. The utilization of MONPs has gained attention due to its cost-effectiveness and environmentally friendly nature [12,13]. The review explores advanced green synthesis techniques that are environmentally friendly for making MONPs from plants. The effectiveness and environmental benefits of the green manufacture of MONPs are emphasized in this article, highlighting their potential as antibacterial agents. The article explains new, plant-based approaches to producing NPs and investigates their varying antimicrobial effects at different concentrations.

Green Synthesis

Green synthesis is an approach that adheres to sustainable principles by reducing the utilization of harmful substances, resulting in advantages for both human well-being and the environment. [14–16]. The synthesis of NPs through green chemistry principles involves three phases: using environment-friendly solvent mediums, reducing agents, and stabilization agents. Plant extracts from leaves, seeds, and stems can synthesize nanoparticles using their stabilizing or reducing characteristics [17,18]. The synthesis of MONPs using plant extracts follows a sequential processing approach, as depicted in Fig 1.

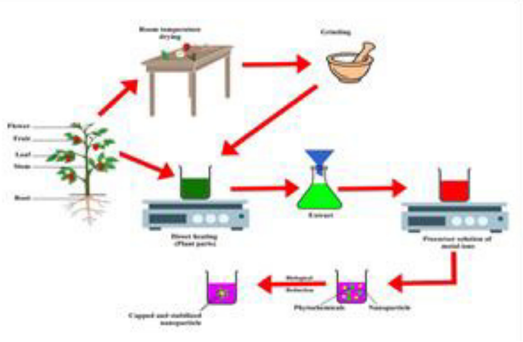

Figure 1: Illustration depicting synthesizing MONPs using natural plant extracts.

The green route involves the following steps. Initially, selected plant parts are soaked in distilled water to eliminate debris. Subsequently, the cleaned plant parts are dried and converted into powder by grinding or cutting. Later, the powder was boiled at a particular temperature in the desired solvent, filtered, and refrigerated for further use [19,20]. Filtration is carried out to isolate the phytochemicals, like amino, carboxylic, hydroxyl, allyl, alkoxy, and sulfhydryl groups [21]. The resultant plant extracts were combined with the respective salt solutions to synthesize NPs. A change in colour of the solution can indicate the early stages of NPs formation. Green synthesized NPs have extensive applications in contaminant remediation and antibacterial, antifungal, high catalytic, and photochemical activities [22]. The resulting plant-based metal oxide nanoparticles exhibit diverse beneficial properties [23,24].

MONPs Mechanism of Antimicrobial Activity

MONPs have attracted significant attention recently owing to their distinct physical and chemical properties and their diverse applications in disciplines such as environmental remediation, medicine, and electronics [25]. Currently, MONPs are being investigated as potential treatments for microbial infections due to their numerous applications. MONPs have several advantages over conventional antibiotics [26]. This review focuses on the antimicrobial effects of some MONPs. The efficacy of NPs is impacted by consistency, shape, and size [27]. Research indicates that the NPs interact with bacteria and fungi, altering the membrane shape and restricting their growth. Its disruption impedes proper mobility during plasma membrane formation, ultimately resulting in cell death [28]. The produced MONPs, smaller in size compared to micro-sized particles and having a high surface-to-volume, come into contact with sulphur or phosphorus in the DNA, causing cessation of protein synthesis and subsequent cell death. Reactive Oxygen Species (ROS) are crucial in promoting antimicrobial actions, as they are integral to the regular metabolic processes of living organisms [29]. The destruction of cells is attributed to the generation of ROS, which forms highly reactive radicals and breaks down cell wall proteins, the cytoskeleton system, and DNA [30]. Moreover, the electrostatic interaction of nanoparticles with the membrane may induce charge imbalances (+, -, and o), disrupting the membrane's equilibrium and forming hole pairs near its surface. eventually leading to the release of proteins RNA, DNA, and lipids, which culminates in cell death [31], as shown in Fig. 2.

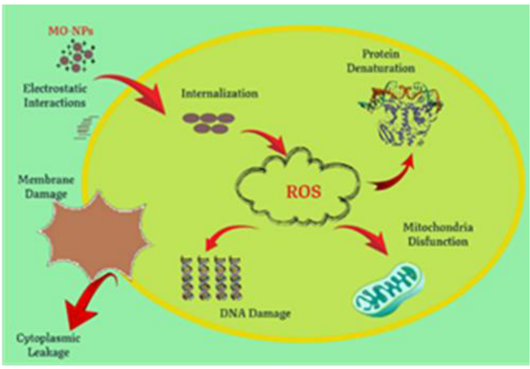

Figure 2: MONPs mechanism of antimicrobial activity.

Table 1 summarizes the green synthesis of MONPs using various extracts, highlighting their morphology, size, and notable antimicrobial activity against microbial species as reported in several publications [32-46]. Muthu et al. prepared ZnO nanoparticles using an extract derived from *Pisonia alba* leaves, identifying them as hexagonal crystalline structures with an average size of 48 nm through SEM, TEM, and XRD. FTIR studies suggested that phenolic compounds, alkaloids, terpenoids, and proteins in the extract are essential for the nucleation and stability of the ZnO Nps. The antibacterial activity was tested at 100 µg/µL, showing a 20 mm zone of inhibition (ZOI) against *S. aureus* (gram-positive) and 11 mm ZOI against *K. pneumoniae* (gram-negative). The NPs were more effective against gram-positive bacteria, which have thicker peptidoglycan cell walls, while gram-negative bacteria possess more complex cell walls [47]. Suresh et al. described the synthesis of ZnO NPs with sizes ranging from 5 to 15 nm utilizing *Cassia fistula* leaf extract, which was tested against four pathogenic Gram-negative bacteria: *K. aerogenes* (ZIO = 7.33 ± 0.33, 9.67 ± 0.33mm, respectively), *E. coli* (ZOI = 3.67 ± 0.33, 4.67 ± 0.33 mm) *P. desmolyticum* (ZOI = 3.00 ± 0.00, 4.00 ± 0.00 mm) and Gram-positive bacteria *S. aureus* (ZOI = 2.67 ± 0.33, 4.67 ± 0.33 mm) at different dosage 500 µg/µL, 1000 µg/µL [48]. Ansari *et al.* synthesized TiO_2 NPs using a leaf extract from *Acorus calamus*. The SEM analysis revealed that the NPs were spherical, with an average size ranging from 15 - 40 nm. The antimicrobial efficacy was assessed using the disc diffusion method, divulging inhibitory effects against gram-negative bacteria such as *P. aeruginosa* (ZOI: 6 ± 0.2, 8 ± 0.3 mm) and *E. coli* (9 ± 0.3, 10 ± 0.2 mm), as well as gram-positive bacteria including *B. subtilis* (12 ± 0.4, 14 ± 0.5 mm) and *S. aureus* (10 ± 0.3, 12 ± 0.3 mm) at nanoparticle concentrations of 10 µg/mL and 20 µg/mL, respectively. The biosynthesized TiO$_2$ NPs shown enhanced antibacterial activity against gram-positive bacteria compared to gram-negative bacteria and exceeded the antimicrobial efficacy of bare TiO$_2$ NPs. The findings suggest that biosynthesized TiO$_2$ NPs have potential as therapeutic agents for bacterial infections due to their significant in vitro antibacterial effectiveness [36]. Anbumani et al. prepared TiO$_2$ NPs using *L. acutangula* leaf extract as an affordable, eco-friendly method. They characterized the NPs using XRD, FT-IR, UV, FE-SEM-EDAX, and TEM techniques to determine their form, size, and structure. The antibacterial activity of TiO$_2$ NPs against various microorganisms, including *B. subtilis* (15 ± 0.46,16

Table 1: A brief summary of the antimicrobial activity of green-synthesized MONPs.

MONPs	Reducing agent	Part of plant	Morphology	Size	Microbial name	Applications	Ref.
ZnO	*Moringa Oleifera*	Leaf	Irregular shape	25 nm	*Pseudomonas, Bacillus*	Antibacterial	[32]
ZnO	*Artemisia pallens*	Leaf	Hexagonal	100 nm	*S. aureus, B. subtilis, E. coli,*	Antibacterial	[33]
ZnO	*Andrographis alata*	whole plant	Flake	35-53nm	*B. subtilis, S.pyogenes, S. aureus, C. diphtheria, S.typhi, E. coli, K. pneumonia, P. aeruginosa,*	Antimicrobial	[34]
CuO	*Luffa acutangula*	Peel	Rectangular	26 nm	*E. coli, K. pneumoniae, S. aureus, B. subtilis*	Antibacterial	[35]
TiO$_2$	*Acorus calamus*	Leaf	Spherical	11–30nm	*E. coli, P. aeruginosa, B. subtilis, S. aureus*	Antibacterial	[36]
TiO$_2$	*Coleus aromaticus*	Leaf	Spherical	12–33 nm	*Shigella boydii, Vibrio cholerae, B. cereus, A. hydrophilia, E. faecalis, B. megatarium*	Antibacterial	[37]
TiO$_2$	*Luffa acutangula*	Leaf	Hexagonal	10 - 49 nm	*B. subtilis, E. faecalis, P. aeruginosa, S. aureus, K. pneumonia*	Antimicrobial	[38]
CuO	*Bougainvillea*	Leaf	Spherical	8–20 nm	*E. coli, E. faecallis* *S. aureus*	Antibacterial	[39]
CuO	*Ocimum americanum*	Leaf	Spherical	67.7 nm	*E. coli, V. cholera* *S. typhimurium* *K. pneumoniae* *A. hydrophila* *P. aeruginosa*	Antibacterial	[40]
FeO	*Phoenix dactylifera*	Seed	Spherical	50 nm	*K. pneumonia* *S. epidermidis* *P. aeruginosa*	Antibacterial	[41]
NiO	*Averrhoa bilimbi*	Fruit	Spherical	100–120 nm	*E. coli, S. aureus*	Antibacterial	[42]
NiO	*Pometia pinnata*	Leaf	Irregular	10–30 nm	*E. coli, S. aureus,*	Antibacterial	[43]
NiO	*Solanum trilobatum*	Leaf	Cylindrical	25- 30nm	*S. aureus, E. coli,* *S. pnemoniae* *E. hermannii*	Antibacterial	[44]
NiO	*Berberis balochistanica*	Leaf	Irregular	23nm	*S. aureus* *P. vulgaris*	Antibacterial	[45]
NiO	*Clitoriaternatea*	Fruit	Hexagonal	10nm	*S. aureus, E. coli*	Antibacterial	[46]

± 0.38, 18 ± 0.56 mm), *E. faecalis* (13 ± 0.35,18 ± 0.32, 21 ± 0.41mm), *S. aureus* (21 ± 0.53, 33 ± 0.48, 42 ± 0.13 mm) and *P. aeruginosa* (33 ± 0.33, 36 ± 0.35, 42 ± 0.45 mm) with varying NPs concentrations 20, 30, 40 µg/mL. The antibacterial mechanism was ascribed to the interaction between positively charged TiO_2 NPs and negatively charged bacterial cell walls. This connection generated an electromagnetic attraction that caused oxidative stress in the microorganisms, resulting in their demise. All the microorganisms exhibited a ZOI, and the highest dosage showed the maximum ZOI [38].

Majid et al. utilized *P. dactylifera* to synthesize spherical FeO NPs. The effectiveness of these green iron oxide NPs in killing bacteria was assessed against three different bacterial strains. The ZOI measurements for *K. pneumonia*, *S. epidermidis*, and *P. aeruginosa* were acquired as 16mm, 15 mm, and 21 mm, respectively, utilizing a 100 µg/mL dosage of NPs. Furthermore, imperfections in nanoparticle surface shape may lead to membrane disruption or misalignment. This may enhance the antibacterial efficiency of nanoparticles by up to tenfold [41]. Haritha et al. synthesized spherical NiO NPs utilizing *A. bilimbi* fruit extract, resulting in an average 100-120 nm size range. The antibacterial efficacy of *A. bilimbi*-enhanced NiO NPs was evaluated employing the disc diffusion technique. The NPs were evaluated against *S. aureus* (ZOI: 6.1 mm) and *E. coli* (ZOI: 7 mm) at a dose of 150 µg/µL. The produced NPs exhibited enhanced antibacterial activity against gram-negative bacteria owing to their capacity to penetrate the complex cell membrane structure. Moreover, the production of reactive oxygen species (ROS) caused interactions with cellular components, including the cytoplasmic membrane, peptidoglycan layer, lipids, proteins, and DNA, disrupting multiple physiological processes. The interaction between cationic nickel molecules and anionic microbial cell membranes leads to the release of proteins and other intracellular components, ultimately resulting in cell destruction. This process is essential for improving biological applications. Prabhu et al. synthesized hexagonal-shaped NiO NPs utilizing *C. ternatea* fruit extract with a mean size of 10 nm and the antibacterial efficacy of NiO NPs towards *E. coli* (ZOI =15 ± 1.0, 17±1.0, and 22 ± 1.0 mm), and *S. aureus* (ZOI=13±1.0, 16±1.0, and 19 ± 1.0 mm) was studied. The antibacterial activity improved as the concentration of NiO NPs increased. At 200 mg/mL, the largest inhibition zone for *E. coli* was 22 ± 1.0mm, and the highest inhibition zone for *S. aureus* was 19 ± 1.0 mm. NiO NPs have a positively charged surface and a negatively charged surface for bacterial cell walls. As a result, it induces an electromagnetic interaction that destroys the bacterial cytoplasm and border. Previous research indicates that NiO NPs exert a pronounced effect on gram-negative bacteria such as *K. pneumoniae* and *P. mirabilis*, showcasing substantial inhibition zones of 32 mm and 28 mm, respectively [46]. Ramzan et al. employed *Cedrus deodara* leaf extract to produce spherical CuO NPs with an average diameter of approximately 20 nm. CuO NPs exhibited strong antibacterial effects, achieving notable ZOI at 125, 150 mg/mL concentrations. The ZOI ranged from 20–29 mm in *E. coli*, 6–16 mm in *S. aureus*, 12–20 mm in S. enterica, and 8–24 mm in *L. monocytogenes*. CuO NPs are vulnerable to various diseases and possess production processes and compatibility with living organisms inspired by biological systems [49].

Conclusion and Future Prospective

The green synthesis of MONPs using natural sources offers a safer, more eco-friendly alternative to traditional synthesis methods, effectively addressing the environmental and health concerns associated with toxic reagents and byproducts. Phytochemical-rich biological sources, such as plant extracts, facilitate the efficient production of nanoparticles with well-defined characteristics and significant antibacterial properties. MONPs synthesised through green methods have demonstrated superior efficacy, particularly in biomedical applications. The future of green-synthesized MONPs lies in expanding their use in advanced biotechnological fields, including nano-sensors, food packaging, targeted drug delivery, and cancer therapy. However, challenges such as scalability, safety concerns, and regulatory standards must be addressed. Further research is needed to refine synthesis methods, explore novel applications, and develop affordable analytical tools like ICP-AES, NMR, and HPLC for improved characterisation of phytochemicals. Innovations in this field can enhance the stability and effectiveness of MONPs, providing solutions to global challenges, including pandemic management and sustainable development.

Reference

1. S Amraei, G Eslami, A Taherpour, and A Hashemi, Micro Nano Bio Aspects 1, 12, 2022.
2. C P Sabino, M Wainwright, M S Ribeiro, F P Sellera, C Dos Anjos, M da Silva Baptista, and N Lincopan, Journal of Photochemistry and Photobiology B: Biology 208, 111893, 2020.
3. L R Duncan, H S Sader, M D Huband, R K Flamm, and R E Mendes, Microbial Drug Resistance 26, 934, 2020.
4. S Morris and E Cerceo, Antibiotics 9, 196, 2020.
5. R Pachaiappan, S Rajendran, G Ramalingam, D V N Vo, P M Priya, and M Soto-Moscoso, Chem Eng & Technol 44, 551, 2021.
6. K Chand, C Jiao, M N Lakhan, A H Shah, V Kumar, D E Fouad, M B Chandio, A A Maitlo, M Ahmed, and D Cao, Chemical Physics Letters 763, 138218, 2021.

7. A A El-Refai, G A Ghoniem, A Y El-Khateeb, and M M Hassaan, J Nanostruct Chem 8, 71, 2018.
8. A Khezerlou, M Alizadeh-Sani, M Azizi-Lalabadi, and A Ehsani, Microbial Pathogenesis 123, 505,2018.
9. G H Matar and M Andac, Inorganic Chemistry Communications 110889, 2023.
10. I Halomoan, Y Yulizar, R M Surya, and D O B Apriandanu, Materials Research Bulletin 150, 111726, 2022.
11. Z Isik, R Bouchareb, H Arslan, S Özdemir, S Gonca, N Dizge, D Balakrishnan, and S V S Prasad, Environmental Research 219, 115072, 2023.
12. S Ahmed, M Ahmad, B L Swami, and S Ikram, Journal of Advanced Research 7, 17, 2016.
13. L Soltys, O Olkhovyy, T Tatarchuk, and M Naushad, Magnetochemistry 7, 145, 2021.
14. M V Arularasu, J Devakumar, and T V Rajendran, Polyhedron 156, 279, 2018.
15. S Krishnan, S K Bhardwaj, S Liu, R Xing, and M Chavali, in Handbook of Greener Synthesis of Nanomaterials and Compounds 785–806, 2021.
16. A Rahman, M A Chowdhury, and N Hossain, Applied Surface Science Advances 11, 100296 2022.
17. A Jayachandran, T R Aswathy, and A S Nair, Biochemistry and Biophysics Reports 26, 100995, 2021.
18. W A Shaikh, S Chakraborty, G Owens, and R U Islam, Appl Nanosci 11, 2625, 2021.
19. P Rama, P Mariselvi, R Sundaram, and K Muthu, Heliyon 9, 2023.
20. J Sukweenadhi, K I Setiawan, C Avanti, K Kartini, E J Rupa, and D C Yang, South African Journal of Chemical Engineering 38, 1, 2021.
21. A Bukhari, I Ijaz, E Gilani, A Nazir, H Zain, R Saeed, S S Alarfaji, S Hussain, R Aftab, and Y Naseer, Coatings 11, 1374, 2021.
22. A H Rather, T U Wani, R S Khan, A Abdal-hay, S Rather, J Macossay, and F A Sheikh, Materials Science and Engineering: B 286, 116022, 2022.
23. G Arya, R M Kumari, N Gupta, A Kumar, R Chandra, and S Nimesh, Artificial Cells, Nanomedicine, and Biotechnology 46, 85, 2018.
24. 24. U P M Ashik, S Kudo, and J Hayashi, Synthesis of Inorganic Nanomaterials 19, 2018.
25. P B Chouke, T Shrirame, A K Potbhare, A Mondal, A R Chaudhary, S Mondal, S R Thakare, E Nepovimova, M Valis, and K Kuca, Materials Today Advances 16, 100314, 2022.
26. H Kotrange, A Najda, A Bains, R Gruszecki, P Chawla, and M M Tosif, International Journal of Molecular Sciences 22, 9596, 2021.
27. S K Jesudoss, J J Vijaya, N C S Selvam, K Kombaiah, M Sivachidambaram, T Adinaveen, and L J Kennedy, Clean Technologies and Environmental Policy 18, 729, 2016.
28. P K Stoimenov, R L Klinger, G L Marchin, and K J Klabunde, Langmuir 18, 6679, 2002.
29. W Lin, Y Huang, X D Zhou, and Y Ma, Int J Toxicol 25, 451, 2006.
30. S H Kim, H S Lee, D S. Ryu, S J. Choi, and D S. Lee, Korean J. Microbiol. Biotechnol 39, 77, 2011.
31. K Niemirowicz, B Durnaś, G Tokajuk, K G\luszek, A Z Wilczewska, I Misztalewska, J Mystkowska, G Michalak, A Sodo, and M Wątek, Nanomedicine: Nanotechnology, Biology and Medicine 12, 2395, 2016.
32. B S Shashikala, K R Ashwini, and K Chandra Babu Naidu. Inorganic Chemistry Communications 170, 113355, 2024.
33. R Gomathi and H Suhana, Inorganic and Nano-Metal Chemistry 51, 1663 2021.
34. S S Dappula, Y R Kandrakonda, J B Shaik, S L Mothukuru, V R Lebaka, M Mannarapu, and G D Amooru, Journal of Molecular Structure 1273, 134264, 2023.
35. P Raji and B K K, Results in Surfaces and Interfaces 16, 100261, 2024.
36. A Ansari, V U Siddiqui, W U Rehman, M K Akram, W A Siddiqi, A M Alosaimi, M A Hussein, and M. Rafatullah, Catalysts 12, 181, 2022.
37. M Narayanan, P Vigneshwari, D Natarajan, S Kandasamy, M Alsehli, A Elfasakhany, and A Pugazhendhi, Environmental Research 200, 111335, 2021.
38. D Anbumani, K vizhi Dhandapani, J Manoharan, R Babujanarthanam, A K H Bashir, K Muthusamy, A Alfarhan, and K Kanimozhi, Journal of King Saud University-Science 34, 101896, 2022.
39. M Abu-Kharma and A Awwad, Chemistry International 7, 3, 2021.
40. D B Manikandan, M Arumugam, S Veeran, A Sridhar, R Krishnasamy Sekar, B Perumalsamy, and T Ramasamy, Environmental Science and Pollution Research 1, 2021.
41. A Majid, F Naz, H A Jamro, B Ansari, S Abbasi, S Lal, and S A Ujjan, Journal of Pharmaceutical Research International 33, 21 2021.
42. V Haritha, S Gowri, B Janarthanan, M Faiyazuddin, C Karthikeyan, and S Sharmila, Inorganic Chemistry Communications 144, 109930, 2022.
43. I Fatimah, P W Citradewi, G Purwiandono, H Hidayat, and S Sagadevan, Inorganic Chemistry Communications 148, 110287, 2023.
44. A A Ezhilarasi, J J Vijaya, K Kaviyarasu, X Zhang, and L J Kennedy, Surfaces and Interfaces 20, 100553, 2020.
45. S Uddin, L B Safdar, J Iqbal, T Yaseen, S Laila, S Anwar, B A Abbasi, M S Saif, and U M Quraishi,

Microscopy Res & Technique 84, 2004, 2021.

46. S Prabhu, T D Thangadurai, P V Bharathy, and P Kalugasalam, Results in Chemistry 4, 100285, 2022.
47. M MuthuKathija, M S M Badhusha, and V Rama, Applied Surface Science Advances 15, 100400, 2023.
48. D Suresh, P C Nethravathi, H Rajanaika, H Nagabhushana, and S C Sharma, Materials Science in Semiconductor Processing 31, 446, 2015.
49. M Ramzan, R M Obodo, S Mukhtar, S Z Ilyas, F Aziz, and N Thovhogi, Materials Today: Proceedings 36, 576, 2021.

A Review: Integration of Computational Material Science with AIoT for Enhanced IoT Applications

Akanksha Verma[1,a], Priyanka Mehta[2], GaneshVandile[3,b], Deoram Nandanwar[3,c], Amar Nandanwar[4,d]

[1] *S. J. College, Naubasta Road, Kanpur-208021, Uttar Pradesh, India.*
[2] *Dayanand Arya Kanya Mahavidyalaya, Jaripatka, Nagpur-440014, Maharashtra, India.*
[3] *Shri Mathuradas Mohota College of Science, Nagpur-440009, Maharashtra, India.*
[4] *J. M. Patel Arts, Commerce & Science College, Bhandara-441904, Maharashtra, India.*

[a] akanksha15v@gmail.com
[b] ganesh9326wandile@gmail.com
[c] dvnandanwar@gmail.com
[d] amarknjmpc@gmail.com

Abstract

The rapid growth of the Internet of Things (IoT) has necessitated the development of systems capable of processing data efficiently and in real-time in computation material science. Traditionally, cloud computing has been used to manage and analyze the vast amounts of data generated by IoT devices to store and analyze observed data (as results of the materials) which further use as survey data application. However, cloud-based solutions often face challenges related to latency, bandwidth consumption, periodically survey, comparison with standard data and energy inefficiency, especially in resource-constrained environments. To address these challenges, edge computing has emerged as a promising solution, bringing computation closer to the data source. The integration of Artificial Intelligence (AI) agents in edge computing through microcontrollers can provide enhanced decision-making capabilities in IoT applications, offering both performance and energy efficiency. This review paper explores the advanced implementation of AI agents in edge computing using microcontrollers for IoT applications for material science as computing agent for data storage, comparison, analyzing and many more, with a specific emphasis on material science applications, highlighting the benefits and challenges of deploying lightweight AI models on resource-constrained devices.

Keywords: AI Agents, Edge Computing, Microcontrollers, IoT Applications, Computation material science, Data Processing.
Received 31 January 2025; First Review 19 March 2025; Accepted 20 April 2025.

*** Address of correspondence**
Akanksha Verma
S. J. College, Naubasta Road, Kanpur-208021, Uttar Pradesh, India.

Email: akanksha15v@gmail.com

How to cite this article
Akanksha Verma, Priyanka Mehta, Ganesh Vandile, Deoram Nandanwar, Amar Nandanwar, A Review: Integration of Computational Material Science with AIoT for Enhanced IoT Applications, J. Cond. Matt. 2025; 03 (02): 50-54.

Available from:
https://doi.org/10.61343/jcm.v3i02.134

Introduction

Despite the potential advantages of microcontrollers in edge computing, their limited processing power and memory make the integration of AI models particularly challenging [1]. However, advancements in lightweight machine learning algorithms and microcontroller architectures have made it increasingly feasible to deploy AI agents directly on edge devices. This paper aims to bridge the existing gap by exploring methodologies for implementing AI on microcontrollers within IoT ecosystems, particularly for material science applications [2,3]. The research focuses on key areas such as energy efficiency, latency reduction, and real-time decision-making in the context of material science, examining various use cases such as predictive maintenance of smart materials, real-time monitoring of material properties, and the development of adaptive materials in smart agriculture, healthcare, and smart cities [4,5]. The study also presents a comprehensive analysis of current tools, frameworks, and techniques for deploying AI on microcontrollers, providing recommendations for future advancements in this field [6-8].

This study highlights the key contributions of microcontroller-based edge computing in enhancing the performance and scalability of IoT applications related to material science [9]. By developing a framework for deploying AI agents on microcontrollers, this paper not only aims to address existing challenges but also lays the groundwork for further research and development in this domain [10]. The methodology used in this study integrates both qualitative and quantitative approaches to evaluate the impact of AI on microcontroller-based edge computing, with a focus on improving the autonomy, efficiency, and sustainability of IoT devices in material science applications [11,12].

Literature Review

Recent studies have investigated the integration of machine learning (AI) with the Internet of Things (IoT), specifically within the realm of computational material research [13]. The integration of edge computing with artificial intelligence has several benefits, such as less reliance on cloud infrastructure, decreased latency, and enhanced energy efficiency [14]. The implementation of AI on resource-limited devices, including microcontrollers that remains underexplored, resulting in an absence of feasible methodologies for integrating artificial intelligence at the boundary in materials research applications [15].

An essential obstacle to computational materials research is the computational limitation of microcontrollers [16]. AI models, especially deep learning techniques, sometimes need considerable processing resources, making their deployment on microcontrollers difficult [17]. Liu et al. (2020) illustrated the use of lightweight AI models on edge devices, including microcontrollers, emphasizing real-time sensor data processing. Their research emphasized AI's capacity to minimize data transmission to the cloud and facilitate expedited decision-making in material science domains [18].

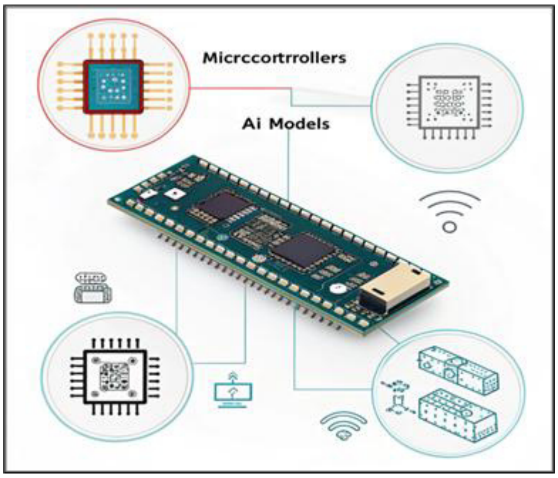

Figure 1: Comparison of latency between edge and cloud computing for IoT applications.

An essential obstacle to computational materials research is the computational limitation of microcontrollers [19]. AI models, especially deep learning techniques, sometimes need considerable processing resources, making their deployment on microcontrollers difficult [20]. Liu et al. (2020) illustrated the use of lightweight AI models on edge devices, including microcontrollers, emphasizing real-time sensor data processing. Their research emphasized AI's capacity to minimize data transmission to the cloud and facilitate expedited decision-making in material science domains [21].

The Comparison of latency between edge and cloud computing for IoT applications is depicted in Figure 1. Internet of Things (IoT) applications rely heavily on latency, which affects the efficiency and responsiveness of the system. High computational power and scalable storage are advantages of cloud computing, which processes data in centralized servers. However, due to long-distance data transmission, cloud computing experiences higher latency, ranging from 50 ms to several seconds. There may be delays in real-time applications and higher bandwidth consumption because of how dependent it is on internet connectivity. As a counterexample, edge computing minimizes bandwidth usage, improves real-time decision-making, and significantly reduces latency (1ms to 20ms) by processing data closer to the source. Autonomous vehicles, industrial automation, and healthcare monitoring are latency-sensitive scenarios that are best handled by edge computing, whereas cloud computing is better suited for storage-intensive applications and large-scale data analytics. When it comes to real-time response, network efficiency, and reliability, edge computing trumps cloud computing, according to graphical comparisons of latency. By dividing up computations between edge nodes and the cloud, hybrid approaches like fog computing are able to reap the benefits of both. Processing speed, network reliance, and data handling efficiency are just a few of the aspects that should be considered when deciding between cloud computing and edge computing for an Internet of Things application.

A further problem in computerized science of materials is the absence of AI frameworks tailored for microcontrollers [22]. Despite the development of frameworks such as Tensor Flow Lite, and Edge Impulse for resource-constrained contexts, they remain in a state of evolution and may not be applicable to all material-related applications. The need for prompt execution exacerbates the difficulties of deploying AI on microcontrollers, since several AI models demand substantial computational power as well as memory bandwidth for maximum efficacy. Furthermore, there is an absence of standardized approaches and protocols to facilitate interaction between microcontroller-based devices inside an edge computing framework [23]. This constrains the capacity to create scalable and extensible IoT systems dependent on edge-based AI processing in materials science.

Gap Analysis

The integration of AI agents with microcontrollers within computational materials science faces several substantial challenges. The main issue is the computational limitation of microcontrollers, which sometimes do not possess the requisite computing power to implement intricate AI models [24]. Notwithstanding the advancement of many lightweight models, several options continue to demand greater power than microcontrollers that can provide, resulting in performance trade-offs in material science applications.

Methodology

This research utilizes a mixed-methods approach, integrating qualitative and quantitative methodologies to evaluate the feasibility and effectiveness of AI agents functioning on microcontrollers that for utilization in cognitive materials science, especially within IoT-based systems. The key components of the methodology are as follows:

The study will use artificial intelligence models on microcontrollers that within materials science, concentrating on intelligent production and environmental monitoring. These domains are chosen for their data-centric characteristics and the need for instantaneous analysis and decision-making, essential for enhancing material qualities and processes [25]. Microcontrollers, namely ARM Cortex-M4 and the ESP32 micro will be used for the deployment of AI agents. These microcontrollers have sufficient processing capability for lightweight algorithms based on AI and are often used in IoT applications [26]. Lite implementations of Tensor Flow for Arduino boards and Edge Impulse will be used to create and implement AI models specifically designed for materials research applications [27].

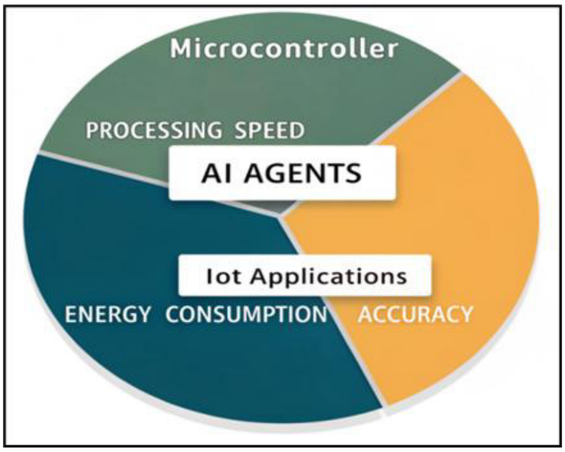

Figure 2: AI gents and IoT applications.

Technology and Gathering Information: Real-time sensor data, including humidity, temperature, pressure, and substance composition, will be collected from IoT devices inside the specified materials science settings. The data will be pre-processed and input into compact AI models operating on the microcontrollers [28]. The models will thereafter be assessed for their capacity to effectively analyse data and facilitate decision-making in the optimization and monitoring of material properties. The efficacy of the artificially intelligent agents will be evaluated by critical parameters such as accuracy, latency, and consumption of energy. Statistical techniques will be used to examine the performance disparities across edge computer systems and platforms running on the cloud [29]. Furthermore, qualitative data will be gathered via field observations to assess the practical usability and efficacy of microcontroller-based artificial intelligence systems in material science settings.

The research design is meticulously organized to guarantee repeatability by providing complete requirements for the hardware, software setups, and code versions used. This will allow other researchers to reproduce the work and verify the results, assuring wider relevance in computerized materials science [30].

Conclusion

The incorporation of AI agents in computing at the edge, especially via microcontrollers, offers a viable resolution to the difficulties encountered by conventional stored in the cloud Internet of Things (IoT) systems in computerized materials science. By analysing information at the edge, near its origin, AI agents may minimize latency, optimize bandwidth, and enhance energy efficiency. This research has shown that microcontrollers as despite their constrained processing capabilities, may be efficiently used for real-time, compact AI projects in materials research IoT settings.

This study underscores the need of enhancing AI algorithms and architectures specifically designed for microcontroller-based edge computing in materials science. Despite ongoing issues with computing limitations and real-time processing, progress in AI model compression as well, pruning, and quantization is facilitating more efficient implementations. Moreover, applications in domains such as intelligent manufacturing, material property assessment, and environmental monitoring demonstrate that microcontroller-based artificially intelligent agents may improve decision-making, resulting in more self-sufficient, responsive, and effective IoT systems within materials science.

The research highlights the revolutionary capabilities of microcontroller-based artificial intelligent agents in cutting-edge computing for materials research applications. This study establishes a foundation for future research by identifying deficiencies in the existing literature and suggesting methodologies for the integration of AI into microcontrollers. The incorporation of AI agents into IoT systems within materials science may catalyse innovation across several industries, enhancing sustainability, effectiveness, and overall system functionality.

References

1. Matin, Abdul, Md Rafiqul Islam, Xianzhi Wang, Huan Huo, and Guandong Xu. *"AIoT for sustainable manufacturing: Overview, challenges, and opportunities."* Internet of Things (2023): 100901.
2. Yan, Jiayi. *"AIoT in Smart Homes: Challenges, Strategic Solutions, and Future Directions."* Highlights in Science, Engineering and Technology 87 (2024): 59-65.
3. Chai, Boon Xian, Maheshi Gunaratne, Mohammad Ravandi, Jinze Wang, Tharun Dharmawickrema, Adriano Di Pietro, Jiong Jin, and Dimitrios Georgakopoulos. *"Smart industrial internet of things framework for composites manufacturing."* Sensors 24, no. 15 (2024): 4852.
4. Rao, Shreyas Suresh, Steven Lawrence Fernandes, Chandra Singh, and Rathishchandra R. Gatti, eds. “*AIoT and Big Data Analytics for Smart Healthcare Applications*”. Bentham Science Publishers, 2023.
5. Al-Turjman, Fadi, Anand Nayyar, Ajantha Devi, and Piyush Kumar Shukla, eds. “*Intelligence of things: AI-IoT based critical-applications and innovations*”. New York, US: Springer, 2021.
6. Haroun, Ahmed, Xianhao Le, Shan Gao, Bowei Dong, Tianyiyi He, Zixuan Zhang, Feng Wen, Siyu Xu, and Chengkuo Lee. *"Progress in micro/nano sensors and nanoenergy for future AIoT-based smart home applications."* Nano Express 2, no. 2 (2021): 022005.
7. Shi, Qiongfeng, Zixuan Zhang, Yanqin Yang, Xuechuan Shan, Budiman Salam, and Chengkuo Lee. *"Artificial intelligence of things (AIoT) enabled floor monitoring system for smart home applications."* ACS nano 15, no. 11 (2021): 18312-18326.
8. Joshua, Salaki Reynaldo, Sanguk Park, and Kihyeon Kwon. *"Knowledge-Based Modeling Approach: A Schematic Design of Artificial Intelligence of Things (AIoT) for Hydrogen Energy System."* In 2024 IEEE 14th Annual Computing and Communication Workshop and Conference (CCWC), pp. 0235-0241. IEEE, 2024.
9. Gouiza, Nissrine, Hakim Jebari, and Kamal Reklaoui. *"Integration of IoT-enabled technologies and artificial intelligence in diverse domains: recent advancements and future trends."* Journal of Theoretical and Applied Information Technology 102, no. 5 (2024).
10. Ullah, Inam, Inam Ullah Khan, Mariya Ouaissa, Mariyam Ouaissa, and Salma El Hajjami, eds. *Future Communication Systems Using Artificial Intelligence, Internet of Things and Data Science*. CRC Press, 2024.
11. Yang, Chao-Tung, Ho-Wen Chen, En-Jui Chang, Endah Kristiani, Kieu Lan Phuong Nguyen, and Jo-Shu Chang. *"Current advances and future challenges of AIoT applications in particulate matters (PM) monitoring and control."* Journal of Hazardous Materials 419 (2021): 126442.
12. Hou, Kun Mean, Xunxing Diao, Hongling Shi, Hao Ding, Haiying Zhou, and Christophe de Vaulx. *"Trends and challenges in AIoT/IIoT/IoT implementation."* Sensors 23, no. 11 (2023): 5074.
13. Pise, Anil Audumbar, Khalid K. Almuzaini, Tariq Ahamed Ahanger, Ahmed Farouk, Kumud Pant, Piyush Kumar Pareek, and Stephen Jeswinde Nuagah. *"Enabling artificial intelligence of things (AIoT) healthcare architectures and listing security issues."* Computational Intelligence and Neuroscience 2022, no. 1 (2022): 8421434.
14. Bhatti, Mughair Aslam, Zhiyao Song, and Uzair Aslam Bhatti. *"AIoT-driven multi-source sensor emission monitoring and forecasting using multi-source sensor integration with reduced noise series decomposition."* Journal of Cloud Computing 13, no. 1 (2024): 65.
15. Rezaei, Sajad, and Amin Ansary, eds. *Artificial Intelligence of Things (AIoT) for Productivity and Organizational Transition*. IGI Global, 2024.
16. Zhang, Zixuan, Xinmiao Liu, Hong Zhou, Siyu Xu, and Chengkuo Lee. *"Advances in machine-learning enhanced nanosensors: From cloud artificial intelligence toward future edge computing at chip level.*" Small Structures 5, no. 4 (2024): 2300325.
17. Chillón Geck, Carlos, Thamer Al-Zuriqat, Moayed Elmoursi, Kosmas Dragos, and Kay Smarsly. *"AIoT-enabled decentralized sensor fault diagnosis for structural health monitoring."* The e-journal of nondestructive testing & ultrasonics (2024).
18. Qiang, Guofeng, Shu Tang, Jianli Hao, and Luigi Di Sarno. *"A BIM and AIoT Integration Framework for Improving Energy Efficiency in Green Buildings."* In Construction Research Congress 2024, pp. 577-585.
19. Chang, Zhuoqing, Shubo Liu, Xingxing Xiong, Zhaohui Cai, and Guoqing Tu. *"A survey of recent advances in edge-computing-powered artificial intelligence of things."* IEEE Internet of Things Journal 8, no. 18 (2021): 13849-13875.
20. Babu, CV Suresh, M. Sowmi Saltonya, Suresh Ganapathi, and A. Gunasekar. *"AIoT Revolution:*

Transforming Networking Productivity for the Digital Age." In Artificial Intelligence of Things (AIoT) for Productivity and Organizational Transition, pp. 108-143. IGI Global, 2024.

21. Khan, Surbhi Bhatia, Mohammad Alojail, Mahesh Thyluru Ramakrishna, and Hemant Sharma. *"A Hybrid WSVM-Levy Approach for Energy-Efficient Manufacturing Using Big Data and IoT."* Computers, Materials & Continua 81, no. 3 (2024).
22. Forkan, Abdur Rahim Mohammad, Yong-Bin Kang, Felip Marti, Abhik Banerjee, Chris McCarthy, Hadi Ghaderi, Breno Costa, Anas Dawod, Dimitrios Georgakopolous, and Prem Prakash Jayaraman. *"Aiot-citysense: Ai and iot-driven city-scale sensing for roadside infrastructure maintenance."* Data Science and Engineering 9, no. 1 (2024): 26-40.
23. Villar, Eneko, Imanol Martín Toral, Isidro Calvo, Oscar Barambones, and Pablo Fernández-Bustamante. *"Architectures for Industrial AIoT Applications."* Sensors 24, no. 15 (2024): 4929.
24. Singh, Arun Kumar. *"Smart Eco-Friendly Manufacturing System with Aiot Applications."* Available at SSRN 4862891 (2024).
25. Said, Sandra, Rowan Ihab, Ossama Hesham, Islam Abou Tabl, Nu Maged, Sherin Youssef, and Mazen Elagamy. *"AIOT-Arch: furthering artificial intelligence in big data IoT applications."* In IOP Conference Series: Materials Science and Engineering, vol. 1051, no. 1, p. 012008. IOP Publishing, 2021.
26. Boobalan, Parimala, Swarna Priya Ramu, Quoc-Viet Pham, Kapal Dev, Sharnil Pandya, Praveen Kumar Reddy Maddikunta, Thippa Reddy Gadekallu, and Thien Huynh-The. *"Fusion of federated learning and industrial Internet of Things: A survey."* Computer Networks 212 (2022): 109048.
27. Divine, I. L. O. H., Chimaoge Peace Aguma, and Adeyemi Oyetoro Olagunju. *"Integrating AI enhanced remote sensing technologies with IOT networks for precision environmental monitoring and predicative ecosystem management."* (2024).
28. Zuo, Yanjun. *"Exploring the Synergy: AI Enhancing Blockchain, Blockchain Empowering AI, and their Convergence across IoT Applications and Beyond."* IEEE Internet of Things Journal (2024).
29. Zuo, Yanjun. *"Exploring the Synergy: AI Enhancing Blockchain, Blockchain Empowering AI, and their Convergence across IoT Applications and Beyond."* IEEE Internet of Things Journal (2024).
30. Badshah, Afzal, Anwar Ghani, Ali Daud, Ateeqa Jalal, Muhammad Bilal, and Jon Crowcroft. *"Towards smart education through internet of things: A survey."* ACM Computing Surveys 56, no. 2 (2023): 1-33.

Critical Mass Thresholds for Neutron Star Stability and Black Hole Formation in Gravitational Collapse

Bijan Kumar Gangopadhyay

Independent Researcher, Chowdhuripara, P.O Makardaha, Dt Howrah,West Bengal 711409, India.

bkgangopadhyay@gmail.com

Abstract

This research investigates the critical mass thresholds for black hole formation during the gravitational collapse of massive stars. Using numerical simulations and analytical techniques, we model the collapse of spherically symmetric, non-rotating neutron stars by solving the Tolman-Oppenheimer-Volkoff (TOV) equation. We first derive an analytical solution for the TOV equation under the assumption of constant density, estimating the maximum neutron star mass to be 2.85 solar masses. We then incorporate a customized density profile, as predicted in our previous work, into the TOV framework. This yields a critical mass of 2.096 solar masses at a radius of approximately 10 km, consistent with current theoretical and observational expectations. The maximum stable mass with this profile is calculated to be 2.36 solar masses, with the mass decreasing to zero beyond 15.5 km. By analyzing different initial masses (2.0, 4.0, and 8.0 solar masses) using a polytropic equation of state (EOS), we examine the mass-radius and pressure-radius relationships. Our results reveal a highly non-linear and abrupt change in mass and pressure distributions, indicating the formation of a dense outer shell. This structural feature could significantly influence neutron star stability and the conditions leading to black hole formation. These findings provide valuable insights into the maximum mass limits of neutron stars, aiding in the interpretation of astrophysical observations and the identification of potential black hole progenitors.

Keywords: Neutron Star, Tolman-Oppenheimer-Volkoff Equation, Black Hole, Gravitational Collapse, Stellar Stability.
Received 28 January 2025; First Review 17 March 2025; Accepted 24 March 2025.

*** Address of correspondence**
Bijan Kumar Gangopadhyay
Independent Researcher, Chowdhuripara, P.O Makardaha, Dt Howrah,West Bengal 711409, India.
Email: bkgangopadhyay@gmail.com

How to cite this article
Bijan Kumar Gangopadhyay, Critical Mass Thresholds for Neutron Star Stability and Black Hole Formation in Gravitational Collapse, J. Cond. Matt. 2025; 03 (02): 55-62.

Available from:
https://doi.org/10.61343/jcm.v3i02.84

Introduction

The probability of existence of neutron star was predicted by scientists after the discovery of neutron by Chadwick in 1932. Among them pioneers were Lev Landau, Walter Baade and Fritz Zwicky (1936). They believed that during supernova explosion of a main sequence star of more than 10 solar mass, neutron star might be formed. However, the history of observation of neutron star begins in 1967 when Jocelyn Bell and her advisor Anthony Hewish discovered radio pulsar (PSR B1919+21) at Cambridge. Various observation and theoretical prescriptions now lead us to believe that pulsars are actually rapid rotating neutron stars. It is difficult to detect any non-rotating neutron star. So, analyzing the radiation emitted by pulsars, properties of neutron stars can be predicted. In 1939 Oppenheimer and E. Salpeter along with different theoreticians realized that like white dwarf, neutron star might have an upper mass limit. Oppenheimer and Volkoff derived an equation of hydrostatic equilibrium of star by using general theory of relativity, as they believed that general theory of relativity might be more fruitful than Newtonian mechanics. They calculated the limiting mass of a neutron star to be 0.7 solar mass [1]. This result seemed to be very low, as it is very much expected that the maximum mass of a neutron star should at least exceed the Chandrasekhar mass limit of 1.4 solar mass [2]. The strong repulsive nuclear force acting between neutrons probably increases the upper mass limit of a neutron star. Different stellar observation of pulsars leads to an idea, that maximum mass of neutron star may lie between 1.4 to 3.0 solar mass. Integrating equation of equilibrium, Rhoades and Ruffini [3] found that the maximum mass of neutron star to be 3.2 solar mass. Nauenberg and Chapline (1973) [4] found this to be 3.6 solar mass. Rotating neutron stars may have higher mass limit. Hartle and Sabbadini (1977) [5] introduced an empirical relation for non-rotating neutron star as,

$$M_{\text{bound}} = 11.4 M_{\odot} \left(\frac{10^{17}}{\rho_0}\right)^{\frac{1}{2}} \tag{1}$$

Friedman and Ipser (1987) [6] have derived an empirical relation for rotational neutron star as,

$$M_{\mathrm{MAX}}^{\mathrm{ROT}} = 14.3 M_{\odot} \left(\frac{10^{17}}{\rho_0} \right)^{\frac{1}{2}} \tag{2}$$

If we use polytrope stellar model with n=1.5, numerically a standard relation [7] can be employed for evaluating mass of neutron star from MR^3 = constant as,

$$M = 1.102 \left(\frac{\rho_0}{10^{18}} \right)^{\frac{1}{2}} M_{\odot} = \left(\frac{15.12 Km}{R} \right)^3 M_{\odot} \tag{3}$$

$$R = 14.64 \left(\frac{\rho_0}{10^{18}} \right)^{-\frac{1}{6}} \tag{4}$$

In equations (1), (2), (3), and, (4) ρ_0 (density) and R (radius) of neutron star are measured in Kg/m^3 and in Km respectively. Whatever be the nature of equation of state, the maximum mass of a neutron star must be greater than 1.4 solar mass [8]. It is expected that at the end point of stellar evolution, if the core of the star contains carbon or heavier element then there is every possibility that the remnant star might be transformed to neutron star. To retain stability of neutron star, it has a critical mass threshold, beyond which it would be collapsed to a black hole.

Methodology

In this work we have used the following equations as per requirement. Equation of Hydrostatic Equilibrium [9]:

$$\frac{dp(r)}{dr} = -\frac{Gm(r)\rho(r)}{r^2} \tag{5}$$

TOV Equation [10]:

$$\frac{dp(r)}{dr} = -\frac{G\left[m(r) + 4\pi r^3 \frac{p(r)}{c^2}\right]\left[\rho(r) + \frac{p(r)}{c^2}\right]}{r^2\left[1 - \frac{2Gm(r)}{c^2 r}\right]} \tag{6}$$

Mass profile of star (Equation of Continuity) [9]:

$$\frac{dm(r)}{dr} = 4\pi r^2 \rho(r) \tag{7}$$

Customized Density profile [11]:

$$\rho(r) = \rho_0 \left(1 - \frac{r^2}{R^2} \right) \tag{8}$$

Non-relativistic degeneracy pressure of neutron star [10]

$$P = 0.542 \times 10^4 \rho_0^{5/3} \quad \text{(S. I. Unit)} \tag{9}$$

Relativistic degeneracy pressure of neutron star [10]

$$P = 1.235 \times 10^{10} \rho_0^{4/3} \quad \text{(S. I. Unit)} \tag{10}$$

Analytical Solution of TOV Equation

Let us start with the TOV equation as,

$$\frac{dp}{dr} = -\frac{G}{r^2}\left[\rho + \frac{p}{c^2}\right]\left[m(r) + \frac{4\pi r^3 p}{c^2}\right]\left[1 - \frac{2Gm(r)}{c^2 r}\right]^{-1} \tag{11}$$

As we do not have any authentic equation of state of neutron star, it is almost impossible to solve this equation analytically. So, to solve it analytically, we have assumed here that the density of the relevant star is constant (ρ = constant). As density is constant, we can write, $m(r) = (4/3)\pi r^3 \rho$. So, TOV equation becomes,

$$\frac{dp}{dr} = -\frac{Gm(r)\rho}{r^2}\left[1 + \frac{p}{\rho c^2}\right]\left[1 + \frac{3p}{\rho c^2}\right]\left[1 - \frac{2Gm(r)}{c^2 r}\right]^{-1} \tag{12}$$

Let, $\frac{p}{\rho c^2} = x$, and $\frac{2Gm(r)}{c^2 r} = y$, then we have,

$$\frac{dx}{dr} = -\frac{y}{2r}(1 + x)(1 + 3x)(1 - y)^{-1} \tag{13}$$

Now, from $y = \frac{2Gm(r)}{c^2 r}$, it follows:

$$\frac{dy}{dr} = \frac{8\pi G\rho}{3c^2} 2r = \frac{y}{r^2} 2r = \frac{2y}{r} \tag{14}$$

Now,

$$\frac{dx}{dr} = \frac{dx}{dy}\frac{dy}{dr} = \frac{dx}{dy}\frac{2y}{r} \tag{15}$$

Hence TOV equation takes the form,

$$\frac{dx}{(1 + x)(1 + 3x)} = -\frac{dy}{4(1 - y)} \tag{16}$$

Integrating,

$$ln\left(\frac{1 + x}{1 + 3x}\right) = -\frac{1}{2} ln(1 - y) + k \tag{17}$$

Here k is the constant of integration. At the surface of the star, pressure is zero (boundary condition), so that, p=0 (x=0) at r=R

Let us take at r=R, $y = y_0 = \frac{2GM}{c^2 R}$ where, M is the mass of the star and R being the radius.

So, we get, $k = \frac{1}{2} ln(1 - y_0)$

Now, the solution becomes on simplification,

$$x = \frac{\sqrt{1 - y_0} - \sqrt{1 - y}}{\sqrt{1 - y} - 3\sqrt{1 - y_0}} \tag{18}$$

At centre of the star, r=0, so, y=0, then let $x = x_0$ (boundary condition). Central pressure of the star can now be expressed as, $p_0 = \rho c^2 x_0$. Again, $x_0 = \frac{\sqrt{1-y_0}-1}{1-3\sqrt{1-y_0}}$

Therefore,

$$p_0 = \rho c^2 \left[\frac{\sqrt{1 - y_0} - 1}{1 - 3\sqrt{1 - y_0}}\right] \tag{19}$$

Now, if the denominator of the above expression is zero, then central pressure goes to infinity and the star cannot maintain its stability, it will be gravitationally collapsed to a black hole. This scenario will occur when, $3\sqrt{1-y_0}=1$

or, $y_0=\frac{8}{9}$,

Hence, $\frac{2GM}{c^2\left(\frac{3M}{4\pi\rho}\right)^{\frac{1}{3}}}=\frac{8}{9}$

On simplification it follows [10]:

$$M=\left[\frac{4c^3}{\sqrt{243\rho\pi G^3}}\right] \tag{20}$$

Numerical Solution of the TOV Equation

To solve the **TOV equation** for stellar structure numerically, we implemented a Python script using the **Runge-Kutta method (RK45)**. The TOV equation models the relationship between the mass (m) and pressure (P) as a function of the radius (r). We used the scipy.integrate.solve_ivp() function, which applies as stepsize **RK45 solver**, ensuring accuracy and efficiency. The differential equations were solved over a radial range $[10^{-5}, R]$ with an initial central mass m_0 and pressure $P_0 = 10^{-2}$. To prevent unphysical solutions, we introduced a **pressure threshold event** that stops the integration when the pressure drops below 10^{-10}, marking the surface of the star. The relationship between pressure P and density ρ is modeled using the polytropic equation of state:

$$P=K\rho^{\gamma}=K\rho^{\left(1+\frac{1}{n}\right)} \tag{21}$$

where, K is the Polytropic constant, determined by the star's initial conditions, Adiabatic index is γ, and n is the Polytropic index. n = 3 stands for relativistic degenerate matter, and n=1.5 for non-relativistic degenerate matter. For this study, we have used a polytropic index n = 3 or γ=4/3 [12] which is appropriate for relativistic stars composed of degenerate matter.

Finally, we plotted the **mass and pressure profiles** for different initial masses as 2.0, 4.0, and 8.0 solar mass, demonstrating how the stellar structure changes with varying central mass. The boundary conditions employed as, at the core (r = 0), m(0) = 0, P(0) = P_C (central pressure), and at the surface (r = R), P(R) = 0, where R is the star's radius.

Results

1. Mass and radius profile for different initial masses

The figure 1 illustrate the **Mass and Pressure profiles** for different initial masses m_0 as a function of the radius $R_{\odot}$. These visual aids are essential for clear understanding of the relation between mass, radius, and pressure distribution in the modeled system. The left panel of figure 1 shows the mass distribution as a function of the radial coordinate $R_{\odot}$ revealing that higher mass cores exhibit steeper gradients near their surfaces, indicative of more concentrated mass distribution. The right panel shows the pressure profile for the same cores, demonstrating that as the initial mass increases, the central pressure grows significantly, which is a critical factor in determining the stability of the core. Mass radius and pressure radius profile of a star depends on its initial mass. The TOV equation (6) describes the pressure gradient inside the relativistic star, balancing pressure support and gravitational pull. This equation ensures hydrostatic equilibrium, where the outward pressure gradient counteracts the inward gravitational pull. The mass continuity equation (7) relates the mass distribution to the radial density profile.

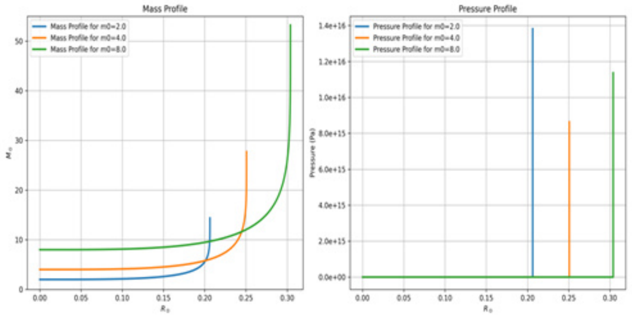

Figure 1: Mass and pressure profile for different initial masses using TOV and polytrope equation.

Mass Profile: The mass profile exhibits the following findings:

Inner Core Uniformity: For small radii, the mass remains nearly constant which indicates a dense, uniform core structure across all initial mass configurations. For initial mass $2M_{\odot}$, mass remains constant up to $0.125R_{\odot}$, For $4M_{\odot}$ it remains constant up to $0.225R_{\odot}$, and for $8M_{\odot}$ it is up to $0.275R_{\odot}$. This uniformity is a consequence of the balance between gravitational and pressure forces within the dense core, where the polytropic equation of state enforces nearly constant density.

Outer Layers: Beyond the core region, the mass increases steeply, reflecting a rapid transition to less dense outer layers. The final masses and radii for the different configurations are:

For, the initial mass $2M_{\odot}$ final mass is $14.5M_{\odot}$ at $0.207R_{\odot}$

For, the initial mass $4M_{\odot}$ final mass is $27.7M_{\odot}$ at $0.251R_{\odot}$

For, the initial mass $8M_{\odot}$ final mass is $53.5M_{\odot}$ at $0.304R_{\odot}$

This steep behavior suggests that while the core holds a smaller fraction of the total mass, the outer regions of the star contribute significantly to the total mass. Furthermore, a linear relationship is observed between the final mass and the initial mass of the star. This proportionality suggests that for the given initial conditions and polytropic index, the total mass scales linearly with the initial core mass, though this relationship may vary with different polytropic indices or initial conditions.

Pressure Profile: The pressure profiles show marked transition:

Low-Pressure Core: For small radii, pressure is relatively low, supporting the uniform core structure.

High-Pressure Outer Layers: Pressure rises sharply beyond the core: For the initial mass $2M_\odot$ peak pressure is $1.3 \times 10^{16} Pa$ at radius $0.205R_\odot$, for the initial mass $4M_\odot$ peak pressure is $1.1 \times 10^{16} Pa$ at radius $0.250R_\odot$, and for the initial mass $8M_\odot$ peak pressure is $1.4 \times 10^{16} Pa$ at radius $0.305R_\odot$.

2. Solution of Hydrostaic equation and density profile

We investigate the mass limit and properties of neutron stars by solving the hydrostatic equilibrium equation using a customized density profile [11]. The degeneracy pressures for non-relativistic and relativistic regimes are incorporated into the analysis [10,11]. In the previous study, the mass-radius relation for neutron stars was investigated using the hydrostatic equilibrium (HE) equation in conjunction with a specific density profile. While this approach provided initial insights, it became evident that the HE equation alone fails to fully capture the relativistic effects essential for accurately modeling compact objects like neutron stars. For instance, the relation $MR^3 = 1.5 \times 10^{42}$, derived under simplified assumptions, predicts a decreasing mass with increasing radius as shown below (Figure 2).

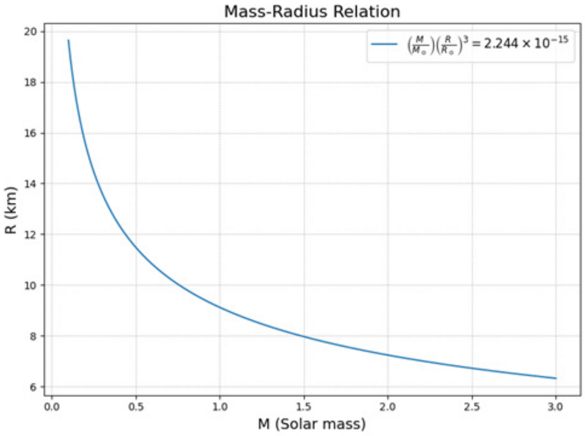

Figure 2: Mass Profile from Analytical Solution using equation of HE, Density Profile, and Degenerate Pressure

Analytical and numerical solution obtained as follows:

1. Analytical Calculation: Using degeneracy pressure for the core neutrons, the maximum mass of the neutron star was calculated analytically as $M_{\max} = 2.75M_\odot$ [11].

2. **Numerical Simulation:** The numerical integration of the mass continuity equation with the density profile as shown in Figure 2 rose monotonically with the radius, reaching $M = 2.84M_\odot$ for R=15Km. This result is slightly higher than the analytically predicted maximum mass.

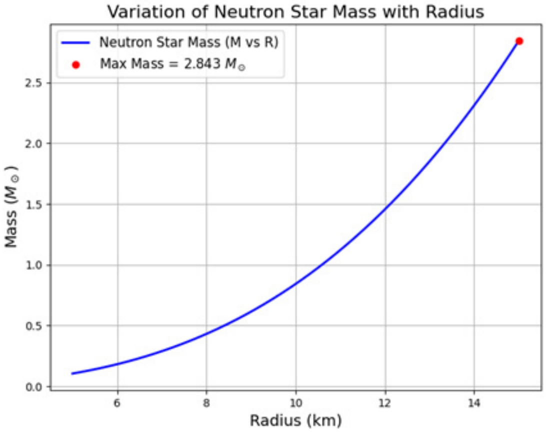

Figure 3: Mass Profile from Numerical Solution using equation of HE, Density Profile, and Degenerate Pressure.

3. TOV Equation and Density Profile

We have here Introduced the significance of neutron stars, emphasizing their unique structure governed by degeneracy pressure and gravitational forces. We have highlighted the existing mass limits (TOV limit) and the theoretical refinement using different density profiles. Starting from equation (20), we can write the relation as:

$$M = \frac{7.175 \times 10^{39}}{\sqrt{\rho}} \text{kg} = \frac{3.61 \times 10^{9}}{\sqrt{\rho}} M_\odot \qquad (22)$$

Where, $M_\odot$ is the solar mass. The challenge here is selecting a suitable value for ρ , the density. Assuming the neutron star's density is analogous to that of a neutron, we estimate ρ using the relation $\rho = 2\frac{m_n}{\frac{4}{3}\pi r_n^3}$, where m_n kilogram is the mass of a neutron and $r_n \approx 10^{-15}$ meters is the neutron radius. This yields a neutron star density of approximately $8 \times 10^{17} \text{kg/m}^3$. Applying this density in the mass-density relation from equation (20), the calculated maximum mass of a neutron star is about $4.036M_\odot$, which notably exceeds experimental values.

4. Stability of neutron star dependence on density

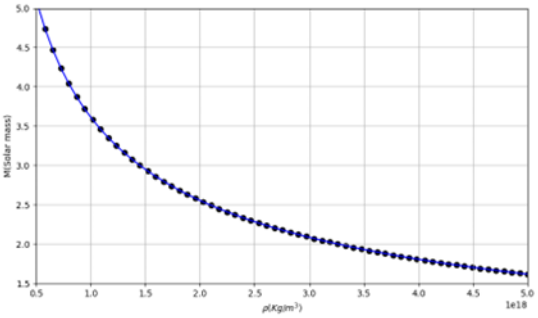

Figure 4: Dependence of Maximum Mass on Density using the TOV Solution.

Figure 4 illustrates the relationship between the maximum mass and density, based on this TOV solution. The plot shows that the limiting mass of neutron star to retain stability gets reduced with the increase of density of neutron star. At density greater than$5 \times 10^{18}\mathrm{Kg/m^3}$ mass limit is less than $1.4M_{\odot}$ (Chandrasekhar mass limit of White Dwarf). This can not be the real scenario of existence of neutron star. So, neutron star might also possess a limiting density less than $5 \times 10^{18}\mathrm{kg/m^3}$ to retain stability as obtained in this approximate solution of TOV equation considering density to be constant.

5. Mass limit of neutron star using TOV and density profile

Finally, we assume a central pressure of $1.2 \times 10^{34}\mathrm{Pa}$ for the neutron star on the eve of collapsing, leading to an estimated maximum density of $1.6 \times 10^{18}\mathrm{Kg/m^3}$. Substituting this density into equation (20) the resulting maximum mass for a neutron star is estimated approximately as $2.85M_{\odot}$, aligning more closely with the observational constraints. Further, by incorporating our predicted density profile (equation 8) into the TOV equation (equation 6) and running a Python simulation to plot limiting mass of neutron star vs its radius, we obtain a critical mass of $2.096M_{\odot}$ and a critical radius of 10.5 Km, with a maximum mass of $2.36M_{\odot}$ as shown in Figure 5.

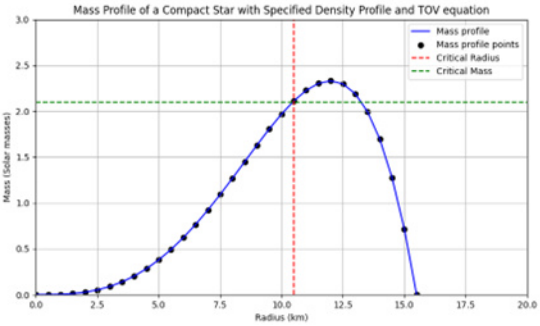

Figure 5: Mass Profile from Numerical Solution using TOV, Density Profile, and Degenerate Pressure.

Critical mass is defined as the limit for non-rotating neutron stars, beyond which neutron stars collapse into black holes, on the other hand maximum mass is the highest mass a neutron star that can be achieved before collapsing in black hole, potentially increased by factors like rotation. Figure 5 indicates an upper mass limit of neutron star, beyond which mass gets decreased to zero. This means that there might be an upper limit of radius of neutron star, no neutron star with greater radius than this upper limit can exist in nature which should be around 15 Km.

Discussion

1. Mass and Radius Profile for Different Initial Masses

The variation in peak pressure with initial stellar mass can be attributed to differences in density gradients and the relation between gravitational and pressure forces. The numerical results, based on the TOV equation and the polytropic equation of state, reveal the following key findings:

A **linear scaling** of the maximum mass with the initial core mass is observed, along with **transition zones** in both the mass and pressure profiles. These transition zones separate the uniform core from the steep outer gradients. The pressure profile shows distinct behavior with varying initial masses: When the initial mass increases from **2.0 to 4.0 solar masses**, the peak pressure **decreases**. However, when initial mass increases further to **8.0 solar masses**, the peak pressure **increases**. This discrepancy is likely due to **transition phenomena** within the stellar structure. For the 4.0 solar mass configuration, the density gradient creates a more gradual transition in density, resulting in a lower peak pressure. In contrast, at 8.0 solar masses, the higher overall density leads to an elevated peak pressure.

The influence of the **polytropic index ($\gamma = 4/3$)**, characteristic of relativistic degenerate matter, plays a critical role in the pressure-density relationship. This index significantly affects the pressure variance across different mass profiles. These mass and radius profiles illustrate how increasing central pressure and mass concentration destabilize the stellar core, eventually exceeding the critical thresholds for neutron star stability. They also provide comparative visualizations that indicate the conditions under which a collapsing core transitions into a black hole. Thus, this analysis offers valuable insights into the internal structure of stars and helps to determine critical mass thresholds, bridging the gap between theoretical models and observed gravitational collapse phenomena.

2. Solution of the Hydrostatic Equation and Density Profile

The observed discrepancy between the numerical simulation and the analytical results can be explained by several factors:

Simplified Density Profile: The numerical simulation uses a **prescribed density profile** without feedback from the pressure or a realistic equation of state (EoS), limiting its accuracy.

Lack of Instabilities: The non-relativistic framework does not account for **gravitational instabilities**, which are essential for predicting the maximum mass and its subsequent decrease.

Relativistic Effects: Analytical calculations include **relativistic effects** through the EoS for neutron degeneracy pressure. These effects govern the balance between gravity and degeneracy pressure, enabling the prediction of the maximum stable mass.

Limitations and Implications

The primary limitation of this approach is its inability to capture the **realistic mass decrease** beyond the maximum stable configuration observed in the analytical results. This shortcoming arises due to the absence of relativistic corrections to gravity and pressure. Additionally, feedback mechanisms between pressure and density are neglected, and the simplified density profile does not accurately reflect the complex internal structure of neutron stars. While the non-relativistic numerical simulation provides **qualitative insights** into the mass-radius relation, it fails to capture the maximum mass and its subsequent decrease caused by gravitational instability. However, the results remain consistent with observational constraints and offer valuable insights into the transition between **non-relativistic and relativistic regimes** in neutron star cores.

3. Mass Limit of Neutron Stars Using the TOV Equation and Density Profile

The results demonstrate that solving the **mass-continuity equation** numerically with the same density profile yields an increasing mass with radius, reflecting the realistic accumulation of matter within the star. However, this trend exposes the limitations of the **Hydrostatic Equilibrium (HE)** framework in high-density regimes.

The discrepancy arises because the HE equation neglects **relativistic effects**, such as spacetime curvature and relativistic pressure gradients, which become significant in dense astrophysical systems. To overcome these limitations, we incorporated the **TOV equation**, which extends the HE framework by including general relativistic effects.

By applying the TOV equation to the same density profile: The inconsistencies observed with the equation were resolved. The results aligned more closely with **realistic neutron star physics**. The corrected mass-radius relation provided deeper insights into the interrelation between gravitational and pressure forces within neutron stars.

Neutron Star Mass Constraints

The observed maximum mass of neutron stars is indeed close to **2.08** solar masses, with one of the most massive confirmed examples being **PSR J0740+6620**, measured at approximately **2.08–2.17** solar masses [13]. Some models suggest that the true upper limit for neutron star masses may lie between **2 and 3 solar masses**. The discrepancy between different models arises from the **uncertainty in the equation of state** for neutron stars. Despite significant progress in modeling, the exact EoS remains uncertain, as the innermost core of neutron stars is still not fully understood.

Conclusion

This study presents a comprehensive numerical analysis of the **Tolman-Oppenheimer-Volkoff (TOV) equations**, coupled with various density profiles, to investigate the critical mass and structural properties of neutron stars. The findings highlight the intricate relationship between **mass, pressure, and radius** in determining the stability of relativistic stars. Specifically, the results reveal significant **non-linearities in the mass and pressure distributions**, suggesting the potential existence of a dense outer shell within the stellar structure. These features may indicate underlying physical phenomena, such as **phase transitions** or variations in the **equation of state (EoS)** at high densities. Throughout this study, different methods were employed to estimate the **maximum mass limit** of a neutron star before it undergoes gravitational collapse into a black hole or another compact object. The key conclusions derived from the analyses are summarized as follows:

1. Equation of Hydrostatic Equilibrium: Analytical calculations of the **hydrostatic equilibrium (HE)** equation, combined with a customized density profile, yielded a maximum neutron star mass of approximately **2.75 solar masses**. Numerical simulations, based on integrating the **mass-continuity equation** with the same density profile, produced a consistent maximum mass estimate of **2.84 solar masses**.

2. Constant Density Model: By solving the TOV equations with a **constant density as** $1.6 \times 10^{18} \mathrm{Kg/m^3}$, the maximum mass was determined to be approximately **2.85 solar masses**. This result aligns closely with the theoretical predictions by **Hartle and Sabbadini (1977)**, demonstrating the reliability of the TOV framework when applied to simple density assumptions.

3. **Customized Density Profile:** Introducing the predicted density profile into the TOV equations yielded a critical mass of approximately **2.09 solar masses** at a radius of around **10 km**. The maximum mass was calculated as **2.36 solar masses** with the stellar mass density tapering to zero at a radius of **15.5 km**. This customized approach provided a refined understanding of the EoS for neutron stars, enabling more precise estimates of **critical mass thresholds**.

4. Implications and Consistency with Observations: Based on these findings, we conclude that a neutron star is likely to **lose stability and collapse** into a black hole or another compact object once it surpasses a mass of approximately **2.09 solar masses**. This conclusion is consistent with empirical findings, such as the upper mass limit established by **researchers at Goethe University Frankfurt** (January 16, 2018), who determined that the maximum mass of a neutron star cannot exceed **2.16 solar masses**.

While the possibility of extremely massive neutron stars beyond **2.3 solar masses** cannot be entirely ruled out [14], the results presented here align well with current **experimental and observational constraints**, providing a robust approximation of the maximum mass limit for neutron stars.

The estimated **2.09 solar mass** limit is consistent with both recent observational data and current theoretical models. Observations of the most massive neutron stars, such as: **PSR J0952-0607** ($2.35 M_\odot$) [15] and **PSR J0348+0432** ($2.01 M_\odot$) [16] demonstrate that neutron stars can indeed reach or exceed this mass threshold.

Additionally, theoretical models indicate that the maximum gravitational mass for **non-rotating neutron stars** is approximately $\mathbf{2.25 \pm 0.07} M_\odot$, further supporting the plausibility of the limit obtained in this study.

5. Population Studies and EoS Constraints: Population studies reveal that while most neutron stars cluster around $\mathbf{1.35–1.50} M_\odot$, those in **high-mass X-ray binaries** or **millisecond pulsars** tend to be more massive, often exceeding $\mathbf{2.0} M_\odot$. The mass limit of $\mathbf{2.09} M_\odot$ fits well within this observational range, aligning with the most massive confirmed neutron stars.

The maximum neutron star mass also serves as a crucial **observational constraint** on the EoS of dense matter. Recent measurements of neutron stars with masses close to $\mathbf{2.0} M_\odot$ have ruled out many softer EoS models, suggesting that the maximum mass likely lies between **2.2 and 2.9**$M_\odot$ (Özel & Freire, 2016) [17]. Given the observational and theoretical constraints, a maximum neutron star mass of approximately **2.09 solar masses** emerges as a reasonable and well-supported upper limit. This value is consistent with current astrophysical observations and aligns with established theoretical models, lending **credibility to its scientific validity**. The conclusion is further reinforced by peer-reviewed references, affirming that **2.09 solar masses** represent a justifiable estimate for the maximum mass of neutron stars.

Implications and Future Work

These findings concentrate on the need for more sophisticated theoretical models that account for the influences of gravitational, nuclear, and quantum forces under relativistic conditions on such compact stars. Future works will focus on additional complexities to refine these models further. For instance, the inclusion of phase transitions in dense anisotropic pressure models, and the effects of strong magnetic matter (e.g., quark deconfinement or hyperon formation), fields may significantly alter predictions of neutron star structure and stability. Such enhancements could bridge the gap between theoretical predictions and astrophysical observations. Gravitational wave signals from neutron star mergers, combined with pulsar timing measurements and X-ray observations of thermal emissions, offer complementary avenues for testing and validating the models proposed in this study. The unavailability of a definitive and authentic EOS remains a significant challenge, our results highlight the power of theoretical modelling and numerical simulations in probing the unveiling physics of neutron stars.

References

1. Oppenheimer, J. R. and Volkoff, G. M., 1939, Phys. Rev., 55, 507.
2. Carvalho, G.A., et al., 2015, J. Phys.: Conf. Ser., 630 012058.
3. Rhoades, C. E and Ruffini, R., 1974, Phys. Rev. Lett., 32, 324.
4. Nauenberg, M. and Chapline, G., 1973, Jr., Astrophys. J., 179, 417.
5. Hartle, J. B. 1978, Phys. Repts., 46, 201.
6. Friedman and Ipser, 1987 March 15, The Astrophysical Journal, 314:594-597.
7. Padmanabhan, T, 2017, Theoretical Astrophysics, Volume2, Cambridge University Press, p 271.
8. Srinivasan, G, 2002, The maximum mass of neutron stars, Bull. Astr. Soc. India 30, 523.
9. Abhayankar, K. D. 2016, *Astrophysics: Stars and Galaxies*, University Press, pp. 177-178.
10. Gangopadhyay, Bijan Kumar 2024, "*Astronomy &*

Astrophysics with Relativity and Particle Physics", Techno World, Kolkata, pp. 228-230.

11. Gangopadhyay, Bijan Kumar, 2018, *"Limiting mass of a neutron star"*, Proceedings of the DAE Symp. on Nucl. Phys. 63.
12. Pols, O. R., 2011 September, *"Stellar Structure and Evolution"*, Astronomical Institute Utrecht, p 28-29.
13. Fonseca, E., Cromartie, H. T., Pennucci, T. T., Ray, P. S., Kirichenko, A. Yu., et al. (2021), *"Refined Mass and Geometric Measurements of the High-mass PSR J0740+6620"*, The Astrophysical Journal Letters, 915(1), L12, https://doi.org/10.3847/2041-8213/ac03b8.
14. Rocha, Lívia S. et al, 2024, *"Mass Distribution and Maximum Mass of Neutron Stars: Effects of Orbital Inclination Angle"*, Universe, 10(1), 3.
15. Romani, R. W., et al. (2022). *"PSR J0952-0607: The most massive neutron star observed, with a mass of approximately 2.35 M."* Astrophysical Journal Letters, 934(2), L17.
16. Antoniadis, J., et al. (2013), *"A Massive Pulsar in a Compact Relativistic Binary"*, Science, 340(6131), 448-450.
17. Özel, F., & Freire, P. (2016), *"Masses, Radii, and the Equation of State of Neutron Stars"*, Annual Review of Astronomy and Astrophysics, 54, 401-440.

Synthesis and Characterization of PANI/GNS and PANI/GNS/TiO_2 Nanocomposites for Room Temperature LPG Gas Sensing Application

S. D. Rokade[1,a], D. V. Nandanwar[2], S. B. Kondawar[3], P. A. Bramhankar[4], A. M. More[5], P. B. Wasnik[1,6], and M. S. Bisen[1]

[1] *Yashwantrao Chawhan Arts, Commerce and Science College, Lakhandur. Maharashtra, India.*
[2] *Shri Mathuradas Mohota Science College, Nagpur, India.*
[3] *R. T. M. Nagpur University, Nagpur, Maharashtra, India.*
[4] *Shri. Shivaji Science College, Nagpur, India.*
[5] *D. B. Science College, Gondia, Maharashtra, India.*
[6] *Department of Physics, Dr. Ambedkar College, Deeksha Bhoomi, Nagpur, India.*

[a] sumitrokade26@gmail.com

Abstract

Pure polyaniline (PANI), PANI/GNS (1%), and PANI/GNS (2%)/TiO_2 (20%) were synthesised by the situ chemical oxidation polymerisation method. Titanium dioxide (TiO_2) was synthesised using the sol-gel method and graphene (GNS) functionalized by acidic treatment. The XRD, FTIR, and SEM characterization for structural, functional, and morphological investigations has been carried out. X-ray diffraction of nanocomposite materials shows the highly crystalline nature of synthesized material. FTIR analysis revealed the existence of a functional group in nanocomposite materials. SEM analysis shows highly porous nanocomposite materials are formed, that exhibit a lack of agglomeration with uniform distribution of GNS, and TiO_2 nanoparticles within the PANI matrix. The resistance change response of synthesised material toward LPG was measured at low and high temperatures at 250 parts per million (ppm), 500 ppm, and 1000 ppm of LPG gas, which determined the characteristics like sensitivity, response, and recovery time of the nanocomposite material. Sensitivity shows that nanocomposite material is highly sensitive towards LPG nearly at 37 °C. In ternary nanocomposite, the response time and recovery time are faster as compared to binary nanocomposite material. The response time of the ternary nanocomposite is 16 seconds and the recovery time is 83 seconds. Study shows that PANI/GNS (2%)/TiO_2 (20%) nanocomposite material shows better sensitivity, response and recovery time as compared to PANI/GNS (1%) nanocomposite material towards the higher concentration of LPG gas.

Keywords: PANI, TiO_2, Graphene (GNS), Polymerization, Nanocomposite, LPG, Sensitivity.
Received 16 February 2025; First Review 22 March 2025; Accepted 24 March 2025.

*** Address of correspondence**
S. D. Rokade
Yashwantrao Chawhan Arts, Commerce and Science College, Lakhandur. Maharashtra, India.

Email: sumitrokade26@gmail.com

How to cite this article
S. D. Rokade, D. V. Nandanwar, S. B. Kondawar, P. A. Bramhankar, A. M. More, P. B. Wasnik, and M. S. Bisen, Synthesis and Characterization of PANI/GNS and PANI/GNS/TiO2 Nanocomposites for Room Temperature LPG Gas Sensing Application, J. Cond. Matt. 2025; 03 (02): 63-71.
Available from:
https://doi.org/10.61343/jcm.v3i02.145

Introduction

Gas sensors are in high demand due to the extensive utilization of various gases for residential and industrial purposes and the rising number of leakage-related incidents. LPG is an explosive gas that poses significant risks to individuals and the environment. Because of its strong flammability, even low concentrations (ppm) represent a considerable risk. The rapid and precise identification of LPG leaks is essential for preventing potential explosions [1]. Liquified petroleum gas (LPG) is a combustible gas mostly made by propane (5-10%), butane (75-80%), and minor quantities of methane, butylene, propylene, and ethylene (1-5%). It poses a significant hazard because of the elevated risk of explosions either from leakage or human mistake as a result, detecting it early on is critical for identifying and effectively controlling it [2]. Nanocomposites are formed by combining two or more nanosized items or nanoparticles. These nanocomposites exhibit distinct physical properties and have various potential applications in multiple fields. The morphology and structure of materials significantly impact the sensing characteristics. Polyaniline (PANI) nanocomposites have been found to possess superior sensing properties due to their high surface-to-volume ratio resulting from the nanostructure. This is evident in sensitivity, response time, and other relevant factors [3]. Conducting polymers are a low-cost sensing material with quick response time, high sensitivity, and room temperature functionality. They also allow for chemical and physical qualities using various substituents [4]. Due to its distinct electrochemical properties, polyaniline (PANI) is the preferred conducting polymer for detecting LPG related to chain nitrogen, as well as its tunable chemical and electrical properties, ease of synthesis, ability to sense ambient temperature and cost-effectiveness [5]. The conductivity of a polymer depends on its capacity to transfer charge carriers along its backbone and hop across chains. Interactions with polyaniline can modify these processes, affecting conductivity [6]. Compared to plain polymers, conducting polymer composites based on graphene exhibit superior properties [7]. Graphene, in contrast to most porous carbon-based materials, is two-dimensional in nature and a single sheet of sp2-hybridized carbon with exceptional conductivity, mechanical strength, and surface area [8]. Graphene (GNS) has attracted a lot of potential applications as gas sensor material this is because of its inherent physical and electrical properties, including its high surface-to-volume ratios, elevated tensile strength, chemical inertness, and outstanding thermal and electrical conductivity [9]. To improve the functionality of electrical sensors that operate at room temperature, it is possible to include sensing materials, including conducting polymers, into the surface of GNS sheets sensors by combining their superior properties [10]. Graphene or CNT interacts with conducting polymers to store energy by electronic and ionic charge separation, as well as charge transfer across the electrode-electrolyte interface [11]. Gas-sensing sensors use inorganic elements, such as metal oxide semiconductors, to detect gas molecules by measuring changes in conductivity. At present, there is an ongoing investigation into semiconducting metal oxides such as TiO_2, WO_3, In_2O, CuO, SnO_2, ZnO, and V_2O_5, focusing on their possible applications in gas sensing [12]. Nanocrystalline TiO2 is a prominent inorganic material for detecting gases such as NO2, H2, NH3, and LPG [13]. Researchers have developed composite PANI/TiO2 materials for use as gas sensors [14]. Titanium dioxide is a significant n-type semiconductor owing to its superior electrical and photocatalytic characteristics [15]. Hybrid carbon-based nanostructures present promising materials for various applications, including flexible batteries, biosensors, solar cells, supercapacitors, chemical sensors, and gas sensing [16]. Researchers have used nanostructured materials, organic/inorganic nanocomposites, conducting polymers and carbon-containing materials to develop gas sensor devices that detect differences in resistance these devices have demonstrated enhanced performance even at ambient temperature [17]. This study effectively produced PANI, PANI/GNS (1%), and PANI/GNS (2%)/TiO_2 (20%) nanocomposites using the chemical oxidation polymerization process for LPG gas sensing. The gas-sensing capabilities of the nanocomposites were investigated at both ambient and high temperatures to evaluate the impact of graphene and TiO_2 on the gas-sensing properties of the conducting polymer polyaniline.

Materials and Methods

Aniline (99.5%), Ammonium persulfate (98%), sulphuric acid (95-97%), Nitric acid (69%), titanium isopropoxide (TTIP), Methanol (99.8%), absolute Ethanol (99.9%), and Graphene flakes (made available from NPL New Delhi). All the chemicals reach the standards of analytical reagent grade. Distilled water (DW) was used as the medium for producing the material.

Synthesis of TiO_2

The sol-gel method successfully synthesized titanium dioxide (TiO_2). In this method, titanium isopropoxide (TTIP) is used as a source of titanium. In a beaker insert 3.9 ml of TTIP into 60 ml of methanol and then place it on magnetic stirring at 50°C for 1 hour. Then, a muffle furnace dried this white precipitate at 600°C for 1 hour. A motor pistol produced a nanostructured form of TiO_2 [18].

Functionalization of Graphene (F-GNS)

An acidic treatment was used to functionalize graphene (GNS). GNS mix with 6M H_2SO_4 and 6M HNO_3 used in a 3:1 ratio and mix it properly for 15 minutes. Graphene flask was added to the solution and ultrasonically processed for 5 hours at 55°C. GNS was functionalized after using centrifugation, filtration, washing, and drying at 80O C for 16 hr. [19].

Synthesis of Polyaniline (PANI)/functionalized Graphene(F-GNS) (1%) and PANI/GNS (2%)/TiO_2 (20%)

In situ chemical oxidation polymerization method was used for the synthesis of Polyaniline (PANI)/F-GNS (1%) and PANI/F-GNS(2%)/TiO_2(20%) nanocomposites [20]. The weight percentage of GNS to aniline was 1%. Divide the 0.2 M H_2SO_4 solution in 50 ml of deionized water into two equal parts. One part, add 0.2 M aniline and functionalized GNS, then ultrasonicate for 35 minutes. After ultrasonication, stir the mixture for 5–6 hours at 0–5° C to achieve the optimal yield. In another part, add 0.2 M ammonium persulfate (APS) to the stirring monomer solution and add it drop by drop. After mixing the reactants, the solution initially appears greenish and then turns violet. After around 6 to 7 hours, the black precipitate formed. We left the precipitate overnight and diluted it with deionized water until it became colourless. After washing with ethanol, it was oven-dried overnight at 80ºC. The same procedure carried out for synthesize the PANI/GNS/TiO_2 ternary composite, with a weight proportion of GNS (2%) and TiO_2 (20%) used in the 0.2M aniline ratio.

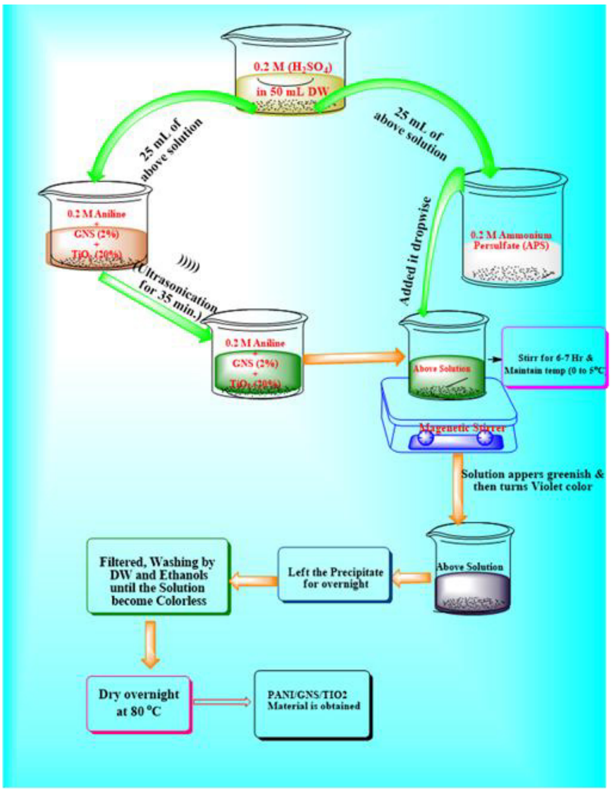

Figure 1: Flowchart of synthesis of PANI/GNS (1%) and PANI/GNS (2%)/TiO_2 (20%) Nanocomposite

Characterizations

Table 1: Table shows characterization techniques and the instrument model used for characterization of materials.

Sr. No.	Characterization Techniques	Instrument Model
1	X-Ray diffraction (XRD)	Rigaku Mini-Flex 600, Rigaku Japan
2	Fourier Transform Infrared radiation (FTIR)	Model: Spectrum 400FT-IR/FIR, Spectrometer. Perkin Elmer, USA
3	Scanning electron microscopy (SEM)	SEM Model - Carl Zeiss EVO-18
4	The average particle size	Image-J application
5	Gas sensing	Tabletop static Gas sensing unit equipped with two probes and temperature controller

1. XRD analysis

Figure 2 (a) shows XRD patterns for Pure Polyaniline (PANI) characteristic peaks are observed at 2θ= 15.24°, 20.78°, and 25.26°, corresponding to the (110), (002), and (112) crystal planes. This indicates that the material is semi-crystalline in nature [21]. In Figure 2 (b) Distinct diffraction peaks for pure TiO_2 are noted at approximately 2θ values of 25.28°, 37.81°, 47.99°, 53.95°, 55°, 62.9°, and 75°. These peaks align with the crystallographic orientations of (101), (004), (200), (105), (211), (204), (116), (220), and (215) a tetragonal structure of the material has obtained. The individual peaks observed in the TiO_2 sample may be accurately matched to the anatase phase (JCPDS-ICDD card: 21-1272) [15]. When graphene was added to the PANI matrix, a strong and clear extra diffraction peak of GNS was

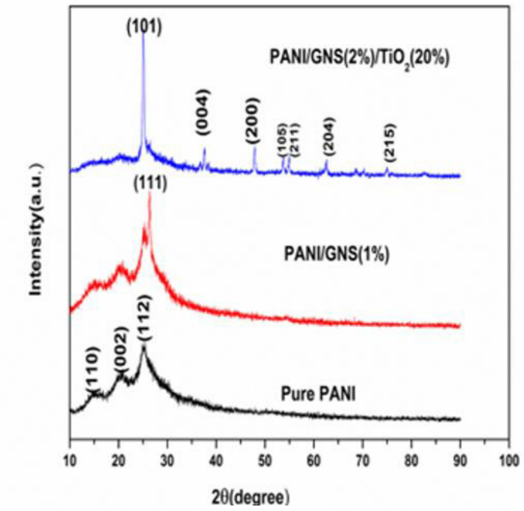

(a)

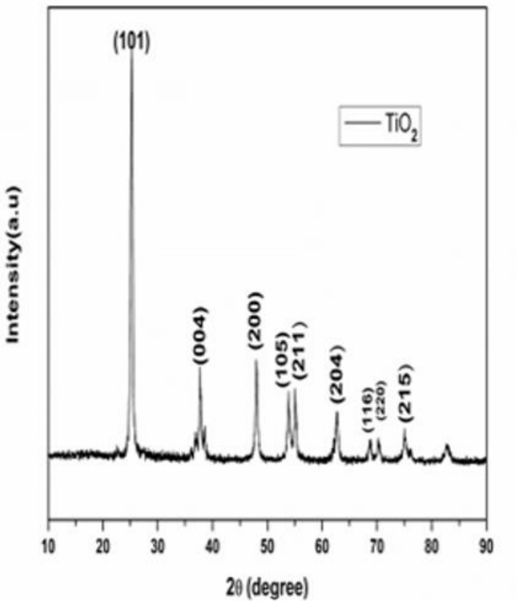

(b)

Figure 2: (a) Polyaniline (PANI), PANI/GNS (1%), and PANI/GNS (2%)/TiO_2(20%) **(b)** Pure TiO_2

seen at 26.46°, which is the same angle as the (111) crystal plane. When TiO_2 (20%) was added to the PANI/GNS (2%) composite which observed sharp and intense diffraction peaks are observed in the PANI/GNS(2%)/TiO_2(20%) nanocomposite matrix, which overlaps with the peak of the TiO2, GNS and PANI matrix. The results display sharp and intense defined peaks, indicating the highly crystallographic nature of the synthesized material.

2. FTIR analysis

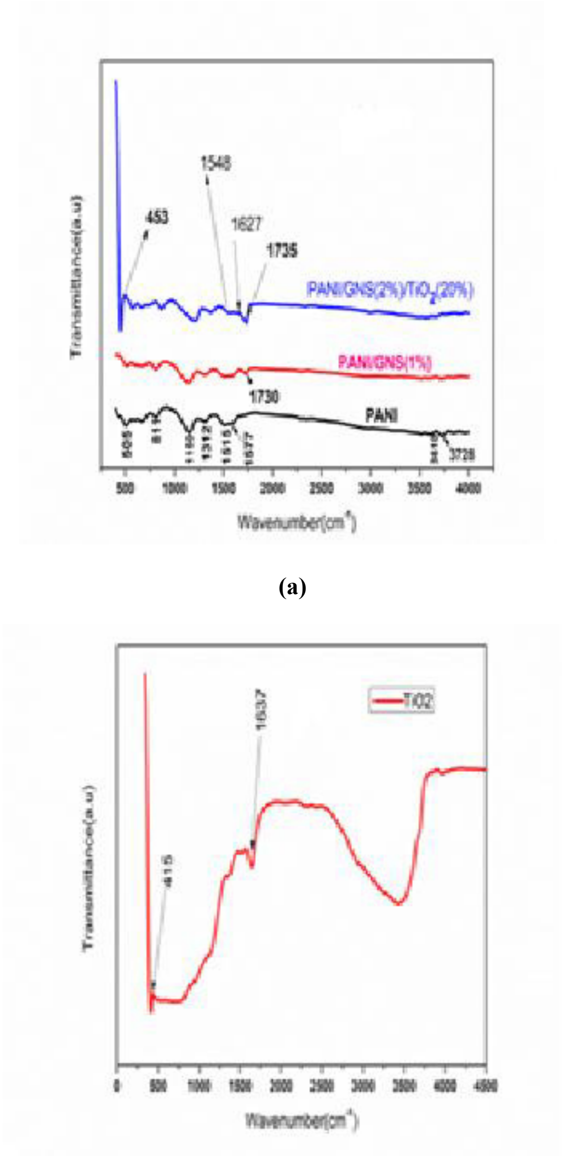

(a)

(b)

Figure 3: (a) Polyaniline (PANI), PANI/GNS (1%), PANI/GNS (2%)/TiO_2 (20%) **(b)** Titanium dioxide (TiO_2)

The FTIR spectroscopic analysis of pure polyaniline (PANI), titanium dioxide (TiO_2), PANI/GNS (1%), and PANI/GNS (2%)/TiO_2 (20%) nanocomposites. FTIR spectroscopy investigation of PANI displays multiple distinct peaks. The observed peak at 505 cm^{-1} and 1150 cm^{-1} shows the stretching vibrations of the C-H bond. The peak recorded at 811 cm^{-1} is due to the stretching of N-H bending. The peak at roughly 1312 cm^{-1} corresponds to the stretching vibrations of the C-N bond. The peaks at around 1515 cm^{-1} and 1577 cm^{-1} have been assigned to the stretching vibrations of the C=N bond in the benzenoid and quinoid rings, respectively [22]. The peaks identified in the 3605-3728 cm^{-1} range correspond to the stretching vibrations of the N-H bond in the aromatic amine. In Figure 3(b), the TiO_2 band is detected at a frequency of approximately 415 cm^{-1} during strong vibration. Furthermore, the frequency of 1637 cm^{-1} corresponds with the stretching frequencies of antisymmetric Ti-O-Ti and O-H bonds [15]. In the PANI/GNS (1%) nanocomposite, functionalized graphene displays a peak at 1730 cm^{-1}, and PANI/GNS (2%)/TiO_2 (20%) displays a peak at 1735 cm^{-1} which showing a characteristic band of the stretching mode of C=O carboxylic acid groups [11]. When GNS combines with PANI. The PANI/GNS (2%)/TiO_2 (20%) nanocomposite exhibits a slight shift in PANI frequencies and the presence of the TiO_2 band. The FTIR analysis clarifies the presence of titanium dioxide (TiO_2) and functionalized graphene (GNS) embedded within the polyaniline (PANI) matrix.

3. SEM Analysis

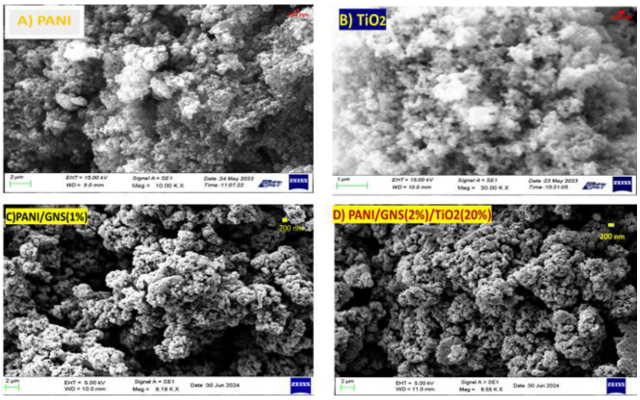

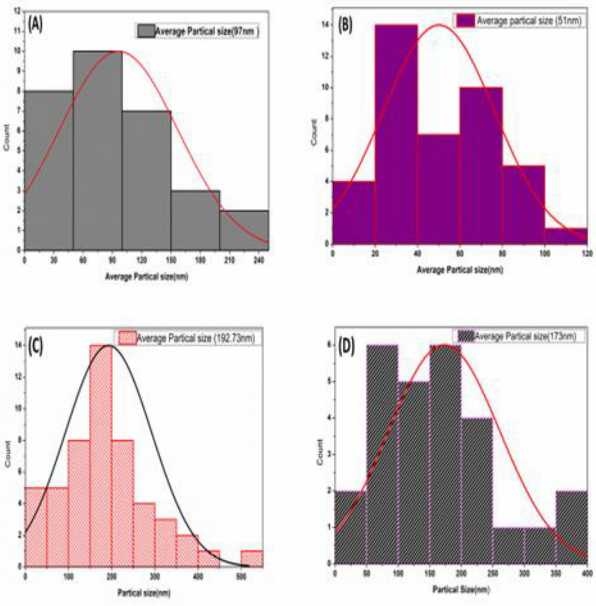

Figure 4: (A) Polyaniline (PANI) **(B)** Titanium Dioxide (TiO_2) **(C)** PANI/GNS (1%) and **(D)** PANI/GNS (2%)/TiO_2 (20%).

In Figure 4 (A) The grain structure of pure PANI is spherical and interconnected networks. However, it is not uniformly distributed throughout, as depicted in the image. The average particle size of this structure was measured to be 97 nm. In figure 4 (B) TiO_2 nanoparticles have a nearly spherical morphology, comprising randomly distributed tiny grains with an average particle size measured to be 51 nm. Figure 4 (C) illustrates the incorporation of polyaniline (PANI) into functionalized graphene (GNS (1%)) which highlights its potential for enhanced absorptivity [19]. PANI/GNS (1%) nanocomposite shows an average particle size of around 192.7nm. In PANI/GNS (2%)/TiO_2(20%) nanocomposite, TiO_2 particles were believed to be embedded within the GNS sophisticated core-shell structure Constructed by PANI chains. Highly Porous nanostructured materials are obtained which is very useful for absorption of LPG gas. The formation of such a structure layer of PANI embedded in Graphene (GNS) and TiO_2 nanoparticles results in nanocomposite with increased surface area. This increased surface area is advantageous for attracting molecules. which shows an average particle size of around 173 nm. Nanocomposites with GNS and TIO_2 nanoparticles distributed uniformly throughout the PANI matrix show no signs of agglomeration.

Gas sensing experimental setup

The table top static gas sensing apparatus used to measure the resistance of LPG It has equipped with two probe systems, a stainless steel 304 closed chamber and a digital temperature controller with a range of (250 °C). The nanocomposites pallet (1.94 mm thickness and 12 mm diameter) is placed on the surface of the alumina substrate and two probes are placed on the surface of the pallets then insert a specified volume (corresponding to 250 ppm, 500 ppm, and 1000 ppm) of LPG gas into the experimental chamber by using a syringe. Extracted the electrical leads from the chamber to enable the monitoring of electrical parameters. The resistance of the pallet is measured with a specific temperature. a multimeter used to measure the resistance variation. The resistance variation of the sensing material at various temperatures measures it to both clean air and LPG gas. Measure the resistance of the sample, which should fall within a range from 2 KΩ to 20 MΩ, using an adjustable scale that depends upon temperature and gas concentration.

1. Mechanism of LPG sensing

The gas-sensing process of nanocomposite materials is based on changes in barrier height or resistance generated by physisorption and chemisorption on their surface at room temperature or high temperature [12]. Oxygen molecules physically adsorb on the active surface of nanocomposite materials when exposed to air, capturing electrons from the conduction band and trapping them at the surface as various oxygen ions species such O-2(ads), O-(ads) O2-(ads) [16]. The sample later interacts with reducing gases like LPG, which in turn removes the oxidizing ions through a process known as chemisorption. LPG (butane and propane) reacting with superoxide anions which may create by-products such as carbon dioxide (CO_2) and water (H_2O) which react with normal operating temperatures signifies various compositions. The conduction band transfers the released electron after adsorption. The reversing change occurs during their capture. As a result, the resistance of the semiconductor increases in the carrier conduction current which decreases the electron depletion layer of the molecules that make up LPG which tends to transfer an electron to the surface which leads to further increases [23]. At normal temperatures, graphene can change its conductivity in the presence of many chemical compounds, regardless of how differently these compounds behave chemically, making them an extremely sensitive material. Their increased responsiveness to atmospheric conditions is a result of GNS atomic arrangement on their surface and their high area/volume ratio, both of which promote adsorption processes. There are two possible outcomes when the chemical agent interacts with the surface of the GNS, changing their electrical conductivity either the analyte acts as a scattering potential or the GNS facilitates charge transfer from the analyte to the nanomaterials. When the compound that is adsorbed is an electron attractor (hole donation), the conductivity is increased due to charge transfer. Analytes that donate electrons reduce the electrical conductivity of nanomaterials by reducing their hole density [24]. The PANI/GNS blend and PANI/GNS/TiO_2 nanocomposite material interact with pre-adsorbed oxygen species on the active sensing surface upon exposure to LPG at the specified concentration in the gas chamber. The "gas resistance of the sensor (R_{gas})” denotes the interaction between chemisorbed oxygen species on the active surface and injected LPG molecules. LPG molecules, including methane (CH_4), propane (C_3H_8), and butane (C_4H_{10}), engage in electron transfer with adsorbed oxygen species. The adsorption of LPG on the nanocomposite material leads to an increase in resistance, while the removal of the doping anion from the main chain of the PANI also contributes to this resistance increase [25]. Nanostructured sensing materials exhibit a superior surface-to-volume ratio, providing an increased number of sites for the adsorption of analyte molecules, hence enhancing sensitivity relative to thin-film materials. Liquid petroleum gas (LPG) acts as an electron donor, leading to an increase in the resistance of the nanocomposite when exposed to LPG. Graphene's high specific surface area can enhance gas responsiveness at room temperature when combined with metal oxides, leading to improved sensitivity and selectivity [26]. The Sensitivity (%) was calculated by using this formula:

$$\text{Sensitivity}(\%) = \left[\frac{R_{Gas} - R_{Air}}{R_{Air}}\right] \times 100$$

Here, R_{Gas} stands for the material's resistance values while exposed to LPG, and R_{Air} for the sensing material's resistance values when exposed to pure air [27].

2. Sensitivity

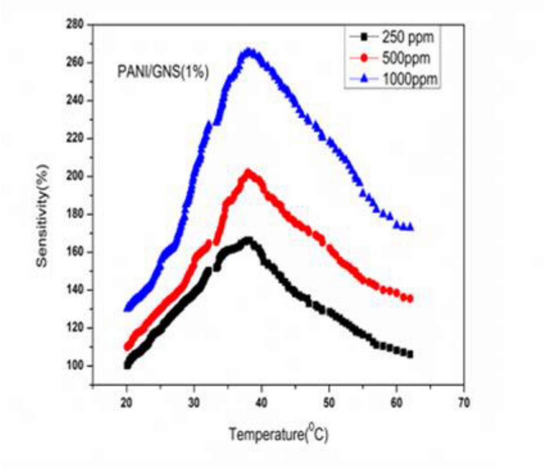

(a)

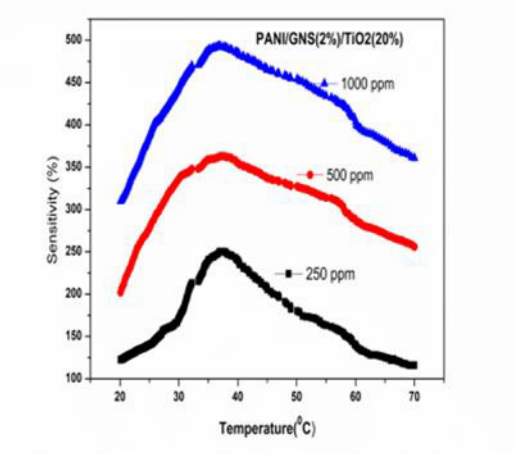

Figure 5: Sensitivity graph of **(a)** PANI/GNS (1%) **(b)** PANI/GNS (2%)/TiO$_2$(20%).

The data in Figure 5 shows the relationship between percentage sensitivity and temperature for the PANI/GNS (1%) and PANI/GNS (2%)/TiO$_2$ (20%) nanocomposite. The resistance of materials was measured in the kΩ to 10 MΩ range. At higher temperatures, the sensitivity was observed to increase before reaching its peak and subsequently decrease at higher temperatures [28]. In Figure. 5 (A), it can be observed that the sensitivity increases initially up to 39oC and then decreases. The PANI/GNS (1%) nanocomposite exhibits maximum percentage sensitivity of 164%, 202%, and 265% for concentrations of 250 ppm, 500 ppm, and 1000 ppm of LPG respectively. In contrast to the PANI/GNS (1%) nanocomposite, figure 5(B) the PANI/GNS (2%)/TiO$_2$ (20%) nanocomposite exhibits improved sensitivity, initially increasing up to 37°C and then declining. They exhibit maximum percentage sensitivity of 250%, 363%, and 493% for concentrations of 250ppm, 500ppm, and 1000ppm, respectively. In the case of the PANI/GNS (2%)/TiO$_2$(20%) nanocomposite, a similar nature was observed, but the sensitivity factor is higher compared to PANI/GNS (1%) for the range of ppm. and temperature range slightly improved which is around 37°C.

3. Response (R_s) and Recovery Time (R_t)

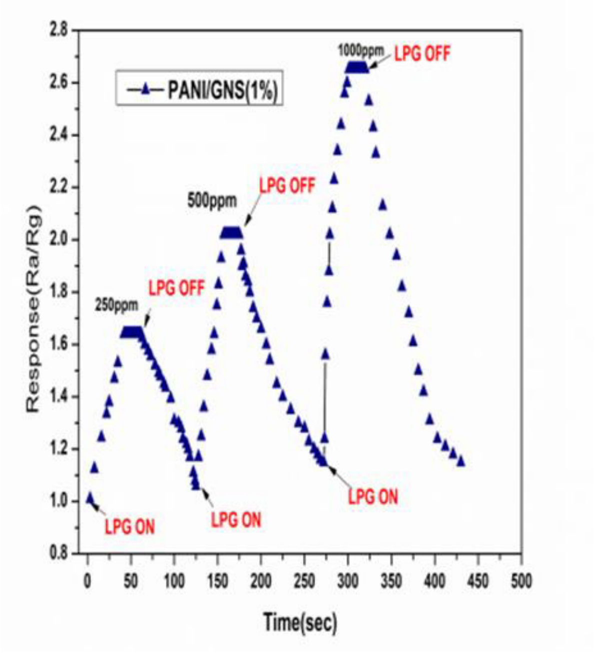

(a)

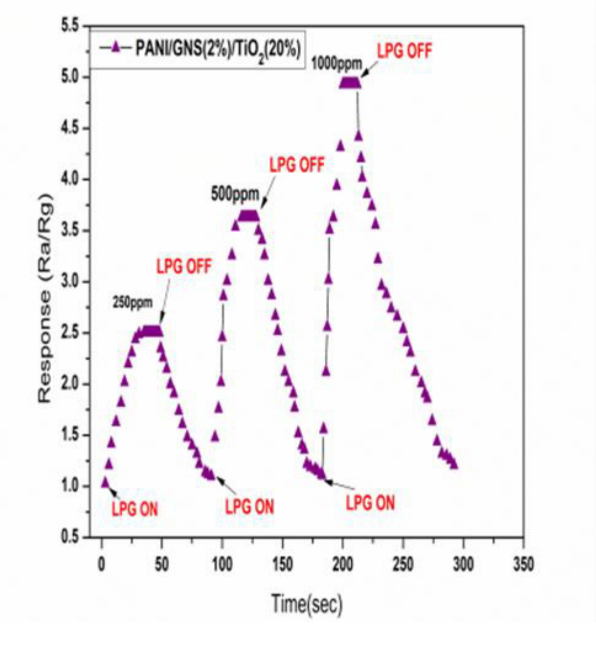

(b)

Figure 6: (a) Polyaniline (PANI)/Graphene (GNS) (1%) **(b)** PANI/GNS (2%)/TiO_2 (20%)

Response (R_s) and recovery time (R_t) is another crucial factor of gas detection. It is the time required by the material to transform its initial resistance to 90% of its original value [29]. Figure 6 illustrates that the nanocomposite material exhibited a notably high and rapid response to LPG concentrations of 250 ppm, 500 ppm, and 1000 ppm. The samples demonstrated a consistent and attainable change in resistance over numerous cycles. Response and recovery times for PANI/GNS (1%) for 1000 ppm LPG were found to be 28 sec and recovery time 109 sec. In PANI/GNS (2%)/TiO_2(20%) for 1000 ppm, the response time are 16 sec and the recovery time is 83 sec. The response and recovery times exhibit an inverse correlation with the LPG concentration. The response and recovery time in ternary nanocomposite material is faster than in binary nanocomposite material. The graph indicates that increased concentrations of LPG resulted in prolonged recovery times. This is likely attributable to the denser characteristics of LPG [30].

4. Sensitivity vs Concentration of LPG Gas

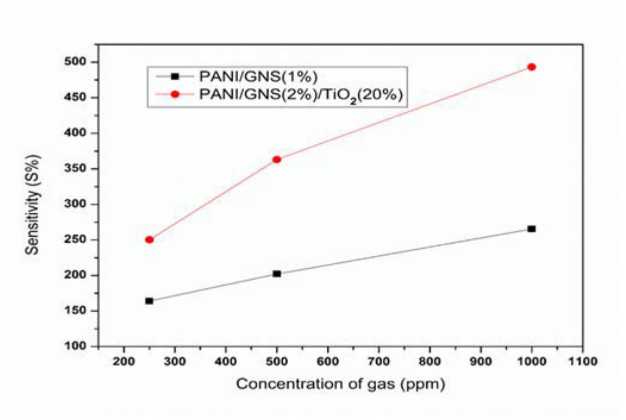

Figure 7: Graph displays the sensitivity versus concentration of LPG gas for the nanocomposites PANI/GNS (1%) and PANI/GNS(2%)/TiO_2(20%).

An analysis of the graph reveals that the sensitivity factor of the PANI/GNS (1%) and PANI/GNS(2%)/TiO_2(20%) nanocomposite increases as the concentration of LPG rises. However, the sensitivity of PANI/GNS (1%) nanocomposite material is lower compared to PANI/GNS(2%)/TiO_2(20%) nanocomposite material. This difference can be attributed to the higher concentration of LPG.

Conclusions

Highly crystalline PANI/GNS (1%) and PANI/GNS(2%)/TiO_2(20%) nanocomposites were successfully synthesized by the chemical oxidation polymerization method and TiO_2 were synthesized by the sol-gel method. FTIR verifies the presence of functional groups in the nanocomposites. By embedding a layer of PANI on functionalized graphene (GNS) and TiO_2 nanoparticles. SEM analysis produces highly porous nanostructured materials that result in a nanocomposite with an increased surface area. In the case of the PANI/GNS(2%)/TiO_2(20%) nanocomposite, the sensitivity is higher as compared to PANI/GNS (1%) in terms of concentration of LPG and temperature. To obtain 1000 ppm LPG at room temperature (37°C), composite nanomaterials of PANI/GNS(2%)/TiO_2(20%) had a response time of 16

Table 2. Compares the data with some other reported work for detection of the LPG.

S. No.	**Materials**	**Methods of Synthesis**	**Operating temperature**	**LPG concentration (ppm)**	**Response time (sec) &, Recovery time (sec)**	**References**
01	Polyaniline/ZnO	Chemical bath deposition	Room Temperature	1040 ppm	100 and 150	[1]
02	PANI/MWCNT	Electrospinning method	Room Temperature	1250 ppm	13 and 80	[6]
03	PANI/TiO_2	Chemical bath deposition and electrodeposition	Room Temperature	1000 ppm	140 and 180	[23]
04	PANI/Cu_2ZnSnS_4	Electrodeposition method.	Room Temperature	750 ppm	120 and 125	[24]
05	PANI/CNT/V_2O_5	Chemical oxidation polymerization method	Room Temperature	50 ppm	20 and 15	[25]
06	PANI/ZnO	Electrospinning method	Nearly Room temperature	1000 ppm	110 and 185	[28]
07	Polyaniline/Nb_2O_5	Chemical oxidation polymerization method	Room Temperature	500 ppm	30 and 50	[31]
08	**Polyaniline/GNS/TiO_2**	**Chemical oxidation polymerization method**	**Room Temperature**	**1000 ppm**	**16 and 83**	**Present study**

seconds and a recovery time of 83 seconds. The response and recovery times vary with the concentration of LPG. Compared to binary PANI/GNS (1%) nanocomposite materials, ternary nanocomposite PANI/GNS (2%)/TiO_2 (20%) materials showed better sensitivity and response and recovery time.

References

1. Dhawale, D. S., Dubal, D. P., More, A. M., Gujar, T. P., & Lokhande, C. D. (2010). *Room temperature liquefied petroleum gas (LPG) sensor. Sensors and Actuators,* B: Chemical, 147(2), 488-494.
2. Patil, D., Patil, V., & Patil, P. (2011). *Highly sensitive and selective LPG sensor based on α-Fe_2O_3 nanorods. Sensors and Actuators*, B: Chemical, 152(2), 299-306.
3. Gangopadhyay, R., & De, A. (2000). *Conducting polymer nanocomposites: a brief overview*. Chemistry of materials, 12(3), 608-622.
4. Fratoddi, I., Venditti, I., Cametti, C., & Russo, M. V. (2015). *Chemiresistive polyaniline-based gas sensors: A mini-review*. Sensors and Actuators B: Chemical, 220, 534-548.
5. Kotresh, S., Ravikiran, Y. T., SC, V. K., VV, R. C., & Batoo, K. M. (2017). *Solution-based–spin cast processed LPG sensor at room temperature. Sensors and Actuators*, A: Physical, 263, 687-692.
6. Patil, P. T., More, P. S., & Kondawar, S. B. (2020). *LPG sensing properties of electrospun in-situ polymerized polyaniline/MWCNT composite nanofibers*. In NAC 2019: Proceedings of the 2nd International Conference on Nanomaterials and Advanced Composites (pp. 3-18). Springer Singapore.
7. Das, T. K., & Prusty, S. (2013). *Graphene-based polymer composites and their applications*. Polymer-Plastics Technology and Engineering, 52(4), 319-331.
8. Zhang, Q., Li, Y., Feng, Y., & Feng, W. (2013). *Electro polymerization of graphene oxide/polyaniline composite for high-performance supercapacitor*. Electrochimica Acta, 90, 95-100.
9. Lee, S. W., Lee, W., Hong, Y., Lee, G., & Yoon, D. S. (2018). *Recent advances in carbon material-based NO2 gas sensors*. Sensors and Actuators B: Chemical, 255, 1788-1804.
10. Guo, Y., Wang, T., Chen, F., Sun, X., Li, X., Yu, Z., ... & Chen, X. (2016). *Hierarchical graphene–polyaniline nanocomposite films for high-performance flexible electronic gas sensors*. Nanoscale, 8(23), 12073-12080.
11. Ghosh, D., Giri, S., Kalra, S., & Das, C. K. (2012). *Synthesis and characterisations of TiO_2 coated multiwalled carbon nanotubes/graphene/polyaniline nanocomposite for supercapacitor applications*. Open Journal of Applied Sciences, 2(02), 70.
12. Thangamani, G. J., Deshmukh, K., Nambiraj, N. A., & Pasha, S. K. (2021). *Chemiresistive gas sensors based on vanadium pentoxide reinforced polyvinyl 116687.alcohol/polypyrrole blend nanocomposites for room temperature LPG sensing*. Synthetic Metals, 273,
13. Dey, A. (2018). *Semiconductor metal oxide gas sensors: A review*. Materials Science and Engineering: B, 229, 206-217.
14. Yang, S., Ishikawa, Y., Itoh, H., & Feng, Q. (2011). *Fabrication and characterization of core/shell structured TiO_2/polyaniline nanocomposite*. Journal of colloid and interface science, 356(2), 734-740.
15. Praveen, P., Viruthagiri, G., Mugundan, S., & Shanmugam, N. (2014). *Structural, optical and morphological analyses of pristine titanium di-oxide nanoparticles–Synthesized via sol-gel route*. Spectrochimica Acta Part A: Molecular and Biomolecular Spectroscopy, 117, 622-629.
16. Seekaew, Y., Pon-On, W., & Wongchoosuk, C. (2019). *Ultrahigh selective room-temperature ammonia gas sensor based on tin–titanium dioxide/reduced graphene/ carbon nanotube nanocomposites by the solvothermal method*. ACS omega, 4(16), 16916-16924.
17. Hashemi Karouei, S. F., Milani Moghaddam, H., & Saadat Niavol, S. (2021). Characterization and gas sensing properties of graphene/polyaniline nanocomposite with long-term stability under high humidity. Journal of Materials Science, 56, 4239-4253.
18. Ramteke, J. N., Nerkar, N. V., & Kondawar, S. B. (2020). Comparative Study of Dye Removal Using PANI/TiO2 and PANI/GNS Nanocomposites. In NAC 2019: Proceedings of the 2nd International Conference on Nanomaterials and Advanced Composites (pp. 87-94). Springer Singapore.
19. Georgakilas, V., Otyepka, M., Bourlinos, A. B., Chandra, V., Kim, N., Kemp, K. C., ... & Kim, K. S. (2012). Functionalization of graphene: covalent and non-covalent approaches, derivatives and applications. Chemical reviews, 112(11), 6156-6214.
20. Modak, P., Kondawar, S. B., & Nandanwar, D. V. (2015). Synthesis and characterization of conducting polyaniline/graphene nanocomposites for electromagnetic interference shielding. Procedia Materials Science, 10, 588-594.
21. Yang, S., Ishikawa, Y., Itoh, H., & Feng, Q. (2011). Fabrication and characterization of core/shell structured TiO2/polyaniline nanocomposite. Journal of Colloid and Interface Science, 356(2), 734–740
22. Liu, A., Wang, C., Yang, X., Liu, F., Li, S., Wang,

J. & Lu, G. (2020). Polyaniline@ porous nanosphere SnO2/Zn2SnO4 nanohybrid for selective room temperature flexible NH3 sensor. Sensors and Actuators B: Chemical, 317, 128218.

23. Dhawale, D. S., Salunkhe, R. R., Patil, U. M., Gurav, K. V., More, A. M., & Lokhande, C. D. (2008). Room temperature liquefied petroleum gas (LPG) sensor based on p-polyaniline/n-TiO2 heterojunction. Sensors and Actuators B: Chemical, 134(2), 988-992.
24. Patil, S. J., Lokhande, A. C., Yadav, A. A., & Lokhande, C. D. (2016). Polyaniline/Cu2 ZnSnS4 heterojunction-based room temperature LPG sensor. Journal of Materials Science: Materials in Electronics, 27, 7505-7508.
25. Albaris, H., & Karuppasamy, G. (2019). Fabrication of room temperature liquid petroleum gas sensor based on PANI–CNT–V2O5 hybrid nanocomposite. Applied Nanoscience, 9, 1719-1729
26. Chatterjee, S. G., Chatterjee, S., Ray, A. K., & Chakraborty, A. K. (2015). Graphene–metal oxide nanohybrids for toxic gas sensor: A review. Sensors and Actuators B: Chemical, 221, 1170-1181.
27. Tai, H., Jiang, Y., Xie, G., Yu, J., & Chen, X. (2007). Fabrication and gas sensitivity of polyaniline–titanium dioxide nanocomposite thin film. Sensors and Actuators B: Chemical, 125(2), 644-650.
28. Patil, P. T., Anwane, R. S., & Kondawar, S. B. (2015). Development of electrospun polyaniline/ZnO composite nanofibers for LPG sensing. Procedia Materials Science, 10, 195-204.
29. Kumar, R., Al-Dossary, O., Kumar, G., & Umar, A. (2015). Zinc oxide nanostructures for NO 2 gas–sensor applications: A review. Nano-Micro Letters, 7, 97-120.
30. Dhawale, D. S., Dubal, D. P., Jamadade, V. S., Salunkhe, R. R., Joshi, S. S., & Lokhande, C. D. (2010). Room temperature LPG sensor based on n-CdS/p-polyaniline heterojunction. Sensors and Actuators B: Chemical, 145(1), 205-210.
31. Kotresh, S., Ravikiran, Y. T., SC, V. K., VV, R. C., & Batoo, K. M. (2017). *Solution-based–spin cast processed LPG sensor at room temperature*. Sensors and Actuators A: Physical, 263, 687-692.

Reflectance, Transmission and Absorption Spectra of Te/PS Multilayer Structure with Defect of Metamaterial at Terahertz Region

Asish Kumar[1,a], Prabal P. Singh[2], Balraj Singh[1], Arjundev Bharti[3] and Khem B. Thapa[4]

[1] *University Institute of Engineering and Technology, Babasaheb Bhimrao Ambedkar University, Lucknow (UP), India.*
[2] *University Institute of Engineering and Technology, Chhatrapati Shahu Ji Maharaj University, Kanpur-208012 (UP), India.*
[3] *Department of Home, Uttar Pradesh Secretariat, Lucknow (U.P.) India.*
[4] *Department of Physics, School of Physical and Decision Sciences, Babasaheb Bhimrao Ambedkar University, Lucknow (UP), India.*

[a] kumar2013asish@gmail.com

Abstract

The interaction of wave with matter defines the optical properties of periodic of one-dimensional periodic structure (1DPS) of the materials. The optical properties like reflectance, transmittance and absorption spectra of one dimensional(1D) tellurium and polystyrene based symmetric and asymmetric periodic structure theoretically analysed with defect of meta-material using the transfer matrix method (TMM). Reflectance, transmittance and absorption spectra are analysed for symmetric structure found an enormous band gap which works as a broadband reflector and asymmetric structure shows the separated huge band gap in two parts. The defect of meta-material inserted in the tellurium and polystyrene based periodic structures are analysed the broadband reflector, multichannel filter and sensor applications at terahertz region.

Keywords: Tellurium, Polystyrene, Meta-material, Photonic Crystal, Broadband multichannel filter and Sensor.
Received 28 January 2025; First Review 21 February 2025; Accepted 30 March 2025.

*** Address of correspondence**
Asish Kumar
University Institute of Engineering and Technology, Babasaheb Bhimrao Ambedkar University, Vidya Vihar, Raebareli Road, Lucknow-226025 (UP), India.

Email: kumar2013asish@gmail.com

How to cite this article
Asish Kumar, Balraj Singh, Arjundev Bharti and Khem B. Thapa, Reflectance, Transmission and Absorption Spectra of Te/PS Multilayer Structure with Defect of Metamaterial at Terahertz Region, J. Cond. Matt. 2025; 03 (02): 72-76.

Available from:
https://doi.org/10.61343/jcm.v3i02.74

Introduction

A periodic stack structure of different dielectric materials, called photonic crystals (PCs), that controls the electromagnetic wave propagation by varying the parameters of dielectric constant. In 1987 first time Yablonovitch and John have proposed concept of photonic band gap (PBG) of the PCs due to wave resonance in the periodicity of the dielectric materials [1, 2]. A PBG depends upon the index of refraction, number of stacks, fraction of filling, and incident wave frequency range etc. [3]. The PBG periodic structures are used in various applications due to their unique properties for controlling the electromagnetic waves. These materials have potential candidates for the development in science and technology, particularly in the development of optical devices. The simplest PCsare the layered media having the periodicity of materials in one direction, called 1DPS, and can be fabricated easily using the technology of thin-film. 1DPS has various applications in optical and photonic devices, tunable filters, multichannel filters, broadband reflectors, microwave absorbers, optical sensors, optoelectronic devices, and omni-directional filters [4-23].

In 1968, Veselago theoretically predicted the concept of electric permittivity and magnetic permeability of the materials are the fundamental characteristics and it determines the electromagnetic wave propagation in the matter [24]. These materials, also known as meta-materials, double negative (DNG) materials, or negative index materials (NIMs), have both magnetic permeability and electric permittivity values that are negative at the same time. Double positive (DPS) materials, on the other hand, have positive magnetic permeability and electric permittivity. The Kramers-Kronig relation states that meta-materials are both dispersive and lossy. Therefore, meta-materials must have a complicated refractive index. The wave's propagation is shown by the real component of the refractive index, while the wave's attenuation or decay is indicated by the imaginary part. Meta-photonic crystals are double negative and double positive periodic formations. Because of factors including thickness, refractive index, contrast, and incident angles, these meta-photonic crystals also displayed two different kinds of band gaps: Bragg's gap and zero index gap [25-32].

Theoretical Methodology

The reflectance, transmittance and absorption of 1DPS containing tellurium and polystyrene and defect with meta-material are calculated using TMM. 1DPC is taken as symmetric structure $(AB)^N$ asymmetric structure $(AB)^{N/2}(AB)^{N/2}$ and $(AB)^{N/2}(M)(AB)^{N/2}$ where N=6 is a number of lattice period; A and B are represented as tellurium and polystyrene, and M denotes the meta-material, respectively. The relationship is used to determine the meta-material's magnetic permeability and electric permittivity [33].

$$\varepsilon_m(\omega)=1+\frac{5^2}{0.9^2-\omega^2-i\omega\gamma_e}+\frac{10^2}{11.5^2-\omega^2-i\omega\gamma_e}$$

$$\mu_m(\omega)=1+\frac{3^2}{0.902^2-\omega^2-i\omega\gamma_m}$$ and the index of refraction, $n_m=\sqrt{\varepsilon_m\mu_m}$, ω is the angular frequency in THz, γ_e and γ_m are the electric and magnetic damping frequencies.

By examining the characteristic matrix for the photonic crystal, the optical property of the structure is ascertained. i.e. $(AB)^N$ and it can be expressed by [34].

$$M(d)=\begin{pmatrix} m_{11} & m_{12} \\ m_{21} & m_{22} \end{pmatrix} \tag{1}$$

where $M(d)=(AB)^N$; N is number of lattice period, M_A and M_B are the characteristics matrices of material A and B, respectively.

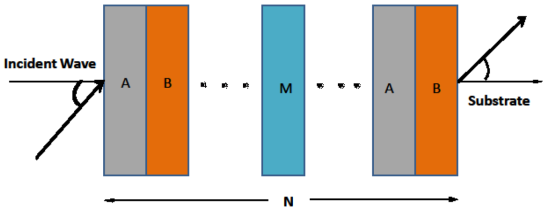

Figure 1: shows the tellurium (A) and polystyrene (B) with defect of meta-material (M) based 1D symmetric periodic structure.

The matrix M_i for each layer where $i = A \& B$ is calculated for the TE wave at the angle of incidence θ_0.

$$M_i=\begin{bmatrix} \cos\eta_i & -\frac{i}{p_i}\sin\eta_i \\ -ip_i\sin\eta_i & \cos\eta_i \end{bmatrix} \tag{2}$$

where $\eta_i=\frac{\omega}{c}n_i d_i\cos\theta_i$, c is the speed of light in vacuum, θ_i is the ray angle inside i^th layer with a refractive index as, $n_i=\sqrt{\mu_i\varepsilon_i}$, $p_i=\sqrt{\frac{\varepsilon_i}{\mu_i}}\cos\theta_i$ and $\cos\theta_i=\sqrt{1-\frac{n_0^2\sin^2\theta_0}{n_i^2}}$ in which n_0 is the index of refraction of the air.

The coefficient of transmission of the 1DPS is calculated by,

$$t=\frac{2p_0}{(m_{11}+m_{12}p_s)p_0+(m_{21}+m_{22}p_s)} \tag{3}$$

where $p_0=n_0\cos\theta_0$ and $p_s=n_s\cos\theta_s$ where n_s is the index of refraction of the substrate, Θ_s is the ray angle.

The transmittance of the 1DPS is given by,

$$T=\left(\frac{p_s}{p_0}\right)|t^2| \tag{4}$$

The coefficient of reflection of the 1DPS is calculated by given relation-

$$r=\left|\frac{m_{11}+\frac{m_{12}}{p_0}-m_{21}p_0-m_{22}}{(m_{11}+\frac{m_{12}}{p_0})+(m_{21}p_0+m_{22})}\right| \tag{5}$$

where $p_0=n_0\cos\theta_0$ and $p_s=n_s\cos\theta_s$, n_s is the index of refraction of substrate.

The reflection spectra 1DPS are calculated by-

$$R=|r|^2 \tag{6}$$

Using the relations of T and R, the absorption spectra of 1DPS are given by;

$$A=1-R-T \tag{7}$$

Results Analysis

In this research article, we have theoretically analysed the reflectance, transmittance and absorption spectra of tellurium (Te) and polystyrene (PS) based 1Dperiodic symmetric, asymmetric and defect with meta-material using well known simple TMM. The parameters for tellurium (Te) and polystyrene (PS) material are $\varepsilon_{Tellurium}=21.16$,

$\mu_{Telluriumc} = 1, n_{Tellurium} = \sqrt{\varepsilon_{Tellurium}\mu_{Tellurium}}$

$d_{Tellurium} = \dfrac{\lambda}{4n_{Tellurium}}$ and $\varepsilon_{Polystyrene} = 2.56$,

$\mu_{Polystyrene} = 1, n_{Polystyrene} = \sqrt{\varepsilon_{Polystyrene}\mu_{Polystyrene}}$

$d_{Polystyrene} = \dfrac{\lambda}{4n_{Polystyrene}}$ where wavelength $\lambda = 1.55 \times 10^{-6}\,m$. The permittivity and permeability of the meta-material are calculated by using the relation [33].

$$\varepsilon_m(\omega) = 1 + \frac{5^2}{0.9^2 - \omega^2 - i\omega\gamma_e} + \frac{10^2}{11.5^2 - \omega^2 - i\omega\gamma_e},$$

$\mu_m(\omega) = 1 + \dfrac{3^2}{0.902^2 - \omega^2 - i\omega\gamma_m}$ and refractive index of the material $n_m = \sqrt{\varepsilon_m \mu_m}$ where ε_m and μ_m are the permittivity and the permeability and the thickness of meta-material $d_m = \dfrac{\lambda}{4n_m}$ of the meta-material (M) layer and ω is the frequency in THz.

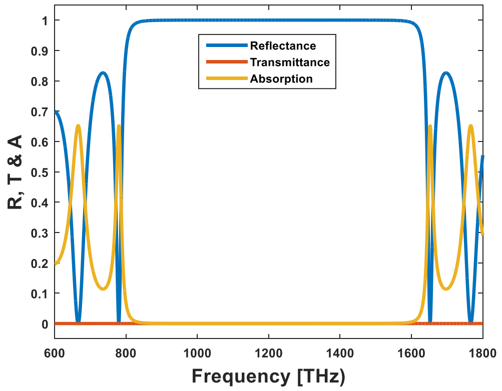

Figure 2: shows the reflectance, transmittance and absorption spectra of tellurium and polystyrene based 1D symmetric periodic structure.

The electromagnetic wave interaction with material plays a key role to analyse the optical properties of periodic structure. The optical properties like reflectance, transmittance and absorption spectra of tellurium and polystyrene based one dimensional symmetric and asymmetric periodic structure with defect of artificial meta-material are analysed using the concept of transfer matrix method in terahertz (THz) range of electromagnetic spectrum. The analysed result of tellurium and polystyrene based symmetric structure shows a huge band gap in terahertz region. Photonic band gap is the key role in the direction of optical properties of the periodic structure of the materials that controls the wave propagation in periodic structure. On the variation of the variable parameters the band gap can be tuned of the periodic structure. On the basis of the behaviour of tuned band gap that decides the applications in the direction of science and technology. The band gap of considered symmetry exists nearly frequency (800-1600 THz) region and this acts as a broadband reflector as shown in Fig 2. On changing the symmetry of considered periodic structure shows a huge band gap that separated in two parts and size of the band gap also increases on the variation of frequency (THz) range as shown in Fig 3.

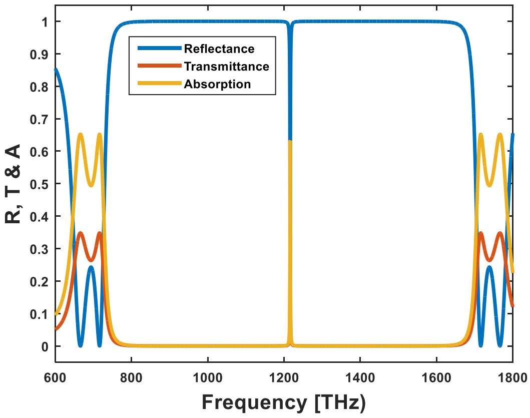

Figure 3: shows the reflectance, transmittance and absorption spectra of tellurium and polystyrene based 1D asymmetric periodic structure.

The defect behaviour is very enormous behaviour to analyse the optical property of periodic structure of the possible materials. The defected periodic structure can be tuning the possible variation of variable parameters that suggested to development of fabrication of optical device in the electromagnetic spectrum.

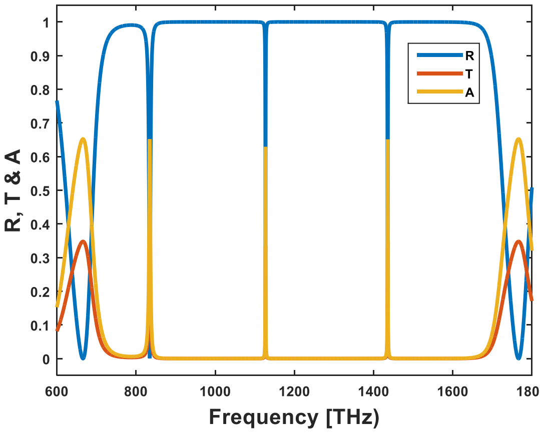

Figure 4: shows the reflectance, transmittance and absorption spectra of tellurium and polystyrene based 1DPS with defect of meta-material structure.

In our study, we have considered simple tellurium and polystyrene based periodic structure with defect of artificial meta-material to understand the concept of device fabrication. Reflectance, transmittance and absorption spectra of tellurium and polystyrene based periodic structure with defect of meta-material theoretically investigated the concept of multichannel filter at terahertz region. As we inserted the defect of meta-material layer in the considered periodic structure the behaviour of reflectance, transmittance and absorption spectra shows extremely behaviour to develop the multichannel filter and sensor and absorption-based devices at terahertz region as shown in Fig 4.

Conclusion

The calculated results of tellurium and polystyrene based one dimensional symmetric, asymmetric periodic structure and defect with meta-material shows exclusive result in terahertz region. The calculated results of considered one dimensional symmetric periodic structure acts as broadband reflector and asymmetric periodic structure shows the behaviour of tuned band gap on changing the symmetry of periodic structure. The defect of meta-material inserted in the tellurium and polystyrene based periodic structure and obtain innovative idea to fabricate the multichannel filter and sensor at terahertz region.

Conflict of interest

There is no conflict of interest.

References

1. E. Yablonovitch, "*Inhibited spontaneous emission in solid-state physics and electronics*", Phys. Rev. Lett. 58 2059 (1987).
2. S. John, "*Strong localization of photons in certain disordered dielectric super lattices*", Phys. Rev. Lett. 58, 2486 (1987).
3. J. D. Joannopolos, Johnson, R. D. Meade and J. N. Winn, *"Photonic crystals: Molding the flow of light"*, Princeton, NJ, USA: Princeton Univ. Press (2007).
4. Y. Fink, J. N. Winn, S. Fan, C. Chen, J. Michel, J. D. Joannopoulos and E. L. Thomas, *"A dielectric omnidirectional reflector"*. Science, 282 1679–1682(1998).
5. T. F. Krauss; and R. M. De La Rue, *"Photonic crystals in the optical regime: past, present and future"*, Progress Quant Electron 23 51-96 (1999).
6. D. N. Chigrin, A. V. Lavrinenko, D. A. Yarotsky, and S. V. Gaponenko, *"Observation of total omnidirectional reflection from a one-dimensional dielectric lattice"*, Appl. Phys., 68, 25 –28(1999).
7. K. Sakoda, *"Optical Properties of Photonic Crystals"*, (Berlin: Springer, 2004).
8. X. Gu., X. F. Chen, Y. P. Chen X. L. Zheng, Y. X. Xia and Y. L. Chen, *"Narrowband multiple wavelengths filter in aperiodic optical super lattices"*, Opt. Com. 237, 53 –58(2004).
9. S. Massaoudi, A. de Lustrac, and I. Huynen, *"Properties of metallic photonic band gap material with defect at microwave frequencies: calculation and experimental verification"*, JEMWA, 20(14), 1967–1980 (2006).
10. Q. R. Zheng, B. Q Lin. and N. C. Yuan, *"Characteristics and applications of a noval compact spiral electromagnetic band gap (EBG) structure"*, J. Elec. Mag. Waves Appl., 21, 199–213(2007).
11. K. Busch, G. von Freymann; S. Linden, S. F. Mingaleev, L. Tkeshelashvili and M Wegener, *"Periodic nanostructures for photonics"*, Phys. Rep. 444 101-202(2007).
12. S. V. Gaponenko, *"Introduction to Nano-photonics"*, Cambridge University Press, Cambridge 2010.
13. A. Kumar and K. B. Thapa, *"Study of optical property of defect mode in one dimensional double negative photonic crystal with plasma"*, Adv. Sci. Eng. Med. 10 1-5 (2018).
14. A. Kumar, P. P. Singh and K. B. Thapa, *"A new idea for broadband reflector and tunable multi-channel filter of one dimensional symmetric photonic crystal with magnetized cold plasma defects"*, AIP Conference Proceedings 1953 060043 (2018).
15. A. Kumar, N. Kumar and K. B. Thapa, *"Tunable broadband reflector and tunable narrowband filter of a dielectric and magnetized cold plasma photonic crystal"*, Eur. Phys. J. Plus, 133, 250 (2018).
16. A. Kumar, K. B. Thapa and S. P. Ojha, *"A tunable broadband filter of ternary photonic crystal containing plasma and superconducting material"*, Indian J Phys 93: 791 (2019).
17. A. Kumar, K. B. Thapa, *"Multichannel filter application of a magnetized cold plasma defect in periodic structure of ZnS/TiO$_2$ materials"*, Opt. Quant. Electron51(11) (2019) 355-14.
18. A. Kumar, K. B. Thapa and A. K. Yadav, *"Enhancement of absorption property of one-dimensional ternary periodic structure containing plasma based hyperbolic material for the application of microwave devices"*, J. Mag. Mag. Mater 93 165371-9(2019).
19. A. Kumar, N. Kumar, G. N. Pandey, D. Singh and K. B. Thapa, *"Metamaterial-plasma based hyperbolic material for sensor, detector and switching application at microwave region"*, J. Phys.: Cond. Matt. 32 325701-13(2020).
20. A. Kumar, P. Singh, K. B. Thapa, *"Study of super absorption properties of 1D graphene and dielectric photonic crystal for novel applications"*, Opt. Quant. Electron, 52(10) 01-12(2020).
21. A. Kumar, G. N. Pandey, A. Gautam, N. Kumar, K. B. Thapa, A. K. Shukla, *"Periodic structure containing host hyperbolic material for nano-guiding, sensing and imaging applications"*, Materials Today: Proc., 67 804-806(2022).

22. A. Kumar, D. Pandey, V. K. Nautiyal, V. Singh, A. Gautam and K. B. Thapa, *"Enhanced absorption in a dielectric/silver one-dimensional photonic crystal in the UV band"*, Eur. Phys. J. Plus 139(3) 232-8 (2024).
23. P. Mahesh, D. Panigrahy and C. Nayak, *"A comprehensive study of tunable properties broadband terahertz absorber based on graphene-embedded random photonic crystals"*, Phys. B: Condens, 650 414581 (2023).
24. V. G. Veselago, Sov. Phys. Usp. 10:509 (1968).
25. D. R. Smith and N. Kroll, *"Negative refractive index in left-handed materials",* Phys. Rev. Lett. 85:2933-2936 (2000).
26. L. Wu, S. He and L. Chen, *"On unusual narrow transmission bands for a multilayered periodic structure containing left-handed materials"*, Opt. Exp. 11 1283–1290 (2003).
27. Z. M. Zhangand. C. J. Fu, *"Unusual photo tunneling in the presence of a layer with a negative index"*, Appl. Phys. Lett.80:1097–1099 (2002).
28. J. Gerardin and L. Lakhtakia, *"Negative index of refraction and distributed Bragg reflectors"*, Microw. Opt. Technol. Lett. 34:409–411 (2002).
29. C. Sabah and S. Uckun, *"Electromagnetic wave propagation through frequency-dispersive and lossy double-negative slab"*, Opto-Electron. Rev. 15:133–143 (2007).
30. W. H. Lin, C. J. Wu and S. J. Chang, *"Analysis of angle-dependent unusual transmission in lossy single-negative (SNG) materials"*, Solid State Commun. 150:1729–1732 (2010).
31. J. Li, L. Zhou, C. T. Chan and P. Sheng, *"Photonic band gap from a stack of positive and negative index materials"*, Phy. Rev. Lett. 90:083901-083904 (2003).
32. Q. Jhu, D. Wangand Y. Jhang, *"Control of photonic band gaps in one-dimensional photonic crystals"*, Opt. Comm. 122:330-332 (2010).
33. A. Aghajamali, T. Alamfard, and M. Barati, *"Effects of loss factors on zero permeability and zero permittivity gaps in a 1D photonic crystal containing DNG materials"*, Phys. B 454:170–174 (2014).
34. P. Yeh, *"Optical Waves in Layered Media"*, John Wiley &Amp; Sons, New York, (1988).

Study on Structural and Thermoelectric Properties of $Fe_{2+x}Ni_{1-x}Ti$ (x=0, 0.25, 0.5) based Intermetallics: A First-Principles DFT Study

Shabeer Ali PC[1,3,a], Manoj Raama Varma[2,3,b], KN Narayanan Unni[1,3,c]

[1] *Centre for Sustainable Energy Technologies, CSIR-National Institute for Interdisciplinary Science and Technology (CSIR-NIIST), Industrial Estate, P.O. Thiruvananthapuram-695019, India.*
[2] *Materials Science and Technology Division, CSIR- National Institute for Interdisciplinary Science and Technology (CSIR-NIIST), Industrial Estate, P.O., Thiruvananthapuram-695019, India.*
[3] *Academy of Scientific and Innovative Research (AcSIR), Ghaziabad-201002, India.*

[a] shabeeralionline7@gmail.com
[b] manoj@niist.res.in
[c] unni@niist.res.in

Abstract

The structural, electronic, and thermoelectric properties of the series of full heusler alloys Fe_2NiTi and its $Fe_{2+x}Ni_{1-x}Ti$ (x=0, 0.25, 0.5) have been investigated theoretically. Here, we primarily concentrate on the thermoelectric properties of this new class of Heusler compounds, known as all-3d Heusler alloys. A_2BTi type alloys of Fe_2NiTi and its Fe (Iron) excess in Ni (Nickel) sites like $Fe_{2+x}Ni_{1-x}Ti$ (x=0, 0.25, 0.5) were studied using Density Functional Theory (DFT) and predicted the electronic structure and thermoelectric properties. The WIEN2k code's implementation of the full potential linearized augmented plane wave (FP-LAPW) method is a framework for first-principle computations. The electronic structure shows the material is metallic. The Seebeck coefficient (S) is found to increase, and the thermoelectric power factor is found to decrease with Fe addition on the Ni sites due to the increase in thermal (κ) and decrease in electrical conductivity (σ).

Keywords: Density Functional Theory, FP-LAPW, GGA-PBE, WIEN2k code, BoltzTraP code.
Received 29 January 2025; First Review 19 March 2025; Accepted 30 March 2025.

*** Address of correspondence**
Shabeer Ali PC
Centre for Sustainable Energy Technologies, CSIR-National Institute for Interdisciplinary Science and Technology (CSIR-NIIST), Industrial Estate, P.O. Thiruvananthapuram, 695019, India.

Email: shabeeralionline7@gmail.com

How to cite this article
Shabeer Ali PC, Manoj Raama Varma, KN Narayanan Unni, Study on Structural and Thermoelectric Properties of $Fe_{2+x}Ni_{1-x}Ti$ (x=0, 0.25, 0.5) based Intermetallics: A first-principles DFT Study, J. Cond. Matt. 2025; 03 (02): 77-82.

Available from:
https://doi.org/10.61343/jcm.v3i02.98

Introduction

Thermoelectric (TE) materials have garnered considerable interest in the quest for efficient energy conversion and advanced technological applications. With their unique properties and potential applications, these materials offer innovative solutions to some of the most pressing challenges in energy and technology[1-3]. Thermoelectric materials are pivotal in advancing energy conversion technologies, particularly waste heat recovery and power generation. These materials, which can directly convert temperature differentials into electric voltage and vice versa, have gained considerable attention due to their potential to create sustainable energy solutions [4].

Computational techniques have been essential to discover novel TE materials with economically viable performance in recent years. DFT has become one of these techniques that is particularly effective in predicting the characteristics of materials [5]. We used DFT to study the thermoelectric and magnetic properties in the present investigation.

The thermoelectric characteristics of this new class of A_2BC Heusler compound, referred to as an all-3d Heusler alloy, are quite promising [6, 7]. Fe_2NiTi crystallizing in the $C1_b$ structure has been taken as the parent material. This alloy possesses quite tunable characteristics by changes in the phase compositions, doping, and site disorder. Heusler alloys have a significant magneto crystalline anisotropy, as shown in several investigations [8]. The anisotropy may also be tuned by interstitial doping, strain, and local atom ordering, making them a promising contender for permanent magnet applications. Here, we primarily concentrate on the thermoelectric characteristics of this new class of Heusler compounds [9].

Fe_2NiTi has a high electrical resistivity (120 μΩcm), a medium compressive strain (5%), and a high compressive strength (1280 MPa) [10]. In the current study, we used first-principles calculations using the full potential linearized augmented plane wave (FP-LAPW) approach, which is employed in the WIEN2k program, to determine the structural and electrical characteristics of $Fe_{2+x}Ni_{1-x}Ti$ (x=0,0.25,0.5) [11-13]. The thermoelectric properties of the same system have also been examined using the semi-classical Boltzmann transport theory. The Perdew–Burke–Ernzerhof (PBE) framework includes the Generalized Gradient Approximation (GGA) to handle the exchange-correlation effects [14]. Hence, in the present investigation, we report our theoretically predicted thermoelectric characteristics, such as the power factor, figure of merit, thermal conductivity, electrical conductivity, and Seebeck coefficient.

Method

The density functional theory implemented through the WIEN2K program is used for theoretical calculations [15]. The full-potential linearized enhanced plane-wave method (FPLAPW) is the cornerstone of this package. According to our calculations, RMT is the minimum radius, and Kmax is the highest reciprocal lattice vector; $RMT \times K_{\max}$ is set at 7, and RMT is the unit cell's smallest atomic sphere radii, while K_{max} is the plane wave cut-off. We selected the Perdew-Burke Ernzerhof generalized gradient schemes (PBE-GGA) as the exchange-correlation potential in our calculation. For Fe and Ni atoms, the muffin-tin radii were set at 2.3 atomic units, while for Ti atoms, they were set at 2.24. The maximum value for partial waves within the muffin-tin spheres was expanded in spherical harmonics up to l_{max}=10 to accomplish energy and charge convergence. An energy cutoff of −6.0 Ryd and 5000 k points were used for these calculations., The stable structure was produced, assuming the self-consistency converged at a total energy of 0.00001 Ry. The exchange-correlation potential considered in the calculations GGA-PBE is given as

$$E_{xc}^{GGA-PBE} = \int \epsilon_{xc}^{PBE} (\rho,\ \nabla\rho)\ d^3r \qquad (1)$$

E_{xc} denotes the exchange-correlation energy and ϵ_{xc}^{PBE} represents the PBE exchange-correlation energy density as a function of the electron density ρ and its gradient $\nabla\rho$ [16].

The Kohn–Sham (K-S) equations are a set of one-electron equations derived from DFT. These maps the many-body problem of interacting electrons and nuclei and are the primary framework for first principles computations. The linearized-augmented-plane-wave (LAPW) approach, which is used, for instance, in the computer code WIEN2k to explore crystal characteristics on the atomic scale, is one of the most accurate ways to solve the K-S equations [17]. APW + local orbital method (linearized) is a sophisticated computer method used to calculate the electronic structure of solids using DFT. The self-consistent field (SCF)technique aims to achieve self-consistency between the input and output electron densities or potentials.

By minimizing the total energy functional for the electron density, the DFT variational technique ensures that the estimated ground state energy is an upper bound on the actual ground state energy [18, 19]. The system's absolute ground state density and ground state energy are determined by repeatedly solving the Kohn-Sham equations using the SCF technique. With reasonable computational effort, this method enables DFT to characterize the electronic structure of many-electron systems precisely [20, 21].

The total energy minimization method using Birch-Murnaghan's equation of state has been used to optimize the equilibrium lattice parameters of $Fe_{2+x}Ni_{1-x}Ti$ (x=0, 0.25, 0.5). The energy curve's minimal value shows the equilibrium condition of the system. The ground-state energy with the associated ground-state volume has the lowest energy. The lattice parameters were computed using the minimal volume.

The package BoltzTraP, which contains the Boltzmann transport characteristics program for computing semi-classical transport coefficients, was used for thermoelectric calculations. This software, which relies on the density functional theory within the FPLAPW technique, is interfaced with the WIEN2k code.

Discussion

1. Structural Properties

Fig 1-(a,b) are the generated crystal structures of the samples using the software XCrysDen with a new molecular surface with constant Gaussian function having pseudo-density surface type of resolution about 0.035 Å. Theoretically calculated structures of the first sample Fe_2NiTi is optimized successfully with space group F-43m (No. #216) having Cubic symmetry with a lattice parameter of 5.83 Å. This value is very close to the experimental value of the structural lattice parameter reported by Marathe et al. [22] and YANG Jihan et al [23]. For the second sample, $Fe_{2.25}Ni_{0.75}Ti$, the volume is optimized with a space group of P-43m (No. #215) with a lattice parameter of 5.827 Å,

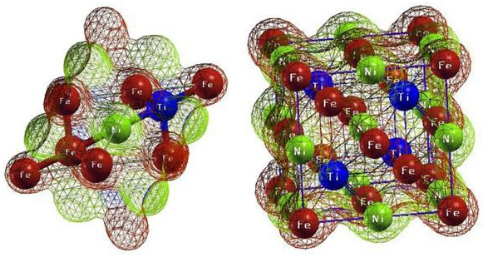

Figure 1: *Type A_2BC unit cells for common Heusler alloys: (a) primitive 4-atom unit cell (b) conventional 16-atom unit cell.*

Table 1: The calculated lattice constants (a_0, c_0) in (Å), bulk modulus (B) in (G_{pa}), volume in (Å^3), the derivative of bulk modulus ($B^{/}$), and the ground state energy (eV) for $Fe_{2+x}Ni_{1-x}Ti$ (x=0, 0.25, 0.5).

Compound	**a_0 (Å)**	**c_0 (Å)**	**V (Å^3)**	**B (G_{Pa})**	**$B^{/}$**	**E_o (eV)**
Fe_2NiTi	5.8268	—	333.77	162.98	12.95	-9840.53
$Fe_{2.25}Ni_{0.75}Ti$	5.8270	—	1335.14	114.82	0.12	-38866.09
$Fe_{2.5}Ni_{0.5}Ti$	4.1123	5.8140	663.5318	178.84	5.14	-19185.02

and the third sample, $Fe_{2.5}Ni_{0.5}Ti$ has tetragonal symmetry with space group of P-4m2 (No. #115) with lattice parameter of a=4.1123 Å and c/a=1.41. The stable phase of these structures has been determined by analysing the structural characteristics using Birch–Murnaghan's equation of state, which describes the energy of a solid as a function of volume given below

$$E(V) = E_o + \frac{9V_oB_o}{16}\left\{\left[\left(\frac{V_o}{V}\right)^{\frac{2}{3}} - 1\right]^3 B_o' + \left[\left(\frac{V_o}{V}\right)^{\frac{2}{3}} - 1\right]^2 \left[6 - 4\left(\frac{V_o}{V}\right)^{\frac{2}{3}}\right]\right\} \quad -(2)$$

Fitting the total energy versus volume of the unit cell is being done as shown in Fig. 2(a-c) [24]. In this equation of state, E_0, B_0, V_0, V, and B are the minimum energy, bulk modulus, reference volume, deformed volume, and derivative of the bulk modulus with respect to pressure, respectively, shown in Table 1.

2. Electronic Properties

The energy band gap and density of states Fig. 3 (a-f) show the band structures of Fe_2NiTi, $Fe_{2.25}Ni_{0.75}Ti$, and $Fe_{2.5}Ni_{0.5}Ti$ samples along the first Brillouin zone's $W - L - \Lambda - \Gamma - \Delta$ -X- $Z - W - K$ high symmetry directions. Our band structure plots show that all the materials are metallic.

The conduction band minimum and valence band maximum indicate the boundaries for the electronic band gap and the zero-energy reference in eV is Fermi level E_F. It reveals that the compositions are metallic as the conduction and valance bands overlap. The total density of states (TDOS) and partial density of states (PDOS) provide further insight into the electronic properties and the contribution of individual atoms toward the band structure. We can see that in Fig.4(a-f) that Fe, Ni, and Ti atom's s and p states of Fe_2NiTi, $Fe_{2.25}Ni_{0.75}Ti$, and $Fe_{2.5}Ni_{0.5}Ti$ has very small contributions to the band structure. In addition, their d state significantly contributes to the conduction band compared to its s and p states. The transition metal atom's d states are found to be crossing the Fermi level in these compositions, giving rise to their metallic nature.

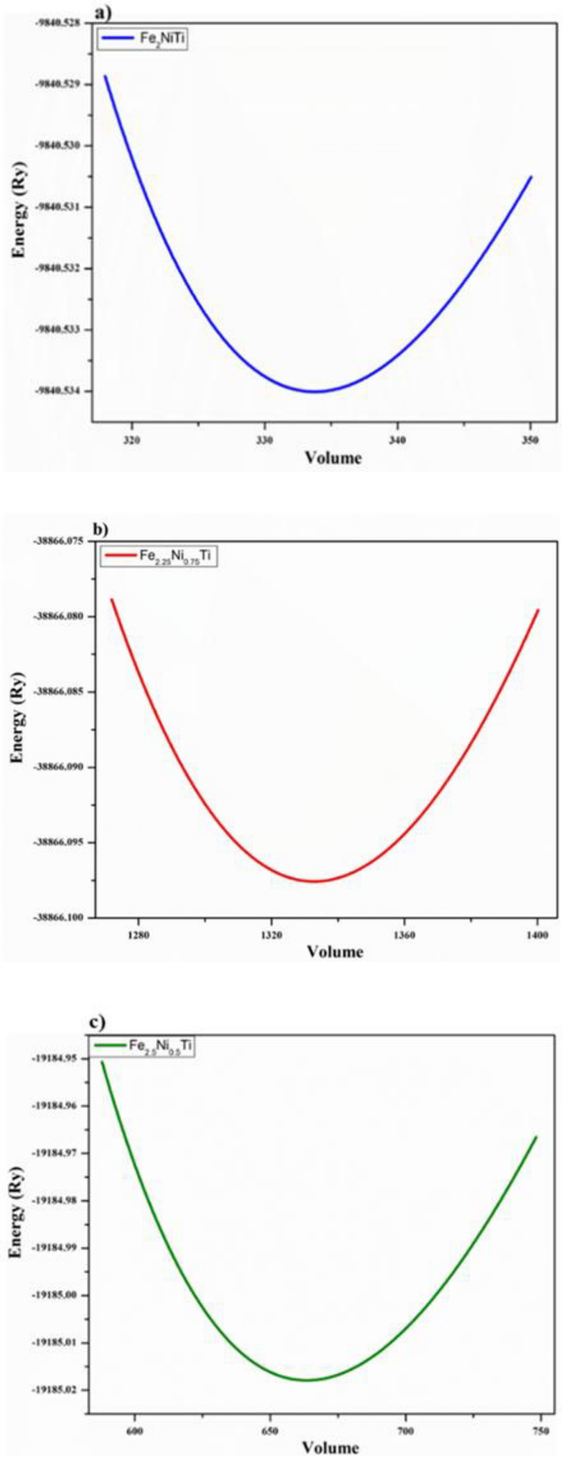

Figure 2: Energy versus volume curves of the optimized structure of **a)** Fe_2NiTi, **b)** $Fe_{2.25}Ni_{0.75}Ti$, and **c)** $Fe_{2.5}Ni_{0.5}Ti$ alloys.

3. Thermoelectric Properties

We used semi-classical Boltzmann transport theories based on a smoothed Fourier interpolation of the bands, as implemented in the BoltzTraP code, to investigate the thermoelectric characteristics of the compounds [11]. Fig.5(indicates calculated thermoelectric parameters as a function of temperature at the Fermi level, including the Seebeck coefficient, electrical conductivity, electronic thermal conductivity (κ_e), and power factor ($S^2\sigma$). l. Fig.5-a, b displays the Seebeck coefficient for the compositions $Fe_{2+x}Ni_{1-x}Ti$ (x = 0, 0.25, 0.5). In Fe_2NiTi, both spin channels have negative Seebeck values, indicating that it is an n-type material. It shows a Seebeck value of -1.5 µV/K at the spin-up channel and -35 µV/K at the spin-down channel at room temperature. $Fe_{2.5}Ni_{0.5}Ti$ is found to be a p-type material. In the case of $Fe_{2.25}Ni_{0.75}Ti$, both spin-up and spin-down channels show a negative Seebeck coefficient, indicating that it is an n-type material. S values attain their room temperature value of -15 µV/K value, which remains a constant throughout the temperature range of 100 to 900 K. From the plots, it can be noticed that the maximum value of the Seebeck coefficient is S~ 11.5 µV/K for $Fe_{2.5}Ni_{0.5}Ti$ spin up channel and 7.5 µV/K at room temperature, and it goes on decreasing with increasing temperature. $Fe_{2.5}Ni_{0.5}Ti$ also has a positive Seebeck value of 2.5 µV/K with an increasing Seebeck coefficient increasing with temperature, and this compound has both spin channels showing positive values for the Seebeck coefficient.

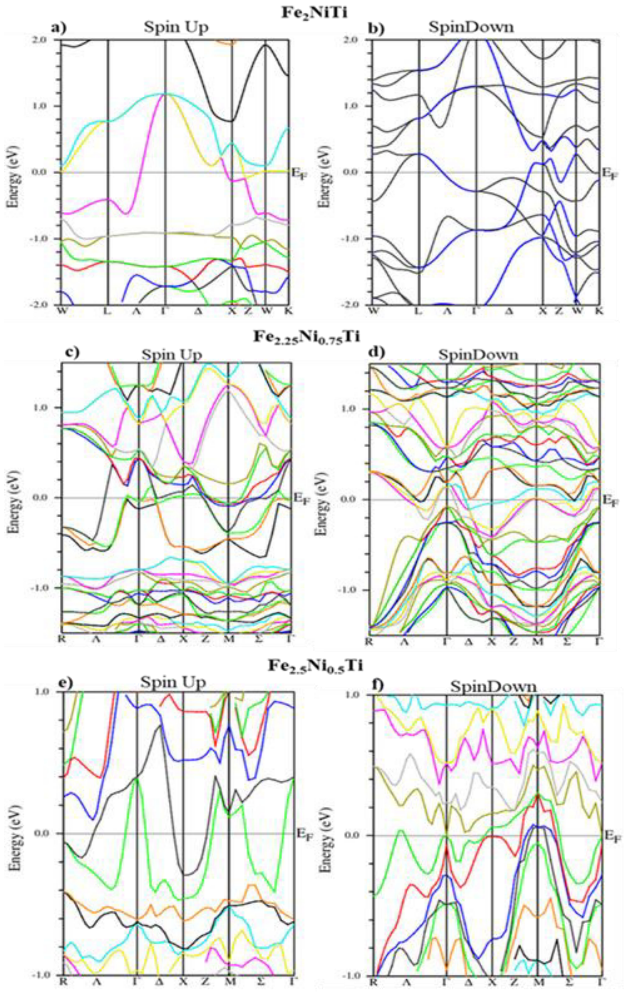

Figure 3: Spin up and spin down energy Band structures of Fe_2NiTi, $Fe_{2.25}Ni_{0.75}Ti$, and $Fe_{2.5}Ni_{0.75}Ti$.

The total Seebeck coefficient value of the samples, using the spin up and spin down channel values, are calculated using $S_{tot}=(S\uparrow\sigma\uparrow+S\downarrow\sigma\downarrow)/\sigma_{tot}$ where $\sigma_{tot}=\sigma\uparrow+\sigma\downarrow$ [5], is shown in Fig 5-b. It is visible that $Fe_{2.5}Ni_{0.5}Ti$ has a positive value of Seebeck with 5.5 µV/K at room temperature and the other [14] two samples have negative values, -16 µV/K and – 20 µV/K for $Fe_{2.25}Ni_{0.5}Ti$ and Fe_2NiTi respectively [5]. The Seebeck plot shows the different trends in the sample's different spin channels; at room temperature, the Seebeck coefficient reaches its highest value; at higher temperatures, it reaches its minimal value. The decreasing trend in the Seebeck coefficient may be related to increased charge carrier concentration with increasing temperatures.

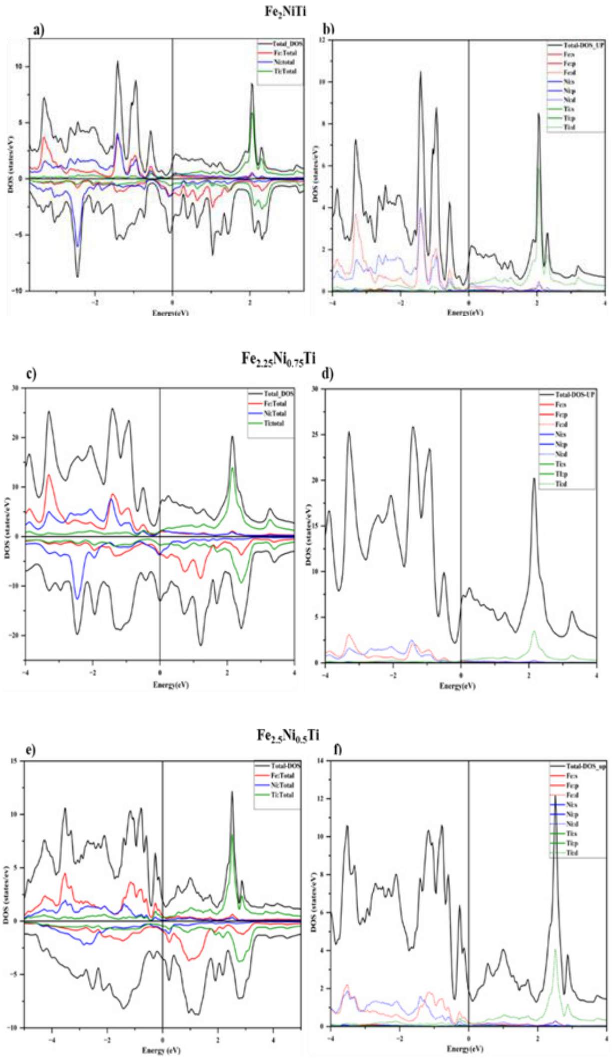

Figure 4 (a-f). Total DOS/PDOS OF (a-b) Fe_2NiTi, (c-d) $Fe_{2.25}Ni_{0.75}Ti$, and (e-f) $Fe_{2.5}Ni_{0.5}Ti$.

Better and more efficient thermoelectric material needs high values of electrical conductivity. The highest electrical conductivity per relaxation time exhibited at room temperature is $3.6 \times 10^{20}\ \Omega^{-1}m^{-1}s^{-1}$ of Fe_2NiTi, and the lowest value of $1.5\times10^{20}\ \Omega^{-1}m^{-1}s^{-1}$ for $Fe_{2.25}Ni_{0.5}Ti$. Low thermal conductivity values are needed for a better figure of merit. $Fe_{2.25}Ni_{0.75}Ti$ spin down has the smallest value with 1

W/(mKs) and the highest value of 2.5 W/(mKs) for Fe_2NiTi spin down channel, and all materials show increased thermal conductivity with temperature. The power factor (PF), given by $S^2\sigma$, indicates how well a material converts heat into electricity. Fe_2NiTi spin-up has a good power factor value of 45×10^{10} $Wm^{-1}K^{-2}s^{-1}$; the remaining samples have very low ranges compared to this. Fig 5-d shows total spins power factor values, making it clear that Fe_2NiTi has the highest value of 26×10^{10} $Wm^{-1}K^{-2}s^{-1}$ and $Fe_{2.25}Ni_{0.75}Ti$ and $Fe_{2.5}Ni_{0.5}Ti$ have PF values viz. 9.5×10^{10} $Wm^{-1}K^{-2}s^{-1}$ and 1.5×10^{10} $Wm^{-1}K^{-2}s^{-1}$ respectively. As temperature increases, the power factor also increases. This is because metals have a dominant electronic contribution to thermal conductivity, where the movement of free electrons primarily carries heat energy. generally, this contribution has a direct correlation with electrical conductivity. According to the Wiedemann-Franz law, the electronic component of thermal conductivity rises with temperature, raising the overall power factor. Because of their excellent thermoelectric response, these compositions offer a good energy-harvesting option for thermoelectric devices.

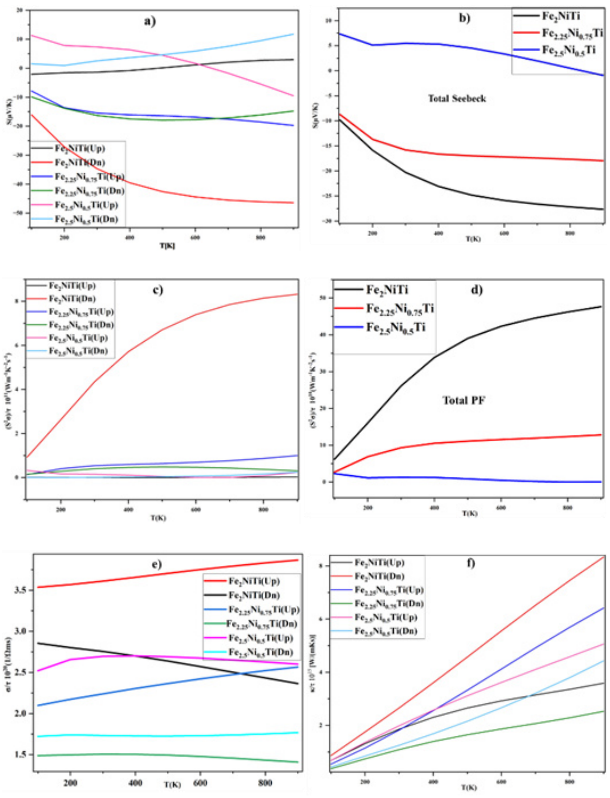

Figure 5: a) Seebeck effect for both spins, **b)** Total Seebeck effect of three samples, **c)** Electrical conductivity **d)** Power factor for both the spin channels, **e)** Total power factor value of three samples, **f)** Thermal conductivity.

The figure of merit (ZT) as a function of temperature from 100 K to 900 K is shown in Fig. 6. Fe_2NiTi has the highest ZT value at 900 K. The ZT values for the Fe_2NiTi, $Fe_{2.25}Ni_{0.75}Ti$, and $Fe_{2.5}Ni_{0.5}Ti$ alloys are 0.045, 0.012, and 0.0046, respectively.

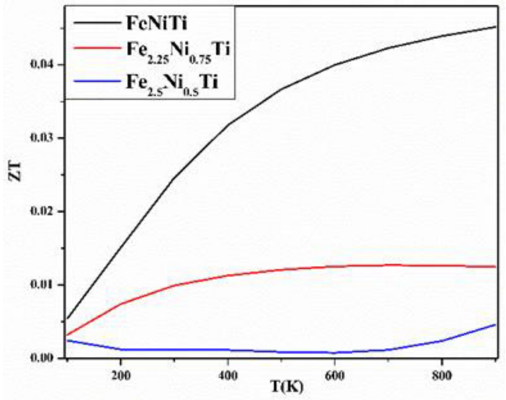

Figure 6: Figure of merit of Fe_2NiTi, $Fe_{2.25}Ni_{0.75}Ti$, and $Fe_{2.5}Ni_{0.5}Ti$.

Conclusion and Future Prospective

DFT-based WIEN2k code examines the structural, electronic, and thermoelectric properties of the Fe-based $Fe_{2+x}Ni_{1-x}Ti$ (x=0, 0.25, 0.5). It has been found that the stable, optimized structure of Fe_2NiTi and $Fe_{2.25}Ni_{0.75}Ti$ have space group of cubic with F-43m (No. #216) and P-43m (No. #215), respectively, while $Fe_{2.5}Ni_{0.5}Ti$ has a tetragonal structure with space group of P-4m2 (No. #115). Calculated structural parameters agree with the reported experimental values. The full potential linearized augmented-plane-wave method within the WIEN2k code was used for the calculations. The metallic nature of these materials stems from their electronic structure derived using band structure and DOS calculations using DFT with spin-orbit coupling. Thermoelectric properties show positive Seebeck for $Fe_{2.5}Ni_{0.5}Ti$ and negative value of Seebeck for Fe_2NiTi, $Fe_{2.25}Ni_{0.75}Ti$.

Acknowledgment

SA, MRV, and KNU thank the director of the CSIR-NIIST institution for the laboratory facilities. SA would like to acknowledge the financial assistance from CSIR-SRF (File. No.: 31/038(0604)/2019-EMR-I, India is duly acknowledged with gratitude. MRV would like to thank CSIR-HRDG for the kind support as an Emeritus Scientist Project.

References

1. S. Yang, P.Q., L. Chen and X. Shi, *Recent Developments in Flexible Thermoelectric Devices*, Small Sci., 2021, 1, 2100005.
2. Mardi, S., et al., *The interfacial effect on the open circuit voltage of ionic thermoelectric devices with conducting polymer electrodes.* Advanced Electronic Materials, 2021. **7**(12): p. 2100506.
3. Zhang, C., et al., *Gibbs Adsorption and Zener Pinning Enable Mechanically Robust High-Performance Bi_2Te_3-Based Thermoelectric Devices.* Advanced Science, 2023. **10**(26): p. 2302688.

4. Hou, Y., et al., *Programmable and Surface-Conformable Origami Design for Thermoelectric Devices.* Advanced Science, 2024. **11**(10): p. 2309052.
5. Gutiérrez Moreno, J.J., et al., *A review of recent progress in thermoelectric materials through computational methods.* Materials for Renewable and Sustainable Energy, 2020. **9**(3): p. 16.
6. Marathe, M. and H.C. Herper, *Exploration of all-3 d Heusler alloys for permanent magnets: An ab initio based high-throughput study*. Physical Review B, 2023. 107(17): p. 174402.
7. Tas, M., et al., *High Spin Magnetic Moments in All-3 d-Metallic Co-Based Full Heusler Compounds.* Materials, 2023. **16**(24): p. 7543.
8. Matsushita, Y., et al., *Large magnetocrystalline anisotropy in tetragonally distorted Heuslers: a systematic study.* Journal of Physics D: Applied Physics, 2017. **50**(9): p. 095002.
9. Herper, H.C., *Ni-based Heusler compounds: How to tune the magnetocrystalline anisotropy.* Physical Review B, 2018. **98**(1): p. 014411.
10. YAN, H.-L., et al., *Phase Stability, Magnetism and Mechanical Properties of A2BTi: Ab-initio Calculations and Experimental Studies.* Acta Metall Sin, 2023: p. 0-0.
11. Singh, D.J. and L. Nordstrom, *Planewaves, Pseudopotentials, and the LAPW method*. 2006: Springer Science & Business Media.
12. Grad, G.B. and E.V. Bonzi, *First principles study of the binding energies of pure metals using FP-LAPW method.* Journal of Electron Spectroscopy and Related Phenomena, 2013. **189**: p. 45-50.
13. Benkraouda, M. and N. Amrane, *Full potential linear augmented plane wave calculations of Electronic and Optical properties in ZnO.* Journal: JOURNAL OF ADVANCES IN PHYSICS. **11**(5).
14. Yan, J., et al., *Material descriptors for predicting thermoelectric performance.* Energy & Environmental Science, 2015. **8**(3): p. 983-994.
15. Wang, S., et al., *Assessing the Thermoelectric Properties of Sintered Compounds<? format?> via High-Throughput Ab-Initio Calculations.* Physical Review X, 2011. **1**(2): p. 021012.
16. Kohn, W., *Nobel Lecture: Electronic structure of matter—wave functions and density functionals.* Reviews of Modern Physics, 1999. **71**(5): p. 1253.
17. Koch, W. and M.C. Holthausen, *A chemist's guide to density functional theory*. 2015: John Wiley & Sons.
18. Singh, R. and B.M. Deb, *Developments in excited-state density functional theory.* Physics reports, 1999. **311**(2): p. 47-94.
19. Levi, G., A.V. Ivanov, and H. Jónsson, *Variational calculations of excited states via direct optimization of the orbitals in DFT.* Faraday Discussions, 2020. **224**: p. 448-466.
20. Perdew, J., K. Burke, and M. Ernzerhof, *Phys Rev Lett 77: 3865, Errata:(1997).* Phys. Rev. Lett., 1996. **78**: p. 1396.
21. Kohn, W. and L.J. Sham, *Self-consistent equations including exchange and correlation effects.* Physical review, 1965. **140**(4A): p. A1133.
22. Marathe, M.a.H.C.H., *Exploration of all-3 d Heusler alloys for permanent magnets: An ab initio based high-throughput study*. Physical Review B, 2023. 107(17): p. 174402.
23. YANG Jinhan, Y.H., LIU Haoxuan, ZHAO Ying, YANG Yiqiao, ZHAO Xiang, ZUO Liang. *Phase Stability, Magnetism, and Mechanical Properties of A2BTi: First-Principles Calculations and Experimental Studies*. Acta Metall Sin, 2024, 60(12): 1701-1709.
24. Katsura, T. and Y. Tange, *A simple derivation of the Birch–Murnaghan equations of state (EOSs) and comparison with EOSs derived from other definitions of finite strain*. Minerals, 2019. 9(12): p. 745.

Polaronic Variable Range Hopping Mediated Electrical Transport Mechanisms in Ferromagnetic Pr_2FeMnO_6

Kaipamangalath Aswathi[1,a], Manoj Raama Varma[2,b]

[1] Sensors and Energy Materials Group, Center for Materials for Electronics Technology (CMET), Thrissur, Kerala, India.
[2] CSIR-National Institute for Interdisciplinary Science and Technology (NIIST), Thiruvananthapuram, Kerala, India.

[a] aswathi1444@gmail.com
[b] manojraamavarma@gmail.com

Abstract

The electrical transport properties of oxide materials are largely dictated by electron-phonon interactions, which often lead to the formation of polarons, significantly influencing the conduction mechanism. In the case of the ferromagnetic orthorhombic perovskite oxide Pr_2FeMnO_6, the material exhibits insulating behaviour at room temperature, with a resistivity of approximately 4.1×10^3 Ω·m. As the temperature decreases, the resistivity increases markedly, reaching 73.47×10^3 Ω·m at 122 K, with a pronounced rise occurring below 160 K. To elucidate the conduction mechanism, the Variable Range Hopping (VRH) model is applied. This model describes electron hopping between non-nearest neighbour sites, which becomes favourable when the thermal energy is insufficient for nearest-neighbour hopping. Instead, electrons preferentially hop to sites with lower potential differences. The temperature dependence of resistivity is well-described by the VRH model, confirming its applicability in this system. In addition to electrical transport, the structural and magnetic properties of Pr_2FeMnO_6 have also been investigated. Notably, the material exhibits a magnetization reversal at low temperatures, further enriching its magnetic behaviour and potential applications.

Keywords: Conduction mechanisms; Variable range hopping; Sign reversal of Magnetization.
Received 30 January 2025; First Review 19 March 2025; Accepted 01April 2025.

*** Address of correspondence**
Kaipamangalath Aswathi
Sensors and Energy Materials Group Center for Materials for Electronics Technology (CMET), Thrissur, Kerala, India.

Email: aswathi1444@gmail.com

How to cite this article
Kaipamangalath Aswathi, Manoj Raama Varma, Polaronic Variable Range Hopping Mediated Electrical Transport Mechanisms in Ferromagnetic Pr_2FeMnO_6, J. Cond. Matt. 2025; 03 (02): 83-88.

Available from:
https://doi.org/10.61343/jcm.v3i02.125

Introduction

Perovskite oxides have become a focal point in materials science research because of their exceptional versatility and diverse range of physical properties, including superconductivity, ferroelectricity, magnetoresistance, and catalytic functionality [1, 2]. These properties arise from their characteristic crystal structure, typically represented as, where and are cations of different sizes and is an anion, often oxygen. Substitutions at the sites provide immense tunability in their structural, electronic, and magnetic characteristics, making perovskites ideal candidates for technological applications such as sensors, spintronics, and energy storage devices [3]. Among the various physical properties of perovskite oxides, their electrical transport behavior has been the subject of extensive study. The conduction mechanism in these materials is predominantly governed by the interactions between electrons and phonons, often leading to the formation of polarons. These quasiparticles, arising due to the coupling of charge carriers with lattice vibrations, play a critical role in determining the transport characteristics. Depending on the specific material and its structural and electronic configuration, different conduction mechanisms may dominate. These include: Band Conduction: In materials with sufficient carrier density and delocalized electronic states, conduction occurs through band-like motion [4]. In systems with localized states, carriers hop between these states, overcoming energy barriers [5]. This mechanism is often described by the small polaron hopping model, with resistivity expressed as: Variable Range Hopping (VRH): In disordered systems at low temperatures, electron hopping between non-nearest neighbours becomes dominant. These mechanisms highlight the interplay between the structural disorder, carrier localization, and thermal activation in oxides, leading to diverse electrical transport behaviours. This study focuses on understanding the conduction mechanisms in the ferromagnetic perovskite oxide, which exhibits insulating behaviour at room temperature and shows a temperature-dependent resistivity consistent with the VRH model [6]. The insights gained contribute to the broader understanding of electron-phonon interactions and transport processes in perovskite oxides, offering valuable implications for their potential applications in advanced technologies [7].

Method

The polycrystalline powder was synthesized using the modified auto-combustion method. Precursors (Pr $(NO_3)_3 6H_2O$, Fe $(NO_3)_2 6H_2O$, and $Mn(NO_3)_2 4H_2O$) were dissolved in stoichiometric ratios in distilled water. The solutions were mixed in a 1000 ml beaker in equal weights. The citric acid in appropriate amounts, was added to the mixture and stirred continuously. The colloid was combusted in air at 250 °C for 2 hours to produce precursors. Pre-calcination was done at 600 °C for 2 hours to remove all organic materials and nitrates. Calcination is done in the temperature range of 800-900°C for 12 hours with intermediate grinding. A PANalytical X'Pert powder diffractometer was used for structural analysis. Rietveld refinement was performed using GSAS software. Microstructural images were recorded using a JEOL JSM-5600LV Scanning Electron Microscope (SEM). Physical Property Measurement System (PPMS, Quantum Design Dynacool) used for electrical and magnetic measurements.

Discussion

Structural Properties

The X-ray diffraction (XRD) measurements were performed over a 2 range of 10° to 90°. The diffraction pattern was analyzed using the Rietveld refinement method, and the simulated patterns are presented in figure 1(a). The refinement confirmed the orthorhombic structure with the pbnm space group. The refinement yielded a good fit, with reliability factors, and. Scanning Electron Microscopy (SEM) images of the sintered pellet, recorded at a magnification of 15,000× and an accelerating voltage of 10 kV, are shown in figure 1(b). These images reveal that the sample exhibits a homogeneous microstructure [8].

Magnetic properties

The magnetic measurements in the temperature range of 2–380 K were carried out for various external magnetic field strengths according to the measurement protocols. The FC magnetization exhibited a sign reversal, becoming negative below a specific temperature when the applied field was 20 Oe, 1000 Oe (figure 2) and 1 kOe. For ZFC magnetization at 20 Oe, a similar sign reversal was observed at low temperatures, but this phenomenon diminished as the external field strength increased. At 10 kOe, the FC magnetization remained positive across the entire temperature range(figure 3) [8, 9].

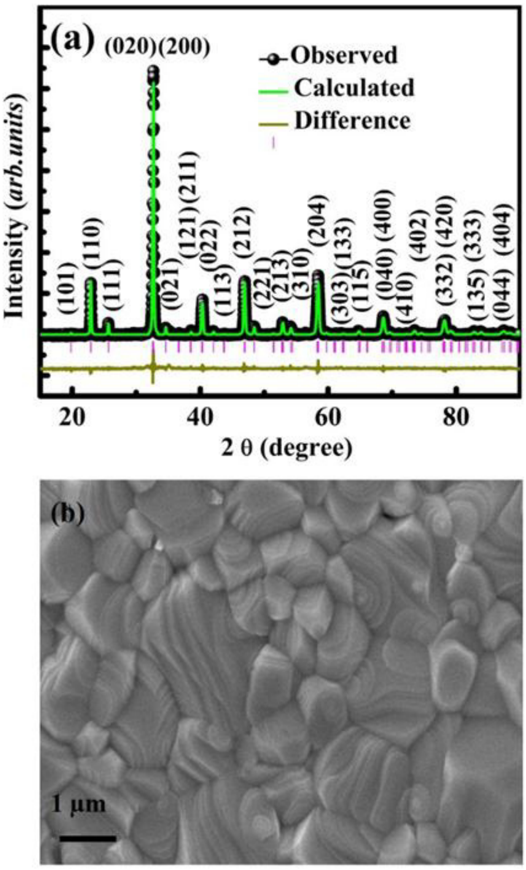

Figure 1: (a) XRD pattern of PFMO derived from Rietveld refinement within the 2**θ** range of 10° to 90°, and **(b)** SEM image of the sintered PFMO pellet captured at 10 kV with a magnification of x15000.

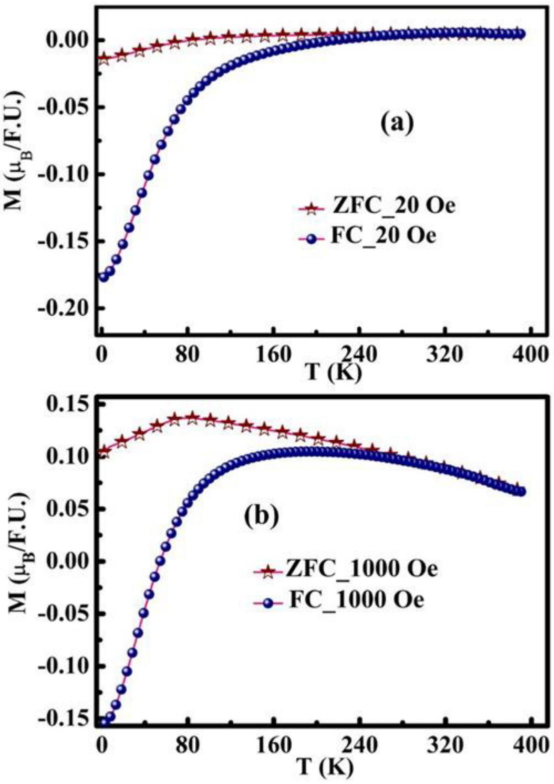

Figure 2: Dc magnetization measured at **(a)** 20 Oe, **(b)** 200Oe, **(c)** 1000Oe (d) and 10KOe at 2-380K.

In the FC process, as the temperature decreases, the magnetization also reduces. Upon further cooling, it sharply drops and becomes negative below a specific temperature known as the compensation temperature (Tcomp). The *M-T* data at 20 Oe reveals a bifurcation between FC and ZFC magnetization at 213 K, where the magnetization becomes negative. As the applied magnetic field increases, the ZFC magnetization no longer shows a sign reversal, while the FC magnetization continues to exhibit negative values up to 1 kOe. Beyond this field strength, no sign reversal in magnetization is observed (Fig. 3(d)). The negative magnetization in different materials can be influenced by various factors, including artifacts like the trapped field from the superconducting magnet in the PPMS. To rule out such artifacts, the sign reversal of magnetization was verified through an FC field polarity test. For this test, FC measurements were conducted twice under magnetic fields of opposite polarity So we have measured variation of magnetization with temperature under FC conditions for applied fields of ±500 Oe. When the sample was cooled from 380 K to 2 K under an external field of +500 Oe, the magnetization gradually increased, reaching a peak at 174 K. Subsequently, it decreased, crossing zero at Tcomp = 57 K, and became negative, indicating that the magnetization direction opposed the applied field. Conversely, when a field of -500 Oe was applied, the magnetization showed a mirror-image behavior: it was negative at high temperatures but became positive below Tcomp. This observation confirms that the negative magnetization in the material is not caused by the trapped field in the PPMS-VSM. Below the compensation temperature, negative magnetization is observed, especially at low magnetic fields, due to interactions between Fe ions and the paramagnetic contributions of Pr and Mn ions. [10].

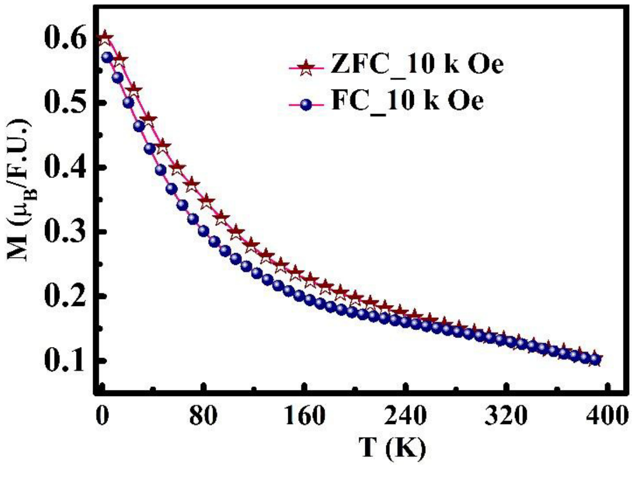

Figure 3: DC magnetization measured at 10KOe in the temperature range of 2-380K.

Electrical Properties

Materials are generally classified into three categories-conductors, semiconductors, and insulators-depending on their behavior in response to an electric field. The concept of energy bands, which defines the range of energies an electron can occupy, is fundamental to understanding a material's electrical conductivity. These energy bands include the conduction band and the valence band In insulators, the valence band is fully occupied, while the conduction band remains empty, separated by a significant energy gap [11]. In contrast, conductors allow an electric current to pass through effortlessly because their conduction band overlaps with the valence band, effectively eliminating any band gap. Semiconductors occupy an intermediate position, with their electrical conductivity falling between that of insulators and conductors. In semiconductors, the valence band is almost full, and the conduction band is nearly empty, with a relatively small energy gap of about 1 eV. Their band structure and atomic interactions largely influence the electrical behavior of these materials [12, 13].

In transition metal oxides, the conduction band is predominantly composed of oxygen 2p orbitals and metal d orbitals. The transport properties in these materials are influenced by the directional properties of the p and d orbitals and the Coulomb interactions within the d orbitals. The outer d electrons play a key role in determining the electrical behavior of these compounds. Metal oxides with disordered double perovskite structures are usually insulators, where the hopping of charge carriers governs the conduction mechanism [14].

In insulators, the movement of electrons is slow, leading to distortions in the surrounding lattice. These distortions create quantized lattice structures known as polarons, which facilitate conduction through hopping. This hopping mechanism can involve either electrons or polarons and varies across different materials (figure 4). There are three primary mechanisms for polaron hopping, each illustrated in figures 5 and 6. The first mechanism is thermally assisted tunneling, where carriers transition from a lower energy state to a higher one with the aid of thermal energy. The second mechanism is temperature-independent tunneling, where carriers move between states of equal energy without being influenced by temperature. The third mechanism involves carriers transitioning from a higher energy state to a lower one, accompanied by photon emission. figure 5 highlights the three mechanisms of polaron hopping, labeled as (i), (ii), and (iii). Specifically, the mechanisms are as follows: (i) thermally assisted tunnelling, where carriers hop from a lower energy state to a higher energy state, (ii) temperature-independent tunnelling, where carriers hop between states of equal energy, and (iii) temperature-independent tunnelling, where carriers move from a higher energy state to a lower energy state, accompanied by photon emission [15]. Several models describe the hopping conduction mechanism, including the Arrhenius thermal activation conduction or bandgap model (TAC), nearest-neighbour hopping or small polaron hopping (NNH/SPH), and Mott's variable range hopping model (Mott-VRH). In the Arrhenius TAC model, the resistivity follows the Arrhenius law: $\rho = \rho_0 \exp\left(\frac{E_A}{k_B T}\right)$ where is a constant, E_A is the activation energy.

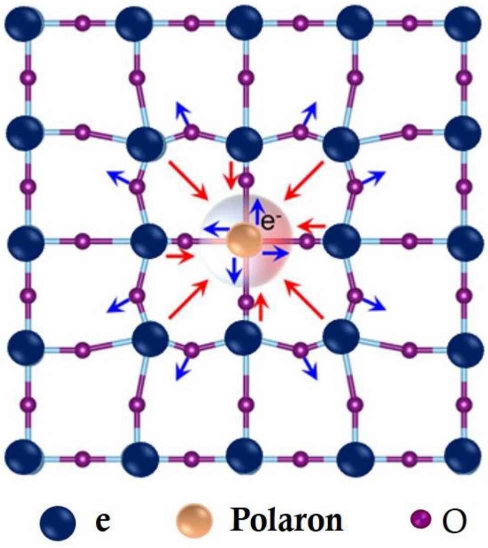

Figure 4: Polaron formation and conduction happening in peovskite structure.

VRH follows the equation, $\rho = \rho_0 \exp\left(\frac{T_0}{T}\right)^{1/4}$ where ρ_0 and T_0 are constants. The equation , $N(E_F) = \frac{24}{\pi k_B T_0 \varepsilon^3}$, representing the density of localized charge carriers, where ε is the percolation length of the localized wave function. At higher temperatures, sufficient thermal energy enables nearest-neighbour hopping of small polarons between localized donor and acceptor sites. The NN-SPH model is represented by an equation where $\rho = A k_B T \exp\left(\frac{E_A}{k_B T}\right)$. Figure 6 illustrates the VRH and NN-SPH mechanisms[16].

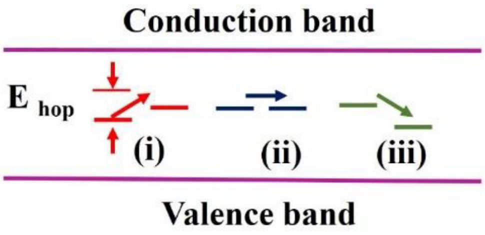

Figure 5: Electron /polaron hopping in insulating materials.

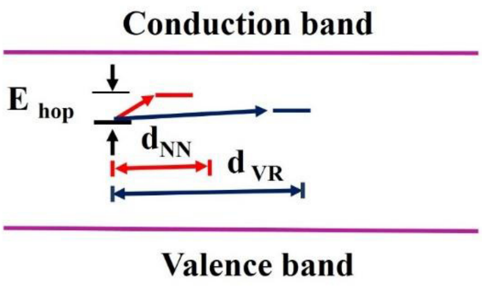

Figure 6: Mott's Variable range hopping polarons in perovskite materials.

In certain instances, the conduction process involves the combined contribution of both variable range hopping (VRH) and small polaron hopping (SPH) mechanisms. This cooperative behaviour, referred to as variable range hopping of small polarons (VR-SPH), can be mathematically described by integrating the respective equations for these two mechanisms.

$$\rho = BT\exp\left(\frac{E_A}{k_B T} + \left(\frac{T_0}{T}\right)^{1/4}\right)$$

where B is a constant.

Figure 7 (a) presents the resistivity (ρ) with temperature (122–300 K). At room temperature, PFMO exhibits insulating behaviour with a resistivity of approximately 4.1x10^{3}Ωm, which is aligned with previous reports. As the temperature decreases, the resistivity increases, reaching 73.47 x10^3 Ωm at 122 K. A sharp rise in ρ is observed below 160 K, consistent with earlier reports. The resistivity in the temperature range of 2–300 K, as depicted in figure 7, adheres to the VRH model, The ln ρ vs. 1/T$^{1/4}$ plot is shown in figure 7 (b). Parameters obtained after fitting (Red Line), T_0 = 0.866X10^9 K and ρ_0 = 40.42103 Ωm. N(EF) = 1 7.57x10^{-25} ev^{-1}m^{-3}. Activation energy E_A ($E_A = \frac{k_B}{4} T_0^{1/4} T^{3/4}$)is calculated and observed as varying from 0.13 to 0.26 eV for 122 K to 300 K [6].

Disorder-induced localization of charge carriers in transition metal oxides plays a crucial role in determining the hopping conduction mechanism, as described by Mott's theory [17]. In Pr_2FeMnO_6, Fe/Mn site disorder and oxygen vacancies significantly influence the density of localized states near the Fermi level, affecting electrical transport. Cationic disorder at the Fe/Mn sites disrupts hybridization between B-site transition metals and oxygen, reducing the effective hopping integral and favouring polaronic conduction [18]. Similarly, oxygen vacancies act as electron donors, introducing localized states that facilitate hopping transport, as observed in $La_{1-x}Sr_xMnO_3$ [19]. Our resistivity

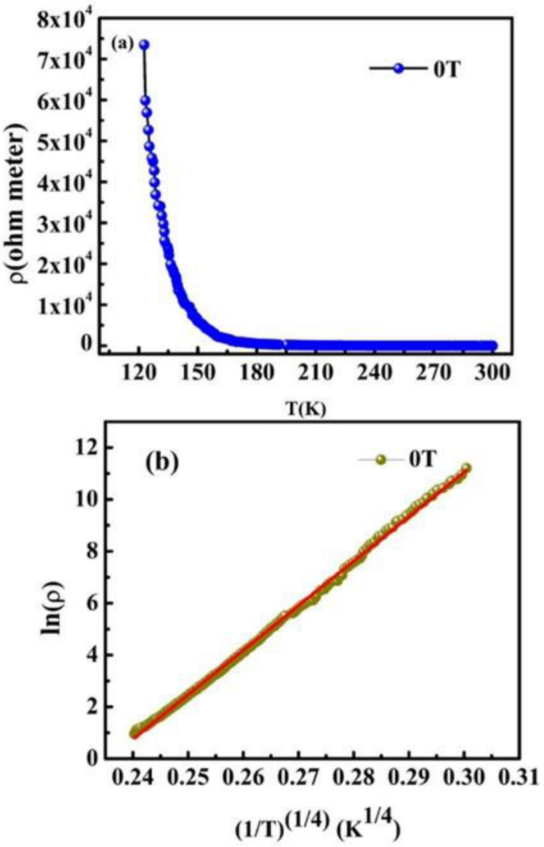

Figure 7: (a) Temperature-dependent resistivity, and **(b)** resistivity fitted using the VRH model.

data follows the Mott VRH model, indicating that charge carriers hop between localized states at different energy levels. The extracted hopping parameters, such as localization length and density of states near the Fermi level, align with previous reports on perovskite oxides exhibiting polaronic conduction. These findings suggest that disorder-induced localization in Pr_2FeMnO_6 is a dominant factor in its transport behaviour [20].Our analysis provides a broader understanding of how structural disorder impacts VRH conduction, reinforcing the significance of disorder-driven transport mechanisms in Pr_2FeMnO_6. Many double perovskites, such as La_2NiMnO_6 ,Gd_2NiMnO_6 and Sm_2FeMoO_6, exhibit polaronic transport, but the degree of disorder and electron-phonon coupling varies significantly across different systems [21, 22]. In La_2NiMnO_6, the transport mechanism is influenced by Ni/Mn cation ordering, which determines the balance between metallic and insulating phases. In contrast, Sr_2FeMoO_6 displays a unique interplay between spin-polarized transport and disorder-driven localization, which differs from the strong polaronic hopping seen in Pr_2FeMnO_6. Our study demonstrates that in Pr_2FeMnO_6, Fe/Mn site disorder and oxygen vacancies play a dominant role in the VRH mechanism, making its conduction behaviour distinct from these related systems. Unlike $La_{1-x}Sr_xMnO_3$, where hole doping tunes the transport from insulating to metallic Pr_2FeMnO_6 remains insulating due to stronger carrier localization effects. The activation energy and hopping parameters extracted from our data also suggest stronger electron localization than in many previously studied perovskites, reinforcing the novelty of our findings. This comparative analysis places our results within the broader context of perovskite transport studies and further validates the distinct nature of VRH conduction in Pr_2FeMnO_6.

Conclusion and Future Prospective

The double perovskite PFMO was synthesized using the citrate-gel combustion method. This compound adopts an orthorhombic crystal structure belonging to the Pbnm space group. Below the compensation temperature, negative magnetization is observed, especially at low magnetic fields, due to interactions between Fe ions and the paramagnetic contributions of Pr and Mn ions. The anomaly associated with the compensation temperature is examined using established theoretical models. Electrical transport studies indicate that PFMO behaves as a semiconductor, with its conduction governed by the VRH mechanism. The resistivity data within the 122–300 K temperature range conform to the VRH model, while the density of charge carrier states confirms the dominance of localized states in transport properties. These findings emphasize the material's semiconducting nature and offer important insights into its charge transport behavior.

References

1. Y. Moritomo, A. Asamitsu, H. Kuwahara, Y. Tokura, *Giant magnetoresistance of manganese oxides with a layered perovskite structure*, Nature, 380 (1996) 141-144.
2. A. Maignan, V. Caignaert, C. Simon, M. Hervieu, B. Raveau, *Giant magnetoresistance properties of polycrystalline praseodymium-based manganese perovskites: from* $Pr_{0.75}Sr_{0.25}MnO_{3-\delta}$ *to* $La_{0.75}Sr_{0.25}MnO_3$, Journal of Materials Chemistry, 5 (1995) 1089-1091.
3. T. Goto, T. Kimura, G. Lawes, A. Ramirez, Y. Tokura, *Ferroelectricity and giant magnetocapacitance in perovskite rare-earth manganites,* Physical review letters, 92 (2004) 257201.
4. C. Ganeshraj, R.N. Mahato, D. Divyaa, P. Santhosh, *Magnetic, electrical transport and structural investigations of orthorhombic perovskite* Pr_2MnFeO_6, Journal of Applied Physics, 107 (2010).
5. R. Ang, Y. Sun, Y. Ma, B. Zhao, X. Zhu, W. Song, *Diamagnetism, transport, magnetothermoelectric power, and magnetothermal conductivity in*

electron-doped $CaMn_{1-x}V_xO_3$ manganites, Journal of applied physics, 100 (2006).

6. R. Laiho, K. Lisunov, E. Lähderanta, V. Stamov, V. Zakhvalinskii, *Variable-range hopping conductivity in $La_{1-x}Ca_xMnO_3$*, Journal of Physics: Condensed Matter, 13 (2001) 1233.
7. K. Aswathi, J.P. Palakkal, P.N. Lekshmi, M.R. Varma, *A Griffiths-like phase and variable range hopping of polarons in orthorhombic perovskite Pr_2CrMnO_6*, New Journal of Chemistry, 43 (2019) 17351-17357.
8. K. Aswathi, J.P. Palakkal, M. RaamaVarma, *Magnetization sign reversal, exchange bias, and Griffiths-like phase in orthorhombic perovskite Pr_2FeMnO_6, Journal of Magnetism and Magnetic Materials*, 476 (2019) 45-53.
9. K. Aswathi, J.P. Palakkal, R. Revathy, M.R. Varma, *Sign reversal of magnetization in Sm_2CrMnO_6 perovskites*, Journal of Magnetism and Magnetic Materials, 483 (2019) 89-94.
10. A. Kumar, S. Yusuf, *The phenomenon of negative magnetization and its implications*, Physics Reports, 556 (2015) 1-34.
11. A. Tiwari, K. Rajeev, *Electrical transport in*, Journal of Physics: Condensed Matter, 11 (1999) 3291.
12. N. Tsuda, *Electronic conduction in oxides*, Springer Science & Business Media, 2000.
13. S. Khadhraoui, A. Triki, S. Hcini, S. Zemni, M. Oumezzine, *Variable-range-hopping conduction and dielectric relaxation in $Pr_{0.6}Sr0.4Mn_{0.6}Ti_{0.4}O_{3\pm\delta}$ perovskite*, Journal of magnetism and magnetic materials, 371 (2014) 69-76.
14. M. Javed, A. A. Khan, J. Kazmi, N. Akbar, S.N. Khisro, A. Dar, A. D. K. Tareen, M. A. Mohamed, *Variable range hopping transport and dielectric relaxation mechanism in $GdCrO_3$ rare-earth orthochromite perovskite*, Journal of Rare Earths, 42 (2024) 1304-1316.
15. Y. K. Vekilov, Y. M. Mukovskii, *Variable range hopping conductivity in manganites*, Solid state communications, 152 (2012) 1139-1141.
16. F. Zheng, L.-w. Wang, *Large polaron formation and its effect on electron transport in hybrid perovskites*, Energy & Environmental Science, 12 (2019) 1219-1230.
17. N. F. Mott, E. A. Davis, *Electronic processes in non-crystalline materials*, OUP Oxford, 2012.
18. D. Serrate, J. De Teresa, P. Algarabel, C. Marquina, J. Blasco, M. Ibarra, J. Galibert, *Magnetoelastic coupling in $Sr_2(Fe_{1-x}Cr_x)ReO_6$ double perovskites*, Journal of Physics: Condensed Matter, 19 (2007) 436226.
19. L. Zhang, D.J. Singh, M.-H. Du, *Density functional study of excess Fe in Fe_{1+x} Te: Magnetism and doping*, Physical Review B—Condensed Matter and Materials Physics, 79 (2009) 012506.
20. Y. Tokura, *Critical features of colossal magnetoresistive manganites*, Reports on Progress in Physics, 69 (2006) 797.
21. A.K. Biswal, *Exploring the Physics and Application of biphasic La_2NiMnO_6 based Double Perovskites*, in, 2016.
22. S. Anirban, A. Dutta, *Structure, small polaron hopping conduction and relaxor behavior of Gd_2NiMnO_6 double perovskite*, Journal of Physics and Chemistry of Solids, 159 (2021) 110292.

Study of Elastic Anisotropy of Compounds RhBiX (X = Hf, Ti and Zr)

S. Rajpurohit

School of Science and Technology, Vardhman Mahaveer Open University, Kota, Rajasthan, India.

sushilrajpurohit21@gmail.com

Abstract

The study shows the minimum and maximum values of Young's modulus, Poisson's ratio and shear modulus of compounds RhBiHf, RhBiTi and RhBiZr at zero pressure using ELATE software. Anisotropy parameters A_G and A^U for RhBiTi are slightly greater than the respective values of these parameters for RhBiHf and RhBiZr. The ratios of maximum to minimum values of Young's modulus (E_{max}/E_{min}), linear compressibility (β_{max}/β_{min}), shear modulus (G_{max}/G_{min}) and Poisson's ratio (ν_{max}/ν_{min}) for RhBiTi are 1.12, 1.00, 1.14 and 1.26, respectively. The investigation shows the spatial dependence of Young's modulus, linear compressibility, Poisson's ratio and shear modulus of compound RhBiTi through polar plots.

Keywords: Elastic, Anisotropy, Young's Modulus, Linear Compressibility, Shear Modulus.
Received 29 January 2025; First Review 13 February 2025; Accepted 02 April 2025.

*** Address of correspondence**
S. Rajpurohit
School of Science and Technology, Vardhman Mahaveer Open University, Kota, Rajasthan, India.

Email: sushilrajpurohit21@gmail.com

How to cite this article
S. Rajpurohit, Study of Elastic Anisotropy of Compounds RhBiX (X = Hf, Ti and Zr), J. Cond. Matt. 2025; 03 (02): 89-94.

Available from:
https://doi.org/10.61343/jcm.v3i02.99

Introduction

Half-Heusler compounds have been given attention, as they are likely to be promising thermoelectric energy materials [1-5]. Half-Heusler compounds are considered suitable thermoelectric materials [1-5]. Wei *et al.* [5] studied the properties of compounds RhBiX (X = Hf, Ti and Zr) within density functional theory using the WIEN2k Code [6]. Carrete *et al.* [7] and Feng *et al.* [8] also studied the thermal conductivities of these Half-Heusler compounds. Half-Heusler compounds XYZ exhibit crystal structure with space group $F\bar{4}3m$ [5, 8-10]. The reported optimized lattice constants are 6.406 Å, 6.444 Å and 6.265 Å for RhBiHf, RhBiZr and RhBiTi, respectively [5]. As per Wei *et al.* [5], RhBiHf is a direct band gap semiconductor. Compound RhBiHf has direct band gap of 0.33 eV [5]. Compound RhBiZr is an indirect band gap semiconductor with a band gap of 1.06 eV [5]. Thermoelectric parameters (such as power factor, Seebeck coefficient, etc.) for compounds RhBiX (X=Hf, Ti and Zr) were studied by Wei *et al.* [5]. At 300K, reported [5] lattice thermal conductivities of RhBiHf, RhBiZr and RhBiTi are 7.71 WmK^{-1}, 10.15 WmK^{-1} and 10.60 WmK^{-1}, respectively. By ratio of bulk modulus to shear modulus, compounds RhBiX (X = Hf, Ti and Zr) are expected to have ductile nature, as predicted by Wei *et al.* [5]. The computation of forces induced by small displacements was carried out by Wei *et al.* [5] using VASP software [11-17]. To the best of my knowledge, elastic anisotropy of the compounds RhBiHf, RhBiZr and RhBiTi has not yet been explored. For the design and fabrication of thermoelectric devices, elastic anisotropy plays a key role in determining the preferred orientation of the crystals. The elastic analysis provides the knowledge of the flexibility limit of device material to bend or stretch without losing the optimum functionality. The degree of malleability allows for thermoelectric devices to be designed from the point of view of adaptability for ideal applications. The durability of thermoelectric devices may decrease with repeated bending or stretching. From the point of view of long-term stability, the investigation of the elastic anisotropy of these compounds would be beneficial for the design of devices.

Computational details

Wei *et al.* [5] calculated the values of elastic constants C_{11}, C_{12} and C_{44} of RhBiHf, RhBiTi and RhBiZr using first-principles methods. Simulations were conducted within density functional theory [18-20] using GGA functional PBE [21, 22] by Wei *et al.* [5]. In the present investigation, values of elastic constants C_{ij} of compounds RhBiX (X = Hf, Ti and Zr) have been taken from the reported work of Wei *et al.* [5]. Using these values of elastic stiffness constants [5], the Voigt-Reuss-Hill scheme [23-25] bulk modulus, shear modulus and Young's modulus are

Table 1: Using values of elastic constants C_{ij} of compounds RhBiX (X = Hf, Ti and Zr) [5], calculated[a] values of bulk modulus K (in GPa unit), shear modulus G (in GPa unit) and Young's modulus E (in GPa unit) of compounds RhBiX at zero pressure.

Compound	K_V	K_R	K_H	G_V	G_R	G_H	E_V	E_R	E_H
RhBiHf	126.78	126.78	126.78	49.15	48.98	49.06	130.57	130.18	130.37
RhBiTi	124.90	124.90	124.90	39.20	39.05	39.13	106.47	106.10	106.29
RhBiZr	122.99	122.99	122.99	51.46	51.41	51.43	135.48	135.37	135.43

[a] Using computational ELATE software [26, 27].

Table 2: Using values of elastic constants C_{ij} of compounds RhBiX (X = Hf, Ti and Zr) [5], calculated[b] lowest and largest values of Young's modulus E (in GPa unit), linear compressibility β [in $(\mathrm{TPa})^{-1}$ unit], Poisson's ratio v (unitless) and shear modulus G (in GPa unit) of compounds at zero pressure.

Compound	$G_{\min}$	$G_{\max}$	$E_{\min}$	$E_{\max}$	$\beta_{\min} = \beta_{\max} = \beta$	$v_{\min}$	$v_{\max}$
RhBiHf	46.77	52.72	124.95	138.89	2.63	0.293	0.370
RhBiTi	37.20	42.21	101.52	113.81	2.67	0.319	0.402
RhBiZr	50.18	53.38	132.52	139.89	2.71	0.298	0.338

[b] Using computational ELATE software [26, 27].

Table 3: Using values mentioned in Table 1 and Table 2, elastic anisotropy parameters: ratio of largest to lowest values of Young's modulus E, linear compressibility β, shear modulus G and Poisson's ratio v for compounds RhBiX (X = Hf, Ti and Zr). Elastic anisotropy parameters A_K, A_G and A^U for compounds RhBiX.

Compound	Anisotropy						
	$\frac{E_{\max}}{E_{\min}}$	$\frac{\beta_{\max}}{\beta_{\min}}$	$\frac{G_{\max}}{G_{\min}}$	$\frac{v_{\max}}{v_{\min}}$	A_K	A_G	A^U
RhBiHf	1.11	1.00	1.13	1.26	0.00	0.0017	0.0174
RhBiTi	1.12	1.00	1.14	1.26	0.00	0.0019	0.0192
RhBiZr	1.06	1.00	1.06	1.13	0.00	0.0005	0.0048

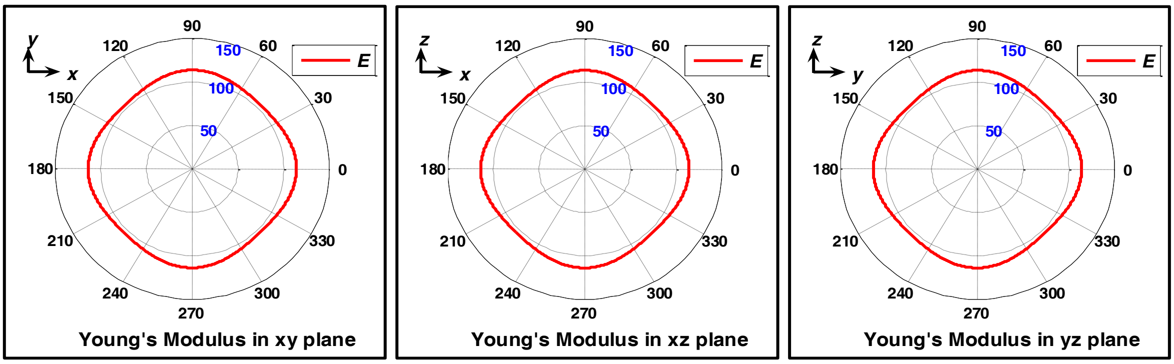

Young's Modulus in xy plane

Young's Modulus in xz plane

Young's Modulus in yz plane

Figure 1: Spatial variation (polar plot) of Young's modulus E (in GPa unit) of RhBiTi.

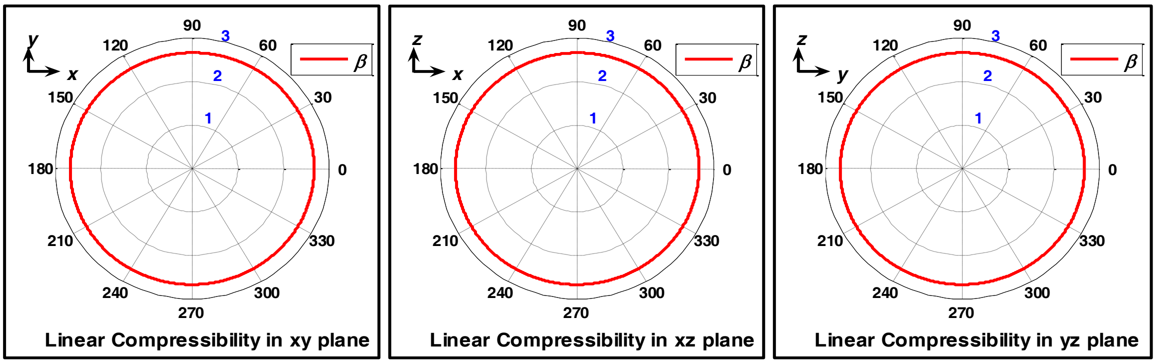

Figure 2: Spatial variation (polar plot) of linear compressibility [in $(\mathrm{TPa})^{-1}$ unit] of RhBiTi.

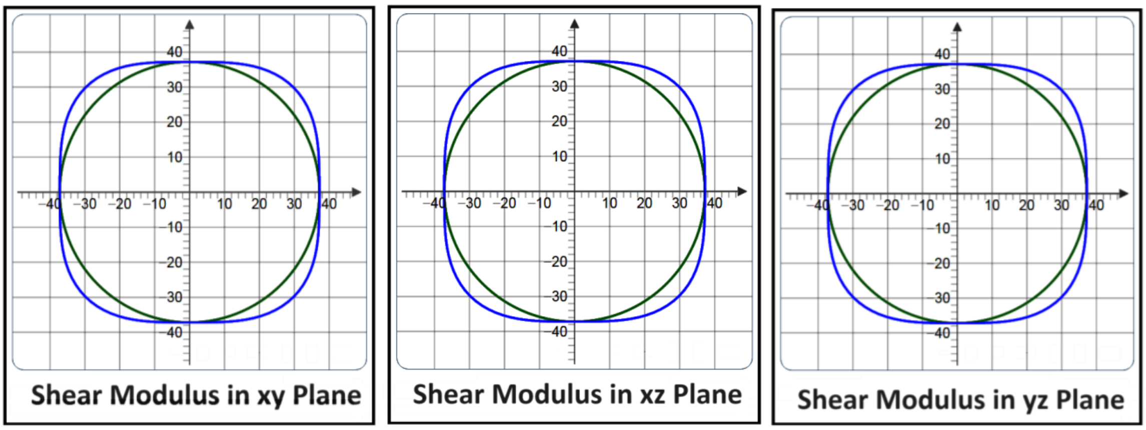

Figure 3. Spatial variation of shear modulus (in GPa unit) of RhBiTi using computational ELATE software [26, 27].

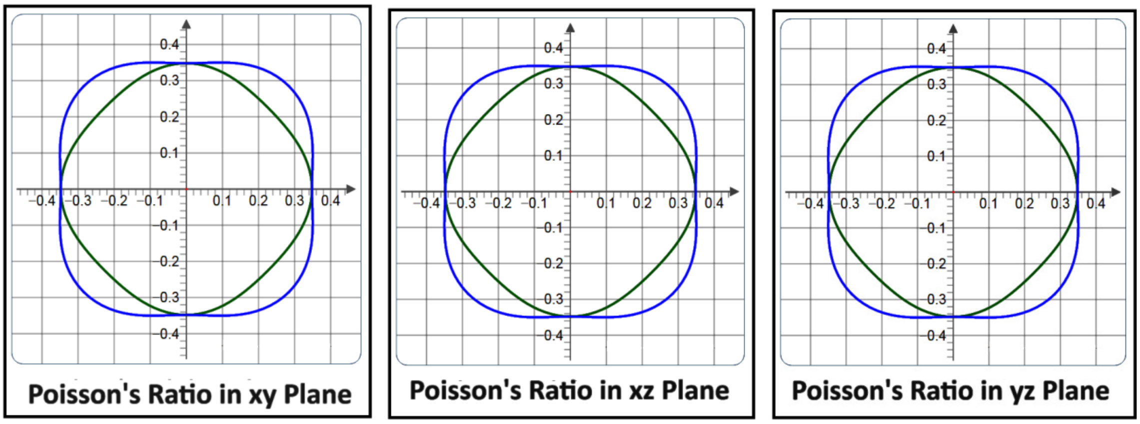

Figure 4. Spatial variation of Poisson's ratio of RhBiTi using computational ELATE software [26, 27].

computed by means of computational ELATE software [26, 27]. The lowest values of quantities Young's modulus, linear compressibility, Poisson's ratio and shear modulus of compounds RhBiX at zero pressure are also computed using computational ELATE software. The largest values of these elastic quantities are also computed. Elastic anisotropy parameters are calculated for these compounds. The spatial dependence of Poisson's ratio and shear modulus are investigated by means of computational ELATE software.

Results and discussion

Wei *et al.* [5] reported elastic stiffness constants C_{11} = 181.18 GPa, C_{12} = 96.76 GPa, and C_{44} = 37.20 GPa for RhBiTi and C_{11} = 194.16 GPa, C_{12} = 87.41 GPa, and C_{44} = 50.18 GPa for RhBiZr. Elastic stiffness constants are C_{11} = 197.07 GPa, C_{12} = 91.64 GPa, and C_{44} = 46.77 GPa for RhBiHf as calculated by Wei *et al.* [5]. The bulk modulus and shear modulus of compounds RhBiX (X = Hf, Ti and Zr) were reported by Wei *et al.* [5]. The Young's modulus and Poisson's ratio of these compounds RhBiX were also reported [5].

Table 1 shows the calculated values of quantities bulk modulus, shear modulus and Young's modulus of compounds RhBiX (X = Hf, Ti and Zr) at zero pressure as per the Voigt-Reuss-Hill scheme [23-25]. Using elastic stiffness constants C_{ij} for RhBiX as reported by Wei *et al.* [5], these elastic moduli (shown in Table 1) are computed by means of computational ELATE software [26, 27]. For the calculation of elastic anisotropy, Voigt and Reuss elastic moduli [23, 24] of compounds RhBiX are calculated in this work. The values of quantities bulk modulus, shear modulus and Young's modulus of compounds RhBiX (X = Hf, Ti and Zr) as computed by Wei *et al.* [5] and the respective elastic moduli values (K_H, G_H and E_H in Table 1) are almost the same.

All these three compounds have sufficiently high values of bulk modulus. It is clear from Table 1 that the values of bulk modulus of these compounds are not much different from each other. Table 1 shows that compound RhBiTi has the lowest value of shear modulus among these compounds. There is about 31% difference in the value of shear modulus between RhBiZr and RhBiTi. It is evident from Table 1 that the value of Young's modulus is the lowest for RhBiTi among these compounds. As per the Voigt-Reuss-Hill scheme [23-25], Young's modulus E_H of RhBiTi is 106.29 GPa. Thus, Table 1 shows the ample mechanical strength of these compounds RhBiX.

In terms of elastic compliance constants (S_{ij}), Young's modulus E along the unit vector l_i for the cubic crystal may be shown as [28].

$$E = \left[S_{11} - 2\left(S_{11} - S_{12} - \frac{1}{2} S_{44} \right)\left(l_1^2 l_2^2 + l_2^2 l_3^2 + l_1^2 l_3^2 \right) \right]^{-1} \quad (1)$$

where the direction cosines are denoted by l_1, l_2 and l_3.

The directional linear compressibility β for cubic crystal may be shown as [28].

$$\beta = S_{11} + 2S_{12} \quad (2)$$

Using the values of elastic stiffness constants C_{ij} [5], computed lowest and largest values of Young's modulus, linear compressibility, Poisson's ratio and shear modulus of compounds RhBiHf, RhBiTi and RhBiZr at zero pressure are shown in Table 2. For calculations of these values (shown in Table 2), ELATE software [26, 27] is utilized. For linear compressibility, there is no variation in its value for each compound. Variations in the values of shear modulus of RhBiHf, RhBiTi and RhBiZr are 12.7%, 13.5% and 6.4%, respectively, concerning their respective minimum values. The maximum percentage changes in the values of Young's modulus of compounds RhBiHf, RhBiTi and RhBiZr are 11.2%, 12.1% and 5.6%, respectively, with reference to their respective minimum values. It is obvious that RhBiZr has a lower percentage change in the quantities of shear modulus and Young's modulus in comparison to those of RhBiHf and RhBiTi. The variation in the value of Poisson's ratio is nearly 26% each for RhBiHf and RhBiTi, whereas it is 13.4% for RhBiZr relative to their respective minimum values.

Table 3 reveals the various elastic anisotropy parameters. The ratios of largest to lowest values of Young's modulus, shear modulus and Poisson's ratio of compounds RhBiX are represented in Table 3.

There are different ways to represent elastic anisotropy. The elastic anisotropy parameters (A_K and A_G) may be represented in the following way [29, 30]:

$$A_G = \frac{G_V - G_R}{G_V + G_R} \quad (3)$$

$$A_K = \frac{K_V - K_R}{K_V + K_R} \quad (4)$$

It is evident from Table 3 that the value of the elastic anisotropy parameter A_K for each compound RhBiX (X = Hf, Ti and Zr) is zero. The value of the elastic anisotropy parameter A_G for compound RhBiZr is lower than those of compounds RhBiHf and RhBiTi.

Ranganathan et al. [31] defined the universal elastic anisotropy index (A^U) in the following way:

$$A^U = \frac{K_V}{K_R} + 5\frac{G_V}{G_R} - 6 \quad (5)$$

The value of A^U of compound RhBiZr is 0.0048. The values of A^U of compounds RhBiHf and RhBiTi are 0.0174 and 0.0192, respectively.

Figure 1 shows the spatial variation of Young's modulus E (in GPa unit) of RhBiTi. Spatial variation of linear compressibility [in $(\mathrm{TPa})^{-1}$ unit] of RhBiTi is shown in Figure 2.

The spatial variation of shear modulus (in GPa unit) of RhBiTi is illustrated in Figure 3. For the Poisson ratio of RhBiTi, spatial variation is represented in Figure 4. For plotting, Figure 3 and Figure 4, convention as described by Marmier et al. [32] is implemented.

In order to plot Figure 1 to Figure 4, elastic constants C_{11}, C_{12} and C_{44} of RhBiTi as reported by Wei *et al.* [5] are used as input parameters.

Conclusion and Future Prospective

The present study reveals the elastic anisotropy of compounds RhBiX (X = Hf, Ti and Zr). The shear modulus of RhBiHf varies from 46.77 GPa to 52.72 GPa. The maximum change in values of shear modulus of RhBiHf, RhBiTi and RhBiZr are 12.7%, 13.5% and 6.4%, respectively, with reference to their respective minimum values. Directional Young's modulus of RhBiTi varies from 101.52 GPa to 113.81 GPa. Compound RhBiZr has a lower percentage change in Young's modulus in comparison to those of RhBiHf and RhBiTi. The values of the universal elastic anisotropy index (A^U) for RhBiTi and RhBiZr are 0.0192 and 0.0048, respectively. From the point of view of mechanical stability, the results of the present investigation may be utilized for the preferred orientation of crystals for the fabrication of devices using these compounds. In this calculation, our elastic anisotropy results depend on the values of elastic constants. As far as the experimental values of the elastic constants of these compounds are concerned, to the best of my knowledge, these values are not known. The computed elastic constants may vary significantly with computed lattice parameters. The calculated elastic constants by the first principle method also depend on the used exchange-correlation functional. Hence, our elastic anisotropy results are also dependent on the used PBE functional in the reported work of Wei et al. Nevertheless, the low order of values of the universal elastic anisotropy index of these compounds clearly indicates that the order of elastic anisotropy would be low. Our results may be validated by future experimental research. Elastic properties of compounds RhBiX (X=Hf, Ti and Zr) with doping of appropriate elements may be investigated in future research to reveal the possibilities of appropriate utilization of these compounds in devices. Future research may shed light on investigations of pressure-dependent elastic properties.

References

1. Wei, J., Yang, L., Ma, Z., Song, P., Zhang, M., Ma, J., Yang, F. and Wang, X., 2020. *Review of current high-ZT thermoelectric materials*. Journal of Materials Science, 55(27), pp.12642-12704. https://doi.org/10.1007/s10853-020-04949-0
2. Fu, C., Bai, S., Liu, Y., Tang, Y., Chen, L., Zhao, X. and Zhu, T., 2015. *Realizing high figure of merit in heavy-band p-type half-Heusler thermoelectric materials*. Nature Communications , 6(1), p.8144. https://doi.org/10.1038/ncomms9144
3. Zhu, H., Mao, J., Li, Y., Sun, J., Wang, Y., Zhu, Q., Li, G., Song, Q., Zhou, J., Fu, Y., He, R., Tong, T., Liu, Z., Ren, W., You, L., Wang, Z., Luo, J., Sotnikov, A., Bao, J., Nielsch, K., Chen, G., Singh, D.J. and Ren, Z., 2019. *Discovery of TaFeSb-based half-Heuslers with high thermoelectric performance*. Nature Communications, 10(1), p.270. https://doi.org/10.1038/s41467-018-08223-5
4. Graf, T., Klaer, P., Barth, J., Balke, B., Elmers, H.J. and Felser, C., 2010. *Phase separation in the quaternary Heusler compound CoTi(1− x)MnxSb–A reduction in the thermal conductivity for thermoelectric applications*. Scripta Materialia, 63(12), pp.1216-1219. https://doi.org/10.1016/j.scriptamat.2010.08.039
5. Wei, J., Guo, Y. and Wang, G., 2023. *Exploring structural, mechanical, and thermoelectric properties of half-Heusler compounds RhBiX (X= Ti, Zr, Hf): A first-principles investigation*. RSC Advances, 13(17), pp.11513-11524. https://doi.org/10.1039/D3RA01262J
6. Blaha, P., Schwarz, K., Tran, F., Laskowski, R., Madsen, G.K.H. and Marks, L.D., 2020. WIEN2k: *An APW+ lo program for calculating the properties of solids.* The Journal of Chemical Physics, 152(7), p. 074101. https://doi.org/10.1063/1.5143061
7. Carrete, J., Li, W., Mingo, N., Wang, S. and Curtarolo, S., 2014. Finding Unprecedentedly *Low-Thermal-Conductivity Half-Heusler Semiconductors via High-Throughput Materials Modeling*. Physical Review X, 4(1), p.011019. https://doi.org/10.1103/PhysRevX.4.011019
8. Feng, Z., Fu, Y., Zhang, Y. and Singh, D.J., 2020. *Characterization of rattling in relation to thermal conductivity: Ordered half-Heusler semiconductors*. Physical Review B, 101(6), p.064301. https://doi.org/10.1103/PhysRevB.101.064301
9. Ma, J., Hegde, V.I., Munira, K., Xie, Y., Keshavarz, S., Mildebrath, D.T., Wolverton, C., Ghosh, A.W. and Butler, W.H., 2017. *Computational Investigation of Half-Heusler Compounds for Spintronics Applications*. Physical Review B, 95(2), p.024411. https://doi.org/10.1103/PhysRevB.95.024411
10. Graf, T., Felser, C. and Parkin, S.S.P., 2011. *Simple rules for the understanding of Heusler compounds. Progress in Solid State Chemistry*, 39(1), pp.1-50. https://doi.org/10.1016/j.progsolidstchem.2011.02.001
11. Kresse, G. and Hafner, J., 1993. *Ab initio molecular dynamics for liquid metals*. Physical Review B, 47(1), pp.558-561. https://doi.org/10.1103/PhysRevB.47.558
12. Kresse, G. and Hafner, J., 1993. *Ab initio molecular dynamics for open-shell transition metals*. Physical Review B, 48(17), pp.13115-13118. https://doi.org/10.1103/PhysRevB.48.13115
13. Kresse, G. and Hafner, J., 1994. *Ab initio molecular-dynamics simulation of the liquid-metal–amorphous-semiconductor transition in germanium.* Physical Review B, 49(20), pp.14251-14269. https://doi.org/10.1103/PhysRevB.49.14251

14. Kresse, G. and Furthmüller, J., 1996. *Efficient iterative schemes for ab initio total-energy calculations using a plane-wave basis set*. Physical Review B, 54(16), pp.11169-11186. https://doi.org/10.1103/PhysRevB.54.11169
15. Kresse, G. and Furthmüller, J., 1996. *Efficiency of ab-initio total energy calculations for metals and semiconductors using a plane-wave basis set*. Computational Materials Science, 6(1), pp.15-50. https://doi.org/10.1016/0927-0256(96)00008-0
16. Kresse, G. and Joubert, D., 1999. *From ultrasoft pseudopotentials to the projector augmented-wave method*. Physical Review B, 59(3), pp.1758-1775. https://doi.org/10.1103/PhysRevB.59.1758
17. Hafner, J., 2008. *Ab-initio simulations of materials using VASP: Density-functional theory and beyond*. Journal of Computational Chemistry, 29(13), pp.2044-2078. https://doi.org/10.1002/jcc.21057
18. Cramer, C.J., 2004. *Essentials of Computational Chemistry: Theories and Models*. 2nd ed. England: John Wiley & Sons Ltd.
19. Fermi, E., 1928. *Eine statistische Methode zur Bestimmung einiger Eigenschaften des Atoms und ihre Anwendung auf die Theorie des periodischen Systems der Elemente*. Zeitschrift für Physik, 48(1), pp.73-79. https://doi.org/10.1007/BF01351576
20. Thomas, L.H., 1927. *The calculation of atomic fields*. Mathematical Proceedings of the Cambridge Philosophical Society, 23(5), pp.542-548. https://doi.org/10.1017/S0305004100011683
21. Perdew, J.P., Burke, K. and Ernzerhof, M., 1996. *Generalized Gradient Approximation Made Simple*. Physical Review Letters, 77(18), pp.3865-3868. https://doi.org/10.1103/PhysRevLett.77.3865
22. Perdrew, J.P., Burke, K. and Ernzerhof, M., 1997. *Erratum: Generalized Gradient Approximation Made Simple* [Physical Review Letters, 77, 3865 (1996)]. Physical Review Letters, 78(7), p.1396. https://doi.org/10.1103/PhysRevLett.78.1396
23. Voigt, W., 1928. Lehrbuch der Kristallphysik. BG Teubner, Leipzig und Berlin.
24. Reuss, A. and Angew, Z., 1929. *Berechnung der Fliesgrenze von Mischkristallen auf Grund der Plastizatsberechnung fur Einkristalle*. Journal of Applied Mathematics and Mechanics, 9(1), pp.49–58. https://doi.org/10.1002/zamm.19290090104
25. Hill, R., 1952. *The Elastic Behaviour of a Crystalline Aggregate. Proceedings of the Physical Society*, Section A, 65(5), p.349-354. https://doi.org/10.1088/0370-1298/65/5/307
26. Gaillac, R., Pullumbi, P. and Coudert, F.X., 2016. *ELATE: An open-source online application for analysis and visualization of elastic tensors.* Journal of Physics: Condensed Matter, 28(27), p.275201. https://doi.org/10.1088/0953-8984/28/27/275201
27. http://progs.coudert.name/elate
28. Nye, J.F., 1985. *Physical Properties of Crystals: Their Representation by Tensors and Matrices*. New York: Oxford University Press Inc.
29. Chung, D.H. and Buessem, W.R., 1967. *The Elastic Anisotropy of Crystals*. Journal of Applied Physics, 38(5), pp.2010-2012. https://doi.org/10.1063/1.1709819
30. Chung, D.H. and Buessem, W.R., 1968. *Anisotropy in Single Crystal Refractory Compounds: Vol. 2.* (Eds. Vahldiek, F.W. and Mersol, S.A.), New York: Plenum Press. pp. 217–246
31. Ranganathan, S.I. and Ostoja-Starzewski, M., 2008. *Universal Elastic Anisotropy Index*. Physical Review Letters, 101(5), p.055504. https://doi.org/10.1103/PhysRevLett.101.055504
32. Marmier, A., Lethbridge, Z.A.D., Walton, R.I., Smith, C.W., Parker, S.C. and Evans, K.E., 2010. *ElAM: A computer program for the analysis and representation of anisotropic elastic properties*. Computer Physics Communications, 181(12), pp.2102-2115. https://doi.org/10.1016/j.cpc.2010.08.033.

Vanadium Oxide Nanorods: Synthesis, Morphology, and Luminescence Characteristics

Kajal[a] and Hafiz A. K.

Centre for Nanoscience and Nanotechnology, Jamia Millia Islamia, New Delhi, India.

[a] kajalthagela95@gmail.com

Abstract

A highly cost-effective synthesis approach has been adopted to prepare stable V_2O_5 nanorods for energy storage device applications. The as synthesized nanorods are thoroughly characterized using advanced techniques, including scanning electron microscopy (SEM), X- ray diffraction (XRD), UV visible and photoluminescence (PL). The mentioned techniques were performed to provide the valuable insight into the morphological, structural, optical and photoluminescence properties of as-synthesized V_2O_5 nanorods. X-ray diffraction exhibits the structural properties with the highest Bragg's angle observed at 8.66 degree. Surface morphology of the as prepared and calcinated nanorod's samples was studied by using the scanning electron microscope (SEM). The observed bandgap of NRs was calculated using tauc- plot and achieved at 2.61 eV. The photoluminescence spectroscopy demonstrates the luminescence behaviour of as synthesized nanorods. Aforementioned synthesis and results achieved through characterizations exhibits its potential suitability for photodetector applications.

Keywords: V_2O_5, Hydrothermal, Nanorods (NRs), Photodetector.
Received 27 January 2025; First Review 28 February 2025; Accepted 09 April 2025.

*** Address of correspondence**
Kajal
Centre for Nanoscience and Nanotechnology, Jamia Millia Islamia, New Delhi, India.

Email: kajalthagela95@gmail.com

How to cite this article
Kajal and Hafiz A. K., Vanadium Oxide Nanorods: Synthesis, Morphology, and Luminescence Characteristics, J. Cond. Matt. 2025; 03 (02): 95-99.

Available from:
https://doi.org/10.61343/jcm.v3i02.68

Introduction

Nanostructured materials are at the forefront of cutting-edge technological advancements, particularly in energy storage, catalysis, and optoelectronic devices. Their nanoscale dimensions and high surface-to-volume ratio result in unique physical and chemical properties that outperform their bulk counterparts. Among these materials, vanadium pentoxide (V_2O_5) has received significant attention due to its superior electrochemical properties, high thermal stability, and wide bandgap, making it an excellent candidate for lithium-ion batteries, supercapacitors, and photodetectors [1,2].

In recent years, one-dimensional (1D) nanostructures, such as nanorods, have gained prominence due to their anisotropic morphology, which enhances electron mobility and facilitates efficient light-matter interaction [3]. V_2O_5 nanorods, in particular, exhibit remarkable structural and optical properties, making them highly suitable for energy storage and optoelectronic applications [4,5]. However, the challenge lies in synthesizing V_2O_5 nanorods with precise morphological and structural control while maintaining cost-effectiveness and scalability.

Our study presents a hydrothermal synthesis approach that enables fine-tuning of nanorod dimensions, crystallinity, and luminescent properties. By optimizing critical reaction parameters such as precursor concentration, reaction temperature, reaction time, and pH, we have successfully synthesized uniform V_2O_5 nanorods with enhanced optical and electronic characteristics. The hydrothermal method, known for its ability to control particle size and morphology through aqueous-phase reactions at elevated temperatures and pressures, provides a reliable and eco-friendly route to high-purity V_2O_5 nanostructures. This synthesis strategy enhances the material's optical properties by reducing structural defects and optimizing bandgap energy, making it suitable for high-performance optoelectronic applications.

A thorough characterization of these nanorods was conducted using advanced techniques, including SEM for morphological analysis, XRD for structural properties, UV-visible spectroscopy for bandgap estimation, and PL spectroscopy for evaluating luminescence behavior. These analyses provide deep insights into the material properties, which are crucial for tailoring their performance in optoelectronic and energy storage devices [8,9].

The luminescence properties of vanadium-based nanostructures have been extensively studied, with reports suggesting that the presence of oxygen vacancies and defect states plays a significant role in determining emission characteristics [10,11]. Additionally, previous studies have demonstrated that the luminescence behavior of V_2O_5 can be tuned by controlling synthesis parameters, doping elements, and nanostructure morphology, making them versatile candidates for applications in optoelectronics, bio-imaging, and sensing [12-14].

Furthermore, compared to other synthesis methods, such as sol-gel or chemical vapor deposition, the hydrothermal approach used in this work is advantageous in terms of simplicity, scalability, and precise control over the growth environment. The resulting V_2O_5 nanorods exhibit superior crystallinity, reduced grain boundary defects, and enhanced charge transport properties, making them promising candidates for applications in lithium-ion batteries, supercapacitors, and photodetectors [15,16].

In conclusion, our cost-effective synthesis method, combined with detailed characterization, demonstrates the potential of V_2O_5 nanorods for high-performance applications. Their promising structural, optical, and luminescent properties suggest their suitability for lithium-ion batteries, supercapacitors, photodetectors, and light-emitting diodes [17-19].

Method

A standard protocol for producing a nano-structured V_2O_5 compound at a low temperature using the hydrothermal method is Dissolve 1.304 gm of $VOSO_4$ in 80 mL of deionized water (DI) while agitating the mixture vigorously until the solution becomes translucent blue. Gradually add 5 mL of 1% NH_4OH to the solution drop by drop, while continuously stirring. Slowly raise the temperature of the solution to 65°C in a water bath, maintaining gentle stirring. Hold this temperature for 90 minutes. As the solution cools, it will turn green After cooling, pour the solution into a 100 mL stainless steel autoclave lined with Teflon and bake it for 12 hours at 120°C. After the hydrothermal treatment, collect the product by vacuum filtration [4]. Dry the collected materialovernight in an oven at 60°C.The resulting dry V_2O_5 powder was then subjected to structural, morphological, and electrochemical analysis. Figure 1 illustrates the formation of V_2O_5 nanorods through this step production process. The hydrothermal method was chosen for its capability to produce high-purity nanorods with controlled growth parameters. This technique offers advantages such as precise morphology control, high crystallinity, and eco-friendliness. Key parameters influencing the nanorod formation include precursor concentration, reaction temperature, duration, and pH. These factors were carefully optimized to ensure the synthesis of high-quality nanorods with desirable properties.

Figure 1: Schematic diagram of V_2O_5 nanorods.

X-Ray Diffraction (XRD) Analysis

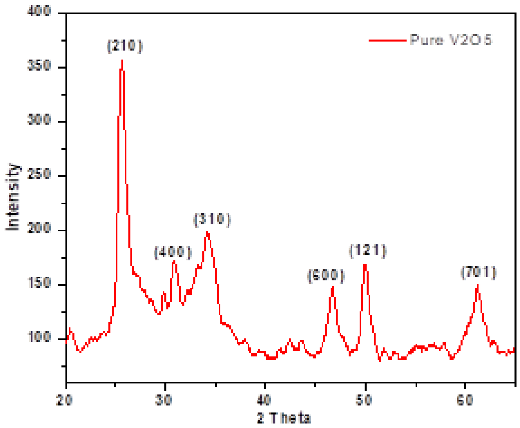

Figure 2: The XRD pattern of V_2O_5 powders obtained via modified hydrothermal method usingof 1% NH_4OH.

The XRD pattern of V_2O_5 nanorods, obtained via a modified hydrothermal method, exhibits well-defined peaks corresponding to an orthorhombic crystal structure. The crystallinity and phase evolution of V_2O_5 were investigated using XRD. The synthesized V_2O_5's XRD pattern is displayed in Figure 2, with prominent peaks at 2θ = 25.5°, 26.1°, 32.3°, 34.2°, 47.2°, 49.4°, and 61.9°. According to the Shcherbianite phase (JCPDS-89-2483), these peaks line up with the (210), (101), (011), (301), (600), (121), and (701) crystal planes of the orthorhombic structure of V_2O_5 [4]. A well-ordered crystalline structure was indicated by the highest Bragg's angle, which was found to be 8.66°.

UV-Visible Spectroscopy

The UV-Vis absorption spectrum of the V_2O_5 nanorods shows strong absorption in the visiblerange. Using a Tauc plot, the optical bandgap was calculated to be 2.61 eV, indicating their suitability for optoelectronic applications, such as photodetectors. As shown in Figure 3, the absorbance characteristics highlight the material's capability to interact effectively with visible light. This wide bandgap allows the nanorods to effectively absorb visible light, making them ideal for devices requiring high optical sensitivity [10].

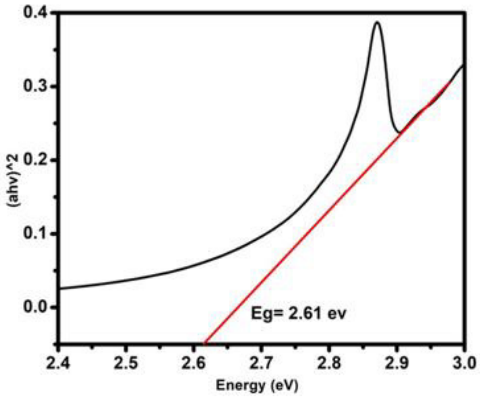

Figure 3: The shows the UV–visible reflectance spectra of V_2O_5 NRs.

Scanning Electron Microscope (SEM)

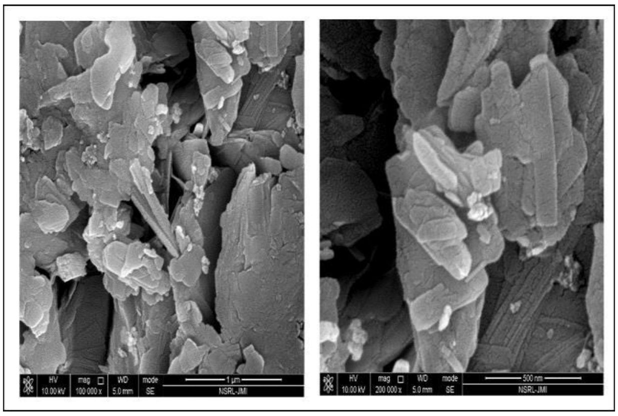

Figure 4: SEM micrographs and their magnified images of as prepared VO_2 nanorods.

The scanning electron microscope (SEM) was used to examine the surface morphology of the as-prepared and calcined samples. Figure 4 displays the SEM picture of the produced sample, which reveals the nanorod-based microspheres [11]. Each microsphere is between two and three millimetres in size. The surface morphology of the produced and calcined samples was examined using scanning electron XRD to investigate the crystallinity and phase development of V_2O_5, as demonstrated by the microstructure. The morphology of V_2O_5 nanorods significantly influences their luminescence properties. Structural variations lead to changes in defect states and oxygen vacancies, which, in turn, affect radiative recombination processes. A more detailed discussion has been added to explain the role of morphology in modifying optical emission characteristics.

SEM analysis reveals the surface morphology and size distribution of the nanorods, highlighting their uniformity and elongated 1D structure, which is essential for efficient electron transport [12]. XRD patterns confirm the crystalline structure of V_2O_5, with the highest Bragg's angle observed at 8.66°, indicating the presence of well-ordered crystal planes, which is critical for the stability and performance of the material in energy storage applications [13-15].

Furthermore, UV-visible spectroscopy is used to calculate the optical bandgap of the nanorods using a Tauc's plot, yielding a bandgap of 2.61 eV. This relatively wide bandgap suggests that the V_2O_5 nanorods are well-suited for optoelectronic devices, particularly photodetectors, where high optical sensitivity is required [16]. The bandgap of 2.61 eV, observed in the UV-visible spectroscopy analysis, is relatively modest but aligns well with previous studies on V_2O_5 nanorods. This value is justified based on structural and defect-related modifications. Additional references have been cited to support this observation.

Photoluminescence Spectrum (PL)

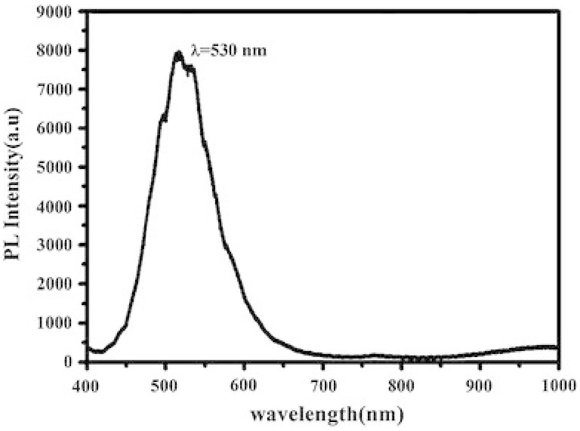

Figure 5: PL spectrum with a peak at 530 nm, indicating green light emission.

The photoluminescence (PL) spectrum shows a strong emission peak at 530 nm, highlighting efficient radiative recombination, characteristic of vanadium-based nanostructures. Figure 5 illustrates this PL spectrum, emphasizing the emission profile of the synthesized V_2O_5 nanorods. The PL properties of V_2O_5 are of particular interest for applications in light- emitting devices and sensors, where their ability to emit light at specific wavelengths can be tuned based on the nanostructure's size and composition. The observed luminescence further supports the potential of V_2O_5 nanorods in optoelectronic applications [17]. SEM analysis shows uniform, elongated V_2O_5 nanorods, essential for efficient electron transport. XRD confirms a crystalline structure with a Bragg's angle of 8.66°, vital for stability in energy storage [18,19]. UV-visible spectroscopy reveals a bandgap of 2.61 eV, indicating suitability for optoelectronic devices. Photoluminescence studies highlight the tuneable luminescent properties, supporting their use in light-emitting devices and sensors [20]. To ensure practical applicability, luminescence stability over time was assessed. Our findings indicate that the emission peaks remain stable under continuous exposure, with only minor degradation observed over extended periods

Conclusion and Future Prospective

A cost-effective hydrothermal approach was used in this study to successfully synthesize and fully characterize V_2O_5 nanorods. The orthorhombic crystalline structure was validated using XRD, and homogeneous, elongated nanorods were observed in SEM analysis. The bandgap, determined to be 2.61 eV, was assessed using UV-visible spectroscopy, while luminescence properties were investigated via PL spectroscopy. These findings indicate that V_2O_5 nanorods are suitable for optoelectronic applications, including photodetectors, light-emitting devices, and energy storage applications such as supercapacitors and lithium-ion batteries. Future work will focus on doping strategies to further tailor the optical properties and enhance stability.

Acknowledgements

The author would like to thank Prof. A. K. Hafiz and Dr. Manika Khanuja for their continuous support, help and guidance.

Declaration of Interest Statement

Regarding this work's publication, the authors declare that they have no conflicts of interest.

References

1. Mounasamy, V., Srividhya, G., & Ponpandian, N. (2023), *"Well-defined 2D Transition Vanadium Pentoxide (V_2O_5) Flat Nanorods with Large-Scale Synthesis Feasibility as an Electrocatalyst for the Oxygen Evolution Reaction (OER)"*, Energy Advances, 2(6), 1234-1245. doi:10.1039/d3ya00100h.
2. Zhang, S., Li, Y., & Wang, J. (2018), *"V_2O_5-Based Nanomaterials: Synthesis and Their Applications"*, RSC Advances, 8(15), 7890-7910. doi:10.1039/c7ra12523b.
3. Chen, L., Liu, X., & Zhang, H. (2019), *"Synthesis of Vanadium Oxide Nanorods Coated with Carbon: Characterization and Electrochemical Properties",* Journal of Solid State Electrochemistry, 23(9), 2455-2463. doi:10.1007/s11581-019-03203-1.
4. S. S. Karade, S. Lalwani, J.-H. Eum, and H. Kim, *"Coin cell fabricated symmetric supercapacitor device of two-steps synthesized V_2O_5 Nanorods",* J. Electroanal. Chem., vol. 864, p. 114080, May 2020, doi: 10.1016/j.jelechem.2020.114080.
5. J. Pan et al., *"Microwave-assisted hydrothermal synthesis of V_2O_5 nanorods assemblies with an improved Li-ion batteries performance",* Mater. Res. Bull., vol. 74, pp. 90–95, Feb. 2016, doi: 10.1016/j.materresbull.2015.10.020.
6. W. M. Zhang, X. L. Wu, J. S. Hu, Y. G. Guo, and L. J. Wan, *"α-Fe_2O_3 nanotubes in gas sensor and lithium-ion batteries applications",* Adv Mater, vol. 17, pp. 582–586, 2005.
7. Subramani, K, & Venkatesan, M. (2016) ,*"Vanadium based materials as electrode materials for high performance supercapacitors - ScienceDirect.*" Accessed: Dec. 14, 2024. [Online]. Available: https://www.sciencedirect.com/science/article/abs/pii/S0378775316310382
8. I. Pradeep, E. Ranjith Kumar, N. Suriyanarayanan, Ch. Srinivas, and M. V. K. Mehar, *"Effects of doping concentration on structural, morphological, optical and electrical properties of tungsten doped V_2O_5 nanorods",* Ceram. Int., vol. 44, no. 6, pp. 7098–7109, Apr. 2018, doi: 10.1016/j.ceramint.2018.01.149.
9. M. S. Raman, N. S. kumar, J. Chandrasekaran, R. Priya, P. Baraneedharan, and M. Chavali, *"Thermal annealing effects on structural, optical and electrical properties of V_2O_5 nanorods for photodiode application",* Optik, vol. 157, pp. 410–420, Mar. 2018, doi: 10.1016/j.ijleo.2017.11.030.
10. T. Zahra et al., *"Fabrication of V_2O_5@g-C3N4 nanocomposite by hydrothermal route for use as an improved electrochemical property in supercapacitor applications",* J. Energy Storage, vol. 87, p. 111470, May 2024, doi: 10.1016/j.est.2024.111470.
11. M. R. Charlotte and L. R. Viannie, *"Tailoring vanadium pentoxide nanoparticles for humidity sensing: impact of microwave annealing",* J. Mater. Sci., vol. 59, no. 48, pp. 22034–22052, Dec. 2024, doi: 10.1007/s10853-024-10485-y.
12. *Liu, Y., Chen, Q., Zhang, L., & Wang, J. (2019), "Facile Fabrication of Composite Vanadium Oxide Thin Films with Enhanced Thermochromic Properties | ACS Applied Materials & Interfaces",* Accessed: Dec. 14, 2024. [Online]. Available: https://pubs.acs.org/doi/abs/10.1021/acsami.9b11376
13. M. Kaseem, A. R. Safira, M. Aadil, T. T. Thanaa, and A. Fattah-alhosseini, *"Developing an efficient anticorrosive system through advanced modification of plasma-electrolyzed MgO with CeNiLDH complexed with V_2O_5 nanoparticles and (2E)-But-2-enedioic acid",* J. Magnes. Alloys, vol.

12, no. 10, pp. 4205–4218, Oct. 2024, doi: 10.1016/j.jma.2024.10.015.

14. B. Singh et al., *"Anomalous lattice behavior of vanadium pentaoxide (V_2O_5): X-ray diffraction, inelastic neutron scattering and ab initio lattice dynamics",* Phys. Chem. Chem. Phys., vol. 19, no. 27, pp. 17967–17984, Jul. 2017, doi: 10.1039/C7CP01904A.
15. D. Mc Nulty, *"Synthesis, structure and electrochemical performance of V_2O_5 nanostructures as cathode materials for advanced lithium-ion batteries",* thesis, University of Limerick, 2014. doi: 10.34961/researchrepository-ul.23654103.v1.
16. A. S. Rao, B. S. Sannakashappanavar, A. Jayarama, and R. Pinto, *"Study of rectifying properties and true Ohmic contact on Sn doped V2O5 thin films deposited by spray pyrolysis method",* Results Chem., vol. 7, p. 101533, Jan. 2024, doi: 10.1016/j.rechem.2024.101533.
17. *Kim, H., Park, J., & Lee, S. (2016), "Optoelectronic and Electrochemical Properties of Vanadium Pentoxide Nanowires Synthesized by Vapor-Solid Process",* Accessed: Dec. 14, 2024. [Online]. Available: https://www.mdpi.com/2079-4991/6/8/140
18. J. Yao, Y. Li, R. C. Massé, E. Uchaker, and G. Cao, *"Revitalized interest in vanadium pentoxide as cathode material for lithium-ion batteries and beyond",* Energy Storage Mater., vol. 11, pp. 205–259, Mar. 2018, doi: 10.1016/j.ensm.2017.10.014.
19. D. Jha, B. Somapur, A. Paul, C. Kavitha, and N. Kambhala, *"Enhanced super capacitance performance of $V_2O_5{\cdot}nH_2O/g\text{-}C_3N_4$ nanocomposites: Synthesis, characterizations, and electrochemical properties",* Mater. Chem. Phys., vol. 332, p. 130244, Feb. 2025, doi: 10.1016/j.matchemphys.2024.130244.
20. S. Ruzgar, *"The effect of strontium doping on optoelectrical properties of V2O5/p-Si photodiode,"* Opt. Mater., vol. 157, p. 116087, Nov. 2024, doi: 10.1016/j.optmat.2024.116087.

Investigation of Structural and Magnetic Properties in Aluminium-Substituted Cobalt-Zinc Ferrite Metal Oxides

S. R. Sarve[1,a], K. G. Rewatkar[1,b], S. W. Awaghade[1,c], D. S. Bhowmick[2,d], A. N. Wazalwar[3,e], and P. B. Wasnik[3,f]

[1] *Vidya Vikas Arts Commerce & Science College, Samudrapur, Maharashtra, India.*
[2] *Arunrao Kalode Mahavidyalay, Nagpur, Maharashtra, India.*
[3] *Dr. Ambedkar College, Deekshabhoomi, Nagpur, Maharashtra, India.*

[a] sarve.sadanand@gmail.com
[b] kgrewatkar@gmail.com
[c] awaghadeshital87@gmail.com
[d] pakm.principal@gmail.com
[e] aartiwazalwar@yahoo.com
[f] pranaybwasnik@gmail.com

Abstract

In recent years, spinel ferrites have attracted considerable research interest due to their distinctive structural, magnetic and electrical properties, positioning them as promising candidates for a wide range of advanced technological applications. Aluminium substituted cobalt-zinc spinel ferrite with chemical composition $Co_{0.2}Zn_{0.8}Fe_{2-x}Al_xO_4$ (x = 0.0, 0.2, 0.4, 0.6, 0.8, 1.0) were synthesized by the sol-gel auto-combustion technique. The structural properties of the synthesized ferrites were studied by X-ray diffraction (XRD), Fourier transform infrared (FTIR) spectroscopy, energy dispersive X-ray (EDX) analysis, transmission electron microscopy (TEM) and magnetic properties were analyzed by vibrating sample magnetometry (VSM). XRD results confirmed the formation of a single-phase cubic spinel structure with a space group Fd-3m and particle sizes were in the range of 12 nm to 72 nm. The FTIR spectra showed distinct absorption bands around 570 cm^{-1} and 450 cm^{-1}, which were attributed to the stretching vibrations of metal-oxygen bonds at tetrahedral and octahedral sites, respectively. The magnetic studies demonstrated a progressive reduction in magnetic properties with increasing aluminium substitution concentration, culminating in the observation of superparamagnetic behavior at higher substitution levels. This behaviour is indicative of the significant influence of aluminium substitution on the magnetic characteristics of the material.

Keywords: Nano Size Ferrites, Spinel Structure, Sol-Gel Auto-Combustion, FTIR, VSM.
Received 29 January 2025; First Review 8 February 2025; Accepted 09 April 2025.

*** Address of correspondence**
S. R. Sarve
Vidya Vikas Arts Commerce & Science College, Samudrapur, Maharashtra, India.

Email: sarve.sadanand@gmail.com

How to cite this article
S. R. Sarve, K. G. Rewatkar, S. W. Awaghade, D. S. Bhowmick, Investigation of Structural and Magnetic Properties in Aluminium-Substituted Cobalt-Zinc Ferrite Metal Oxides, J. Cond. Matt. 2025; 03 (02): 100-106.

Available from:
https://doi.org/10.61343/jcm.v3i02.73

Introduction

Recently, metal-oxide nanoparticles have gained significant attention owing to their unique properties that distinguish them from bulk materials. Among these, spinel ferrites are particularly important in both industry and research because of their outstanding electrical and magnetic properties. Spinel ferrites have diverse applications in medicine, electronics, energy storage and environmental photocatalysis [1-3]. Zinc substituted cobalt ferrite nanoparticles are utilized in electronic devices such as transducers, transformers, and sensors due to their high magnetic, optical, and electrical properties [4-5]. Zinc ferrite nanomaterials with doped variants are the most suitable for magnetic hyperthermia therapy and targeted drug delivery because of their excellent biocompatibility and magnetic properties [6]. Therefore, research on non-magnetic doped cations in cobalt-zinc ferrite is crucial due to its potential benefits to society. Spinel-type ferrite is characterised by chemical formula MFe_2O_4 (M = Co, Ni, Mn, Mg, or different divalent cations) with interstitial tetrahedral (A) and octahedral (B) sites. The distribution of cations within these interstitial sites plays a crucial role in determining the essential properties of the ferrites [7-8]. Spinel ferrites are often categorized as normal, inverse or mixed depending on occupancy of divalent cations and Fe^{3+}

ions at interstitial sites. Mixed ferrites are regarded as important materials among these three categories due to their wide range of tunability in its properties. The spinel structure of $ZnFe_2O_4$ is normal, with all Fe^{3+} ions present in B sites and all Zn^{2+} ions in the A sites. In contrast, the spinel structure of $CoFe_2O_4$ is inverse, with Fe^{3+} ions distributed almost equally between the B and A sites and the Co^{2+} ions primarily in the B sites. Thus, cobalt zinc ferrite has a structure similar to mixed spinel [9-10]. The structural and magnetic characteristics of mixed spinel ferrites have been significantly impacted by the substitution of nonmagnetic Al^{3+} ions [11]. Over recent decades, multiple studies have been conducted to explore and enhance the magnetic and electrical properties of mixed ferrites through various synthesis techniques that involve substituting different divalent and trivalent cations. Several synthesis techniques, such as sol-gel auto-combustion [12], co-precipitation [13], hydrothermal [14], high-energy ball milling [15] and micro-emulsion [16] have been developed for synthesizing cobalt zinc ferrite nanoparticles. The sol-gel auto-combustion technique is particularly advantageous due to its ability to produce nanocrystallites with minimal contamination, low cost, high reactivity, straightforward processing and enhanced control over particle size and uniformity [17]. This study investigates the impact of aluminium substitution on the structural and magnetic properties of cobalt zinc ferrite ($Co_{0.2}Zn_{0.8}Fe_{2-x}Al_xO_4$, where x = 0.0, 0.2, 0.4, 0.6, 0.8, 1.0) synthesized via the sol-gel auto-combustion method. The synthesized samples were characterized using X-ray diffraction (XRD), transmission electron microscopy (TEM), energy-dispersive X-ray spectroscopy (EDX), Fourier transform infrared spectroscopy (FTIR), and vibrating sample magnetometry (VSM). The obtained results are systematically analysed and discussed in this paper. Overall, this study contributes valuable insights into the influence of Al doping on the properties of cobalt zinc ferrite, offering potential pathways for the customization of ferrites in various applications.

Method

Nanoparticles of aluminium-substituted cobalt zinc ferrite, with the chemical composition $Co_{0.2}Zn_{0.8}Fe_{2-x}Al_x O_4$ (where x = 0.0, 0.2, 0.4, 0.6, 0.8, 1.0), were synthesized using the sol-gel microwave assisted auto-combustion method. The precursor materials included cobalt nitrate hexahydrate, zinc nitrate hexahydrate, ferric nitrate nonahydrate and aluminium nitrate nonahydrate, all of analytical reagent (AR) grade with 99% purity, procured from Merck. Urea was used as a fuel in a stoichiometric ratio. The metal nitrates and urea were dissolved in deionized water to form a homogeneous gel solution, which was continuously stirred using a magnetic stirrer at 70°C until gel formation. The formed gel spontaneously ignited in a microwave oven, producing a loose powder. This powder was then finely ground using a mortar and pestle and annealed at 800°C for 4 hours to obtain the final nanoparticle phase.

The characterization of the synthesized samples was conducted using various analytical techniques. Fourier Transform Infrared Spectroscopy (FTIR) was performed using a Bruker 3000 Hyperion Microscope with a Vertex 80 FTIR System. Powder X-ray diffraction (XRD) analysis was carried out using Rigaku Miniflex 1800 with Cu-Kα radiation (operating at 40 kV and 15 mA) over a 2θ range of 10°–80°. For elemental microanalysis, a JEOL JSM-7600F Field Emission Gun-Scanning Electron Microscope (FEG-SEM) equipped with an Energy Dispersive X-ray Spectroscopy (EDS) detector was used. Transmission electron microscopy (TEM) was performed using Tecnai G2 F30 Field Emission Gun-Transmission Electron Microscope (FEG-TEM) operating at 300 kV for high-resolution imaging. Finally, magnetic measurements were conducted at room temperature using a Lakeshore 7410S Vibrating Sample Magnetometer (VSM).

Result and Discussion

FTIR Analysis

FTIR spectroscopy is a valuable technique for analysing cation distribution in spinel ferrites, as well as lattice vibrational modes. Figure 1 shows the infrared spectra of $Co_{0.2}Zn_{0.8}Fe_{2-x}Al_xO_4$ in frequency range 400-4000 cm^{-1}.

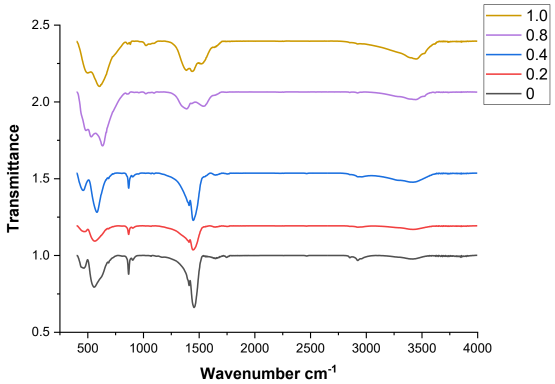

Figure 1: FT-IR spectrum of $Co_{0.2}Zn_{0.8}Fe_{2-x}Al_xO_4$.

Tetrahedral and octahedral clusters are identified by the existence of distinctive absorption bands in the frequency range of 450 cm^{-1} and 570cm^{-1}, that validate the stretching vibration resulting from interaction between the oxygen atom and cations in tetrahedral and octahedral sites in the spinel lattice structure [18]. The values of the corresponding bands have been presented in Table 1. It is found that both tetrahedral and octahedral vibrational frequencies shift towards higher frequencies as the Al^{3+} ions' concentration increases. This shift indicates changes in force constants and bond lengths within the lattice as well as the expansion of sites due to cation migration among them. The following relation is used to calculate the force constant values.

$$K= 4\pi^2c^2\nu^2\mu \qquad (1)$$

Where c = speed of light, ν denotes the vibrational frequency. The reduced mass μ is calculated by finding molecular weight of cations in octahedral sites, tetrahedral sites and oxygen atom. Where K_t and K_o is the force constant in accordance with both the sites i.e., tetrahedral and octahedral and K_a is the average force constant. In the Al-substituted cobalt zinc ferrite, we observe notable trends in band edge positions and force constants as shown in Table 1.

Table 1: The absorption bands (ν_1, ν_2) and force constant (K_t, K_0) in $Co_{0.2}Zn_{0.8}Fe_{2x}Al_xO_4$.

x	Position of band edge, cm^{-1}		Force constants, N/m		
	ν_1	ν_2	K_t	K_o	K_a
0	462.9	556.93	161.4	254.23	207.815
0.2	467.14	563.45	157.55	258.54	208.045
0.4	459.16	582.12	143.15	273.98	208.565
0.6	476.93	594.05	139.82	282.84	211.33
0.8	483.34	632.72	118.96	318.05	218.505
1	500.89	604.31	76.3	287.14	181.72

The low-frequency band (ν_1) fluctuates initially but generally increases, indicating changes in cation distribution and lattice dynamics, while the high-frequency band (ν_2) consistently rises, suggesting lattice stiffening due to Al^{3+} ions. The tetrahedral force constant (K_t) decreases significantly, implying weaker tetrahedral bonds as Fe^{3+} is replaced by Al^{3+}. The octahedral force constant (K_o) initially increases, peaking at x = 0.8, before decreasing, indicating structural imbalance. The average force constant (K_a) follows a similar trend. Moderate Al substitution (x ≈ 0.6 - 0.8) stabilizes the lattice, while excessive substitution weakens it.

X-RD Patterns Analysis

The X-ray diffraction patterns of Al-substituted cobalt-zinc ferrite ($Co_{0.2}Zn_{0.8}Fe_{2-x}Al_x O_4$; x = 0.0, 0.2, 0.4, 0.6, 0.8, 1.0) confirm the formation of a single-phase spinel ferrite structure. Figure 2 presents the diffraction patterns, where the most intense reflection is observed for the (311) plane, along with additional peaks corresponding to the (220), (400), (422), (511), and (440) planes. These characteristic reflections indicate the formation of a cubic spinel structure with the Fd-3m space group [19].

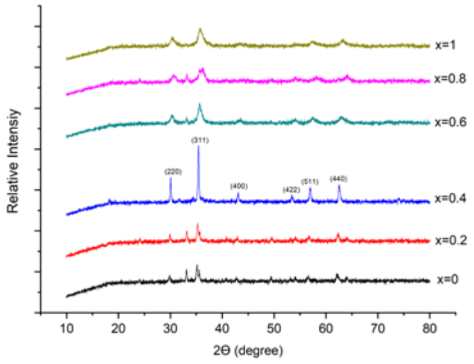

Figure 2: X-RD Pattern for $Co_{0.2}Zn_{0.8}Fe_{2-x}Al_xO_4$ (x = 0.0, 0.2, 0.4, 0.6, 0.8,1.0).

The absence of secondary phases suggests the successful incorporation of Al^{3+} ions into the ferrite lattice without disrupting its fundamental structure, making the material suitable for further investigation. All the peaks in the diffraction are indexed and refined by Powder X software. The crystallite size (D) of the samples was determined using the Debye-Scherrer equation (2).

$$D = \frac{0.89\lambda}{\beta\ \mathrm{Cos}\theta} \qquad (2)$$

where λ is the X-ray wavelength, β represents the full-width at half-maximum (FWHM) of the (311) peak, and θ is the Bragg diffraction angle [20]. The calculated crystallite sizes for different compositions are presented in Table 2. The results show that crystallite size varies significantly with Al^{3+} substitution, initially increasing and then decreasing at higher concentrations.

Table 2: Structural parameters of $Co_{0.2}Zn_{0.8}Fe_{2-x}Al_xO_4$.

(x)	Crystallite size (nm)	Interplanar spacing d (A^0)	Lattice Constant a (A^0)	X-ray density ρ_m (g/cm³)
x=0	47	2.5497	8.4566	0.3766
x= 0.2	48	2.5406	8.4263	0.3689
x= 0.4	72	2.5323	8.3987	0.3610
x= 0.6	17	2.5112	8.3288	0.3545
x= 0.8	12	2.4878	8.2513	0.3456
x= 1.0	13	2.5139	8.3379	0.3329

The initial increase in crystallite size (x = 0.4) suggests that Al^{3+} enhances grain growth up to a certain limit. The sharp decrease in crystallite size at x ≥ 0.6 indicates that excessive Al^{3+} substitution inhibits crystal growth, possibly due to lattice distortion and increased strain. This trend implies that aluminium incorporation inhibits grain growth at higher concentrations by introducing lattice strain and increasing nucleation sites, resulting in finer crystallite sizes. The lattice constant (a), determined using interplanar spacing (d) through Bragg's law, shows a systematic decrease with increasing Al^{3+} concentration, as presented in Table 2. The observed contraction in lattice constant is attributed to the smaller ionic radius of Al^{3+} (0.59 Å) compared to Fe^{3+} (0.63 Å) [21]. As Fe^{3+} ions are progressively replaced by Al^{3+} ions, the shorter bond lengths lead to an overall reduction in lattice size. The slight increase at x = 1.0 suggests a possible rearrangement of cations within the spinel lattice. The X-ray density (ρ_x) was calculated using the formula:

$$\rho_x = \frac{8\,M}{N_A\ a^3} \qquad (3)$$

where M is the molecular weight of the sample, N_A is Avogadro’s number, and a is the lattice parameter. The calculated X-ray density values, presented in Table 2, show a continuous decline with increasing Al^{3+} substitution. This continuous decrease in X-ray density is primarily due to the lower atomic weight of Al^{3+} (26.98 g/mol) compared to Fe^{3+} (55.85 g/mol). As Al^{3+} replaces Fe^{3+} in the lattice, the overall molecular weight of the unit cell decreases, leading to a corresponding reduction in X-ray density. This trend further confirms the successful incorporation of Al^{3+} ions into the ferrite structure and the associated lattice contraction. The XRD study indicate that moderate Al^{3+} substitution (x = 0.4–0.6) promotes crystallinity, while higher concentrations ($x \geq 0.8$) induce lattice distortion and grain refinement, affecting the overall microstructural stability of Co-Zn ferrite.

EDS Analysis

The elemental composition of aluminium-substituted cobalt zinc ferrites, was analysed using energy dispersive X-ray (EDS) spectroscopy.

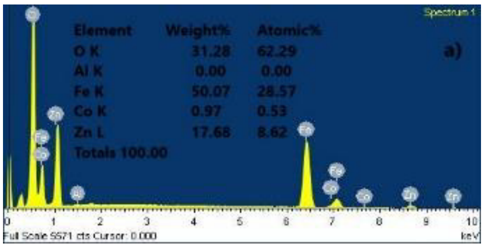

Element	Weight%	Atomic%
O K	31.28	62.29
Al K	0.00	0.00
Fe K	50.07	28.57
Co K	0.97	0.53
Zn L	17.68	8.62
Totals 100.00		

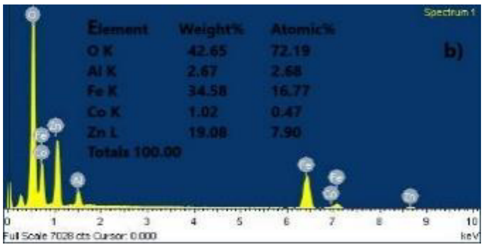

Element	Weight%	Atomic%
O K	42.65	72.19
Al K	2.67	2.68
Fe K	34.58	16.77
Co K	1.02	0.47
Zn L	19.08	7.90
Totals 100.00		

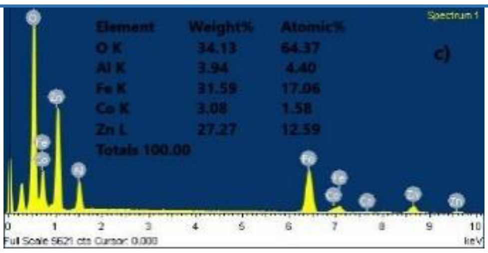

Element	Weight%	Atomic%
O K	34.13	64.37
Al K	3.94	4.40
Fe K	31.59	17.06
Co K	3.08	1.58
Zn L	27.27	12.59
Totals 100.00		

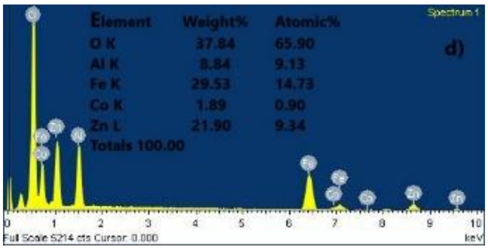

Element	Weight%	Atomic%
O K	37.84	65.90
Al K	8.84	9.13
Fe K	29.53	14.73
Co K	1.89	0.90
Zn L	21.90	9.34
Totals 100.00		

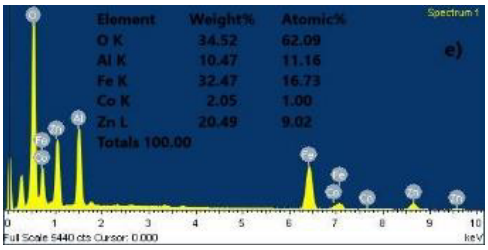

Element	Weight%	Atomic%
O K	34.52	62.09
Al K	10.47	11.16
Fe K	32.47	16.73
Co K	2.05	1.00
Zn L	20.49	9.02
Totals 100.00		

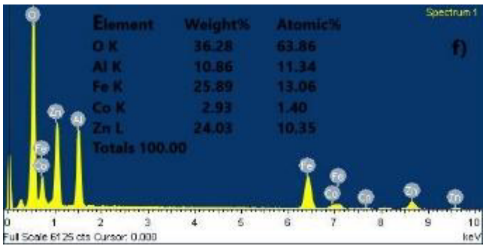

Element	Weight%	Atomic%
O K	36.28	63.86
Al K	10.86	11.34
Fe K	25.89	13.06
Co K	2.93	1.40
Zn L	24.03	10.35
Totals 100.00		

Figure 3: Energy dispersive X-ray analysis spectra of $Co_{0.2}Zn_{0.8}Fe_{2-x}Al_xO_4$ (a) x = 0 (b) x = 0.2 (c) x = 0.4 (d) x = 0.6 (e) x = 0.8 and (f) x = 1.00 samples.

The characteristic EDS spectra, shown in Figure 3(a)–(f), confirm the presence of Co, Zn, Fe, Al, and O elements, indicating the successful incorporation of aluminium into the ferrite lattice.

The experimentally obtained elemental percentages closely align with the nominal composition, validating the accuracy of the synthesis process. Furthermore, the absence of significant material loss or extraneous elements within the detection limits ensures the high purity and compositional integrity of the synthesized samples.

TEM Analysis

According to the HRTEM images, the obtained sample's particles are agglomerated and have a size that is entirely consistent with the information obtained from the X-RD investigations.

The agglomeration is due magnetic nature of the sample and large surface to volume ratio.

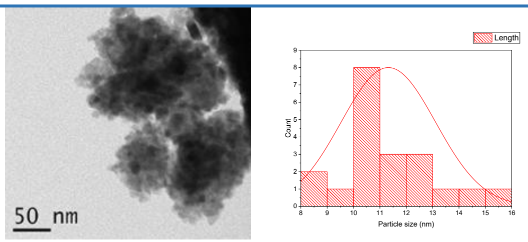

Figure 4: TEM Image of $Co_{0.2}Zn_{0.8}Fe_{2-x}Al_xO_4$ (x=0.6) and Histogram.

The Figure 4 indicates the HRTEM image of synthesised sample for the composition x=0.6 its particle size distribution histogram.

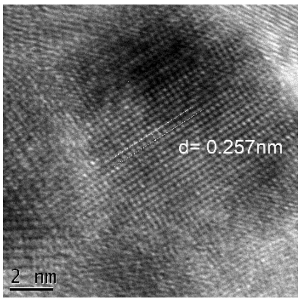

Figure 5: HR TEM Image of $Co_{0.2}Zn_{0.8}Fe_{2-x}Al_xO_4$ (x=1.0).

The Figure 5 gives the HRTEM image for the composition x= 1.0 at the scale of 2nm indicates the crystalline nature with interplanar spacing equal to 0.257nm, which is closely matched with the data of X-ray diffraction.

Magnetic Measurement

The typical hysteresis loop of $Co_{0.2}Zn_{0.8}Fe_{2-x}Al_xO_4$ with varying composition of x are shown in Figure.5 there is gradual decrease in saturation magnetization (M_S) from 5.444 emu/g to 1.799 emu/g with negligible value of coercivity (H_C) from 8.2353 Oe to 1.3504 Oe. The spinel ferrite's A-site and B-site cation occupancy and exchange interaction strength causes the variation in saturation magnetization (M_s).

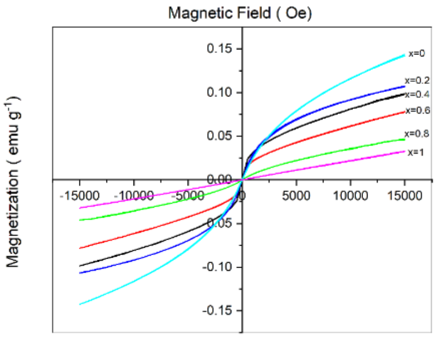

Figure 5: Hysteresis loop of $Co_{0.2}Zn_{0.8}Fe_{2-x}Al_xO_4$.

Tetrahedral A-site magnetism in spinel ferrite is anti-parallel to octahedral B-site magnetization. Neel's molecular field model indicates that A–B super-exchange interactions predominate over the A–A and B–B interactions [22].

The equation (4) provides net magnetic moment in ferrites.

$$n_B(x) = M_B(x) - M_A(x) \qquad (4)$$

The B- and A-sublattice magnetic moments in Bohr magneton (μB) are represented as $M_B(x)$ and $M_A(x)$, correspondingly. The saturation magnetization depends on the concentration of aluminium, and it is found that as aluminium' concentration increases, saturation magnetization decreases. The lower magnetic moment of the Al^{3+} ion relative to the Fe^{3+} ion (5μB) is the cause of this declining tendency. Based on particle sizes that ranged from 17nm to 12nm, the decline in saturation magnetization with $x > 0.4$ can also be elucidated. As the size of the grains increases, their contribution reduces, and Neel's two sub lattices indicate that the magnetization value surpasses the theoretical limit. The relationship between coercivity (Hc) and grain size can be understood through the domain structure, critical diameter, and crystal anisotropy. Due to thermal factors, coercivity in single domain region falls as grain size decreases. In single domain region, the coercivity H_c is given following equation.

$$H_c = g - \frac{h}{D^2} \qquad (5)$$

Where g and h are constants. 'D' represents particle diameter [23]. Even at the greatest applied magnetic fields, the single domain structure with superparamagnetic nature is indicated by the negligible values of coercive field and remanence magnetization (M_r) and the lack of full saturation.

Conclusion

The Aluminium-substituted Cobalt Zinc Ferrite, $Co_{0.2}Zn_{0.8}Fe_{2-x}Al_x O_4$ (x = 0.0, 0.2, 0.4, 0.6, 0.8, 1.0), was successfully synthesized using the sol-gel microwave-assisted auto-combustion method. The infrared spectrum, displaying fundamental peaks at 450 cm^{-1} and 570 cm^{-1}, confirms the formation of metal oxide bonds in the synthesized mixed ferrite. X-ray diffraction analysis identified a single-phase cubic spinel structure with the Fd-3m space group, exhibiting particle sizes ranging from 12 nm to 72 nm. Magnetic measurements reveal a superparamagnetic nature characterized by a single domain structure and a negligible coercivity value of 1.3504 Oe, particularly in particles as small as 12 nm. The study demonstrates that Aluminium substitution leads to lattice contraction and enhanced crystallinity up to an optimal concentration of x = 0.6; higher concentrations result in lattice distortion and inhibited crystal growth due to induced stress and altered cation distributions. Furthermore, the non-magnetic nature of Aluminium dilutes the overall magnetic properties of the material, affecting saturation magnetization and coercivity. Thus, controlled Al^{3+} doping is essential for optimizing the structural and magnetic characteristics of ferrites, making it significant for tailored industrial applications.

Acknowledgement

The authors are grateful to Sophisticated Analytical Instrumentation Facility (SAIF) at the Indian Institutes of Technology in Bombay and Chennai for their essential support in the characterization of our synthesized samples. Their contributions were pivotal to the advancement of our research.

References

1. Hgjh Vinosha, P., Manikandan, A., Ceicilia, A., Dinesh, A., Nirmala, F., Preetha, A., Slimani, Y., Almessiere, M., Baykal, A., & Xavier, B. (2021), "*Review on recent advances of zinc substituted cobalt ferrite nanoparticles: Synthesis characterization and diverse applications", Ceramics International, 47, 10512-10535. https://doi.org/10.1016/J.CERAMINT.2020.12.289.
2. Chahar, D., Taneja, S., Bisht, S., Kesarwani, S., Thakur, P., Thakur, A., & Sharma, P. (2021), *"Photocatalytic activity of cobalt substituted zinc ferrite for the degradation of methylene blue dye under visible light irradiation"*, Journal of Alloys and Compounds, 851, 156878. https://doi.org/10.1016/j.jallcom.2020.156878.
3. Sahoo, P., Choudhary, P., Laha, S., Dixit, A., & Mefford, O. (2023), *"Recent advances in zinc ferrite ($ZnFe_2O_4$) based nanostructures for magnetic hyperthermia applications"*, Chemical communications. https://doi.org/10.1039/d3cc01637d.
4. Jnaneshwara, D., Avadhani, D., Prasad, B., Nagabhushana, B., Nagabhushana, H., Sharma, S., Prashantha, S., & Shivakumara, C. (2014), *"Effect of zinc substitution on the nanocobalt ferrite powders for nanoelectronic devices"*, Journal of Alloys and Compounds, 587, 50-58. https://doi.org/10.1016/J.JALLCOM.2013.10.146.
5. Sathiyamurthy, K., Rajeevgandhi, C., Guganathan, L., Bharanidharan, S., & Savithiri, S. (2021), *"Enhancement of magnetic, supercapacitor applications and theoretical approach on cobalt-doped zinc ferrite nanocomposites"*, Journal of Materials Science: Materials in Electronics, 32, 11593 - 11606. https://doi.org/10.1007/s10854-021-05764-2.
6. Shaterabadi, Z., Nabiyouni, G., Asadi, Z., Iglesias, G., & Soleymani, M. (2023), *"Enhanced magnetic hyperthermia efficiency in poly vinyl alcohol-coated zinc-substituted cobalt ferrite nanoparticles: Correlated effects of zinc content and applied magnetic field strength"*, Ceramics International. https://doi.org/10.1016/j.ceramint.2023.08.088.
7. H S Ahamad, N. S. (2017), *"Structural properties of $Cu_xNi_{1-x}Fe_2O_4$ nano ferrites prepared by urea-gel microwave auto combustion method"*, Ferroelectrics, 516(1), 146-160. https://doi.org/10.1080/00150193.2017.1362285.
8. Sathiya Priya, D. G. (2019), *"Effect of Al substitution on the structural, electric and impedance behavior of cobalt ferrite"*, Vacuum, 160, 453-460. https://doi.org/10.1016/j.vacuum.2018.12.004.
9. Akshay B. Kulkarni, S. N. (2019), *"Variation in structural and mechanical properties of Cd-doped Co Zn ferrites"*, Volume 2, Issue 3,2019, Pages 455 462, ISSN 2589-2991, Materials Science for Energy Technologies, 2(3), 455-462. https://doi.org/10.1016/j.mset.2019.03.00.
10. N. N. Sarkar, S. A. (2019), *"Effect of Cobalt and Nickel Substitution on Structural and Magnetic Properties of Spinel Ferrite"*, Integrated Ferroelectrics, 203(1), 61 66. https://doi.org/10.1080/10.
11. Sathiya Priya, D. G. (2019), *"Effect of Al substitution on the structural, electric and impedance behavior of cobalt ferrite"*, Vacuum, 160, 453-460. https://doi.org/10.1016/j.vacuum.2018.12.004.
12. P. S. Hedaoo, D. B. (2019), *"Structural and Magnetic Studies of Zn Doped Nickel Nanoferrites Synthesize by Sol-gel Auto Combustion Method"*, Materials Today: Proceedings, 15(3), 416-423. https://doi.org/10.1016/j.matpr.2019.04.102.
13. Uzma, G., Ayesha, R., Zarfa, L, & Kainat, K. (2020). *"Effect of Synthesis Techniques on the Structural Properties of Cobalt doped Zinc Nano-Ferrites"*, International Journal of Engineering Research and, 9. https://doi.org/10.17577/IJERTV9IS030067.
14. Coppola, P., Silva, F., Gomide, G., Paula, F., Campos, A., Perzynski, R., Kern, C., Depeyrot, J., & Aquino, R. (2016), *"Hydrothermal synthesis of mixed zinc–cobalt ferrite nanoparticles: structural and magnetic properties"*, Journal of Nanoparticle Research, 18, 1-15. https://doi.org/10.1007/s11051-016-3430-1.
15. Sinha, M., & Pradhan, S. (2010), *"Synthesis of nanocrystalline Cd–Zn ferrite by ball milling and its stability at elevated temperatures"*, Journal of Alloys and Compounds, 489, 91-98.

https://doi.org/10.1016/J.JALLCOM.2009.09.019.

16. Viet, T., Hong, C., Quoc, T., & Dac, T. (2020), *"Study on synthesis and characterization of nano scale spinel* $Mn_{0.5}Fe_{2.5}O_4$ *by micro-emulsion method"*, Vietnam Journal of Catalysis and Adsorption. https://doi.org/10.51316/JCA.2020.066.
17. Tianfu, H., Qiu, Z., Hu, Z., & Lu, X. (2021), *"Novel method of preparing hierarchical porous* $CoFe_2O_4$ *by the citric acid-assisted sol-gel auto-combustion for supercapacitors",* Journal of energy storage, 35, 102286. https://doi.org/10.1016/J.EST.2021.102286.
18. Rathod, V., Anupama, A., Kumar, R., Jali, V., & Sahoo, B. (2017), *"Correlated vibrations of the tetrahedral and octahedral complexes and splitting of the absorption bands in FTIR spectra of Li-Zn ferrites"*, Vibrational Spectroscopy, 92, 267-272. https://doi.org/10.1016/J.VIBSPEC.2017.08.008.
19. Humbe, A., Kounsalye, J., Shisode, M., & Jadhav, K. (2017), *"Rietveld refinement, morphology and superparamagnetism of nanocrystalline* $Ni_{0.70-x}Cu_xZn_{0.30}Fe_2O_4$ *spinel ferrite"*, Ceramics International, 44, 5466-5472. https://doi.org/10.1016/J.CERAMINT.2017.12.180.
20. Cullity, B. D. (1976). Elements of X-raydiffraction. Addison-Wesley Publishing Co. Inc.
21. Ramesh, C., Maniysundar, K., & Selvanandan, S. (2016), *"Structural and magnetic study on al substituted MgZn mixed ferrite powders prepared by sol-gel method"*, Materials Today: Proceedings, 3, 1363-1369. https://doi.org/10.1016/J.MATPR.2016.04.016.
22. Smart, J. S. (1955). The Néel Theory of Ferrimagnetism. Am. J. Phys., 23(6), 356-370. https://doi.org/10.1119/1.1934006.
23. Li, Q., Kartikowati, C., Horie, S., Ogi, T., Iwaki, T., & Okuyama, K. (2017), *"Correlation between particle size/domain structure and magnetic properties of highly crystalline* Fe_3O_4 *nanoparticles",* Scientific Reports, 7. https://doi.org/10.1038/s41598-017-09897-5.

An Effective Supramolecular Mg(II)-Metallohydrogel based Non-Volatile Memory Device with Supreme Endurance

Arpita Roy and Soumya Jyoti Ray[a]

Department of Physics, Indian Institute of Technology Patna, Bihar-801106, India.

[a]ray@iitp.ac.in

Abstract

Traditional computer systems are becoming unable to handle the needs of upcoming data-intensive applications. Resistive random access memory devices (RRAM), which offers a potential advancement in existing computing design, are preferred as promising alternatives for the application in neuromorphic computing. In this work supramolecular Mg(II)-based metallohydrogel, referred as Mg@5AP was synthesized by 5amino 1pentanol as Low Molecular Weight Gelator (LMWG) at normal temperature. From scanning and transmission electron microscopy (FESEM and TEM), we observed a unique network of rectangular, pebble-like structures within Mg@5AP. From Fourier-transform infrared (FT-IR) spectroscopy, we identified organic compounds which were present in this metallohydrogel. Here, we prepared schottky diode with the configuration of metal-semiconductor-metal using Mg@5AP. To investigate its charge transportation property, we developed Mg@5AP based RRAM device with lateral and vertical configurations which exhibited a bipolar resistive switching behavior. Behind this switching mechanism, formation and rapture of conduction filament between two electrodes were responsible. It demonstrated impressive endurance with a high ON/OFF ratio (~120) upto 5000 switching cycles. Here, 2×2 crossbar array based on Mg@5AP was also prepared to demonstrate logic gate operation. In this work, it was confirmed that it worked as in-memory computing where storage and processing both were occurred simultaneously. Therefore, it provided a cost-effective and environmentally friendly alternative to conventional heavy metal-based memory systems for high-performance data storage.

Keywords: Supramolecular Mg(II) metallogel, Schottky Diode, Resistive Switching, Conduction filament, Neuromorphic computing.

Received 30 January 2025; First Review 8 April 2025; Accepted 18 April 2025.

*** Address of correspondence**
Soumya Jyoti Ray
Department of Physics, Indian Institute of Technology Patna, Bihar-801106, India.

Email: ray@iitp.ac.in

How to cite this article
Arpita Roy and Soumya Jyoti Ray, An Effective Supramolecular Mg(II)-Metallohydrogel based Non-Volatile Memory Device with Supreme Endurance, J. Cond. Matt. 2025; 03 (02): 107-113.

Available from:
https://doi.org/10.61343/jcm.v3i02.104

Introduction

A supramolecular metallogel [1-3] refers to a gel designed by the self-assemble of metal ions or metal by non-covalent interactions such as H-bonding, π-π stacking, van der Waals force. Unlike traditional gels formed by covalent bonds, supramolecular gels are held together by these reversible interactions, allowing for dynamic and versatile properties. Molecules in these gels organize themselves into a 3d network, trapping solvent or liquid within this structure. Besides this, low molecular weight gelator (LMWG) is a small molecule which is capable of forming gels by self-assembly at relatively low concentrations. They have the unique ability to form gel networks through non-covalent interactions. In this work, 5amino 1pentanol serve pivotal role as a LMWG within this metallohydrogel. There are lots of applications of this metallogel in diverse fields such as sensors, memory gadgets, catalysis, semiconducting diodes, magnetic performance etc.

Here, we have successfully synthesized a novel mechanically stable metallogel using 5amino 1pentanol only as single LMWG and Mg(II) metal ions sourced in N, N-dimethylformamide solvent. Notably, we accomplished this without any requirement of additional supporting ligands. This work mainly highlights the capability of metallogels to contribute as a crucial component in constructing metal-semiconductor (MS) junction devices exhibiting Schottky barrier properties and non-volatile memory device functionalities [4-6]. Owing to its compatibility with CMOS design, simple configuration, cost-effectiveness, low power consumption [4], fast data transfer speed, stability [7], reliability [8], resistive random-access memory (RRAM) technology [9-13] is advantageous for upcomimg generation memory design, and also neuromorphic [14-15] and in memory computing [16,17]. Recently, researchers have already demonstrated switching performance of transition metal oxide-based RRAM device [18-21]. Nevertheless, researchers seek alternative devices

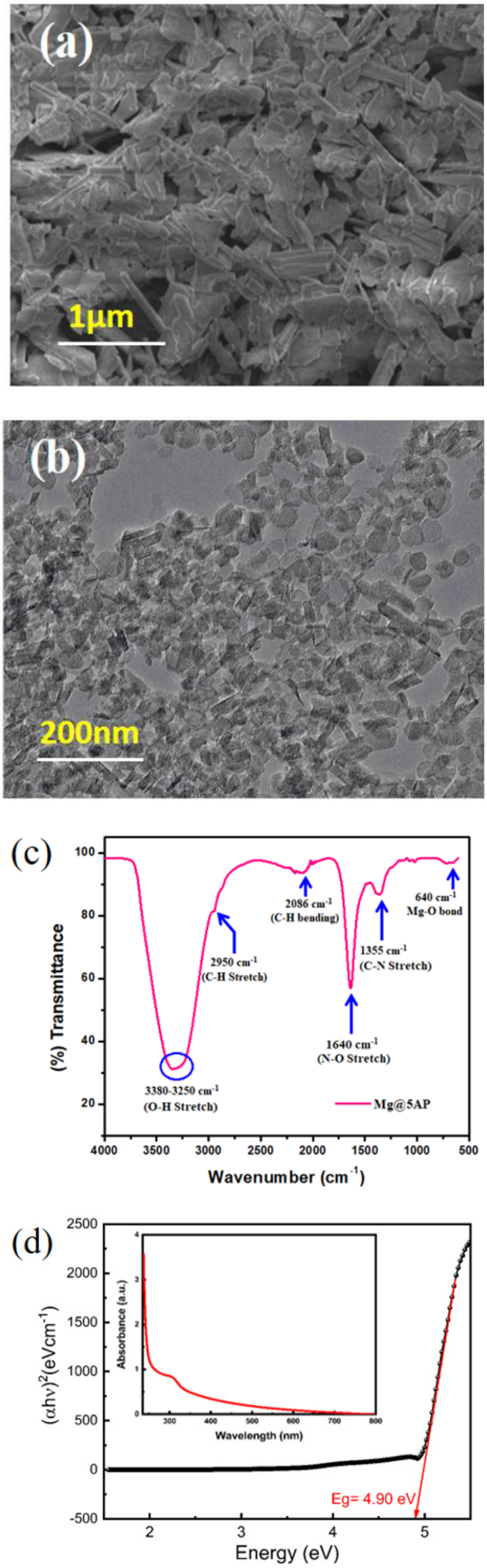

Figure 1: (a) FESEM pattern of Mg@5AP metallogel, **(b)** TEM image of Mg@5AP metallogel, **(c)** FT-IR spectra of Mg@5AP, **(d)** Tuac's plot for Mg@5AP metallogel and UV-Vis absorption spectra (inset).

to enhance the switching performance, with metallogel presenting potential due to their semiconducting behavior and capacity for device fabrication. Our research begins by introducing the key synthetic strategies and characterization methods for Mg(II) based metallogel. Next, it provides an overview of this metallogel-based memristive material and their commonly used switching mechanisms. Moreover, flexible electrical and optoelectronic devices with memory, sensing, and optical detecting capabilities can be made by developing metallohydrogel-based RRAM structures on flexible substrates.

However, memristors hold significant applications in designing logic gate circuits because of their nonlinearity and non-volatility [22-23]. This work provides a clear outline of logic gate and assesses their part in the memory related application. Here, we have demonstrated the applications of this device in memristor arrays for logic implementation. The work also explores recent advancements in metallogel based memristor for neuromorphic computing, data storage, artificial synapses, logic circuit etc. At last, it discusses the experiments, development trends, and future perspectives by offering a guidance for development of efficient supramolecular Mg(II)-metallogel based memristors and their applications in information technology.

Methodology

1. Material

Magnesium Nitrate Hexahydrate and 5amino 1pentanol were used to synthesize the metallohydogel (Mg@5AP). Both chemicals were utilized in their as-received state without additional purification. Double-distilled water was consistently used in all experiments.

2. Preparation of Mg(II) metallohydrogel (Mg@5AP)

A 500 µL clear solution containing $Mg(NO_3)_2 \cdot 6H_2O$ (0.256 g, 1 mM) and 500 µL of 5amino 1pentanol are rapidly combined within 5 mL glass vial at normal temperature. Following a gentle shaking of this vial, a white-coloured Mg@5AP is instantly created.

3. Fabrication of device

We created a device with a Schottky diode structure with lateral configuration such as ITO /Mg@5AP/ITO (Device 1) (Fig. 2(a)) to show their electrical behavior in this study. To create MS junction, we have drop-casted Mg@5AP metallogel on an ITO (Indium Tin Oxide) substrate. ITO is a perfect material for photo-excitations because it is both an excellent electrode and transparent substance optically in visible area. We also fabricated two RRAM devices with vertical configurations of ITO/Mg@5AP/Cu (Device 2) (as shown in Fig. 3(a): inset) and Cu/Mg@5AP/Cu (Device 3)

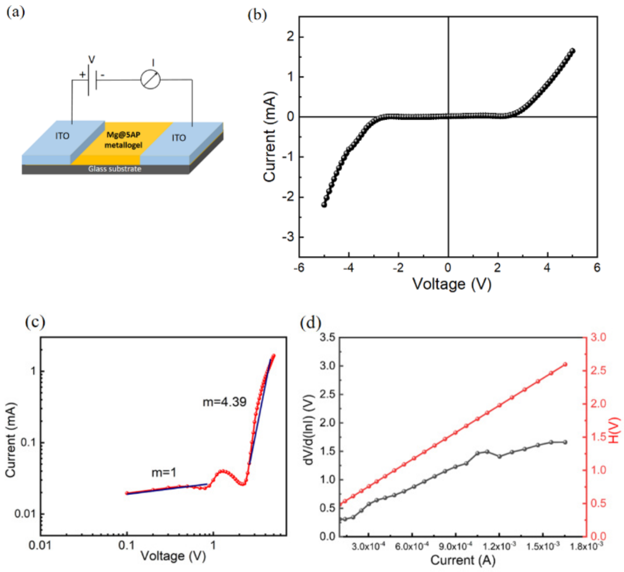

Figure 2: **(a)** Representation of Mg@5AP based-device-(ITO/Mg@5AP/ITO), **(b)** IV curve for same device on linear scale, **(c)** IV curve on logarithmic scale, **(d)** H versus. I graph; dV/d(ln I) versus. I graph for same device.

(as shown in Fig. 4(a): inset) to develop RRAM device. In both configurations, Mg@5AP was deposited onto the substrate (bottom electrode). Then, the topmost electrode (Cu) is kept onto the material for making this device.

Outcomes

1. Structural Analysis of Mg@5AP metallohydrogel

FESEM and TEM images of Mg@5AP metallogel shows a distinctive hierarchical network of flake-like patterns which are shown in Fig.1 (a,b) respectively. EDX mapping further corroborates the composition of the network which confirms the existence of carbon (C), oxygen (O), nitrogen (N), magnesium (Mg) arising from $Mg(NO_3)_2$, 5-amino-1-pentanol and DMF molecules (as shown Fig.S1).

2. Analysis of Fourier Transform Infrared Spectra (FT-IR) of Mg@5AP metallohydrogel

FT-IR spectra of the Mg@5AP provides insights into the primary interactions between 5amino 1pentanol and the source of Mg(II) in this gel formation (Fig. 1(c)). Within this spectrum, broad peaks within 3380-3230 cm^{-1} correspond to O-H- stretching, while peaks at 2950 cm^{-1} and 2086 cm^{-1} are corresponded to C-H- stretching vibrations, C-H- bending vibrations respectively. Additionally, 1640 cm^{-1} and 1355 cm^{-1} correspond to N-O- stretching and C-N stretching respectively. Furthermore, to understand the robustness of the interaction between 5amino 1pentanol and the solution of magnesium nitrate, an observable peak at 640 cm^{-1} is identified (Fig. 1(c)). This specific peak signifies the presence of Mg-O bonds, providing further confirmation of the metallohydrogelation process.

3. Optical characterization

To establish the optical behaviour of the synthesised Mg@5AP, Ultra-violet-visible spectra (inset of Fig. 1(d)) were analysed using the Tuac's Plot, as shown in Fig. 1(d). A wavelength range from 250 nm to 800 nm was taken for the measurement. From the UV-vis spectrum, we used Tauc's equation (1) to estimate the direct bandgap (E_g) of this metallogel Mg@5AP:

$$(\alpha h\nu)^n = A\,(h\nu - E_g) \qquad (1)$$

Where α = Coefficient of Absorption, E_g = band gap, h = Planck's constant, and ν = frequency of the light. In the processes, "n" is the constant (n=2); "A" is also constant (A=1). We determined E_g, which is 4.90 eV, by ranging the linear area of the plot $(\alpha h\nu)^2$ versus hν (Fig. 1(d)) up to the region where there is no absorption. This type of high bandgap materials typically absorb less in the visible spectrum which makes the device more optically transparent. This is useful in transparent electronics, UV photodetectors, and solar cells with wide-spectrum coverage. They are often more thermally stable, which could make the device suitable for use in high-temperature or harsh environmental conditions. This also leads to lower leakage currents and better control over charge transport, which is beneficial for low-power electronic applications.

4. Electrical Characterization of Device

In order to provide an accurate measurements of the material's semiconductor nature, the charge transportation properties of Mg@5AP based RRAM devices are done by two-probe arrangements. I-V curve of ITO/Mg@5AP/ITO (device-1) in the voltage (-5 V to +5V) is displayed in Fig. 2(b) on linear scale. In both +ve and -ve polarity, the current increased with voltage beyond this region. By using thermionic emission theory (TE Theory), Schottky diode parameters are derived from the IV curve. Cheung [24] proposed this technique. The equations (2-3) are used to evaluate the measured IV curve:

$$I = I_0 \, exp\left(\frac{qV}{\eta k_B T}\right)\left[1 - exp\left(\frac{-qV}{\eta k_B T}\right)\right] \qquad (2)$$

$$I_0 = A\,A^*\,T^2 \, \exp\left(\frac{-q\phi_B}{k_B T}\right) \qquad (3)$$

Here, I_0 = Current of saturation; q = Charge of electron; k_B = Boltzmann Constant; T = Temp; V = Voltage; Φ_B = Height of barrier potential; A = Effective Area of Diode; R_S = Resistance in series; η = Factor of ideality; A* = Effective Richardson Constant (~32 $AK^{-2}cm^{-2}$).

Here, log(I) versus. log(V) graph is plotted (Fig. 2(c)) to define the conduction mechanism. At lower voltage zone, it followed Ohomic conduction with the slope of 1; but in higher voltage region, it followed Space-Charge-Limited Conduction mechanism with the slope of m=4.39.

$$\frac{dV}{d(\ln I)} = \left(\frac{\eta k_B T}{q}\right) + IR_S \tag{4}$$

$$H(I) = V - \left(\frac{\eta k_B T}{q}\right)\ln\left(\frac{I}{AA^*T^2}\right) \tag{5}$$

$$H(I) = IR_S + \eta\phi_B \tag{6}$$

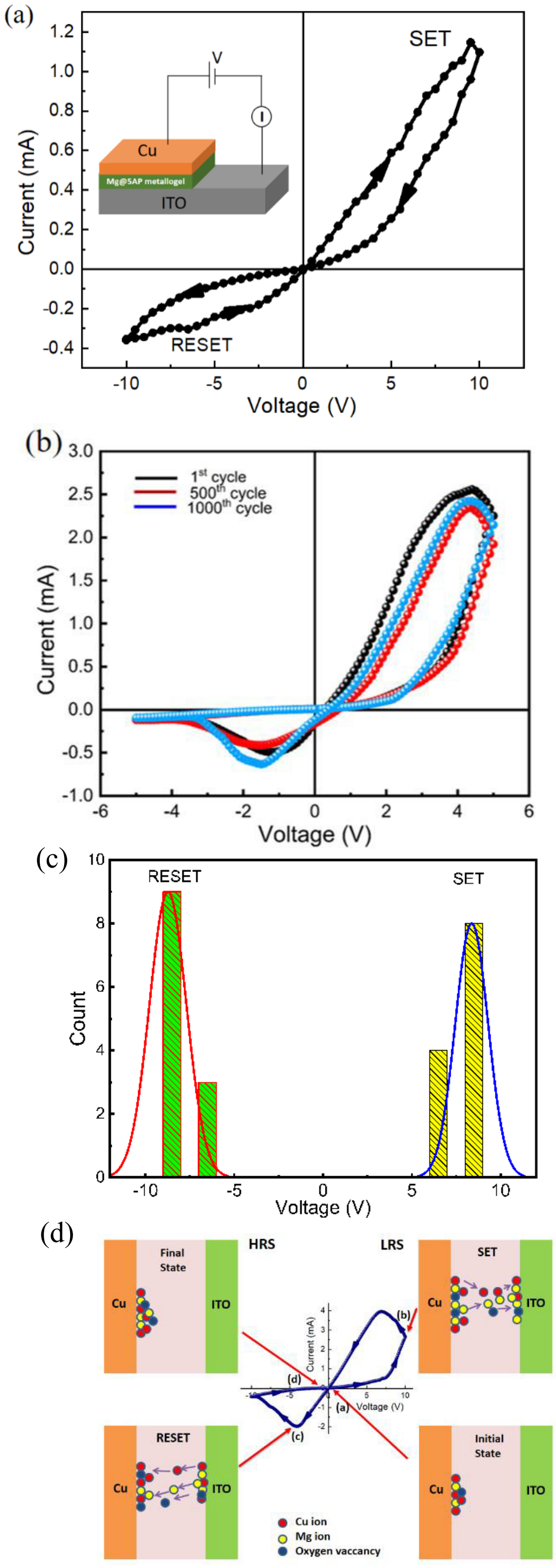

Figure 3: (a) Diagram of ITO/Mg@5AP/Cu device (inset), with IV curve of this device in linear scale, **(b)** I-V characteristics upto 1000th cycle, **(c)** Voltage distribution function of SET and RESET voltage for multiple devices, **(d)** Conductive filament model of this device. The following places have been located using the *I–V* curve: (a) The ions move towards the intermediate layer after applying a positive voltage of 0.5 V; (b) at 9.94 V, the Cu ions, Mg ions, and oxygen vacancies produced a conducting filament-type structure; (c) at −4 V, all the ions including Cu ions, Mg ions return to the top electrode; and (d) at −0.5 V, all of the ions are gathered at the top electrode and switched into HRS.

The value of R_S; η; and Φ_B are determined from equations (4-6). Here, dV/d(ln I) versus I and H versus I were plotted to obtain the constraints of device 1, as shown in Fig. 2(d). The intercept of H versus. I graph was used to define the height of barrier, and the intercept of this graph was used to get the ideality factor (η). We determined the ideality factor (η) which is 13.497 that is greater than the actual value. The high ideality factor may arise from interface traps, surface roughness, or imperfect contact between ITO and this metallohydrogel, leading to non-uniform potential barriers. This discrepancy of it could be produced by the interfacial resistance, presence of interface states and the impurities in the Schottky barrier itself. The value of (ϕ_B) which is 0.0258 eV, is established for device-1. Therefore, these characteristics such that a lower height of barrier potential and greater value of ideality factor are important for developing Schottky diode. The slope of the graph of dV/d(ln I) versus I and H versus I (Fig. 2(d)) was also calculated to obtain the value of the resistance in series (~1358.04 **Ω**). This diode can be useful for making different electronic devices.

To analyze the resistive switching behavior (RS) of ITO/Mg@5AP/Cu (device-2) we have fixed the Compliance Current (CC) at 10 mA before starting the experiments. IV curve of this device is displayed on linear scale in Fig. 3(a). The applied voltage follows this sequence: 0V→10V→-10V→10V. This IV characteristics display a proper hysteresis that is a signature of memristive behaviour. Firstly, the current rises linearly. When applied voltage increases, the IV graph demonstrates a nonlinear nature above a certain voltage of 5.85V and then the current increases rapidly. Then the device is switched to a Lower Resistance State (LRS) from a Higher Resistance State (HRS), as specified by SET voltage (V_{SET} = 10V) and it stays in ON state. In the negative zone, the voltage decreases, it goes into OFF state and the current decays quickly. After a reverse cycle, it increases until it goes to an LRS. When V_{RESET} is -9.98V, it goes to the HRS. A negative voltage is necessary to restore a device to its initial state, this is essential evidence of the bipolar RS behavior of this device. We have again examined the entire IV curves for device 2 up to 1000th cycles and observed that there isn't much more variation in the current value up to the 1000th cycle (Fig. 3(b)). Therefore, metallohydrogel-based RRAM devices are reliable and do not degrade upto 1000th cycles. We have also plotted voltage distribution function of SET and RESET voltage for multiple devices as shown in Fig. 3(c).

In the semiconducting layers of device 2, conducting filaments [25] are formed and the main reason behind this filament formation is the migration of copper ions, oxygen vacancies and Mg ions (Fig. 3(d)). We can easily explain the change from the HRS to LRS by the development and breaking of Cu conductive filaments. As we already know that their chemical formula is $Cu \rightarrow Cu^{2+} + e^-$. Cu ions may go towards the electric field and then they are ionized. When we apply +ve voltage, Cu^{2+} ions, oxygen vacancies and Mg ions travel to the in-between layer. The device changes to LRS from HRS during SET process and then concentration of all ions will go to the bottommost electrode. Then the device residues in the same state until a negative voltage is applied to the electrode during RESET. When a negative voltage is supplied, it enters the HRS. At the end of the procedure, all ions return to the topmost electrode.

Fig. 4(a) shows I-V curve of device 3 (CuMg@5AP/Cu) with two states (V_{SET} = 7.17V and V_{RESET} = -9.98V). To understand its mechanism, IV curve is fitted in a log scale in SET process (Fig. 4(b)). In the lower voltage range of 0V to 2V, the current is seen to vary linearly with slope of 1.09 and from 2V to 5V, the slope of m= 1.39 that means it shows Ohmic conduction. But in the higher voltage range of 5V to 10V, it follows a SCLC mechanism with slope of 4.10. We have also measured endurance up to 5000 multiple cycles (Fig. 4(c)). The average ON/OFF ratio of this device, which is to be around 120, shows highly robust switching behaviour. This indicates that there won't be any degradation in the device's memory response, that is advantageous for practical application in designing memory circuit. As seen in Fig. 4(d), we have also conducted retention test for devices 3 for up to 10^7 s. Device 3's switching process is reliable for a maximum of 10^7 seconds. Additionally, we have noticed that the device's ON/OFF ratio is approximately 90. It is concluded that these devices have no degradation in data storage for up to 10^7 seconds. We have also described the electrical performance of different RRAM devices as shown in Table 1.

In our study, we have also designed Mg@5AP based 2×2 cross-bar array and demonstrated logic gate operation. We have placed our sample at the interception of two Cu electrodes as shown in Fig. 5. Mg@5AP based RRAM devices are defined as A; B; C; and D.

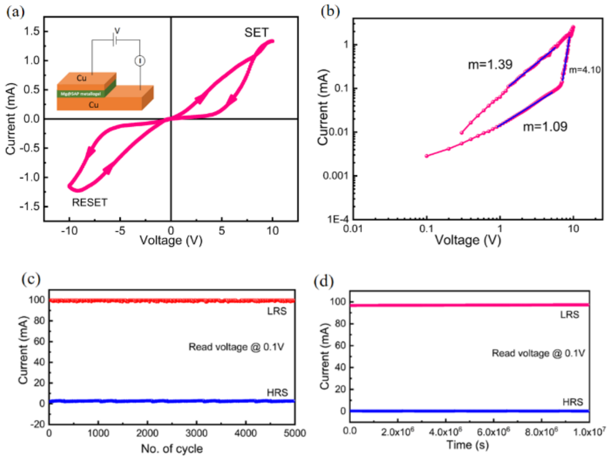

Figure 4: (a) Diagram of Cu/Mg@5AP/Cu-device (inset), with its IV curve on linear scale, **(b)** I-V Curve on a log scale, **(c)** Endurance test of same device, **(d)** Retention test of this device.

Table 1: Comparative studies of different RRAM devices.

RRAM device	Endurance (cycles)	Retention (s)	ON/OFF ratio	Ref.
Al_2O_3/ZnO- based RRAM	10^4	10^4	10^5	[26]
Pt/AlO_X/ZnO/Ti	10^3	10^4	10^2	[27]
Pt/HfO_2/TiO_X/Pt	100	10^4	10^2	[28]
Graphene/HfO_2/TiN	10^3	10^4	10^2	[29]
hBN/AlO_X/TiO_X/ITO	100	10^4	10^2	[30]
Cu/Mg@5AP/Cu	5000	10^7	10^2	This work

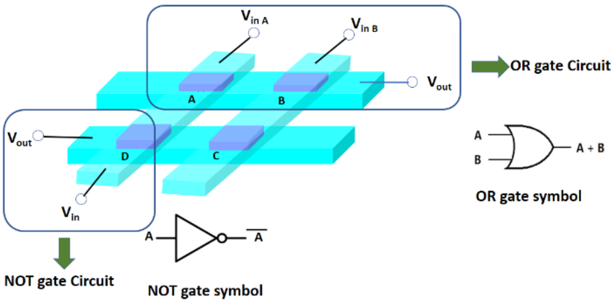

Figure 5: Circuit diagram of Logic gate

In case of OR gate, when there is zero voltage at device A and B, that means both are in "0" state, then V_0 (Output voltage) = 0.09V mentioned to as "0" state. When 5V is applied to A and 0V is provided at B, then V_0 = 4.89V referred to as "1". Similarly, when 0V is provided to A and 5 V is applied to B, then V_0 = 4.86 V which is also mentioned to as "1". When we apply 5 V to the both A and B, then V_0 = 4.85V corresponds to "1". The truth table of OR gate is given in Table 2.

Table 2: OR gate Truth Table.

$V_{A\ input}$	$V_{B\ input}$	V_0	State
0 Volt	0 Volt	0.09 Volt	0
5 Volt	0 Volt	4.89 Volt	1
0 Volt	5 Volt	4.86 Volt	1
5 Volt	5 Volt	4.85 Volt	1

Similarly, we have also designed NOT gate using device-D and it obeys NOT gate truth table (Table 3).

Table 3: NOT gate Truth Table.

V_{input}	V_0	State
0V	4.83V	1
5V	0.06V	0

The current configuration can be further stretched to incorporate larger-cross-bar arrays in order to accomplish more intricate logic and computation processes. This can be the basis for in-memory computing, as demonstrated here, in which regulating and storing information are done at the same circuit level. Thus, a variety of engineering approaches based on the principles of integrated circuit can be investigated through the use of memristor based crossbar arrays in logic gate.

Conclusion

Mg@5AP metallohydrogel was effectively synthesized by rapidly mixing of $Mg(NO_3)_2{\cdot}6H_2O$ with 5-amino-1-pentanol in an aqueous medium at normal temperature. Microstructural investigations from FESEM and TEM exposed the pebble-like structure of this gel, while FTIR spectra characterized intermolecular interactions. Tauc plot showed the semiconducting behaviour of this gel. MS junction-based Schottky diode was developed using this Mg@5AP metallogel. Moreover, ITO/Mg@5AP/Cu and Cu/Mg@5AP/Cu devices are fabricated, both exhibiting bipolar RS behavior. This behavior was recognized to the development and rapture of conduction filaments. Impressively, they demonstrated non-volatile switching behaviour, maintaining an excellent ON/OFF ratio (~120) over 5000 multiple cycles without any electrical degradation. Recent research suggests that this gel is a promising candidate for memory device applications due to its strong RS behavior and significant ON/OFF ratio. It is also a desirable choice for applications in neural circuit design, neuromorphic computing and also for the development of flexible electronic devices by utilizing the thin films of Mg@5AP for cutting-edge technology due to its stable switching performance and adaptable functionalities.

Acknowledgements

Arpita Roy acknowledges the financial support from UGC, India through UGC-NET scholarship.

Conflict of Interest

The authors declare no conflict of interest.

Data Availability Statement

The data that support the findings of this study are available from the corresponding author upon reasonable request.

Author Information

ORCID
Arpita Roy: 0009-0005-9649-3608
Soumya Jyoti Ray: 0000-0002-4640-708X

References

1. R. Kuosmanen, K. Rissanen and Elina Sievänen, *Steroidal supramolecular metallogels*. Chem. Soc. Rev. 49, 1977-1998 (2020).
2. P. Terech, M. Yan, M. Maréchal, G. Royal, J. Galveza, S. K. P. Velua, *Characterization of strain recovery and "self-healing" in a self-assembled metallo-gel*. Phys. Chem. Chem. Phys. 15, 7338-7344 (2013).
3. V. Singh, S. Kala, T. Rom, A. K. Paul, R. Pandey, *A multi-cation responsive Ni (ii)-supramolecular metallogel mimics a molecular keypad lock via reversible fluorescence switching*. Dalton Trans. 52, 7088-7103 (2023).
4. K. Kumari et al., *Structural and resistive switching behaviour in lanthanum strontium manganite-reduced graphene oxide nanocomposite system*. J. Alloys Compd. 815, 152213 (2020).
5. K. Kumari et al., *Temperature-dependent resistive switching behaviour of an oxide memristor*. Mater. Lett. 303, 130451 (2021).
6. K. Kumari, A.D. Thakur, S.J. Ray, *The effect of graphene and reduced graphene oxide on the resistive switching behavior of* $La_{0.7}Ba_{0.3}MnO_3$. *Mater*. Today Commun. 26, 102040 (2021).
7. K. Kumari et al., *Charge transport and resistive switching in a 2D hybrid interface. Mater*. Res. Bull. 139, 111195 (2021).
8. S. Majumder, K. Kumari, S.J. Ray, *Pulsed voltage induced resistive switching behavior of copper iodide and* $La_{0.7}Sr_{0.3}MnO_3$ *nanocomposites*. Mater. Lett. 302, 130339 (2021).
9. N. Alam et al., *A wide bandgap semiconducting*

magnesium hydrogel: moisture harvest, iodine sequestration, and resistive switching. Langmuir 38(34), 10601–10610 (2022).
10. K. Kumari et al., *Role of an oxide interface in a resistive switch*. Curr. Appl. Phys. 35, 16–23 (2022).
11. K. Kumari, S.J. Ray, A.D. Thakur, *Resistive switching phenomena: a probe for the tracing of secondary phase in manganite*. Appl. Phys. A 128(5), 430 (2022).
12. K. Kumari, A.D. Thakur, S.J. Ray, *Structural, resistive switching and charge transport behaviour of (1-x)$La_{0.7}Sr_{0.3}MnO_3$. (x) ZnO composite system*. Appl. Phys. A 128(11), 992 (2022).
13. S. Majumder, K. Kumari, S.J. Ray, *Temperature-dependent resistive switching behavior of a hybrid semiconductor-oxide planar system*. Appl. Phys. A 129(5), 1–10 (2023).
14. M. Pedro et al., *Tuning the conductivity of resistive switching devices for electronic synapses. Microelectron*. Eng. 178, 89–92 (2017).
15. D. Ielmini, *Brain-inspired computing with resistive switching memory (RRAM): devices, synapses and neural networks*. Microelectron. Eng. 190, 44–53 (2018).
16. S. Petzold et al., *Forming-free grain Boundary Engineered Hafnium Oxide Resistive Random-Access Memory devices*. Adv. Electron. Mater. 5(10), 1900484 (2019).
17. K. Moon et al., *RRAM-based synapse devices for neuromorphic systems*. Faraday Discuss. 213, 421–451 (2019).
18. J. Choi et al., *Enhanced endurance organolead halide perovskite resistive switching memories operable under an extremely low bending radius*. ACS Appl. Mater. Interfaces. 9(36), 30764–30771 (2017).
19. H. Ma et al., *Interface state-induced negative differential resistance observed in hybrid perovskite resistive switching memory*. ACS Appl. Mater. Interfaces. 10(25), 21755–21763 (2018).
20. J. Han, Su et al., *Lead-free all-inorganic cesium tin iodide perovskite for filamentary and interface-type resistive switching toward environment-friendly and temperature-tolerant nonvolatile memories*. ACS Appl. Mater. Interfaces. 11(8), 8155–8163 (2019).
21. M. Abbasi, Sehar et al., *Biomaterial-induced stable resistive switching mechanism in TiO_2 thin films: the role of active interstitial sites/ions in minimum current leakage and superior bioactivity*. ACS Omega. 5(30), 19050–19060 (2020).
22. B. Sun et al., *An organic nonvolatile resistive switching memory device fabricated with natural pectin from fruit peel*. Org. Electron. 42, 181–186 (2017).
23. A. Kumar et al., *Graphene mediated resistive switching and thermoelectric behavior in lanthanum cobaltate*. J. Appl. Phys. 127, 23 (2020).
24. S. K. Cheung, N. W. Cheung, *Extraction of Schottky diode parameters from forward current-voltage characteristics*. Appl. Phys. Lett. 49, 85-87 (1986).
25. A. Roy, K. Kumari, S. Majumder, S.J. Ray, *Eco-Friendly Biomemristive Nonvolatile Memory: Harnessing Organic Waste for Sustainable Technology*. ACS Applied Bio Materials. 8, 5147-5157 (2024).
26. J. W. Seo, J.-W. Park, K. S. Lim, S. J. Kang, Y. H. Hong, J. H. Yang, L. Fang, G. Y. Sung, H.-K. Kim, *Transparent flexible resistive random access memory fabricated at room temperature.* Appl. Phys. Lett., 95,133508 (2021).
27. M.-C. Wu, J.-Y. Chen, Y.-H. Ting, C.-Y. Huang, W.-W. Wu, *A novel high-performance and energy-efficient RRAM device with multi-functional conducting nanofilaments.* Nano Energy, 82,105717 (2021).
28. X. Ding, Y. Feng, P. Huang, L. Liu, J. Kang, *Low-power resistive switching characteristic in HfO_2/TiO_x bi-layer resistive random-access memory.* Nanoscale Res. Lett., 14, 157 (2019).
29. S. Lee, J. Sohn, Z. Jiang, H.-Y. Chen, H. S. Philip Wong, Metal oxide-resistive memory using graphene-edge electrodes. Nat. Commun., 6, 8407 (2015).
30. Y. J. Huang et al., *Graphene/h-BN heterostructures for vertical architecture of RRAM design.* Sci. Rep., 7, 9679 (2017).

Structural Study of $LiCoO_2$ Synthesized by Sol-Gel Method at Different Temperatures

Monika[a], Anjali, Ashish Kumar Mishra, Raj Kumar Jagota and Balbir Singh Patial[b]

Department of Physics, Himachal Pradesh University Summerhill, Shimla, Himachal Pradesh-171005, India.

[a] monika2019panghal@gmail.com
[b] bspatial@hpuniv.ac.in

Abstract

Minimizing environmental impact requires efficient energy storage, which is essential for the transition to renewable energy. Lithium-ion batteries (LIBs) are widely recognized for offering high energy density and long lifespan, making them a key technology in this transition. Their lightweight design also helps lower emissions in portable devices, contributing to a more sustainable energy future. A critical component of LIB is the cathode material, which plays a vital role in determining the battery's overall performance, capacity, and stability. Among the various cathode materials, $LiCoO_2$ is widely used due to its excellent electrochemical properties and stability. In order to find out how temperature affects the structural and morphological characteristics of $LiCoO_2$, it was synthesized using the sol-gel process conducted at various temperatures. Utilizing X-ray diffraction (XRD), the study confirmed the crystallinity and defects while field emission scanning electron microscopy (FESEM) was employed to study the surface structure and to determine particle size. The impact of temperature on the structural characteristics of $LiCoO_2$ is reported and discussed in detail.

Keywords: Cathode Material, $LiCoO_2$, Sol-gel Method, FESEM, XRD.
Received 30 January 2025; First Review 21 February 2025; Accepted 13 April 2025.

*** Address of correspondence**
Balbir Singh Patial
Department of Physics, Himachal Pradesh University Summerhill, Shimla, Himachal Pradesh-171005, India.

Email: bspatial@gmail.com

How to cite this article
Monika, Anjali, Ashish Kumar Mishra, Raj Kumar Jagota and Balbir Singh Patial, Structural Study of $LiCoO_2$ Synthesized by Sol-Gel Method at Different Temperatures, J. Cond. Matt. 2025; 03 (02): 114-117.

Available from:
https://doi.org/10.61343/jcm.v3i02.118

Introduction

The development of high-energy density batteries has become a top priority due to ever increasing demand for energy storage. The depletion of non-renewable resources like coal and petroleum along with their environmental impact, serves as a strong push toward a transition to renewable energy sources. Renewable energy sources that are naturally available such as solar, wind, biomass, tidal, and geothermal energy, are safe for the environment and do not contribute to global warming by emitting harmful greenhouse gases.

$LiCoO_2$ is one of the widely used cathode materials due to its better electrochemical properties and high stability. The crystal structure, particle size, and overall distribution of $LiCoO_2$ are greatly influenced by the choice of material and synthesis method. Among the various techniques, the sol-gel method offers significant advantages due to its capability to control factors like surface area, particle size, and morphology, key element for improving Li-ion diffusion and enhancing electrode performance. In this process, precursor solution underwent hydrolysis to form colloidal sol or gel, when the gel is further heated, it transforms into the desired material with enhanced properties. In order to maintain stoichiometry control and produce small, evenly distributed particles, chelating agents are used.

In this study, $LiCoO_2$ was synthesized using the sol-gel method to explore how different temperatures affect its morphology and structure. X-ray diffraction (XRD) was used to analyse the nature, crystallinity and defects, while FESEM was employed to study the surface structure and to deduce particle size. The influence of temperature on $LiCoO_2$'s structural characteristics is investigated to contribute to the development of high-performance cathode materials for LIBs [1-4].

Experimental details

Material Synthesis

To prepare $LiCoO_2$, a solution was created with $LiNO_3$ and $Co(NO_3)_2 \cdot 6H_2O$ in distilled water, maintaining Li: Co ratio as 1.1:1 as outlined by Predoana et al. [5]. A complexing agent, citric acid, was dissolved in water and added to the solution. The mixture was heated to 70–80 °C under continuous magnetic stirring until it formed a gel. After the formation of the gel, one sample $LiCoO_2$ referred as LC80, was maintained at 80 °C until it converted to ash as the final product. Another similar composition sample, $LiCoO_2$ referred as LC300 was heated in the 250–300 °C range until it also transformed into ash completing to the final product. Thereafter, both the samples were placed at room temperature to cool down at its own. The crystalline powders were obtained using a two-step process in a muffle furnace. The first step involved calcination of the materials at 300 °C for 20 to 30 minutes, followed by a second stage of sintering at 700 °C for 24 hours.

X-ray diffraction (XRD) Study

It is one of the essential techniques in materials science, is used to analyze precise information and to examine the atomic-level crystallographic structure of both natural and synthetic materials. Because of the rotational projection of the randomly oriented reciprocal lattices, the powder diffraction pattern yields one-dimensional data instead of the three-dimensional position of each reflection. A prism or grating can be used to separate light into distinct frequencies, similar to the mechanism of an infrared prism. Every crystalline material has a unique diffraction pattern, and each phase in a mixture of crystalline substances generates a distinct pattern. This pattern is like a fingerprint, making it suitable for the characterization of polycrystalline phases.

The analysis of diffraction is governed by Bragg's law. The peaks that are seen when X-rays are diffracted from a crystal's lattice planes are indication of constructive interference.

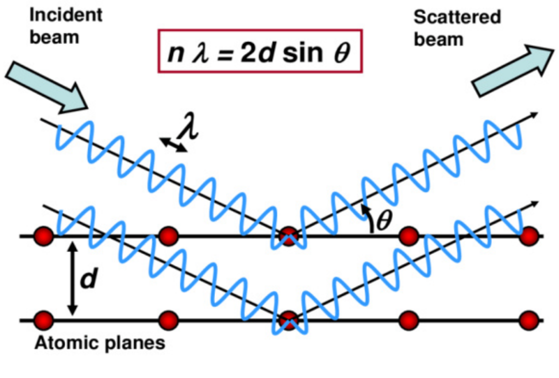

Figure 1: X-ray diffraction.

The inter-planar distance is represented by *d*, X-ray wavelength by "λ", and the incident angle by "θ" in this case, where n represents the order of constructive interference.

XRD measurements were performed across a 2θ range from 0° < 2θ < 90° to examine the structural properties of the samples (LC80 and LC300). Crystalline size (D), dislocation density and microstrain (ε), were determined. The Crystalline size was determined using the Scherrer equation [6]:

$$D = K\lambda / \beta\cos\theta \tag{1}$$

where (K) is the shape factor (here 0.9), (λ) is the wavelength of the X-ray source which is 0.154 nm, (β) is the full width at half maximum (FWHM) in radians, and (θ) is the Bragg angle (half of the 2θ angle), also converted into radians for accurate calculations.

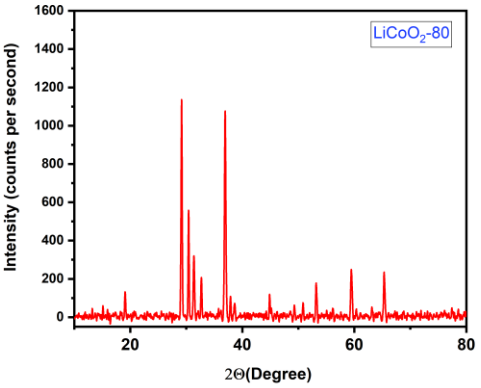

Figure 2: XRD of LC80.

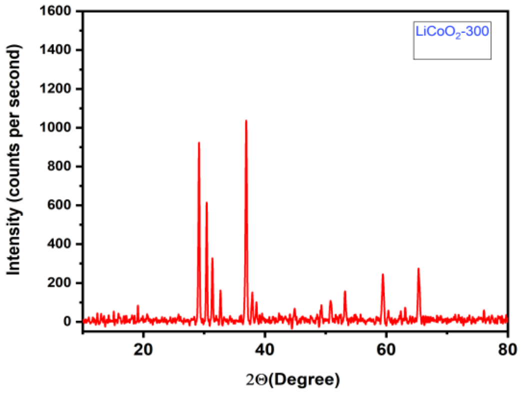

Figure 3: XRD of LC300.

XRD pattern of LC300 displaying a decrease in peak intensity as compared to LC80, suggesting decreasing intensity with the increase in temperature.

Material characterization using FESEM

The incident electrons will exhibit a hemispheric diffusion if the specimen's element has a high atomic number, and a teardrop-shaped diffusion if the element has a low atomic number. The diffusion area can be expanded significantly deeper with higher accelerating voltages. The incident electrons may progressively lose energy during diffusion until they are absorbed by the specimen (shown as absorbed current). Low energy secondary electrons lose a significant amount of energy during this process and are reflected outside the specimen. When incident electrons interact with the constituent atoms of a specimen, most of the electron energy is converted into heat, while some of it is used to generate secondary electrons, Auger electrons, X-rays, and visible or infrared cathodoluminescence. Auger electrons, in particular, are emitted from regions very close to the specimen's surface.

Information describing the specimen's nature is conveyed through X-rays, backscattered electrons, quanta (secondary electrons), and other sources. FESEM makes it possible to observe the material's porosity, surface characteristics, structure, particle size and shape. A beam of electrons is focused on the sample's surface after being accelerated across a potential difference. An electron beam is typically generated using sources such as a tungsten filament cathode, a lanthanum (LaB_6) wire, or an electron gun. In the case of an electron gun, an emitter is maintained at a negative potential relative to a nearby electrode and the resulting potential difference at the emitter surface enables field electron emission.

The analyzer detects the electromagnetic radiation emitted from the sample. In FESEM, image formation is mainly due to secondary electrons, which are the most abundant among the emitted electrons. A current is created and recorded once the secondary electrons arrive at the detector. An image is created by charting the current on the sample's surface against the probe position. Since surface morphology plays a key role in contrast, the final image directly represents the surface structure [7].

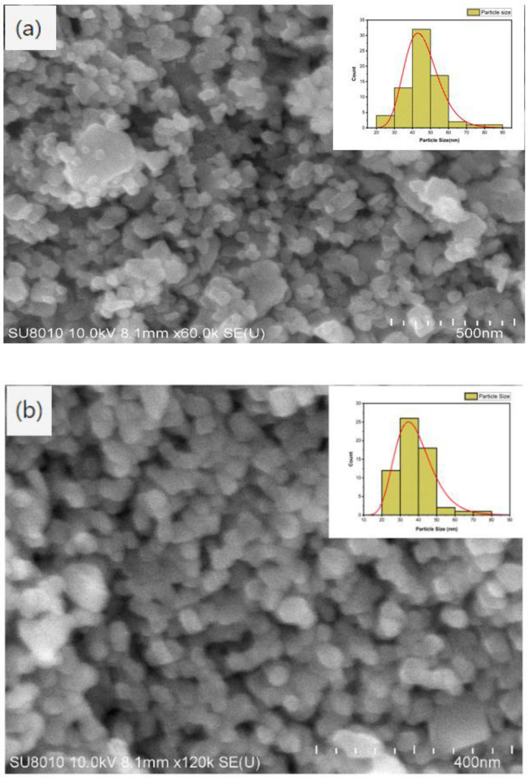

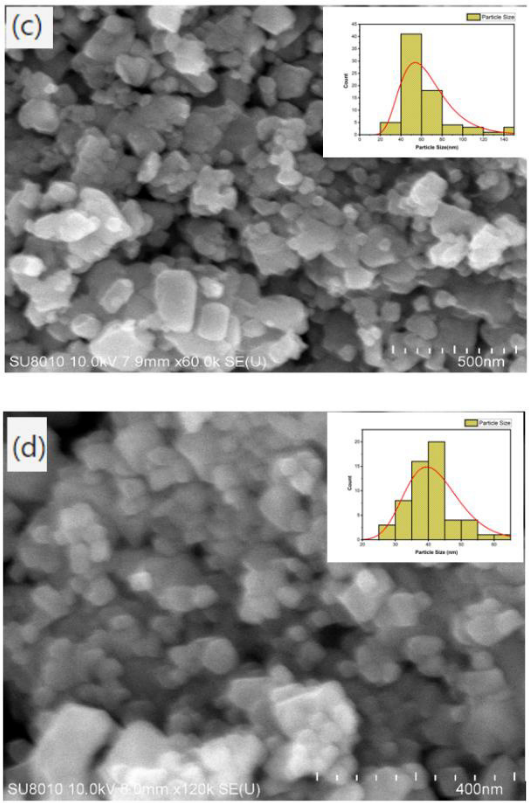

Figure 4: FESEM micrographs **(a) ×60k** (LC80), **(b) ×120k** (LC80), **(c) ×60k** (LC300), **(d) ×120k** (LC300) (inset for all figures shows nanocrystalline particle size distribution).

Results and discussion

The quantity of defects and imperfections within a crystal lattice is represented by the system's dislocation density, calculated using the following relation [8]:

$$\delta = 1/D^2 \qquad (2)$$

Additionally, the microstrain (ε) arises due to the displacement of atoms relative to their ideal lattice positions. It can be determined using the expression:

$$\varepsilon = \beta \cos\theta /4 \qquad (3)$$

For LC80, the crystalline size ranges from a minimum of 32.38 nm (at $2\theta = 36.94°$) to a maximum of 54.10 nm (at $2\theta = 30.41°$). The dislocation density for LC80 varies between 0.342×10^{-3} and 0.954×10^{-3}, and the microstrain ranges from 0.64×10^{-3} to 1.07×10^{-3}. In comparison, LC300 has a crystalline size range from 29.49 nm (at $2\theta = 65.33°$) to 46.67 nm (at $2\theta = 30.41°$), a dislocation density between 0.459×10^{-3} and 1.150×10^{-3}, and a microstrain range of 0.74×10^{-3} to 1.18×10^{-3}. These variations in crystalline size, dislocation density, and microstrain reflect different levels of crystallinity, defect concentration, and lattice distortion, which may influence each sample's performance and stability in applications. Table 1, Table 2 summarizes the XRD data of paper and highlights notable differences between LC80 and LC300 in terms of crystallinity and structural properties. The variations in crystalline size and dislocation density across 2θ values indicate different degrees of lattice integrity and imperfections in the samples.

Table 1: Crystalline Size, Dislocation Density, Microstrain of LC80.

Sample	2θ	FWHM	Crystalline Size (nm)	Dislocation Density ($\times10^{-3}$) (nm^{-2})	Microstrain ($\varepsilon \times10^{-3}$)
LC80	29.16	0.19	41.17	0.59	0.84
	30.41	0.15	54.10	0.34	0.64
	31.36	0.22	36.53	0.74	0.95
	36.94	0.25	32.38	0.95	1.07
	53.20	0.20	42.71	0.54	0.81
	59.48	0.26	34.25	0.85	1.01
	65.34	0.23	39.85	0.63	0.87

Table 2: Crystalline Size, Dislocation Density, Microstrain of LC300.

Sample	2θ	FWHM	Crystalline Size (nm)	Dislocation Density ($\times10^{-3}$) (nm^{-2})	Microstrain ($\varepsilon \times10^{-3}$)
LC 300	29.15	0.21	38.25	0.68	0.91
	30.41	0.17	46.67	0.45	0.74
	31.35	0.18	44.42	0.50	0.78
	36.92	0.25	32.57	0.94	1.06
	53.20	0.22	40.12	0.62	0.86
	59.43	0.30	29.56	1.14	1.17
	65.33	0.31	29.49	1.15	1.18

From XRD, Figures 2 and 3, it is clear that there is a decrease in peak intensity with increasing temperature, suggesting a higher degree of structural disorder. This may introduce more defect sites that act as charge-trapping centres and reduces overall charge storage efficiency. Additionally, the higher synthesis temperature results in more pronounced particle agglomeration, as evidenced by FESEM analysis. This agglomeration can reduce the effective surface area available for lithium-ion diffusion, potentially limiting electrochemical reaction kinetics.

Conclusions

As the temperature increases, corresponding rise in agglomeration is observed, which is evident from the FESEM analysis. The distinction between particle size and crystalline size becomes more pronounced at higher temperatures. In contrast, at lower temperature, there is minimal variation between the particle size and crystalline size. XRD analysis further reveals a decrease in the intensity of XRD peaks with increasing temperature, highlighting structural changes occurring during the process. Defects such as dislocation density and microstrain, which refer to distortions and strain within the crystal lattice, also increase with temperature, further affecting the material's properties.

Acknowledgement

We, first author (Monika), coauthor (Raj Kumar Jagota, Co-PI) and corresponding author (Balbir Singh Patial, Principal Investigator) extend our heartfelt gratitude to the Himachal Pradesh Council for Science, Technology and Environment (HIMCOSTE), Shimla HP (INDIA), for the financial assistance in supporting the research project (Registration No. HIMCOSTE(R&D)/2023 24-7(2)).

References

1. P Ghosh, S Mahanty, M W Raja, R N Basu, and H S Maiti. Journal of Materials Research 22: 1162–1167, 2007.
2. J Graetz, A Hightower, C C Ahn, R Yazami, P Rez, and B Fultz. Journal of Physical Chemistry B 106: 1286–1289, 2002.
3. Monika, A K Mishra, and B S Patial. Sustainable Chemistry One World 5: 100042, 2024.
4. A K Mishra, Monika, and B S Patial. Materials Today Electronics 7: 100089, 2024.
5. L Predoana, A Jitianu, M Voicescu, N G Apostol, and M Zaharescu. Journal of Sol-Gel Science and Technology 74: 406, 2015.
6. A L Patterson. Physical Review 56: 978, 1939
7. S Nallusamy, and A M Babu. Journal of Nano Research 37: 58–67, 2016.
8. Monika, A K Mishra, and B S Patial. Journal of Condensed Matter 1: 65–68, 2023.

Comparative SEM Analysis Study of Titanium Dioxide (TiO_2) Nanoparticles Synthesized by Sol-Gel Method

Khyati Mody[a] and I B Patel[b]

Department of Physics, Veer Narmad South Gujarat University, Surat-395007, Gujarat, India.

[a] kmody1997@gmail.com
[b] ibpatel@vnsgu.ac.in

Abstract

This paper describes the comparative SEM Analyses study of various samples of nanoparticle Titanium Dioxide (TiO_2) synthesized by the Sol-Gel method with different changes in the parameters. Titanium dioxide is not very reactive with chemicals and doesn't harm the environment, so it is widely used as a colour in industry. It comes in three forms: anatase, rutile, and Brookite. Scanning electron microscopy was used to examine the morphological changes of the produced TiO_2 nanoparticles at various calcination temperatures as well as the precursor ratio. SEM analysis was carried out at 10 kV acceleration Voltage. According to the SEM results, the achievement of high temperatures, the alteration of the precursor ratio, and the presence of distinct contents of the two crystalline phases of titanium dioxide are the causes of the increase in particle size and the apparent aggregation of TiO_2 nanoparticles. These results are in agreement with XRD results that showed the particles size of the anatase phase smaller than particles grown at the higher temperature.

Keywords: Titanium Dioxide (TiO_2) nanoparticles, Sol-Gel Method, SEM Analysis, Anatase Phase, Particle size.
Received 31 January 2025; First Review 21 March 2025; Accepted 11 April 2025.

*** Address of correspondence**
Khyati Mody
Department of Physics, Veer Narmad South Gujarat University, Surat-395007, Gujarat, India.

Email: kmody1997@gmail.com

How to cite this article
Khyati Mody and I B Patel, Comparative SEM Analysis Study of Titanium Dioxide (TiO_2) Nanoparticles Synthesized by Sol-Gel Method, J. Cond. Matt. 2025; 03 (02): 118-123.

Available from:
https://doi.org/10.61343/jcm.v3i02.130

Introduction

Titanium Dioxide (TiO_2) which is also defined as titania is one of the most versatile and widely studied materials in modern science and technology. Known for its exceptional chemical inertness, thermal stability, and environmental friendliness, one of titanium's natural oxides is TiO_2. There are three main crystalline forms of it: rutile, brookite, and anatase [1]. Each has distinct chemical and physical characteristics. Among these, the anatase and rutile phases are of particular interest due to their remarkable photocatalytic performance and optical characteristics. The anatase phase is known for its high reactivity and is often used in photocatalysis, while the rutile phase exhibits better thermal and structural stability. Due to its non-toxic nature and strong UV light absorption, TiO_2 has found widespread applications across various industries. In the pigment industry, it serves as an essential component for paints, coatings, and plastics, providing superior opacity and brightness. In the cosmetics sector, it is used in sunscreens and skincare products to protect against harmful UV radiation [2]. Titanium Dioxide used in the pigment industry can also be defined as titanium white or pigment white. Furthermore, TiO_2 has gained significant attention in environmental applications, such as air purification, water treatment, and self-cleaning surfaces, owing to its photocatalytic properties that enable the breakdown of organic pollutants [3,4].

In recent years, TiO_2 has emerged as a key material in renewable energy technologies. It is extensively employed as a photocatalyst for the water splitting process that produces hydrogen and in dye-sensitized solar cells (DSSCs). Its ability to function as a photocatalyst under UV light has also led to innovations in energy-efficient coatings and anti-bacterial surfaces. Moreover, its abundance in nature, low cost, and ease of synthesis have contributed to its growing importance in industrial and research domains [5,6].

Extensive studies are being conducted to further enhance the efficiency and functionality of TiO_2, particularly by tailoring its properties through methods such as doping, surface modification, and nano-structuring [7]. These advancements aim to optimize its performance for specific applications and explore its potential in emerging fields like biomedical devices, sensors, and advanced energy storage systems [8,9].

Overall, the versatility, affordability, and eco-friendly nature of Titanium Dioxide make it an indispensable material in both traditional industries and cutting-edge technological advancements [10].

The Sol-Gel method is a cost-effective and versatile chemical route for synthesizing metal oxide (MO) nanoparticles, offering precise control over particle size and morphology. X-ray diffraction (XRD) is a fundamental tool for phase identification, lattice parameter determination, and crystallite size estimation. This study aims to compare the structural properties of TiO_2 nanoparticles synthesized via the Sol-Gel method under various conditions using XRD analysis [11].

Experimental Methods

- **Materials**

Table 1: Materials used in the synthesis of TiO_2

Chemical Name	Chemical Structure
Titanium tetraisopropoxide (TTIP) [the titanium precursor]	$Ti(OCH(CH_3)_2)_4$
Acetic acid	CH_3COOH
Distilled water	H_2O

- **Methodology**

The Sol-Gel method is a versatile chemical process widely used for synthesizing advanced materials, such as nanoparticles, thin films, and ceramics. It involves a transformation from a liquid solution (sol) into a solid network (gel) through hydrolysis and condensation reactions of metal alkoxides or inorganic salts. This technique allows precise control over material properties, including particle size, morphology, and composition [12].

One of the main benefits of the Sol-Gel method is its ability to synthesize materials at relatively low temperatures, which is an advantage over traditional high-temperature techniques. The process generally starts with the preparation of a precursor solution, typically using metal alkoxides like titanium (IV) isopropoxide. This solution undergoes hydrolysis and condensation, leading to the formation of a gel. Subsequent drying and calcination convert the gel into the desired crystalline phase with specific structural characteristics [13,14].

The Sol-Gel method is highly adaptable and can produce materials in various forms, such as powders, thin films, fibers, or monolithic structures. It is widely employed in applications like optical coatings, catalysts, sensors, and bioactive materials. The technique is especially valued for producing highly pure and homogeneous materials, essential for many advanced technologies [15].

In recent developments, the Sol-Gel process has become increasingly popular for synthesizing metal oxide nanoparticles, including titanium dioxide (TiO_2). This method provides precise control over the structural and surface properties of nanoparticles, making it ideal for applications in photocatalysis, energy storage, and environmental cleanup [16]. Its simplicity, cost-effectiveness, and scalability have made the Sol-Gel method a favoured choice in both academic research and industrial manufacturing [17,18].

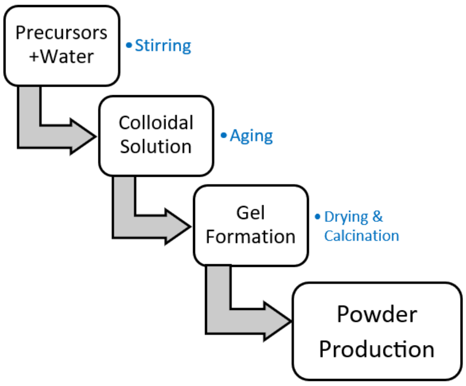

Figure 1: The flowchart of Sol-gel Synthesis.

The Sol-Gel process for Titanium Dioxide involved the hydrolysis and condensation of TTIP. The steps were as follows:

1. Mix 20 ml of titanium isopropoxide with 40 ml of glacial acetic acid.
2. Stir the mixture using a magnetic stirrer until a homogeneous solution forms.
3. Gradually add 120 ml of deionized water to the solution, drop by drop, while stirring continuously for 2 hours to form the sol.
4. Place the solution in an oven set at 90 °C and heat for about 12 hours to facilitate gel formation.
5. Pulverize and dry the gel at 200 °C for 2 hours, resulting in the formation of a white powder [19].

Figure 2: Transformation of Sol to Gel.

I have carried out the experiment by changing different parameters like the precursor ratio, water amount and the calcination temperature by 200 °C, 400 °C, 500 °C which is shown in a table form as follows [20,21]:

Table 2: The change in the different parameters with the different samplings.

Sample	TTIP (ml)	Acetic Acid (ml)	Dist. Water (ml)	Temperature ˚C
S1	20	40	120	200
S2	30	40	120	200
S3	20	40	200	200
S4	20	40	120	400
S5	25	45	125	500

Results and Discussions

• Characterisation

The synthesized TiO_2 nanoparticles samples with different parameters were analyzed using Scanning Electron Microscopy (SEM), revealing the following results [22,23]:

Sample 1

The particles were roughly spherical in shape with a spongy texture.

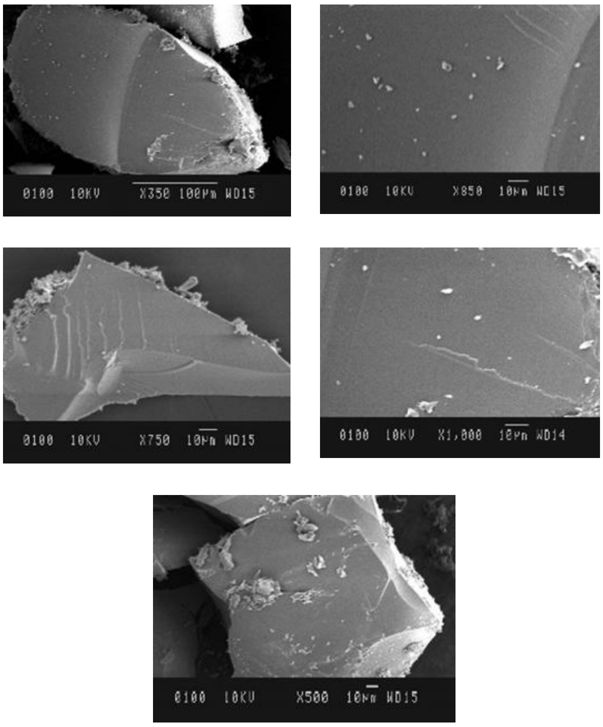

Figure 3: SEM images of the Sol-Gel synthesized TiO_2 nanoparticles (Sample1 as mentioned in Table 2)

Their sizes were in the range of less than 20 nanometres, and the particles were relatively well-distributed. This sample showed the best characteristics in terms of small particle size and distribution, making it highly effective for applications like photocatalysis [24].

Sample 2:

At a higher calcination temperature, the particles exhibited increased size and agglomeration.

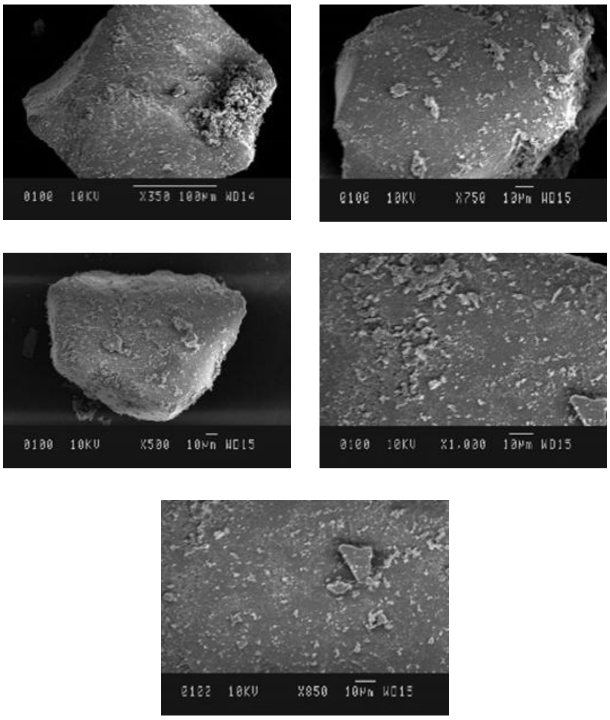

Figure 4: SEM images of the Sol-Gel synthesized TiO_2 nanoparticles (Sample2 as mentioned in Table 2)

The shapes became less uniform due to the initial particles clumping together as crystallinity increased.

Sample 3:

This result shows agglomerated particles with varying shapes and sizes.

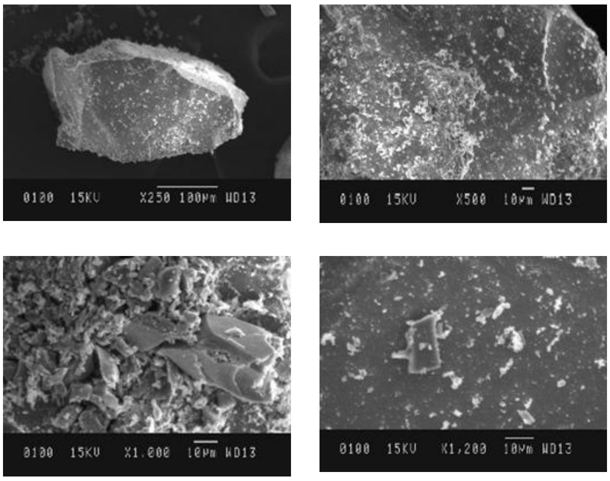

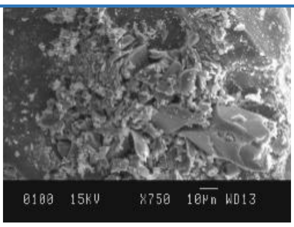

Figure 5: SEM images of the Sol-Gel synthesized TiO_2 nanoparticles (Sample3 as mentioned in Table 2)

Some regions appear porous and spongy, while others show larger, plate-like structures. There is noticeable particle clustering, suggesting possible agglomeration due to high calcination temperatures or synthesis conditions [24].

The presence of larger particles and irregular morphology could indicate increased crystallization and grain growth, leading to agglomeration.

Sample 4:

There appears to show a rough, uneven surface with noticeable cracks and interconnected structures.

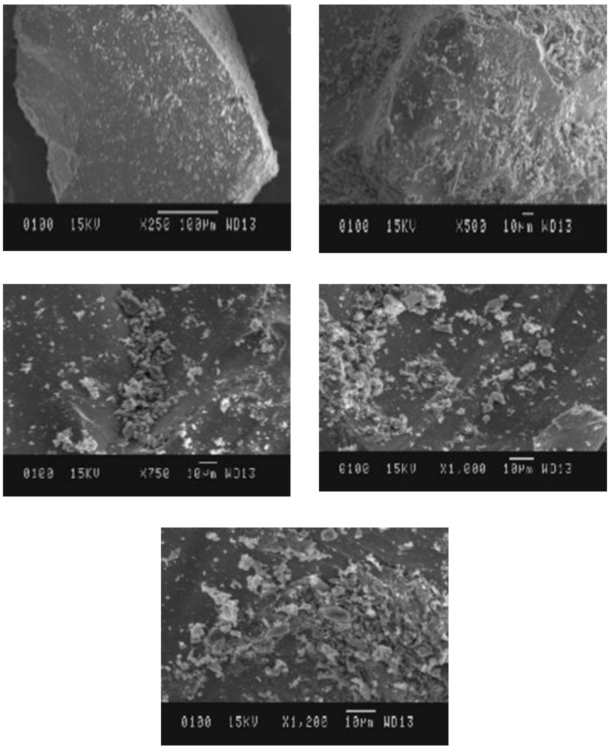

Figure 6: SEM images of the Sol-Gel synthesized TiO_2 nanoparticles (Sample4 as mentioned in Table 2)

The texture looks dense and compact, with some regions displaying porous structures. There are fine grain-like features compared to sample shown before.

Sample 5:

The trend of increased crystallinity continued, but there was a significant anatase-to-rutile phase transformation. This transformation impacts properties like photocatalytic activity and electron mobility [25].

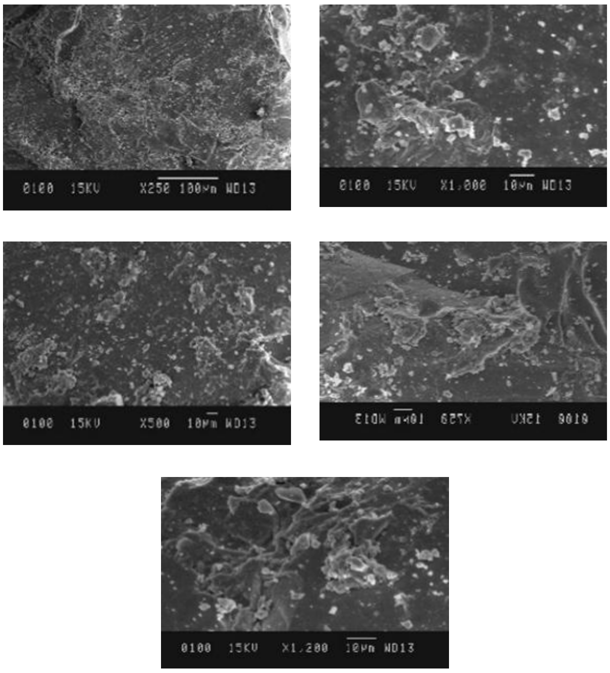

Figure 7: SEM images of the Sol-Gel synthesized TiO_2 nanoparticles (Sample5 as mentioned in Table 2).

Conclusion

1. Effect of Calcination Temperature:

At lower temperatures (e.g., 200°C), the TiO_2 nanoparticles maintained a smaller size and uniform distribution.

Increasing the temperature led to higher crystallinity, which, while beneficial for some properties, also caused agglomeration and phase transformations that may reduce effectiveness in specific applications.

2. Effect of Hydrous Solution Concentration:

Higher water content during synthesis resulted in smaller particle sizes but reduced crystallinity.

This trade-off indicates that optimizing water concentration is essential for achieving the desired balance between particle size and crystallinity.

In conclusion, the sol-gel method offers a versatile and controllable approach to synthesizing TiO_2 nanoparticles. The findings from this study suggest that:

- Sample 1, prepared at 200 °C, had the most promising properties, with smaller particle sizes and better distribution.
- Increasing calcination temperature enhances crystallinity

but leads to agglomeration and phase transformations.

• Optimizing synthesis conditions is crucial for tailoring the properties of TiO_2 nanoparticles to suit specific applications, such as photocatalysis, where smaller and uniform particles are highly advantageous.

Acknowledgement

The authors would be happy to thanks Sophisticated Analytical Instrumentation Facility, Punjab university, Chandigarh for providing XRD instrument to analyse the samples.

References

1. J. Liu, H. Bai, Y. Wang, Z. Liu, X. Zhang, D.D. Sun, *"Self-assembling TiO_2 nanorods on large graphene oxide sheets at a two-phase interface and their anti-recombination in photocatalytic applications"*, Adv. Funct. Mater. 20 (2010) 4175-4181. https://doi.org/10.1002/adfm.201001391.
2. K. Zhou, Y. Zhu, X. Yang, X. Jiang, C. Li, "Preparation of graphene–TiO_2 composites with enhanced photocatalytic activity", New J. Chem. 35 (2011) 353–359. https://doi.org/10.1039/C0NJ00623H.
3. A. Fujishima, K. Honda, "*Electrochemical photolysis of water at a semiconductor electrode"*, Nature 238 (1972) 37–38. https://doi.org/10.1038/238037a0.
4. C. H. Ao, S. C. Lee, *"Indoor air purification by photocatalyst TiO_2 immobilized on an activated carbon filter installed in an air cleaner"*, Chem. Eng. Sci. 60 (2005) 103–109. https://doi.org/10.1016/j.ces.2004.01.073.
5. Y. Yao, G. Li, S. Ciston, R.M. Lueptow, K.A. Gray, *"Photoreactive TiO_2/carbon nanotube composites: synthesis and reactivity"*, Environ. Sci. Technol. 42 (2008) 4952–4957. https://doi.org/10.1021/es800191n.
6. P. Wolkoff, G. D. Nielsen, *"Organic compounds in indoor air-their relevance for perceived indoor air quality"*, Atmos. Environ. 35 (2001) 4407–4417, https://doi.org/10.1016/S1352-2310(01)00244-8.
7. Y. Zhang, Z.-R. Tang, X. Fu, Y.-J. Xu, *"TiO_2 graphene nanocomposites for gas-phase photocatalytic degradation of volatile aromatic pollutant: is TiO_2 graphene truly different from other TiO_2 carbon composite materials"*, ACS Nano 4 (2010) 7303–7314. https://doi.org/10.1021/nn1024219.
8. Y. Paz, *"Application of TiO_2 photocatalysis for air treatment: patents' overview"*, Appl. Catal. B Environ. 99 (2010) 448–460. https://doi.org/10.1016/j.apcatb. 2010.05.011
9. M. Hussain, N. Russo, G. Saracco, *"Photocatalytic abatement of VOCs by novel op timized TiO_2 nanoparticles"*, Chem. Eng. J. 166 (2011) 138–149. https://doi.org/10. 1016/j.cej.2010.10.040.
10. J. Auvinen, L. Wirtanen, *"The influence of photocatalytic interior paints on indoor air quality"*, Atmos. Environ. 42 (2008) 4101-4112. https://doi.org/10.1016/j.atmosenv.2008.01.031.
11. J. Godnjavec, J. Zabret, B. Znoj, S. Skale, N. Veronovski, P. Venturini, *"Investigation of surface modification of rutile TiO_2 nanoparticles with SiO_2/Al_2O_3 on the properties of polyacrylic composite coating"*, Prog. Org. Coat. 77 (2014) 47–52. https://doi.org/10.1016/j.porgcoat.2013.08.001.
12. Y. J. Xu, Y. Zhuang, X. Fu, *"New insight for enhanced photocatalytic activity of TiO_2 by doping carbon nanotubes: a case study on degradation of benzene and methyl orange"*, J. Phys. Chem. C 114 (2010) 2669–2676. https://doi.org/10.1021/ jp909855p.
13. S. Miar Alipour, D. Friedmann, J. Scott, R. Amal, *"TiO_2/porous adsorbents: recent advances and novel applications"*, J. Hazard. Mater. 341 (2018) 404–423. https://doi.org/10.1016/j.jhazmat.2017.07.070.
14. B. L. Diffey, *"Sources and measurement of ultraviolet radiation"*, Methods 28 (2002) 4-13. https://doi.org/10.1016/S1046-2023(02)00204-9.
15. R. Phienluphon, K. Pinkaew, G. Yang, J. Li, Q. Wei, Y. Yoneyama, T. Vitidsant, N. Tsubaki, *"Designing core ($Cu/ZnO/Al_2O_3$)–shell (SAPO-11) zeolite capsule cata lyst with a facile physical way for dimethyl ether direct synthesis from syngas"*, Chem. Eng. J. 270 (2015) 605–611. https://doi.org/10.1016/j.cej.2015.02.071.
16. M. Nuño, R. J. Ball, C. R. Bowen, *"Study of solid/gas phase photocatalytic reactions by electron ionization mass spectrometry: study of photoreactions by mass spectrometry"*, J. Mass Spectrom. 49 (2014) 716-726. https://doi.org/10.1002/jms. 3396.
17. S. Ke, X. Cheng, Q. Wang, Y. Wang, Z. Pan, *"Preparation of a photocatalytic $TiO_2/ZnTiO_3$ coating on glazed ceramic tiles"*, Ceram. Int. 40 (2014) 8891–8895. https://doi.org/10.1016/j.ceramint.2014.01.027.
18. M. Landmann, E. Rauls, W.G. Schmidt, *"The electronic structure and optical response of rutile, anatase and brookite TiO_2"*, J. Phys. Condens. Matter 24 (2012) 195503. https://doi.org/10.1088/0953-8984/24/19/195503.
19. W. J. Yin, S. Chen, J. H. Yang, X. G. Gong, Y.

Yan, S. H. Wei, *"Effective band gap narrowing of anatase TiO_2 by strain along a soft crystal direction"*, Appl. Phys. Lett. 96 (2010). https://doi.org/10.1063/1.3430005 221901.

20. R. Long, N. J. English, *"Band gap engineering of double- cation-impurity-doped anatase-titania for visible-light photocatalysts: a hybrid density functional theory approach"*, Phys. Chem. Chem. Phys. 13 (2011) 13698–13703. https://doi.org/10. 1039/C1CP21454C.
21. S. G. Kumar, L. G. Devi, *"Review on modified TiO_2 photocatalysis under UV/Visible light: selected results and related mechanisms on interfacial charge carrier transfer dynamics"*, J. Phys. Chem. A 115 (2011) 13211–13241, https://doi.org/10.1021/ jp204364a.
22. Z. Li, Y. Hou, B. Ma, X. Wu, Z. Xing, K. Li, *"Super-hydrophilic porous TiO_2-ZnO composite thin films without light irradiation"*, Environ. Prog. Sustain. Energy 35 (2016) 1121–1124. https://doi.org/10.1002/ep.12308.
23. Y. Liang, H. Wang, H. Sanchez Casalongue, Z. Chen, H. Dai, *"TiO_2 nanocrystals grown on graphene as advanced photocatalytic hybrid materials"*, Nano Res. 3 (2010) 701–705. https://doi.org/10.1007/s12274-010-0033-5.
24. M. Nuño, G. L. Pesce, C. R. Bowen, P. Xenophontos, R. J. Ball, *"Environmental performance of nano-structured $Ca(OH)_2/TiO_2$ photocatalytic coatings for buildings"*, Build. Environ. 92 (2015) 734-742. https://doi.org/10.1016/j.buildenv.2015.05. 028.
25. M. Nuño, R. J. Ball, C. R. Bowen, R. Kurchania, G. D. Sharma, *"Photocatalytic activity of electrophoretically deposited (EPD) TiO_2 coatings"*, J. Mater. Sci. 50 (2015) 4822-4835. https://doi.org/10.1007/s10853-015-9022-0.

Facile Synthesis and Electrical Properties of Chromium Oxide Nanoparticles

Azra Parveen

Department of Applied Physics, Z.H. College of Engineering & Technology, Aligarh Muslim University, Aligarh-202002, India.

azrap2001@gmail.com

Abstract

The synthesis of Cr_2O_3 nanocrystal has been done by chemical precipitation method using ammonia as a precipitating agent. The hexagonal crystal structure and single crystalline nature of Cr_2O_3 powder were verified by X-ray diffraction (XRD) analysis. Debye-Scherrer formula was utilized to ascertain the average size of crystallites. The structure, shape, size, and composition of Cr_2O_3 nanoparticles were probed by SEM (Scanning Electron Microscopy) and EDX (Energy Dispersive X-ray Spectrometry). Optical band gap energy was estimated by UV-Vis spectroscopy. The various functional groups in Cr_2O_3 nanoparticles were reckoned by FTIR (Fourier transform infrared spectroscopy) findings. Inductance, Capacitance, and Resistance (LCR) meter was used to ascertain the electrical behavior of Cr_2O_3 nanoparticles. These finding suggests that the synthesized nanocrystal may be used in development of the electrical and optoelectronic devices.

Keywords: Cr_2O_3 nanoparticles, X-ray diffraction (XRD), SEM, LCR.
Received 27 January 2025; First Review 21 February 2025; Accepted 24 April 2025.

*** Address of correspondence**
Azra Parveen
Department of Applied Physics, Z.H. College of Engineering & Technology, Aligarh Muslim University, Aligarh-202002, India.
Email: azrap2001@gmail.com

How to cite this article
Azra Parveen, Facile Synthesis and Electrical Properties of Chromium Oxide Nanoparticles, J. Cond. Matt. 2025; 03 (02): 124-127.

Available from:
https://doi.org/10.61343/jcm.v3i02.70

Introduction

Semiconductor metal oxide nanostructures are highly enviable for nanotechnological research despite of their peculiar structural geometry because of their large surface area and smaller size. This class of compounds often exhibit new and exciting features compared to their coarse-grained equivalent [1]. Chromium (III) oxide (Cr_2O_3) is one such metal oxide that is found in nature as an Eskolaite mineral. It is also called dichromium trioxide, or chromia, or chromium sesquioxide possessing a wide band gap and comes under the category of p-type metal oxide nanostructures [2]. G. Carta et al. found that chromium oxide (Cr_2O_3) is the hardest metal oxide with low friction coefficients [3]. Cr_2O_3 crystallizes into a rhombohedral structure having space group R-3c with lattice constants a = b = 4.953 Å and c = 13.578 Å [2]. G. Yasmeen and Jaswal *et al.* found that it may also crystallize into hexagonal shape [4, 5]. M. M. Abdullah *et al.* showed the ac conductivity of the Cr_2O_3 nanoparticles in the high frequency region and explained it according to the frequency power law. Cr_2O_3 nanoparticles can be used for applications such as pigment production, catalysts, solar energy collectors, thermal coating materials, optical storage materials, liquid crystal displays, and hydrogen storage [2,4]. This paper reports the synthesis and characterization of Cr_2O_3 nanoparticles via the facile chemical precipitation method. The characterizations were done by XRD, FTIR, UV-Vis spectroscopy, SEM and LCR.

Synthesis of Chromium Oxide

In a veritable synthesis process, 6g of chromium nitrate nonahydrate $Cr(NO_3)_3.9H_2O$ was dissolved in 100 ml of double distilled water (DDW). Drop by drop aqueous ammonia was added to the above solution along with the constant stirring. This was continued until the pH of the solution reached to 12 and the green precipitate was formed. The obtained precipitate was stirred on the magnetic stirrer at 80°C until it was burned out in ashes. The obtained residual ash was crushed and further calcined in a muffle furnace at 750°C for 4 hrs and then was again ground to attain a fine powder.

Results and Discussion

XRD Analysis

The X-ray diffraction spectrum of synthesized Cr_2O_3 nano powder is demonstrated in Figure 1. The distinct and intense peaks reveals that the prepared Cr_2O_3 nanoparticles is of high crystalline nature. The pattern matches with the standard JCPDS card number 38-1479 [3]. The XRD pattern does not contain any extra peaks other than Cr_2O_3 nano powder peaks showing that synthesized nano powder possesses a high degree of purity. These patterns also confirm the hexagonal structure of Cr_2O_3 nano powder with crystal parameters a = b = 4.9477 Å and c = 13.4534 Å and matches well with earlier studies [2]. In XRD pattern the peak broadening elucidate that small nanocrystals are present in samples. The intensity of the peak, its position, width, full-width at half-maximum (FWHM), and crystallite size were ascertained by using Powder X software. The experimental values of (d) are in a good agreement with the values which is reported in the previous studies [2]. Debye-Scherrer formula was used to evaluate the mean crystallite size (D) [6] and came out to be 25.12 nm.

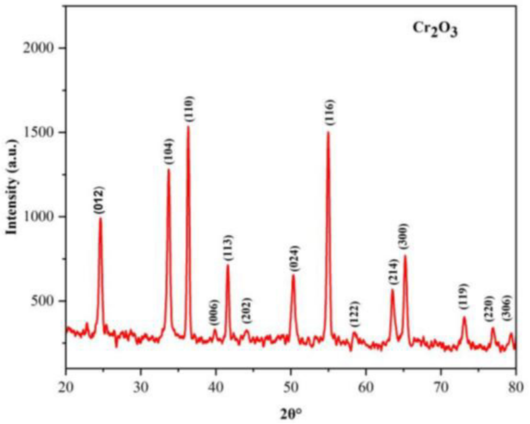

Figure 1: XRD pattern of Cr_2O_3 nanoparticles.

SEM and EDX Analysis

The surface structure of the produced Cr_2O_3 nanoparticles were examined by using a SEM microscope.

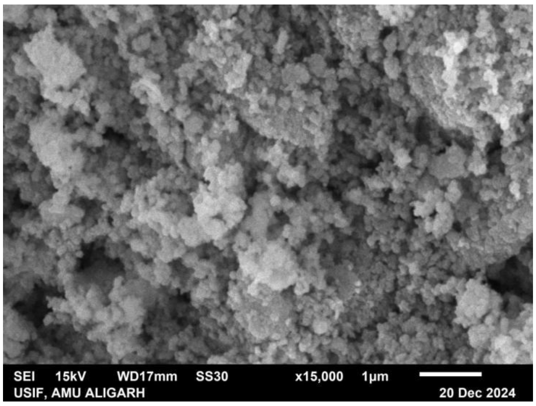

Figure 2 (a): SEM micrograph of Cr_2O_3 nanoparticles.

Figure 2 shows that all of the chromium oxide particles are having spherical shape and possesses a high degree of agglomeration The synthesized sample own good porosity as is clear from the micrograph. The shape of Cr_2O_3's spherical and agglomerating behaviour is in good agreement with the earlier research article [7]. Figure 2 (b) confirms the elemental composition of Cr_2O_3 through EDX spectra.

FTIR Analysis

FTIR technique in the range of 4000–500 cm^{-1} was used to ascertain the chemical composition and different functional groups (Figure 3). Generally, interatomic vibrations in metal oxides are characterized by the peaks below 1000 cm^{-1}. The broad bands at 3411 cm^{-1} and 1629 cm^{-1} owed to O-H stretching vibration because of adsorbed water from air and hydroxyl group.

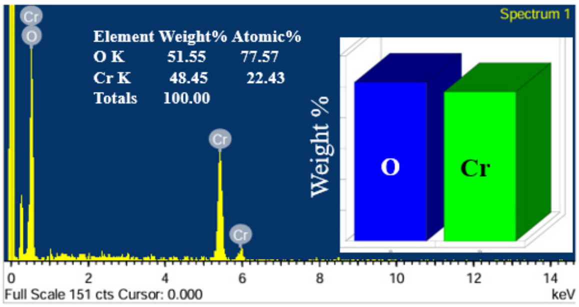

Figure 2 (b): EDX of Cr_2O_3 nanoparticles showing the elemental composition.

The C-O absorption of the Cr_2O_3 surface is depicted by the peaks at 1347 and 1182 cm^{-1}. The peaks at 1045, 639, and 563 cm^{-1} are the signature peaks of crystalline Cr_2O_3 nanoparticles. The band at 639 cm^{-1} is the identification of the chromium oxide nanoparticles as the Cr_2O_3 phase and the peak at 560 cm^{-1} characterizes the Cr–O distortion vibration [8]. The FTIR spectrum along with the XRD analysis confirm the successful creation of Cr_2O_3 nanoparticles.

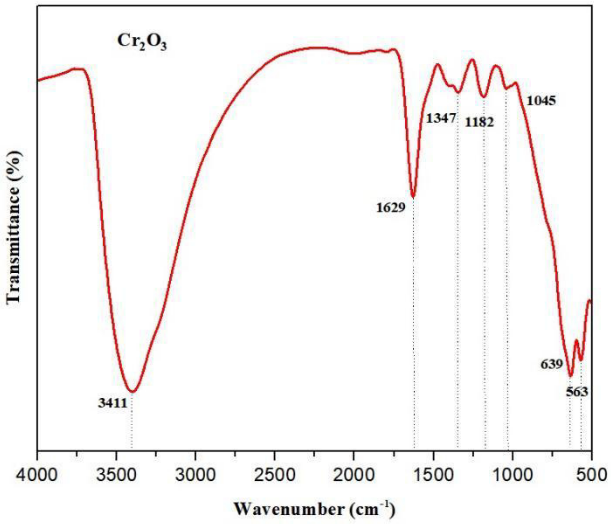

Figure 3: FTIR spectrum of Cr_2O_3 nanoparticles.

Optical Properties

Perkin Elmer Spectrophotometer was utilized to attain the absorption spectrum of Cr_2O_3 nanoparticles which reveals a strong absorption peak at 404 nm (Figure 4 (a)) confirming the d3 transition of chromium ion. A weak shoulder peak is also present at 480 nm [9]. This spectrum was further utilized to estimate the optical direct band gap (Figure 4 (b)), with the help of Tauc relation [10]. The obtained value of band gap energy with the value of 4.21 eV is in good agreement of the wide band gap nature of Cr_2O_3 nanoparticles.

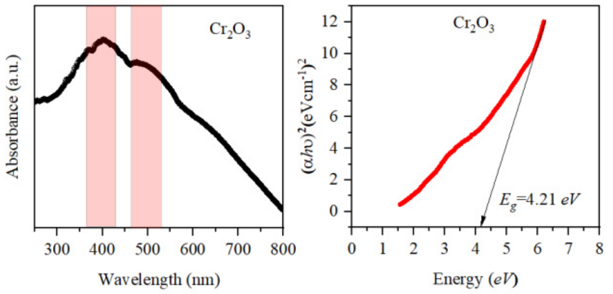

Figure 4: (a) Absorption spectrum and **(b)** band gap of Cr_2O_3 nanoparticles.

Electrical properties of Cr_2O_3 nanoparticles

Dielectric study was performed by LCR (Inductance Capacitance and Resistance) meter. Figures 5 (a to e) shows the frequency dependent behaviour of Cr_2O_3 nanoparticles with dielectric constant, loss, ac conductivity, and impedance. Both real and imaginary part of dielectric constant shows a decrease and a constant behaviour at high frequency value (Figures 5 (a) and (b)).

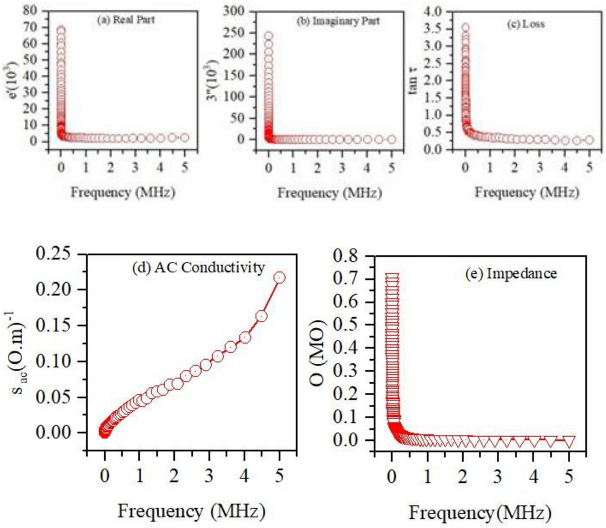

Figure 5: (a-e) Electrical behaviour of Cr_2O_3 nanoparticles.

High value at low frequency may occur due to the interfacial or space charge polarization caused by porosity and grain structure. The porosity of the prepared nanoparticles is clearly visibly for SEM image also. Decreasing trend may be due to the dielectric relaxation whereas the constant nature may be attributed to the fact that electric dipole freezes through the relaxation process.

Figure 5 (c) shows the decrease in dielectric loss with the increasing frequency and may be due to the marginal resistance of the grain. Figure 5 (d) indicates the increasing trend with increasing frequency and clearly suggest the good ac conductivity of Cr_2O_3 nanoparticles [11]. Thus, the results show that Cr_2O_3 nanoparticles have significant dielectric dispersion at low frequencies due to polarization effects and improved conductivity with reduced impedance at higher frequencies, making them appropriate for high-frequency applications. Cr_2O_3 is showing an identical frequency-dependent dielectric behavior with other transition metal oxides, such as CoO, NiO, and ZnO [12]. The dielectric constant (ε') in metal oxide nanoparticles generally shows a significant drop with increasing frequency due to the inability of dipoles to keep up with rapid field oscillations. Studies on Cr_2O_3 nanoparticles have reported high dielectric values at low frequencies, primarily due to interfacial polarization, followed by a sharp decline as frequency increases, aligning with the Maxwell-Wagner polarization model [11]. Thus, the prepared Cr_2O_3 nanoparticles exhibits similar dielectric and electrical properties as to other transition metal oxides with a minor variation in values reported across different studies that may be due to the differences in synthesis methods, particle size, and processing conditions. Overall, our experimental results align well with literature reports, further validating the frequency-dependent behaviour of Cr_2O_3 nanoparticles.

Conclusions

The facile precipitation approach of creating Cr_2O_3 nanoparticles utilizing ammonia and $Cr(NO_3)_3.9H_2O$ as a chromium source has been presented in this work. The high crystalline character of the Cr_2O_3 lattice with a hexagonal phase is supported by the XRD examination, which also demonstrates the notable pure synthesis of Cr_2O_3 nanoparticles. The sample's spherical shape and aggregation are shown by its morphology through SEM. EDX confirms the elemental composition. Functional groups in Cr_2O_3 nanoparticles were detected by FTIR spectra. The band gap energy of 4.21 eV shows a wide band gap nature of prepared sample. Dielectric and ac conductivity studies shows that Cr_2O_3 nanoparticles may turn up a meriting candidate in electrical and optoelectronic applications.

Acknowledgment

This work is fully supported by the Council of Science and Technology (CST) U.P. India for providing financial assistance under project no. CST/D-1519.

References

1. A M Abu-Dief, J Nanotechnol. Nanomaterials, 1(1):5-10, 2020.
2. M M Abdullah, F M Rajab and S M A Abbas, AIP Adv., 4:0–11, 2014.
3. G Carta, M Natali, G Rossetto, P Zanella, G Salmaso, S Restello, V Rigato, S Kaciulis and A Mezzi, Chem. Vap. Depos., 11:375–380, 2005.
4. G Yasmeen, S Hussain, A Tajammal, Z Mustafa, M Sagir, M Shahid, M Ibrar, M Nisa, Z M Elqahtani, and M Iqbal, Arabian Journal of Chemistry, 16 (8): 104912, 2023.
5. V S Jaswal, A K Arora, M Kinger, V D Gupta, and J Singh, Orient J Chem., 30(2), 2014.
6. H S Mahdi, A Parveen, and A Azam, AIP Conf. Proc., 1953: 030031, 2018.
7. T M A Saadi, and N A Hameed, Advances in Physics Theories and Applications, 44, 2015.
8. A D Khalaji, Nanochem Res., 5(2): 148-153, 2020.
9. A D Khalaji, Nanochem Res., 6(1): 18-24, 2021.
10. A Parveen, S A Ahmad, and A Azam, AIP Conference Proceedings, 2115: 030079, 2019.
11. M H Abbas, A Hadi, B H Rabee, M A Habeeb, M K Mohammed, and A Hashim, Journal of Composite and Advanced Materials, 33(4), 261-266, 2023.
12. T Wang, J Hu, H Yang, L Jin, X Wei, C Li, F Yan, Y Lin, Ceramics. J. Appl. Phys., 121 (8): 084103, 2017.

Structural, Morphological, Compositional, Electrical, and Optical Characterizations of CuZnS Thin Films Prepared using Chemical Bath Deposition Method

Preetha K C[1,2,a] and Bini S[1,b]

[1] Department of Physics, Sree Narayana College, Nattika, University of Calicut, Kerala, India.
[2] Research Department of Physics, Sree Kerala Varma College, Thrissur, University of Calicut, Kerala, India.

[a] preethasajitht@gmail.com
[b] binis@keralavarma.ac.in

Abstract

The universality, affordability and abundance of solar energy combined with its free and high energy output make it an exceptional renewable energy source. Solar cells play a vital role in converting sunlight into electrical energy. CuZnS has gained significant attention as a potential absorber material for solar cells. In the present work, we report the preliminary results of the preparation of CuZnS thin films using a relatively low-cost Chemical Bath Deposition technique, from a precursor solution containing 0.1M concentrations of copper chloride, zinc chloride, and thiourea. Triethanolamine (TEA) is used as the complexing agent, and ammonia is used to control the pH of the solution. The samples were prepared by keeping the pH at 11.6, maintaining the temperature at 80°C, and a deposition time of 1 hour. Structural, morphological, compositional, electrical, and optical analyses of the prepared samples were done. From the SEM analysis grain size calculated is 177 nm. The observed bandgap value was 2.61 eV at a Cu/(Cu+Zn) ratio of 83%. The prepared sample is a p-type semiconductor with a conductivity $1.646 \mathrm{X} 10^{-3} \Omega^{-1} \mathrm{cm}^{-1}$. XRD [Bruker Kappa Apex II], SEM-EDAX [Jeol 6390LA/OXFORD XMX N], Hall effect measurement system [Ecopia HMS 3000s], and UV-Vis Spectrophotometry [JASCO V-670 UV-Vis NIR Spectrophotometer] were used for the characterization of the samples.

Keywords: CuZnS, Chemical bath deposition, Preparation of thin film, Characterization of thin film.
Received 28 January 2025; First Review 22 March 2025; Accepted 24 April 2025.

*** Address of correspondence**
Preetha K C
Department of Physics, Sree Narayana College, Nattika, University of Calicut, Kerala, India.

Email: preethasajitht@gmail.com

How to cite this article
Preetha K C and Bini S, Structural, Morphological, Compositional, Electrical, and Optical Characterizations of CuZnS Thin Films Prepared using Chemical Bath Deposition Method, J. Cond. Matt. 2025; 03 (02): 128-132.

Available from:
https://doi.org/10.61343/jcm.v3i02.77

Introduction

CuZnS is a semiconductor with highly desirable photovoltaic properties, including a high absorption coefficient and a direct bandgap. The direct bandgap energy varies from 1.8 to 3.5 eV as the Cu/(Cu+Zn) ratio increases from 0 to 67%. CuZnS film prepared using spray pyrolysis with Cu/(Cu+Zn) ratio of 50% exhibited a bandgap of 2 eV [1]). Reported bandgap for the CuZnS films prepared using the SILAR method is 2.4 to 2.6 eV for copper-rich CuZnS samples [2]. In our present study the observed bandgap value was 2.61 eV at a Cu/(Cu+Zn) ratio of 83%. These thin films are used as an absorber or window layer, and their electrical and optical characteristics can be adjusted by changing the atomic ratios of copper and zinc [3-5]. Furthermore, CuZnS cells employ affordable, nontoxic, and plentiful (rare-earth-free) metals [2]. It is a favorable material for numerous applications in photovoltaic cells and photoconductor devices [6-8]. Ternary materials are appropriate for use in window-layer solar cells and optoelectronic devices [9]. The various techniques used to develop thin films include thermal evaporation [10], chemical spray pyrolysis [1], successive ionic layer adsorption and reaction [2], electrochemical deposition [11], photochemical deposition [12], pulsed laser deposition [13] and chemical bath deposition [14]. The chemical bath deposition method has drawn much attention due to its low cost, non-toxicity, ease of use, and compatibility for large-area deposition and film homogeneity [15,16]. In this study, we used the chemical bath deposition method to prepare CuZnS thin films and electrical, optical, morphological, structural, and compositional characterizations of these films were done.

Experimental Details

1. Materials

CuZnS thin film was prepared using a low-cost chemical bath deposition technique. The precursor solution contains copper chloride, zinc chloride, triethanolamine (TEA), ammonia, and thiourea. TEA acts as a complexing agent, and ammonia regulates the pH of the solution. Samples were prepared to optimize the molarity of the reactants, amount of TEA, pH of the solution, deposition time, and temperature. Magnetic stirrer was used to mix the solution during the deposition process. Thoroughly cleaned and dried glass substrates were placed in the precursor solution. The glass plates were kept in the solution for one hour at a temperature of 80 °C. The best sample was obtained from a solution containing 5 ml of 0.1M copper chloride, 5 ml of 0.1M zinc chloride, 10 ml of 0.1M thiourea, 4 ml of TEA, and 3 ml of ammonia. This film was analysed using different characterization techniques.

2. Method

To prepare the thin film, 2 ml of Triethanolamine (TEA) was mixed with 5ml of 0.1M copper chloride solution to form a complex. Then, 2 ml of TEA and 3ml of ammonia were mixed into 5 ml of 0.1 M zinc chloride solution to make another complex. The individually made complexes were combined and thoroughly stirred for 5 minutes until homogeneous. 10 ml of 0.1 M thiourea and 5 ml of distilled water were added dropwise from the burette to the solution while stirring. Then the solution was heated to 80°C using a water bath, and well-cleaned glass substrates were dipped in it for one hour, maintaining a constant temperature. The solution gradually changes its colour from blue to brown, and glass substrates are uniformly coated with CuZnS. These films were washed, dried, and used for various analyses. Figure 1 shows the experimental setup and the CuZnS samples prepared using CBD.

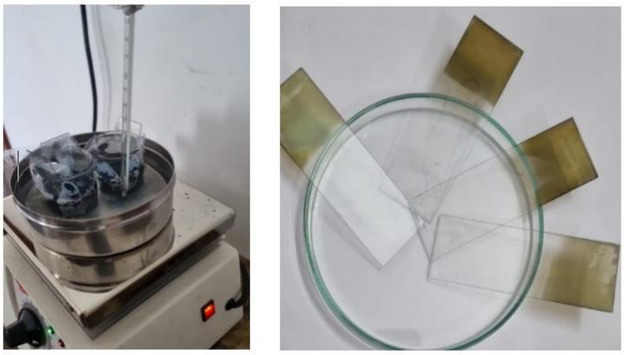

Figure 1: Experimental setup and the CuZnS samples prepared using CBD.

Results and Discussion

X-ray Diffraction Spectroscopy (XRD)

XRD can provide information on the material structure, phase composition, and crystal characteristics of prepared thin films [17]. Additionally, we can identify whether the thin film is crystalline or amorphous. For XRD analysis is, Bruker Kappa Apex II with CuKα wavelength 1.5406 Å was used. The XRD spectrum spans the 2θ range from 10° to 90°. Figure 2 depicts the XRD pattern of the CuZnS thin film, with the broadening of peaks reflecting the formation of nanoparticles.

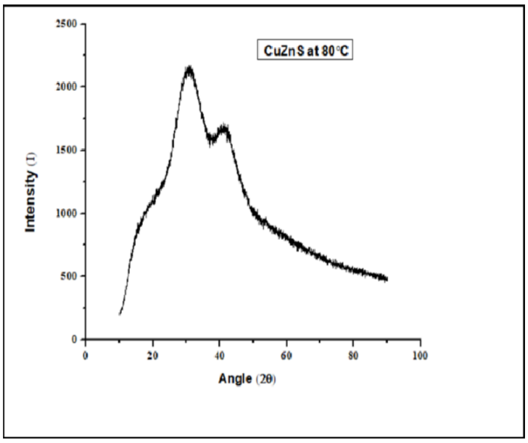

Figure 2: XRD pattern of CuZnS thin films prepared by CBD method.

The structural study of CuZnS thin film samples obtained by XRD shows two peaks, one at 30.881° and the other at 41.066°.

Table 1: Comparison of observed values with ICSD standard reference code.

Chemical formula	Standard 2θ Values	Intensity (in percentage)	Observed 2θ Values	Observed Intensity (in percentage)	hkl	D[Å]
ICSD Reference code: 98-062-8980						
Cu(0.12)Zn(3.88)S2(4)	**30.018**	**100**	**30.881**	**100**	**002**	**2.9745**
	42.967	**50.3**	**41.066**	**79**	**022**	**2.1033**
ICSD Reference code: 98-062-8979						
Cu(3.2)Zn(0.8) S2(4)	**30.683**	**100**	**30.881**	**100**	**002**	**2.9115**
	43.945	**48.7**	**41.066**	**79**	**022**	**2.0587**

These peak values are compared with the standard ICSD reference values (ICSD Ref codes 98-062-8979 and 98-062-8980), which are listed in Table 1. The two peak values correlate to the ICSD values for planes (002) and (022), indicating a cubic structure based on these ICSD values. The hundred percentage peak matched well with ICSD Ref code 98-062-8979, while the second peak has a 1° discrepancy in 2θ value compared to ICSD Ref codes of Cu((0.12)Zn(3.88)S2(4)). The change in results could be attributed to the existence of distinct phases of CuZnS in the sample or to variations in the Cu to Zn ratio. The crystallite size of the material can be calculated using the Debye–Scherrer formula from X-ray diffraction (XRD) data.

$$D = \frac{K\lambda}{\beta \, Cos\theta}$$

Where:
D = average crystallite size
K = Scherrer constant ~ 0.94 (depends on shape factor)
λ = X-ray wavelength in nm or Å, 1.5406 Å for Cu Kα lines
β = Full width at half maximum of the peak in radians
θ = Bragg angle

The crystallite size calculated using Debye-Scherrer formula is 1.35nm.

Energy Dispersive X-ray Spectroscopy (EDAX)

Energy Dispersive X-ray spectroscopy analysis was used to determine the elemental composition of the CuZnS sample [18]. The EDAX spectrum of the sample is displayed in Figure 3.

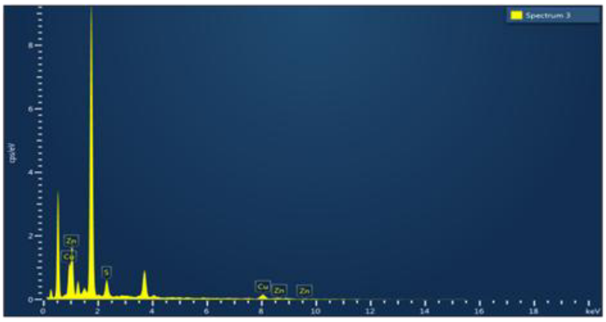

Figure 3. EDAX spectrum of CuZnS thin film prepared by CBD method.

Table 2: Elemental composition of CuZnS.

Element	Line Type	Wt %	Atomic%
Cu	K series	55.43	41.72
Zn	K series	10.77	7.88
S	K series	33.79	50.40
Total	K series	100	100

The atomic and weight percentages of the given sample are shown in Table 2. The CuZnS sample has an atomic percentage ratio of 41.72:7.88:50.40, and weight percentages of 55.43:10.77:33.79. Elemental analysis reveals that the prepared samples are enriched in copper with a low percentage of zinc. Zn deficiency has been reported in CuZnS thin films generated via the Silar technique [2]. Attempts are being made to improve the Zn content in the samples.

Scanning Electron Microscopy (SEM)

SEM examined the surface topography, microstructure and grain size of the CuZnS thin film samples [18,19]. This study exposes characteristics including conductivity and optical behaviour. There are no obvious cracks on the surface of the thin film. The particles are spherical in shape, nanostructured, uniform, and densely packed, making them suitable for photovoltaic applications. The thickness of the thin film was measured using a Dektak stylus profilometer and found to be 131 nm. Figure 4 (a), (b), (c), and (d) displays SEM images of CuZnS at varying resolutions (50 µm, 10 µm, 2 µm, 1 µm). The average particle size calculated from SEM analysis is 177nm. This is different from the value obtained from XRD (less than 5nm). It may be due to the grains themselves must be formed by the merging of closely packed nanocrystallites. This has been reported earlier [18].

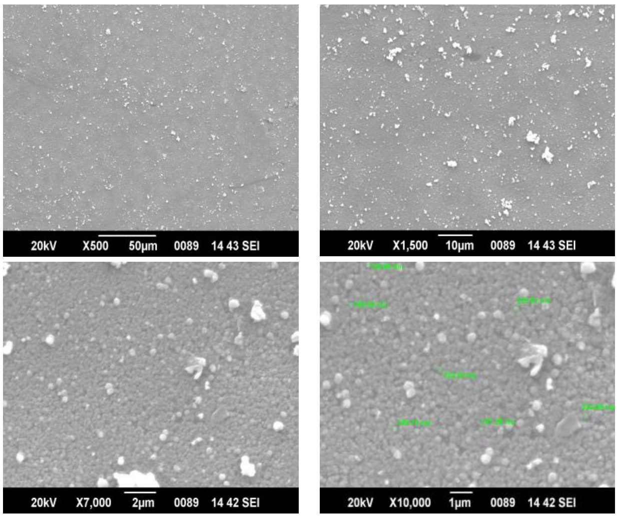

Figure 4: (a), (b), (c), (d) SEM images of CuZnS thin film prepared by CBD method.

UV Visible spectroscopy

The analytical method (UV-Vis) is used to determine the optical properties, electrical structure, and material composition of the sample. JASCO V-670 UV-Vis NIR Spectrophotometer was used for optical analysis. The optical absorption spectra of CuZnS thin films were studied within 350 and 900 nm. Figure 5 shows the absorption spectra of CuZns. The direct bandgap of CuZnS was determined using a Tauc's plot ((αhυ)2 vs. hν plot) [20]. Figure 6 shows the Tauc's plot of CuZnS, with a bandgap value of 2.61eV. This value falls within the standard range 1.8 - 3.5 eV reported in spray pyrolysis [1]) and 2.4 to 2.6 eV reported in SILAR method is for copper-rich CuZnS samples [2].

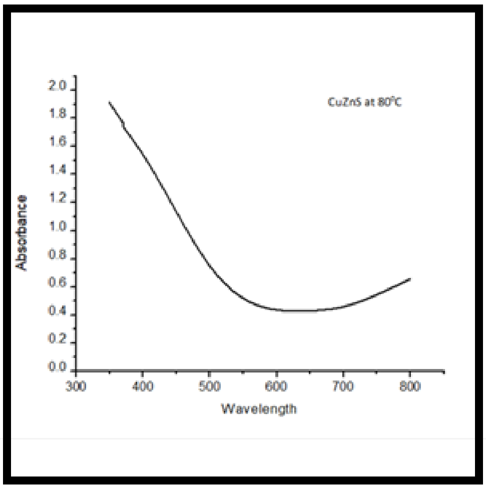

Figure 5: Absorption spectra of CuZnS thin film.

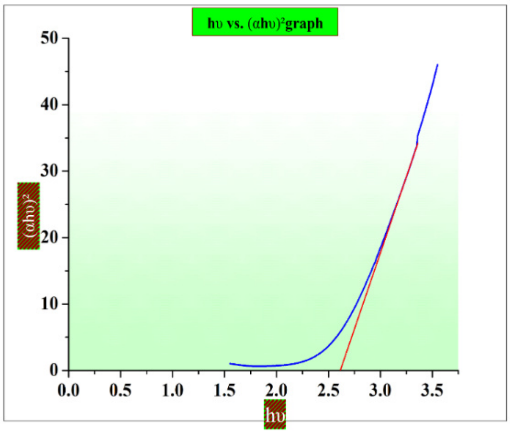

Figure 6: Tauc's plot (Direct bandgap of CuZnS thin film)

Hall Effect measurement

The Hall Effect measurement technique is extremely accurate for electrical analysis. The Hall coefficient value can detect whether the material is p-type or n-type. Thin film samples are analyzed to determine the sample's bulk concentration, mobility, sheet resistance, resistivity, conductivity, and average Hall coefficient. Optimizing semiconductor electrical properties can improve their applications in solar cells as well as sensors. Based on the Hall coefficient measurement of the CuZnS samples, the average Hall coefficient value obtained is $4.701 \times 10^4 cm^3/C$. This clearly indicates that the prepared samples are of p-type conductivity.

The conductivity of the sample is 1.646×10^{-3} $\Omega^{-1}cm^{-1}$. The conductivity value reported earlier for thermal evaporated film is 63.3 $\Omega^{-1}cm^{-1}$ [10] and for MOCVD (Metal oxide chemical vapour deposition method) is 5.48×10^{-1} to 8.0×10^{-1} $\Omega^{-1}cm^{-1}$ [15]. Table 3 shows the Hall parameters of CuZnS thin films.

Table 3. Hall parameters of CuZnS thin film

Hall Parameters	
Bulk concentration in cm^3	1.328×10^{14}
Mobility in cm^2/vs	7.738×10^1
Sheet resistance in Ω/sq	4.637×10^7
Resistivity in Ωcm	6.075×10^2
Conductivity in $\Omega\text{-}^1cm^{-1}$	1.646×10^{-3}
Average Hall coefficient in cm^3/C	4.701×10^4

Conclusion

The CuZnS samples are relatively homogeneous. The XRD study confirms that the hundred percentage peak corresponds to ICSD Ref code 98-062-8980. However, the second peak differs by 1° in 2θ value from the same ICSD Ref code. The EDAX analysis reveals that the prepared samples are enriched in copper with a low percentage of zinc. SEM analysis revealed that the particles exhibited a spherical shape and the average particle size is 177nm. The samples are more or less uniform. Based on the optical characterization, the prepared sample has a bandgap energy of 2.61 eV. The average Hall coefficient value of $4.701 \times 10^4 cm^3/C$ indicates that the prepared sample is a p-type semiconductor. The samples resistivity is 6.075×10^2 and conductivity is 1.646×10^{-3} $\Omega\text{-}^1cm^{-1}$, these values fall within the benchmark value for semiconductors.

Future plans

As the samples exhibit Zn deficiency, further research is needed to increase the Zn content. Attempts are being made to improve the Zn content and to make the film more stoichiometric.

Acknowledgments

The authors truly acknowledge the funding support from DST-FIST & KSCSTE Thiruvananthapuram. We are thankful to DST SAIF COCHIN and SAIF IIT Bombay for providing support and thankful to the Department of Physics, Sree Narayana College, Nattika, the Research Department of Physics, Sree Kerala Varma College, Thrissur and the Directorate of Research, university of Calicut for extending facilities for the research work.

References

1. Kitagawa, N, Ito S, Nguyen D and Nishino H, "*Copper zinc sulfur compound solar cells fabrication by spray pyrolysis deposition for solar cells*", Natural Resources,
   DOI: 10.4236/nr.2013.41A018, 2013
2. Edwin Jose, M C Santhosh Kumar, *"Room temperature deposition of highly crystalline Cu-Zn-*

S thin films for solar cell applications using SILAR method", Alloys and Compounds, DOI:10.1016/j.jallcom.2017.04.097, 2017.

3. M S Sreejith, D R Deepu, C Sudha Kartha, K P Vijayakumar, *"Tuning Of Properties of Sprayed CuZnS Films"*, AIP Conference Proceedings, DOI: 10.1063/1.4873096, 2014.
4. P A, M C S, *"Deposition and characterization of earth abundant CuZnS ternary thin films by vacuum spray pyrolysis and fabrication of p-CZS/n-AZO heterojunction solar cells"*, Int J Energy Res., DOI:10.1002/er.5515, 2020.
5. J. Jubimol, M. S. Sreejith, C. Sudha Kartha, K. P. Vijayakumar, and Godfrey Louis, *"Photoluminescence studies on copper zinc sulfide thin films synthesized through chemical bath deposition"*, AIP Conference Proceedings, DOI:10.1063/1.5093865, 2019.
6. Jubimol J, Sreejith M S, Kartha C S, Vijayakumar K P, Louis G., *"Analysis of spray pyrolysed copper zinc sulfide thin films using photoluminescence"*, Luminescence, DOI: 10.1016/J.JLUMIN.2018.06..079, 2018.
7. Uhuegbu C C and Babatunde E B, *"Spectral analysis of copper zinc sulphide ternary thin film grown by solution growth technique"*, American journal of scientific and industrial research, DOI:10.5251/ajsir.2010.1.3.397.400 2010.
8. W.T.R.S. Fernando, K M D C Jayathilekea, R P Wijesundera and W. Siripala, *"Growth of CuZnS thin films for PV applications"*, Conference: Proceedings of the 33rd Technical Sessions, 33 (2017) 12-18, Institute of Physics at University of Kelaniya, Sri Lanka,2017
9. Uhuegbu C. C. and Babatunde E.B., *"The Study of Copper Zinc Sulphide* ($CuZnS_2$)*, Thin Films"*, Turkish Journal of Physics, Vol. 32, No.1, Article 6 (39 – 47), 2008.
10. Sundaram, Saravanan Krishna, Subramanian, Selladurai, Panneerselvam, Vengatesh, Salammal, Shyju Thankaraj, "*Temperature-dependent phase transition of CuZnS thin films and its effects on morphological"*, optical and electrical properties, Thin Solid Films, DOI:10.1016/j.tsf.2021.138810, 2021.
11. K. Yang, Y. Nakashima and M. Ichimura, *"Electrochemical Deposition of CuxS and CuxZnyS Thin Films with p-Type Conduction and Photosensitivity"*, J. Electrochem. Soc. 159 (2012) H250, DOI:10.1149/2.042203jes, 2012
12. M. Dula, K. Yang and M. Ichimura, *"Photochemical deposition of a p-type transparent alloy semiconductor CuxZnyS"*, Semicond. Sci. Technol., 27 (2012) 125007, DOI:10.1088/0268-1242/27/12/125007, 2012
13. A. M. Diamond, L. Corbellini, K. R. Balasubramaniam, S. Chen, S. Wang, T. S. Matthews, L. Wang, R. Ramesh and J. W. Ager, *"Copper-alloyed ZnS as a p-type transparent conducting material"*, Physica Status Solidi (a), 209 (11) (2012) 2101-2107, DOI:10.1002/pssa.201228181, 2012
14. C. C. Uhuegbu, and E. B. Babatunde, *"Spectral analysis of copper zinc sulphide ternary thin film grown by solution growth technique"*, Am. J. Sci. Ind. Res., 1 (3) (2010) 397-400, DOI:10.5251/ajsir.2010.1.3.397.400, 2010
15. Joseph Onyeka Emegha, Bolutife Olofinjana, Ukhurebor, Joseph Adegbite, *"Electrical Properties of Semiconducting Copper Zinc Sulphide Thin Films"*, Current Applied Science and Technology, DOI:10.55003/cast.2022.01.22.003, 2021.
16. Kavita Sahebrav Jadhav, Nanasaheb Huse, *"Investigation of Optical and Electrical Properties of CuZnS Thin Film Deposited by Chemical Bath Deposition Method"*, Innovative Research in Science, Engineering and Technology (IJIRSET), Volume 10, Issue 8, 2347-6710, 2021.
17. Gardew Dubale, Derejaw, Abza Abshiro, Tizazu, and Gashaw Hone, Fekadu, *"Synthesis and Characterization of Copper Zinc Sulfide* ($Cu_xZn_{(1-x)}S$) *Ternary Thin Film by Using Acidic Chemical Bath Deposition Method"*, Thin Films Science and Technology, 2021, digitalcommons.aaru.edu.jo/ijtfst/vol10/iss1/4.
18. Fatemeh Aghaei, Reza Sahraei , Ehsan Soheyli, Ali Daneshfar, *"Dopant-Concentration Dependent Optical and Structural Properties of Cu-Doped ZnS Thin Films"*, J Nanostruct 12(2): 330-342, Spring 2022, DOI: 10.22052/JNS.2022.02.010, 2022.
19. Adel H. Omran Alkhayatt, Azher Abdul Wahab Habieb, Abbas Hadi Abbas Al-Noaman and Ali Abdulhussein Hameed, *"Structure, surface morphology and optical properties of* $Cu_xZn_{1-x}S$*/Au NPs layer for photodetector application"*. IOP Conf. Series: Journal of Physics: Conf. Series, DOI 10.1088/1742-6596/1234/1/012012, 2012
20. Ifeyinwa Amaka Ezenwa and Okoli Nonso L. *"Characterization of chemically synthesized Copper Zinc Sulphide* ($CuZnS_2$) *thin film"*, European open applied physics journal, Vol.1, No.1, 1-9, 2015.

Synthesis and Photoluminescence in Garnet-type $CaLa_2Al_4SiO_{12}:Dy^{3+}$ Phosphor for Optical Applications

Ganesh C. Vandile[1,a], Deoram V. Nandanwar[1,b], Amar K. Nandanwar[2], Shruti P. Dhale[3], Bhupendra P. Walde[1], Shruti M. Hargude[1], Nilesh S. Ugemuge[3]

[1] *Department of Physics, Shri Mathuradas Mohota College of Science, Nagpur-440009, India.*
[2] *Department of Physics, J. M. Patel Arts, Commerce & Science College, Bhandara-441904, India.*
[3] *IHLR & SS, Department of Physics Anand Niketan College of Science, Arts and Commerce Warora, Dist-Chandrapur, 442914, India.*

[a] ganesh9326wandile@gmail.com
[b] dvnandanwar@gmail.com

Abstract

The series of xDy^{3+} doped $CaLa_2Al_4SiO_{12}$ garnet-structured phosphors were synthesized by conventional combustion method. The prepared materials were studied using various techniques such as x-ray powder diffraction for crystal structure and phase, photoluminescence for optical properties, scanning electron microscopy (SEM) for morphological studies, and energy dispersive spectroscopy analyses for the existence of elements in the prepared materials. The excitation and emission of the prepared garnet-type phosphor were recorded at 351 nm in the transition from $^6H_{15/2} \rightarrow {}^6P_{7/2}$ and 584 nm in the transition from $^4F_{9/2} \rightarrow {}^6H_{13/2}$. The concentration quenching obtained at 7.0 mol.% of dysprosium ions. This phosphor has potential application in w-LED and other optical devices.

Keywords: Photoluminescence; $CaLa_2Al_4SiO_{12}$; Garnet; Dysprosium.
Received 22 March 2025; First Review 17 April 2025; Accepted 18 April 2025.

*** Address of correspondence**
Ganesh C. Vandile
Department of Physics, Shri Mathuradas Mohota College of Science, Nagpur-440009, India.

Email: ganesh9326wandile@gmail.com

How to cite this article
Ganesh C. Vandile, Deoram V. Nandanwar, Amar K. Nandanwar, Shruti P. Dhale, Bhupendra P. Walde, Shruti M. Hargude, Nilesh S. Ugemuge, Synthesis and Photoluminescence in Garnet-type $CaLa_2Al_4SiO_{12}:Dy^{3+}$ Phosphor for Optical Applications, J. Cond. Matt. 2025; 03 (02): 133-136.
Available from:
https://doi.org/10.61343/jcm.v3i02.152

Introduction

Efficient lighting devices based on the light emitting diode have attracted great attention in recent time. The solid-state lighting devices are considered as the energy saving light emitting devices than incandescent bulbs [1]. In order to increase the colour stability and life time, the garnet-type phosphor is used in white light emitting devices (w-LEDs) [2]. The luminescence immunoassays is an example of the many uses for garnet-structure phosphor, which are used in a variety of industries, including clinical studies, environmental surveillance, food hygiene, and pharmaceutical testing [3]. The garnet-type phosphors are mostly used in the industry related to optoelectronics [4]. We mostly used various kinds of highly efficient lighting devices now days because of their luminescence efficiency. Among them, phosphor converted light emitting diodes are used [5]. In order to increase quantum yield and luminous intensity, we are choosing garnet-type phosphor. Dy^{3+} doped garnet phosphor uses in the fields of lighting devices as w-LEDs.

The trivalent dysprosium ions are the best dopant with emission in blue and yellow regions [6]. The $^4F_{9/2} \rightarrow {}^6H_{15/2}$ and $^4F_{9/2} \rightarrow {}^6H_{13/2}$ transitions cause blue and yellow emissions respectively to appear when dysprosium trivalent ions are doped with phosphor [7]. By doping dysprosium trivalent ions (Dy^{3+}) in a suitable phosphor for the proper and pure white lighting devices should be obtained by improving the yellow-blue intensities [8]. As the garnet silicate phosphor host are favourable due to their thermal and chemical equilibrium stabilities [9].

Haipeng *et al.* have prepared garnet-silicate phosphor like $BaY_2Al_4SiO_{12}$, $SrY_2Al_4SiO_{12}$, $CaY_2Al_4SiO_{12}$ and $MgY_2Al_4SiO_{12}$ by solid state reaction synthesis method [10]. In our earlier work we have synthesized $LiCa_3MgV_3O_{12}:Nd^{3+}/Yb^{3+}$ [12], $LiCa_3MgV_3O_{12}$ activated with Er^{3+} [11] and $LiCa_3ZnV_3O_{12}:Nd^{3+}$ [13]. The garnet type phosphor CLASG has high chemical and thermal stability. The emission spectrum was obtained about greenish yellow in visible region while irradiating the material by UV or near-UV radiation [14].

In this paper, we have studied the novel garnet-structured $CaLa_2Al_4SiO_{12}$:Dy^{3+} phosphor first time. The major applications of this phosphor are optoelectronic devices as solid-state lighting and illumination [15].

Experimental

Materials and synthesis

Pristine $CaLa_2Al_4SiO_{12}$ and $CaLa_2Al_4SiO_{12}$:xDy^{3+} prepared by using simple combustion method. Calcium Nitrate ($Ca(NO_3)_2$, MERCK), Aluminium Nitrate ($Al(NO_3)_3$, MERCK), Silicon Oxide (SiO_2, MERCK), Lanthanum Oxide (La_2O_3, MERCK), and Dysprosium Oxide (Dy_2O_3, MERCK) mixed with Urea & Glycine as fuel in stoichiometric ratio. We used glycine as fuel for lanthanum oxide and dysprosium oxide and urea as fuel for rest of the nitrates [16].

Characterization

Excitation and emission spectra were recorded employing a fluorescence spectrophotometer (Hitachi Make F-7100). The phase was determined using the X-ray powder diffraction technique (Rigaku Miniflex, Cu-Kα wavelength 0.154059 nm). The surface study and compositional details were optimized using a FE-SEM JEOL, JSM-6500F.

Results and Discussion

X-Ray Diffraction

Figure 1(a) represent XRD pattern and Figure 1(b) refined XRD pattern of garnet-type phosphor.

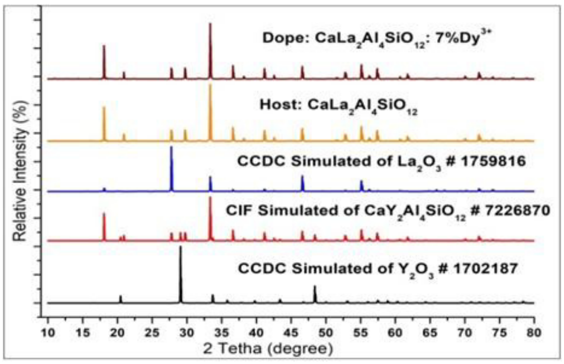

Figure 1: (a) The representation of XRD pattern of $CaLa_2Al_4SiO_{12}$, the comparison of XRD patterns of prepared un-doped and doped garnet materials with CIF simulated file #7226870, #1702157 for Y_2O_3 and #1759816 for La_2O_3.

All XRD peaks were indexed to cubic structure having space group Ia-3d. As the novel phosphor $CaLa_2Al_4SiO_{12}$ the conformation of the crystallographic structure were possible by matching the standard XRD pattern of $CaY_2Al_4SiO_{12}$, La_2O_3 and Y_2O_3 with standard CIF #7226870, CCDC #1759816 and CCDC #1702187. The details of the structural parameters and Wyckoff symbols are shown in Table 1. The lattice parameters (a = b = c=12.00062 A°) with relative error 0.09 % with calculated value [17]. Figure 1(a) shows that there was no effect due to doping in the garnet-structure phosphor.

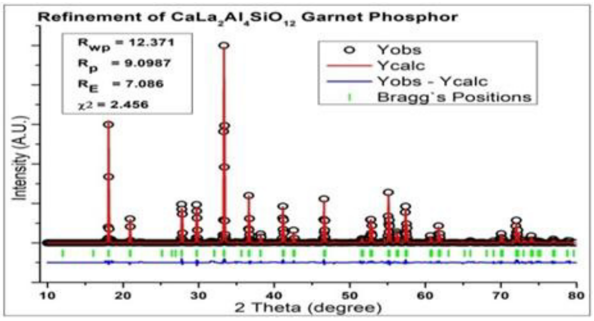

Figure 1: (b) The representation of refined XRD pattern of $CaLa_2Al_4SiO_{12}$.

Table 1: Details of phase identification of XRD data with Rietveld refinement.

<table>
<tr><th colspan="2">Compound</th><th>$CaLa_2Al_4SiO_{12}$</th></tr>
<tr><td colspan="2">Crystal structure type</td><td>Cubic structure</td></tr>
<tr><td colspan="2">Space group</td><td>Ia-3d (230)</td></tr>
<tr><td colspan="2">Translational Lattice -parameters (a = b = c) in Å</td><td>12.00062 Å</td></tr>
<tr><td colspan="2">Volume of unit cell $(nm)^3$</td><td>1728.27 $Å^3$</td></tr>
<tr><td colspan="2">Chi^2</td><td>3.425</td></tr>
<tr><td colspan="2">R_p</td><td>9.0987</td></tr>
<tr><td colspan="2">R_{wp}</td><td>12.371</td></tr>
<tr><td colspan="2">Expected R_w</td><td>7.086</td></tr>
<tr><th colspan="3">Wyckoff symbols</th></tr>
<tr><th>Ions</th><th>Symbols</th><th>Occupancy</th></tr>
<tr><td>Ca^{2+}</td><td>24c</td><td>1/3</td></tr>
<tr><td>La^{3+}</td><td>24c</td><td>2/3</td></tr>
<tr><td>Al^{3+}</td><td>16a</td><td>1</td></tr>
<tr><td>$Al1^{3+}$</td><td>24d</td><td>2/3</td></tr>
<tr><td>Si^{4+}</td><td>24d</td><td>1/3</td></tr>
<tr><td>O (for Ia-3d)</td><td>96h</td><td>1</td></tr>
</table>

Morphology and EDX

Figure 2 depicts FESEM images of the materials with different magnification. This technique is useful to investigate the grain size and surface study. To examine elemental composition of the material, it's characterized by EDX technique. Figure 3 show all elements are present with desired composition. The energy dispersive peaks are shown the host materials Ca, La, Al, Si and O as well as dopant Dy^{3+} ions.

Photoluminescence

Figure 4 (a) shows excitation spectrum of $CaLa_2Al_4SiO_{12}$:$0.07Dy^{3+}$. The excitation spectrum is obtained at the wavelength of 351 nm with emission wavelength 584 nm.

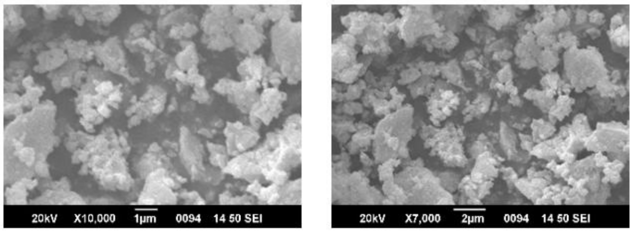

Figure 2: SEM images of as-prepared garnet phosphor $CaLa_2Al_4SiO_{12}$:Dy^{3+}.

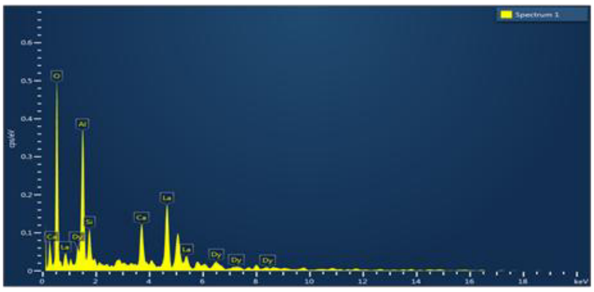

Figure 3: Energy Dispersive X-ray Spectrum of $CaLa_2Al_4SiO_{12}$:Dy^{3+}.

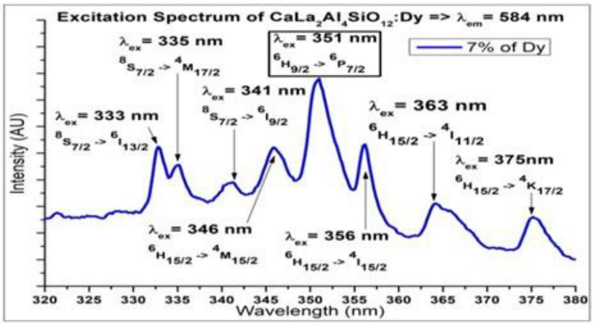

Figure 4 (a): Excitation spectrum of garnet-type phosphor $CaLa_2Al_4SiO_{12}$:Dy^{3+} is observed at 584 nm.

The electronic transition for the excitation is observed from $^6H_{15/2}$ → $^6P_{7/2.}$ There was serval peaks obtained at wavelengths 333, 335, 341, 346, 351, 356, 363 and 375 nm.

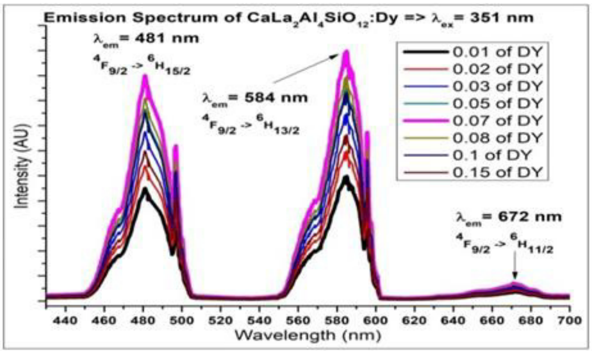

Figure 4 (b): Emission spectrum of garnet-type phosphor $CaLa_2Al_4SiO_{12}$:xDy^{3+} (x = 0.01, 0.02, 0.03, 0.05, 0.07, 0.08, 0.10, 0.15) is excited by 351 nm.

Figure 4 (b) depicts the emission spectrum of the garnet-type phosphor. The PL profile and position of the peaks does not change during the exciting at 351 nm [19]. The prepared material is useful for near UV, green and yellow LEDs.

Conclusion

Using conventional combustion reaction, a series of single phase Dy^{3+}-doped $CaLa_2Al_4SiO_{12}$ garnet phosphors were prepared. The single-phase crystallography was examined by XRD result. The most intense peak was obtained at 584 for $CaLa_2Al_4SiO_{12}$:7%Dy^{3+} in transition from $^4F_{9/2} \rightarrow {}^6H_{13/2}$. By FESEM and EDX, the materials were characterized surface study and chemical composition investigation respectively. The prepared materials were suitable in yellow colour lighting devices and w-LEDs.

References

1. Höppe, H. A. (2009). *Recent developments in the field of inorganic phosphors*. Angewandte Chemie International Edition, 48(20), 3572-3582.
2. Zhang, Q., Hu, Y., Ju, G., Zhang, S., & Xue, F. (2017). *Photoluminescence of a novel Na 3Y(VO_4) 2:Eu^{3+} red phosphor for near ultraviolet light emitting diodes application*. J. Materials Science: Materials in Electronics, 28, 2529-2537.
3. Welker, T. (1991). *Recent developments on phosphors for fluorescent lamps and cathode-ray tubes*. J. luminescence, 48, 49-56.
4. Yang, L., Chen, M., Lv, Z., Wang, S., Liu, X., & Liu, S. (2013). *Preparation of a YAG: Ce phosphor glass by screen-printing technology and its application in LED packaging*. Optics letters, 38(13), 2240-2243.
5. Liu, H., Liao, L., Molokeev, M. S., Guo, Q., Zhang, Y., & Mei, L. (2016). *A novel single-phase white light emitting phosphor $Ca_9La(PO_4)_5(SiO_4)F_2$:Dy^{3+}: synthesis*, crystal structure and luminescence properties. RSC Advances, 6(29), 24577-24583.
6. Shashikala, B. S., Premkumar, H. B., Darshan, G. P., Nagabhushana, H., Sharma, S. C., & Prashantha, S. C. (2019). *Rational design of bi-functional RE^{3+} (RE= Tb, Ce) and alkali metals (M^+= Li, Na, K) co-doped $CaAl_2O_4$ nanophosphors for solid state lighting and advanced forensic applications*. Materials Research Bulletin, 115, 88-97.
7. Dhale, Shruti, Nilesh Ugemuge, Vartika S. Singh, S. R. Dhakate, Aniket Bharti, Rajesh Kumar, and S. V. Moharil, *"Study of Luminescence Behavior in Dy^{3+}-Activated $Ba_3Ca_2(PO4)_3F$"*, J. Electronic Materials (2024): 1-11.
8. Lin, L., Zhonghua, Z. H. A. O., Zhang, W., Zheng, Z., & Min, Y. I. N. (2009). *Photo-luminescence properties and thermo-luminescence curve analysis of a new white long-lasting phosphor: $Ca_2MgSi_2O_7$: Dy^{3+}*. J. Rare Earths, 27(5), 749-752.
9. Ji, H., Wang, L., Cho, Y., Hirosaki, N., Molokeev,

M. S., Xia, Z., & Xie, R. J. (2016). *New Y_2BaAl_4 SiO_{12}:Ce^{3+} yellow microcrystal-glass powder phosphor with high thermal emission stability*. J. Materials Chemistry C, 4(41), 9872-9878.

10. Warutkar, G. N., Ugemuge, N. S., Pusdekar, A., Dhale, S., Sharma, K., Sankapal, B. R., ... & Moharil, S. V. (2025). *Near infrared emission in garnet structured $LiCa_3MgV_3O_{12}$:Nd^{3+}/Yb^{3+} phosphor*. Optik, 322, 172180.
11. Warutkar, G., Ugemuge, N., Dhale, S., Tumram, P. V., Tawalare, P. K., Nafdey, R., & Moharil, S. V. (2024). *Host sensitized mid-infrared emission in $LiCa_3MgV_3O_{12}$ activated with Er^{3+}*. Emergent Materials, 1-7.
12. Warutkar, G. N., Ugemuge, N. S., Sharma, K., Nafdey, R., & Moharil, S. V. (2023). *Nd^{3+} emission in the garnet structure of $LiCa_3ZnV_3O_{12}$ phosphor*. Radiation Effects and Defects in Solids, 178(11-12), 1479-1489.
13. Ji, H., Huang, Z., Xia, Z., Molokeev, M. S., Atuchin, V. V., Fang, M., & Liu, Y. (2015). *Discovery of new solid solution phosphors via cation substitution-dependent phase transition in $M_3(PO_4)_2$:Eu^{2+} (M= Ca/Sr/Ba) quasi-binary sets*. J. Physical Chemistry C, 119(4), 2038-2045.
14. Djamal, M., Yuliantini, L., Hidayat, R., Boonin, K., Yasaka, P., & Kaewkhao, J. (2018). *Glass medium doped rare earth for sensor material*. Materials Today: Proceedings, 5(7), 15126-15130.
15. Gotoh, T., Jeem, M., Zhang, L., Okinaka, N., & Watanabe, S. (2020). *Synthesis of yellow persistent phosphor garnet by mixed fuel solution combustion synthesis and its characteristic*. J. Physics and Chemistry of Solids, 142, 109436.
16. Shikao, S., & Jiye, W. (2001). *Combustion synthesis of Eu^{3+} activated $Y_3Al_5O_{12}$ phosphor nanoparticles*. J. alloys and compounds, 327(1-2), 82-86.
17. Ji, H., Wang, L., Cho, Y., Hirosaki, N., Molokeev, M. S., Xia, Z., ... & Xie, R. J. (2016). *New Y_2BaAl $_4SiO_{12}$:Ce^{3+} yellow microcrystal-glass powder phosphor with high thermal emission stability*. J. Materials Chemistry C, 4(41), 9872-9878.
18. Carnall, W. T., Fields, P. R., & Rajnak, K. (1968). *Electronic energy levels in the trivalent lanthanide aquo ions. I. Pr^{3+}, Nd^{3+}, Pm^{3+}, Sm^{3+}, Dy^{3+}, Ho^{3+}, Er^{3+}, and Tm^{3+}*. J. chem. Phy., 49(10), 4424-4442.
19. Yu, Z., Ye, Z., Yang, Y., & Sun, J. (2023). *Bright white electroluminescence from polycrystalline dysprosium-doped yttrium gallium garnet nanofilms fabricated by atomic layer deposition on silicon*. Nanoscale, 15(20), 9130-9138.
20. McCamy, C. S. (1992). *Correlated colour temperature as an explicit function of chromaticity coordinates*. Color Research & Appl., 17(2), 142-144.

Synthesis of Nickel Selenide Nanoparticles as Cathode Material for Zink Ion Batteries and Study of Their Optical Properties

Jaiveer Singh[1,a], Jitendra Tripathi[1,b], Puja Singh[2,c] and Mayank Sharma[1]

[1]*Department of Physics, ISR, IPS Academy, Indore, M.P., India.*
[2]*Department of Electronics & Communication Engineering, Medi-Caps University, Indore, M.P., India.*

[a] jaiveer24singh@gmail.com
[b] jtripathi00@gmail.com
[c] puja.singh@medicaps.ac.in

Abstract

Porosity of electrode materials has been proven to be very significant in enhancing the performance of Zn-ion batteries (ZIB) in recent studies. On a positive electrode, porosity improves its kinetics by faster electron transport and richer electro active reaction sites. On a negative electrode, porous structure provides increased surface area and reduced local current density, both favorable to the performance of ZIB. Nickel Selenide (NiSe) nanoparticles (NPs) can be considered as more suitable cathode materials also due to their smaller band gap and higher conductivity. We have synthesized NiSe nanoparticles using a chemical method with octylamine as a surfactant with crystallite size of 36 nm. The field emission scanning electron microscopy (FESEM) images shows the formation of spikelike structure making the nanoparticles highly porous making them even more suitable as a cathode material.

Keywords: Nanoparticles, X-Ray Diffraction (XRD), FESEM.
Received 28 January 2025; First Review 11 February 2025; Accepted 27 April 2025.

*** Address of correspondence**
Jaiveer Singh
Department of Physics, ISR, IPS Academy, Indore, M.P., India.

Email: jaiveer24singh@gmail.com

How to cite this article
Jaiveer Singh, Jitendra Tripathi, Puja Singh and Mayank Sharma, Synthesis of Nickel Selenide Nanoparticles as Cathode Material for Zink Ion Batteries and Study of Their Optical Properties, J. Cond. Matt. 2025; 03 (02): 137-140.

Available from:
https://doi.org/10.61343/jcm.v3i02.80

Introduction

Transition Metal Selenides (TMS) have been a subject of interest in the field of nanotechnology recently due to spectrum of properties ranging from insulators to semiconductors and semiconductors to true metals [1,2]. Transition metals are known to make variety of complexes due to their d-block electronic configuration and Nickel is no exception in that regard. In addition, due to small difference in the electronegativity of nickel and selenium they make several different phases of nickel selenides (i.e., NiSe, $NiSe_2$, Ni_3Se_2, and Ni_3Se_4) with different physical and chemical properties [3,4]. The band gap of NiSe falls between the conductor and semiconductors which makes it a very suitable candidate for the cathode material in Zn ion Batteries (ZIB) [5,6].

Another factor that significantly affects the performance of cathode material is their capacity to accommodate the Zn^+. This is where the porosity of the cathode materials plays an important role. A sufficiently porous cathode material can accommodate the Zn^+ ion easily which will allow the chemical reaction to take place with ease and also porosity will significantly increase the surface area available for the chemical reactions.

The phase as well as the size, shape and morphology of the NPs have always been dependent on the synthesis techniques used and various reaction parameters. There are so many physical and chemical methods have been used for the synthesis of metallic nanoparticles. But among of them Chemical method is one of the most convenient and commonly used techniques to synthesize nanoparticles. Due to its low temperature threshold and low-cost ingredients in which precursors are mixed at an elevated temperature (near 200 °C) in an organic solvent which also acts as the surfactant [2-5]. Herein, we have optimized a much simpler method to synthesize single phased nickel selenide NPs with the use of a single surfactant. With this method, we were able to synthesize highly porous nanoparticles of NiSe. The purity and structural properties of the sample was studied with the help of different characterization techniques. The FESEM images clearly show the formation of spike-like structures creating the micropores throughout the sample. The low intensity peaks in powder X-ray diffraction spectroscopy (XRD) further support the formation of micropores.

Experiment

General

All chemicals such Nickel chloride hexahydrate ($NiCl_2 \cdot 6H_2O$) with purity ≥ 98 % and selenium (Se) powder with purity 99.99% trace metals basis of standard grade were used. Octylamine with purity 99 % was used as solvent or reducing material. Octylamine is selected because it has strong solubility in organic systems, mild reactivity, and the capacity to increase dispersion, guide particle development, and give surface passivation. All chemical were purchased from Sigma Aldrich. Ethanol was purchased from Changshu Hongsheng Fine Chemical Co. Ltd

Synthesis

Nickel selenide (NiSe) nanoparticles were synthesized via a bottom-up chemical approach. In this typical procedure, Nickel chloride hexahydrate ($NiCl_2 \cdot 6H_2O$) and selenium (Se) powder were used as precursors in a 1:1 molar ratio of (Ni/Se – 1:1). These precursors were mixed with 6 mL of octylamine in a 50 mL round-bottom flask. The flask was then sealed and heated at 18 ^{0}C for 2h. After the completion of the reaction, the mixture was allowed to cool up to the room temperature (25 ^{0}C). A black precipitate was obtained and indicating the successful formation of NiSe nanoparticles. The product was washed by adding 20 ml of ethanol 4 times to remove the excess amount of octylamine and other byproducts. After washing the resulting NPs sample was dried in oven at 60 °C for 6 hours and ground very well. The NiSe NPs powder was moved to a vacuum-sealed vial and kept in a glove box following synthesis. As a result, the material's integrity was maintained with little exposure to oxygen and moisture. Additionally, characterizations were performed using the produced NPs sample.

Characterizations

The XRD measurement of the sample was done by Bruker D8 Advance- Powder XRD with CuKα radiation (λ = 1.5406 Å) to examine the purity, phase and crystallinity of the sample. The 2θ range was selected from 20° to 90° with step size of 0.02. The morphology of the nanoparticles was studied using FE-SEM in energy range of 20 keV. UV-vis spectroscopy was performed by Shimadzu UV-VIS spectrophotometer Model: UV-1800 was used to analyse the optical properties and band gap of the synthesized NPs.

Results and Discussion

Structural property of the NiSe NPs were determined by XRD measurement. The XRD Pattern of NiSe shown in Figure 1.

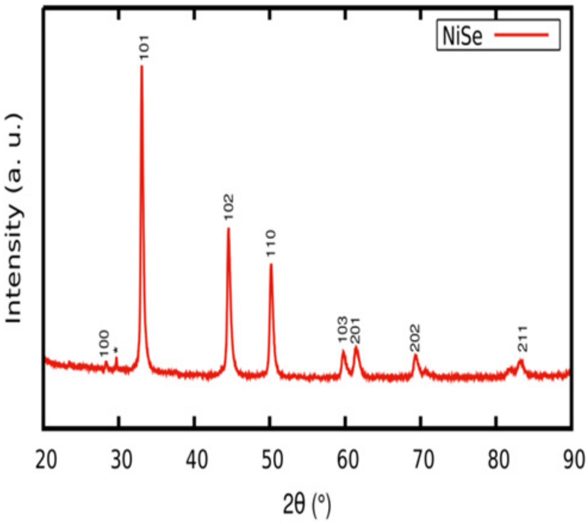

Figure 1: XRD pattern of Hexagonal NiSe sample. The bragg's planes are indicated by their miller indices. The small peaks marked by (*) are due to pure selenium remained in the sample.

Which shows the presence of single phased hexagonal Nickel Selenide crystals (PC-PDF No. - 89-7160) belonging to the space group P-63/mmc (194). The diffraction peaks corresponding to the planes (100), (101), (102), (110), (103), (201), (202) and (211) at 2θ values 28.1, 33.15, 44.69, 50.33, 59.9, 61.7, 69.6 and 83.5 respectively. The highest peak was observed for the plane (101).

The crystallite size was calculated using Dabey-Sherrer method by taking the most intense peak (101) for the calculation using the Debye Scherrer formula. Where D - Crystallite size, K-Scherrer constant (K = 0.9) λ - X-ray wave- length (λ = 1.5406 Å), β - Full width at half maxima (FWHM) and θ is the Braggs' diffraction angle [6].

$$D = \frac{k\lambda}{\beta \cos\theta} \qquad (1)$$

Scherrer formula gives information about the crystallite size based on the peak broadening. The crystallite size was determined to be 36 nm. And dislocation density (δ) is found to be 0.01 $(nm)^{-2}$. A small dislocation density measurement suggests that there was a significant degree of crystallinity in the generated NiSe nanoparticles. The strain (ε) value of NiSe nanoparticles is found 1.5 x 10^{-4} by Williamson Hall plot which is not included here. This result also shows that the nanoparticle product is a lack of strain.

The lattice parameters 'a' and 'c' for hexagonal Nickel Selenide NPs samples were obtained considering all lattice planes by using following formulas:

$$d_{hkl} = \frac{(h^2 + k^2 + hk)}{3a^2} + \frac{l^2}{c^2} = \frac{\lambda^2}{4\sin^2\theta} \qquad (2)$$

Where d is the inter-planer spacing and (hkl) are miller indices. After calculating the lattice parameters corresponding to different lattice planes, precise lattice parameters were obtained using Nelson-Riley Function given by the relation-

$$F(\theta)=\frac{\cos^2\theta}{\sin\theta}+\frac{\cos^2\theta}{\theta} \qquad (3)$$

In this approximation method the lattice parameter obtained for different Braggs' angle (corresponding to different planes) are plotted against the F(θ) and linear regression is used to calculate y-intercept, by extrapolating the straight line to F(θ) = 0 [6]. The obtained values are a = 3.5222 Å and c = 5.1546 Å which are also in good agreement with the standard values of 'a' and 'c' of Nickel Selenide crystals.

FESEM Analysis

In further study, as prepared NiSe NPs sample was characterized for its morphology by FESEM. The results he been shown in FESEM micrograph Figure 2(a, b) at different resolution.

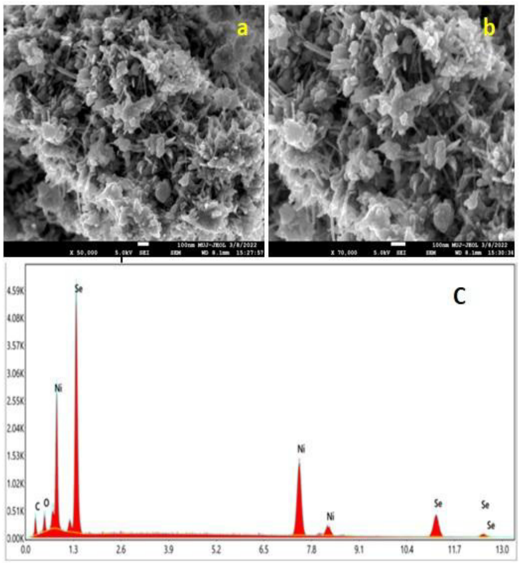

Figure 2: (a, b) FE-SEM and (c) EDX images of NiSe NPs.

It was observed that spikes like structures of size between the range of 20-30nm formed. These spikes cause the formation of random inter-particle micropores of size varying between a few nanometres to micrometers. The elemental components of the nanoparticle specimens produced by chemical method were identified using EDX spectroscopy. Figure 2c shows the range of findings for the NiSe nanoparticles up to a calcination temperature of 500 °C. The Ni and Se elements in the sample are indicated by the pertinent peaks along with weak oxygen peak which may have originated from the molecules that are bound to the surface of NiSe NPs. Consequently, EDX data verified that a chemical method was successfully used to manufacture pure NiSe nanoparticles. The EDX pattern (Fig. 2c) confirms the presence of Ni and Se in sample.

UV-Vis Spectroscopy

UV- Visible spectroscopy measurement was done in the wavelength range 200-900 nm. The UV-vis absorbance spectrum of the sample was obtained from Defused Reflectance Spectroscopy (DRS). Fig. 3 shows the graph between absorbance and wavelength. UV-visible spectroscopy provides a non-destructive method for examining a nanomaterial's optical properties. In order to analyze scattered and absorbed light from an inhomogeneous NiSe nano powder, the Kubelka-Munk (K-M) relation (Eq. 4) may be used efficiently. Although there is absorption of light by the sample throughout the spectrum but there is a significant drop at about 340 nm of wavelength. Tau'c plot was plotted inside the fig.3 using the relation in Eq. 5 (γ = 2) [7-9].

$$F(R_\infty)=\frac{(1-R_\infty)^2}{{R_\infty}^2} \qquad (4)$$

$$(F(R_\infty).h\nu)^{\frac{1}{\gamma}}=B(h\nu-E_g) \qquad (5)$$

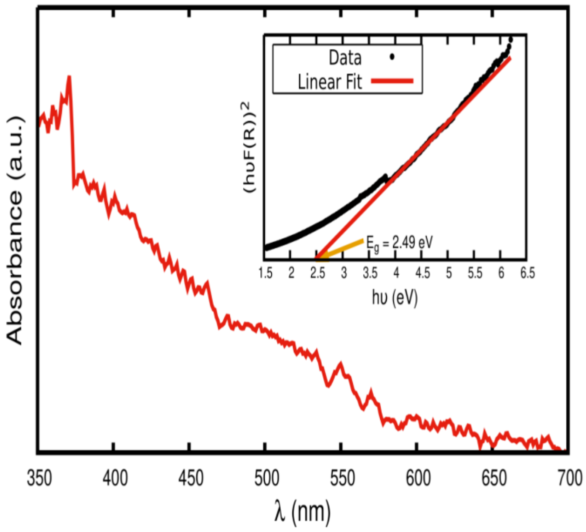

Figure 3: UV-vis absorbance spectrum and in inset Tauc plot for the NiSe NPs.

The band gap of 2.49 eV from a Tauc plot was observed. Which is found in the range of semiconductors with higher conductivity then the conventional electrode such as graphite. While band gap of bulk nickel selenide (NiSe) typically falls in the range of 0.2 to 1.0 eV. It was observed that there is a significant change in band gap from bulk to NPs this is due to the quantum size effect. Here, the quantum size effects become active when the size of NiSe approaches or falls below the exciton Bohr radius. As a result, energy levels become discretized, and electrons and holes are confined in a tiny area. Therefore, the band gap increases as more energy is needed to drive an electron from the valence band to the conduction band.

Electrochemical Analysis

Nickel selenide (NiSe) stands out among zinc-ion battery (ZIB) cathodes due to its high electronic conductivity and decent structural stability, making it a promising alternative to more traditional oxide-based cathodes. Although, we did not per formed electrochemical tests but on the basis of literature, we observed that NiSe is found attractive due to its high electronic conductivity, multiple oxidation states of Ni and layered crystal structure. Compared to manganese dioxide (MnO_2), which offers higher specific capacities (up to 300 mAh/g), NiSe typically delivers moderate capacities in the range of 150–250 mAh/g. However, MnO_2 suffers from poor cycling stability due to structural degradation and manganese dissolution, whereas NiSe maintains better stability over extended cycling. Vanadium-based cathodes like V_2O_5 can provide even higher capacities (300–400 mAh/g), but often face issues with phase transitions and relatively lower conductivity, necessitating conductive additives or structural engineering. Overall, while NiSe may not top the chart in terms of capacity, its superior conductivity, moderate voltage range, and promising stability make it a balanced and practical candidate for next-generation aqueous ZIB cathodes [10].

Conclusion and Future Prospective

In summary, we have successfully synthesized a single phase NiSe nanoparticle which show inter particle microporous structures which has been considered significantly useful in enhancing the performance of ZIB by providing better accommodation capacity for Zn^+ ions. The relatively low intensity peaks of XRD also support the same. The band gap obtained from the UV-Vis Spectroscopy confirms the suitable electrical conductivity of the sample for the propose of electrode materials as well. For the precise measurement of the degree and size of porosity as well as the effect of reaction parameter on the porosity of the nanoparticles, further experimentation will be conducted in our future studies.

References

1. N Abbas, J-M. Zhang, S Nazir, M T Ahsan, S Saleem, U Ali, N Akhtar, M Ikram, R Liaqat, *A comparative study of structural, vibrational mode, optical and electrical properties of pure nickel selenide (NiSe) and Ce-doped NiSe nanoparticles for electronic device applications*, Phys. B Condens. Matter, Volume 649, 414471, 2023. https://doi.org/10.1016/j.physb.2022.414471
2. C T Lu, S Dong, C Zhang, L Zhang, and G Cui, *Fabrication of transition metal selenides and their applications in energy storage*, Coord. Chem. Rev., 332:75-99, 2017. https://doi.org/10.1016/j.ccr.2016.11.005
3. N Moloto, M J Moloto, N J Coville, and S S Ray, *Optical and structural characterization of nickel selenide nanoparticles synthesized by simple methods*, J. Cryst. Growth, 311: 3924–3932, 2009. https://doi.org/10.1016/j.jcrysgro.2009.06.006
4. Z Zhuang, Q Peng, J Zhuang, X Wang, and Y Li, *Controlled Hydrothermal Synthesis and Structural Characterization of a Nickel Selenide Series*, Chem. Eur. J., 12: 211 – 217, 2006. https://doi.org/10.1002/chem.200500724
5. B Yuan, W Luan and S Tu, *One-step solvothermal synthesis of nickel selenide series: Composition and morphology control*, Cryst. Eng. Comm., 14:2145–2151, 2012. https://doi.org/10.1039/C2CE06474J
6. P Kumara, S Pathak, A Singh, H Khanduri, Kuldeep, K Jain, J Tawale, L Wang, G A Basheed, R P Pant, *Enhanced static and dynamic magnetic properties of PEG-400 coated CoFe2−xErxO4 (0.7≤ x≤ 0) nano ferrites*, Journal of Alloys and Compounds, 887:161418, 2021. https://doi.org/10.1016/j.jallcom.2021.161418
7. S Altaf, H Ajaz, M Imran, A Ul-Hamid, M Naz, M Aqeel, A Shahzadi, A Shahbaz, M Ikram, *Synthesis and characterization of binary selenides of transition metals to investigate its photocatalytic, antimicrobial and anticancer efficacy*. Appl. Nanosci., 10: 2113–2127, 2020. https://doi.org/10.1007/s13204-020-01350-w
8. J K Cooper, A M Franco, S Gul, C Corrado and J Z Zhang, *Characterization of Primary Amine Capped CdSe, ZnSe, and ZnS Quantum Dots by FT-IR: Determination of Surface Bonding Interaction and Identification of Selective Desorption*, Langmuir, 27 (13): 8486-8493, 2011. https://doi.org/10.1021/la201273x.
9. P Makuła, M Pacia, and Wojciech Macyk, The J. Phys. Chem. Lett., 9 (23): 6814-6817, 2018. https://doi.org/10.1021/acs.jpclett.8b02892
10. Y Zhang, C Wu, G Liang *et al*, *Recent Advances in Transition Metal Selenide Cathodes for Aqueous Zinc-Ion Batteries*. Adv. Funct. Mater., 30(42), 2004690, 2020. https://doi.org/10.1002/adfm.202004690

Divacancy Binding Energy, Formation Energy and Surface Energy of bcc Alkali Metals Using MEAM Potential

Shweta Uniyal[1,a] and Manesh Chand[2,b]

[1]*Department of Physics, H.N.B. Garhwal University Campus, Badshahithaul, Tehri Garhwal, Uttarakhand, India.*
[2]*Department of Physics, Swami Vivekananda College of Education, Roorkee, Uttarakhand, India.*

[a]shwetauniyal.om@rediffmail.com
[b]maneshchand@gmail.com

Abstract

The Modified Embedded Atom Method (MEAM) potential parameters have been employed to calculate the unrelaxed divacancy formation energy, binding energy, and surface energies for low-index planes in body-centered cubic (bcc) alkali metals. The calculated divacancy binding energies and vacancy formation energies show good agreement with experimental data and other available computational results.

Keywords: Modified embedded atom method; Phonon dispersions; Formation energy; Divacancy binding energy; Surface energy.
Received 04April 2025; First Review 22April 2025; Accepted 27April 2025.

*** Address of correspondence**
Dr. Manesh Chand
Assistant Professor, Department of Physics, Swami Vivekananda College of Education, Roorkee, Uttarakhand, India.

Email: maneshchand@gmail.com

How to cite this article
Shweta Uniyal and Manesh Chand, Divacancy Binding Energy, Formation Energy and Surface Energy of bcc Alkali Metals Using MEAM Potential, J. Cond. Matt. 2025; 03 (02):141-145.

Available from:
https://doi.org/10.61343/jcm.v3i02.154

Introduction

Johnson and Oh [1] presented an analytical EAM model for bcc metals in which the electron density is treated as a decreasing function of distance. The model has been found suitable for bcc alkali and transition metals, except for Cr, due to the negative curvature required for the embedding function. By introducing a few modifications to the Johnson and Oh model [1], Guellil and Adams [2] applied the EAM model to study phonon dispersions, as well as the thermal and surface properties of bcc alkali and transition metals and their alloys. W. Hu *et al.* [3] employed a modified form of the analytical EAM model to investigate various defect-related properties, including interstitial and vacancy formation energies, surface energies, and phonon dispersions. Zhang *et al.* [4] calculated the formation energy of mono-vacancies in bcc metals, along with the binding and formation energies for di- and tri-vacancies.

Cui et al. [5] applied the MEAM model to study the thermal and surface properties of the alkali metal lithium (Li). Yuan *et al.* [6] also conducted a detailed study on bcc Li using the same MEAM model, performing surface energy calculations. In earlier calculations by W. Hu *et al.* [3] on unrelaxed surface and divacancy binding energies, a molecular dynamics approach was used. Most earlier studies on binding and surface energies involved significant computational effort. In recent studies, the MEAM potentials developed by W. Hu *et al.* [3] have been used by Vandana et al. [7, 8] to investigate the vibrational properties of vacancies in bcc transition metals such as Nb, Fe, Mo, and W. Vandana and Semalty [9] further extended this investigation to bcc alkali metals Na and K. Ram P. N. *et al.* [10] also explored the vibrational properties of vacancies in bcc metals.

The aim of the present work is to calculate the unrelaxed divacancy formation, binding, and surface energies of bcc alkali metals using a simplified approach with a minimal set of MEAM potential parameters obtained by Zhang *et al.* [11]. The calculated results show reasonable agreement with some of the earlier reported values.

Method

MEAM Model

In the MEAM model, the total energy is given by:

$$E_t = \sum_i [F(\rho_i) + \frac{1}{2}\sum_{j \neq i} \phi(\mathrm{r_{ij}}) + M(P_i)], \qquad (1)$$

The embedding function $F(\rho)$ and the atomic density $f(r)$are given as:

$$F(\rho) = -F_0[1 - n\ln(\frac{\rho}{\rho_e})](\frac{\rho}{\rho_e})^n , \qquad (2)$$

and

$$f(r) = f_e(\frac{r_1}{r})^\beta \qquad (3)$$

where$F_0 = E_c - E_V$,ρ_e is the equilibrium electron density and$n$is a parameter which can be determine by fitting the empirical energy-volume relationship of Rose *et al.* [12] and β is taken equal to 6.

$$\phi(r) = k_0 + k_1\left(\frac{r}{r_{1e}}\right)^2 + k_2\left(\frac{r}{r_{1e}}\right)^4 + k_3\left(\frac{r}{r_{1e}}\right)^{12} \qquad (4)$$

is the pair potential used for the bcc alkali metals.

The energy modification term is taken as:

$$M(P_i) = \alpha\left(1 - \frac{P}{P_e}\right)^2 \exp[-(\frac{P}{P_e} - 1)^2], \qquad (5)$$

Where α is another adjustable parameter and M(P_i) is the modified embedding function.

In the calculation of Unrelaxed Vacancy formation energy, Binding formation energy and Surface energies, we have considered a MEAM model up to the second neighbors of vacancy. The model parameters α and k_j ($j = 0,1,2,3$) are obtained analytically by fitting to the experimental elastic constants, cohesive energy, formation energy of vacancy.

Unrelaxed Vacancy formation energy

In simple terms, the energy required to create a vacancy in an otherwise perfect lattice is known as the vacancy formation energy. When a vacancy is formed, the atom that would have occupied the vacant site no longer contributes to the charge density at various atomic sites within the lattice.

By including the embedding function and a modification term alongside the pair potential, the monovacancy formation energy can be calculated using the following expression:

$$E_{1V}^F = 8F[\rho_e - f(r_{1e})] + 6F[\rho_e - f(r_{2e})] - [4\phi(r_{1e}) + 3\phi(r_{2e})] - 14F(\rho_e) + 8M[P_e - f^2(r_{1e})] + 6M[P_e - f^2(r_{2e})] - 14M(P_e). \qquad (6)$$

After the formation of a divacancy, 14 atoms lose one of their first nearest neighbors, and 12 atoms lose one of their second nearest neighbors. In total, 26 atoms are affected in the second-neighbor model.

The divacancy formation energy E_{2V}^F at the first-neighbor distance is calculated using the following expression:

$$E_{2V}^F = 14F[\rho_e - f(r_{1e})] + 12F[\rho_e - f(r_{2e})] - 26F(\rho_e) - [8\phi(r_{1e}) + 6\phi(r_{1e})] + \phi(r_{1e}) + 14M[P_e - f^2(r_{1e})] + 12M[P_e - f^2(r_{2e})] - 26M(P_e) \qquad (7)$$

In the case of a divacancy at the second-neighbor distance, the formation of the divacancy results in 8 atoms losing one of their first nearest neighbors, 4 atoms losing two of their second nearest neighbors, and 10 atoms losing one of their second nearest neighbors. Thus, a total of 22 atoms are affected.

Therefore, the divacancy formation energy E_{2V}^F, including the contributions from the embedding and modified embedding energy terms at the second-neighbour distance, is calculated using the following expression:

$$E_{2V}^F = 8F[\rho_e - f(r_{1e})] + 4F[\rho_e - 2f(r_{2e})] + 10F[\rho_e - f(r_{2e})] - 22F(\rho_e) - [8\phi(r_{1e}) + 6\phi(r_{1e})] + \phi(r_{1e}) + 8M[P_e - f^2(r_{1e})] + 4M[P_e - 2f^2(r_{2e})] + 10M[P_e - f^2(r_{2e})] - 22M(P_e) \qquad (8)$$

where r_{1e} and r_{2e} are first neighbour and second neighbour equilibrium distances.

One way to test the suitability of MEAM potentials is to use them for calculating properties that were not included in the fitting process. Accordingly, we have employed the MEAM potential parameters to calculate the unrelaxed binding energy E_{2V}^B of seven transition metals. The unrelaxed binding energy of a divacancy is given by:

$$E_{2V}^B = 2E_{1V}^F - E_{2V}^F \qquad (9)$$

where, E_{1V}^F andE_{2V}^F are the formation energy of monovacancy and divacancy.

The unrelaxed binding energy of divacancy at first neighbour distance is given by:

$$E_{2V}^B = 2F[\rho_e - f(r_{1e})] - 2F(\rho_e) - \phi(r_{1e}) + 2M[P_e - f^2(r_{1e})] - 2M(P_e) \qquad (10)$$

The unrelaxed binding energy of divacancy at second neighbour distance is given by:

$$E_{2V}^B = 8F[\rho_e - f(r_{1e})] - 4F[\rho_e - 2f(r_{2e})] + 2F[\rho_e - f(r_{2e})] - 6F(\rho_e) - \phi(r_{1e}) + 8M[P_e - f^2(r_{1e})] - 4F[\rho_e - 2f(r_{2e})] + 2M[\rho_e - f(r_{2e})] - 6M(P_e) \qquad (11)$$

Unrelaxed Surface Energy

In solid-state physics, surfaces are intrinsically less energetically favorable than the bulk of a material. This is because atoms or molecules at the surface experience fewer bonding interactions, resulting in higher energy compared to those in the bulk. If surface atoms were more stable than bulk atoms, there would be a natural driving force for surfaces to form spontaneously, ultimately leading to the disappearance of the bulk material.

Surface energy can thus be defined as the excess energy at the surface of a material relative to the bulk. The unrelaxed surface energy for three low-index planes is given by:

$$S_{100} = \frac{1}{a^2}[\Delta E_1^{100} + \Delta E_2^{100}] \tag{12}$$

$$S_{110} = \frac{\sqrt{2}}{a^2}[\Delta E_1^{110} + \Delta E_2^{110}] \tag{13}$$

$$S_{111} = \frac{1}{\sqrt{3a^2}}[\Delta E_1^{111} + \Delta E_2^{111}] \tag{14}$$

where ΔE_1 is contribution due the change in embedded and modified embedded energy term and ΔE_2 is the contribution due to change in pair potential part and are given as under:

$$\Delta E_1^{100} = F[\rho_e - 4f(r_{1e}) - f(r_{2e})] + F[\rho_e - f(r_{2e})] - 2F[\rho_e] + M[P_e - 4f^2(r_{1e}) - f(r_{2e})]$$

$$+M[P_e - f^2(r_{2e})] - 2M[P_e] \tag{15}$$

$$\Delta E_2^{100} = -2\phi(r_{1e}) - \phi(r_{2e}). \tag{16}$$

$$\Delta E_1^{110} = F[\rho_e - f(r_{1e}) - 2f(r_{2e})] - F[\rho_e] + M[P_e - f^2(r_{1e}) - 2f^2(r_{2e})] - M[P_e], \tag{17}$$

$$\Delta E_2^{110} = -\phi(r_{1e}) - \phi(r_{2e}), \tag{18}$$

and

$$\Delta E_1^{111} = F[\rho_e - 4f(r_{1e}) - 3f(r_{2e})] - F[\rho_e] + M[P_e - 4f^2(r_{1e}) - 3f^2(r_{2e})] - M[P_e], \tag{19}$$

and

$$\Delta E_2^{111} = -2\phi(r_{1e}) - \frac{3}{2}\phi(r_{2e}). \tag{20}$$

Results and Discussions

For the calculation of unrelaxed vacancy formation, binding, and surface energies, the necessary MEAM potential parameters for all bcc alkali metals (Li, Na, K, Rb, and Cs) are adopted from Zhang *et al.* [11]. The monovacancy and divacancy formation energies are computed using Eqs. (6) and (7), while the unrelaxed divacancy binding energies for both first-neighbor and second-neighbor configurations are calculated using Eqs. (6-11).

As an additional application of the MEAM parameters, the unrelaxed surface energies for three low-index surfaces (100), (110), and (111) are evaluated using the expressions provided in Equations (12-14).

For the bcc alkali metals, the calculated values of unrelaxed divacancy binding energies, monovacancy and divacancy formation energies, and surface energies for the (100), (110), and (111) planes are presented in Table 1 and Table 2, along with available experimental data and other theoretical results.

Unrelaxed Vacancy formation energy and Divacancy binding energy in bcc alkali Metals

Table 1: Calculated values (underlined) of unrelaxedmono vacancy formation energy$\boldsymbol{E_{1V}^F}$, first and second neighbor divacancy formation energy$\boldsymbol{E_{2V}^F}$, first and second neighbour divacancy binding energy$\boldsymbol{E_{2V}^B}$for bcc alkali metals along with other results.

	Li	**Na**	**K**	**Rb**	**Cs**
Cal $E_{1V}^F(eV)$ **Exp**	0.3446 0.48^a 0.34^b 0.34^e	0.3324 0.3408^a 0.42^b 0.34^e	0.3440 0.3413^a 0.42^b 0.34^e	0.3406 0.3420^a ------- 0.341^e	0.3184 0.3249^a ------- 0.322^e
at r_{1e} $E_{2V}^F(eV)$	0.638 0.761^c 0.89^d 0.893^a	0.615 0.665^c 0.631^d 0.6333^a	0.637 0.665^c 0.63^d 0.6342^a	0.631 0.628^c 0.632^d 0.6354^a	0.589 0.592^c 0.598^d 0.6037^a
at r_{2e}	0.645 0.77^c 0.89^d 0.8931^a	0.622 0.673^c 0.632^d 0.6333^a	0.644 0.673^c 0.633^d 0.6344^a	0.637 0.636^c 0.634^d 0.6355^a	0.594 0.599^c 0.599^d 0.6038^a
at r_{1e} $E_{2V}^B(eV)$	0.0514 0.067^c 0.069^d 0.0684^a	0.0494 0.049^d 0.04837 0.055^c	0.0515 0.055^c 0.049^d 0.0484^a	0.0504 0.052^d 0.0486^a 0.052^c	0.048 0.048^c 0.047^d 0.0461^a
at r_{2e}	0.045 0.057^c 0.068^d 0.0683^a	0.043 0.047^c 0.048^d 0.0483^a	0.044 0.047^d 0.047^d 0.0482^a	0.044 0.044^c 0.047^d 0.0485^a	0.043 0.041^c 0.045^d 0.0460^a

Superscripts ^{a,b,c,d} and ^{e} used with data in Table (1) are ref. [4], [2], [13], [14] and [11] respectively.

From our calculations, we find that among the bcc alkali metals, lithium (Li) exhibits the highest monovacancy formation energy, whereas Caesium (Cs) shows the lowest. In general, there is a clear correlation between vacancy formation energy and atomic number: the formation energy tends to decrease with increasing atomic number of the alkali metals, with the exception of potassium (K), which deviates from this trend.

When comparing our calculated results with other available theoretical data, we observe that our unrelaxed vacancy formation energies are in good agreement with those reported by Zhang *et al.* [4], except for Li. In contrast, our results for Li show very good agreement with those obtained by Guellil and Adams [2], compared to the other alkali metals. The experimental values of vacancy formation energy cited by Zhang *et al.* [11] are also found to align closely with our calculated values.

The calculated values of unrelaxed divacancy binding and formation energies, along with earlier reported results, are presented in Table 1. Upon comparison, we find that our values for divacancy formation and binding energies are generally in good agreement with those reported by Hu *et al.* [13], Zhang *et al.* [4], and Ouyang *et al.* [14], except for Li. For lithium, our calculated values are lower than those reported in these studies. However, our results are higher than the earlier pseudopotential calculations of Takai and Doyama [15].

The MEAM model predicts that divacancies are more strongly bound and more stable at the first-neighbor distance compared to the second-neighbor configuration. In the present work, we have neglected relaxation effects in the calculation of divacancy formation and binding energies, primarily due to the significant computational resources required to include these effects. Nonetheless, previous work by Hu and Masahiro [13] indicates that the relaxation effect is relatively small for second-neighbor configurations compared to first-neighbor ones.

The determination of lattice relaxation at a metal surface is influenced by the degree of electron screening of the ionic cores. Therefore, we expect that surface energy calculations are sensitive to the exact form of the three-dimensional electron density profile. A similar consideration applies to the determination of the phonon contribution to the temperature dependence of surface energy.

Unrelaxed Surface energy of bcc alkali metals

The calculated unrelaxed surface energies for the three low-index planes are presented in Table 2. Our calculated results of unrelaxed surface energies are seen to be in an increasing order: S_{111}, S_{110}, S_{100}, i.e., highest for S_{100} and lowest for S_{111}. A similar variation in surface energies was also reported by Rose and Dobson [18], as expected from bond-breaking arguments, which suggest that the denser crystal face possesses lower surface energy.

It is also observed that our calculated surface energies are generally lower than those obtained from other theoretical studies [2,11,13] and experimentally measured values [16, 17]. The discrepancy between calculated and experimental results can be attributed to the fact that experimental values often represent averaged measurements over multiple crystal orientations in bulk samples. Additionally, experimental values, typically extrapolated to 0 K, do not always account for surface orientation-specific energies.

Table 2: Calculated values (underlined) of unrelaxed surface energies S_{100}, S_{110} and $S_{111}$for bcc alkali metals along with other results.

	Li	Na	K	Rb	Cs
S_{100} (erg/cm^2)	199 269^e 215^f 282^g	133 133^e 138^f 154^g	86 83^e 92^f 97^g	74 73^e 77^f -------	58 59^e 63^f -------
S_{110} (erg/cm^2)	182 252^e 203^f 231^g	122 124^e 127^f 138^g	79 78^e 83^f 88^g	68 68^e 69^f -------	54 56^e 56^f -------
S_{111} (erg/cm^2)	133 310^e 264^f	89 153^e 162^f	58 96^e 106^f	50 83^e 88^f	39 68^e 72^f
S_{avg} (erg/cm^2)	472^h 525^i	234^h 260^i	129^h 130^i	104^h 110^i	84^h 95^i

Superscripts $^{e, f, g, h}$ and ^{i} used with data in Table (2) are ref. [11], [13], [2], [16] and [17] respectively.

However, using Tyson's simple model of the "*population density factor*," Tyson and Miller [16] demonstrated that it is possible to estimate the surface energy of a specific crystallographic face from a generalized "average" surface energy. This reinforces the idea that our face-specific MEAM-based calculations provide valuable insight despite the apparent differences with bulk-averaged experimental data.

Conclusions

In this study, the unrelaxed vacancy formation energy, divacancy formation and binding energies, and low-index surface energies for bcc alkali metals have been calculated using MEAM potential parameters.

Our results for unrelaxed monovacancy formation energy show excellent agreement with available experimental data for alkali metals. Additionally, the calculated mono- and divacancy formation energies are in good agreement with previously reported theoretical studies. A clear correlation is observed between vacancy formation energy and the atomic number of the alkali metals: the energy generally decreases with increasing atomic number, except for potassium (K), which deviates from the trend. This correlation also parallels the variation in cohesive energy Ec across the series.

We have also evaluated the divacancy binding energies for bcc alkali metals and found that our results are consistent with both experimental observations and earlier theoretical work. The calculated binding energies suggest that divacancies are more stable in the first-neighbor configuration compared to the second-neighbor configuration.

Overall, our findings are consistent with expected trends and show good agreement with experimental and other theoretical studies, further validating the applicability of MEAM potentials for defect and surface property calculations in bcc alkali metals.

References

1. Johnson R.A., Oh D.J. (1989). *Analytic embedded atom method model for bcc metals*. J. Mater. Res.**4**, 1195–1201.
2. Guellil A.M., Adams J.B. (1992). *The application of the analytic embedded atom method to bcc metals and alloys*. J. Mater. Res.**7**(3), 639–652.
3. Hu W., Shu X., Zhang B. (2002). *Point-defect properties in body-centered cubic transition metals with analytic EAM interatomic potentials*. Comput. Mater. Sci.**23**, 175–189.
4. Zhang J.M., Wen Y.N., Xu K.W. (2006). *Atomic simulation of the vacancies in BCC metals with MAEAM*. Central European Journal of Physics**4**, 481–493.
5. Cui Z., Gao F., Cui Z., Qu J. (2012). *Developing a second nearest-neighbor modified embedded atom method interatomic potential for lithium*. Modelling Simul. Mater. Sci. Eng.**20**(1), 015014.
6. Yuan X., Takahashi K., Yin Y., Onzawa T. (2003). *Development of modified embedded atom method for a bcc metal: lithium. Modelling Simul. Mater*. Sci. Eng.**11**, 447–456.
7. Gairola V., Semalty P.D., Ram P.N. (2013). *Vibrational properties of vacancy in bcc transition metals using embedded atom method potentials*. Pramana – J. Phys.**80**, 1041–1050.
8. Gairola V., Semalty P.D., Ram P.N. (2014). *Vibrational properties of vacancy in bcc Nb using embedded atom method*. Indian J. Phys.**88**, 171–176.
9. Gairola V., Semalty P.D. (2014). *Vibrational Properties of Vacancy in Na and K Using MEAM Potential. Commun*. Comput. Phys.**15**, 556–568.
10. Ram P.N., Gairola V., Semalty P.D. (2016). *Vibrational properties of vacancy in Au using modified embedded atom method potentials*. J. Phys. Chem. Solids**94**, 41–46.
11. Zhang J.M., Wen Y.N., Xu K.W. (2008). *MAEAM Investigation of Phonons for Alkali Metals*. J. Low Temp. Phys.**150**, 730–738.
12. Rose J.H., Smith J.R., Guinea F., Ferrante J. (1984). *Universal features of the equation of state of metals*. Phys. Rev. B**29**, 2963–2969.
13. Hu W., Masahiro F. (2002). *The application of the analytic embedded atom potentials to alkali metals*. Modelling Simul. Mater. Sci. Eng.**10**(6), 707–718.
14. Ouyang Y., Zhang B., Liao S. (1994). *Vacancies in metals*. Sci. China A**24**, 834–839.
15. Takai O., Doyama M. (1987). *Interactions between point defects and migration energies of trivacancies in metals*. Mater. Sci. Forum**15–18**, 161–168.
16. Tyson W.R., Miller W.A. (1977). *Surface free energies of solid metals: Estimation from liquid surface tension measurements.*Surf. Sci.**62**(1), 267–276.
17. De Boer F.R. (1988). *Cohesion in Metals: Transition Metal Alloys*. North-Holland, Amsterdam.
18. Rose J.H., Dobson J.F. (1981). *Face dependent surface energies of simple metals*. Solid State Commun.**37**(2), 91–96.

Peroxide-Cured Silicone Rubber Composites: Structural, Morphological, and X-ray Detector Performance Analysis

Bhawna[1], Kusum[1], Kulvinder Singh[2] and Alka Garg[3,a]

[1] *Baba Mastnath University, Asthal Bohr, Rohtak-124021, Haryana, India.*
[2] *Deen Dayal Upadhaya College, University of Delhi, Delhi. India.*
[3] *Gargi College, University of Delhi, Delhi, India.*

[a] alka.garg@gargi.du.ac.in

Abstract

In this study, a soft and flexible polymer composite of silicone rubber was synthesized by incorporating varying concentrations of a peroxide curing agent using the solution casting method, a cost-effective method at room temperature. The synthesized composites were characterized through Energy Dispersive X-ray Analysis (EDAX) and Scanning Electron Microscopy (SEM) to determine elemental composition and surface morphology. SEM micrographs revealed a smooth surface with uniformly distributed crystallites, forming a matrix-like arrangement. Additionally, X-ray switching response measurements were recorded at different voltages to evaluate the detector performance of the composite material. It was observed that detector is showing the photo-response but the difference in photocurrent and dark current needs to be enhanced by adding conducting fillers in the matrix of silicone rubber. The results suggest that peroxide concentration significantly influences the structural, morphological, and detector response properties of the silicone rubber composite, offering valuable insights into optimizing curing conditions for enhanced material performance and detector efficiency.

Keywords: Polymer Composite, SEM, EDAX, Peroxide Curing.
Received 31 January 2025; First Review 19 March 2025; Accepted 28 April 2025.

*** Address of correspondence**
Dr. Alka Garg
Gargi College, University of Delhi, Delhi, India.

Email: alka.garg@gargi.du.ac.in

How to cite this article
Bhawna, Kusum, Kulvinder Singh and Alka Garg, Peroxide-Cured Silicone Rubber Composites: Structural, Morphological, and X-ray Detector Performance Analysis, J. Cond. Matt. 2025; 03 (02): 146-151.

Available from:
https://doi.org/10.61343/jcm.v3i02.140

Introduction

In this paper we use peroxide cured Silicon rubber. Silicone rubber is a highly versatile elastomer widely recognized for its exceptional thermal stability, chemical resistance, and flexibility, which makes it indispensable across various industries, including medical devices, automotive components, and electronics.

The polymer class known as silicone rubber has special qualities like electrical insulation, biocompatibility, and tolerance to both high and low temperatures. Numerous industries, such as the electrical, medical, and aviation sectors, heavily rely on silicone rubber [1]. Three primary methods are used to create silicone rubber: condensation vulcanization, peroxide curing, and platinum-catalyzed curing.

According to published research, the earliest technique for vulcanizing silicone rubber was peroxide curing, often known as radical curing. Since peroxides start the radical crosslinking reaction, it can be challenging to get rid of some of the tiny molecules created during this process from the synthetic silicone rubber. These tiny molecules can occasionally degrade silicone rubber's mechanical qualities and usage [2]

Silicone rubber composites have garnered significant attention due to their exceptional flexibility, chemical stability, and adaptability across various applications. Poly(siloxane)s of high molecular weight, known as silicone rubbers, are materials based on macromolecules with successive silicon–oxygen bonds as a backbone, with the Si atom having two monovalent organic side groups [3]. Polysiloxanes are materials composed of a (Si–O) backbone with two monovalent organic radicals attached to each silicon atom ($–R_2Si–O–$). They are commonly referred to as "silicone" polymers; Kipping coined this term in 1901 to characterize novel compounds with the formula R_2SiO by drawing a comparison to ketones. Other names for these kinds of polymers are siloxane polymers and polysiloxanes since the (–Si–O–) repeat unit is also known as the "siloxane" bond or linkage. Silicones serve as a crucial link between inorganic and organic polymers since their backbone is "inorganic" and the substituents that are joined to the silicon atom are typically "organic" radicals [4].

These materials are particularly promising for radiation detection, leveraging their intrinsic properties to act as effective X-ray detectors [5]. The base composition of silicone rubber, represented as Silicone rubber composites have garnered significant attention in recent years due to their remarkable flexibility, chemical stability, and adaptability across diverse applications. These materials are particularly promising for radiation detection, leveraging their intrinsic properties to act as effective X-ray detectors. This study investigates peroxide-cured silicone rubber as a soft, flexible material for X-ray detection applications. Digital radiography, dental X-ray imaging, CT scans, and radiation therapy are just a few of the medical diagnostic applications that use low-energy, pulsed X-rays. Even with commercial X-ray detectors in use today, it can be difficult to get consistent, high detector performance over time due to X-ray interactions with the detector material. Researchers must envision new generation X-ray detector materials that are lightweight, portable, economically feasible, simple to produce, and have mechanical flexibility and low-temperature capabilities and high temperature. The discovery of X-rays is regarded as a major scientific breakthrough with numerous uses in the fields of business, medicine, astronomy, and warfare [6]. Certain detectors with great sensitivity, cheap fabrication costs, and high stability at room temperature are necessary for explicit applications [7]. However, these rays have some major negative health impacts in addition to being useful in a variety of applications. Wearable sensors that can function at room temperature with low biased voltage and have good sensitivity to X-rays are necessary to regulate any occupational and war exposures. By employing a cost-effective and laboratory-friendly preparation method that avoids any temperature and mechanical stresses, structurally stable and defect-free materials were synthesized.

Characterization using SEM revealed uniform surface morphology and well-aligned granules, confirming the material's structural integrity. Additionally, EDX analysis indicated the presence of key elemental components such as carbon, oxygen, copper, and hydrogen.

Preliminary X-ray sensing experiments demonstrated photo response behaviour in the material, though with limited differentiation between photocurrent and dark current. To address this, the incorporation of fillers is proposed to enhance the photo response and optimize the material's performance as an X-ray detector. For Further characterization, including XRD analysis, is planned to gain deeper insights into the structural and functional properties of the composite. This work lays the foundation for developing cost-effective, high-performance silicone rubber composites for advanced radiation detection systems.

Method

Experimental Methodology

Sample Preparation

To investigate the effects of curing agent concentration on the properties of silicone rubber, samples were prepared using the solvent casting method [8] at room temperature. This method is advantageous for producing uniform thin films composites for X-ray switching applications at room temperature. Films of varying compositions are synthesised by mixing five ml of silicone rubber with varying amounts of curing agent as tubulated in Table 1. The silicone rubber and curing agent were dissolved in an appropriate solvent to ensure complete homogenization. The solutions were then poured into mould and left to dry at room temperature. The solvent evaporation process took approximately one week, allowing for the formation of well-structured composite films. This approach aligns with methodologies used in the preparation of polymer composites for high-performance, room-temperature direct X-ray detectors [5].

Table 1: Samples of Peroxide – Cured Silicon rubber with varying amounts of curing agent.

Sample	**Amount of Silicone Rubber (ml)**	**Amount of Curing agent (ml)**
Sc 1	5	1
Sc 2	5	2
Sc 3	5	3

Curing Process

After solvent evaporation, the samples underwent a curing process at room temperature. Room temperature curing is beneficial for maintaining the integrity of certain additives and preventing thermal degradation, which is crucial in the development of sensitive detection materials. The curing agent initiates a free-radical mechanism, promoting polymer cross-linking through peroxide-induced reactions. This process contributes to the material's flexibility and mechanical properties, essential for potential use in X-ray detectors.

Physical Characterization

Following preparation, the physical properties of the samples were characterized by measuring thickness, density, diameter, and mass. These parameters are critical as they directly influence the mechanical and functional performance of silicone rubber composites, particularly in sensor applications like X-ray detectors.

Thickness: Measured using a micrometer to ensure uniformity across samples. Uniform thickness is vital for consistent detector response, as variations can affect the material's sensitivity to X-rays.

Density: Calculated by measuring the mass and volume of each film. Density variations can indicate differences in cross-linking density, affecting the material's electrical properties, which are crucial for detector performance.

Diameter and Mass: Measured using a calliper and an analytical balance, respectively. These measurements help correlate the effects of curing agent concentration on the overall performance of the material, as mass and dimensional stability are important for the integration of detector materials into devices.

These physical characteristics of three samples are tabulated in Table 2.

Table 2: Physical characteristics of Peroxide-Cured Silicon rubber samples.

Sample	Thickness (cms)	Mass (gms)	Diameter (cms)	Density (gm/cm^3)
Sc 1	0.38	6.49	4.5	1.074
Sc 2	0.45	7.48	4.5	1.045
Sc 3	0.41	6.82	4.5	1.045

The results from these physical characterizations are essential for correlating the mechanical and functional properties of the samples to their X-ray detection capabilities, which will be evaluated in subsequent sections.

Results and Discussion

Physical Structural Analysis

The solvent casting method yielded uniform composite films with varying thicknesses and densities based on curing agent concentration. Higher concentrations resulted in denser cross-links, improving mechanical strength but slightly reducing flexibility, consistent with findings from previous studies [6].

SEM Investigations

The SEM analysis shows that the synthesized silicon rubber-based material exhibits a uniform surface morphology. Uniformity in the surface indicates consistency in the material preparation process and reflects the absence of unwanted aggregation or segregation of components. The SEM images (Figure 1(a) and 1 (b)) under different magnifications highlight aligned granules across the material's surface. Granular alignment suggests that the internal structure is well-organized, which could contribute to efficient charge transport when exposed to X-rays [7]. Interconnection among aligned granules could provide necessary pathways for charge carriers during charge transport mechanism.

The SEM did not reveal major deformities, such as cracks, voids, or irregularities. These defects typically arise from high-temperature or high-pressure processes [8], which were avoided in this material's synthesis due to the cost-effective, low-stress preparation technique.

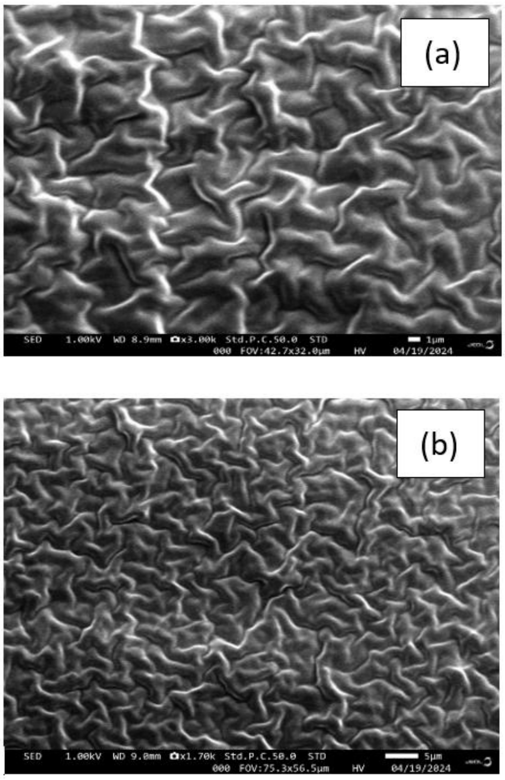

Figure 1: **(a)** and **(b)** depicting aligned granules peroxide cured Silicone Rubber composite films at two magnifications namely 2 and 5 micrometres.

The absence of cracks or deformities ensures that the material maintains its mechanical and structural integrity over time and thus provide stability to the structure. A defect-free material promotes uniform electric field distribution and minimizes the scattering of charge carriers, improving sensitivity and reliability and thus helps in achieving better charge transport characteristics.

It is expected that with smooth and periodically aligned granules at microlevel, the composite films are less likely to degrade under repeated exposure to radiation or stress, enhancing its lifespan as a detector.

Energy Dispersive X-ray Analysis

The Energy-Dispersive X-ray Spectroscopy (EDX) analysis provides valuable insights into the elemental composition of the silicon rubber-based material.

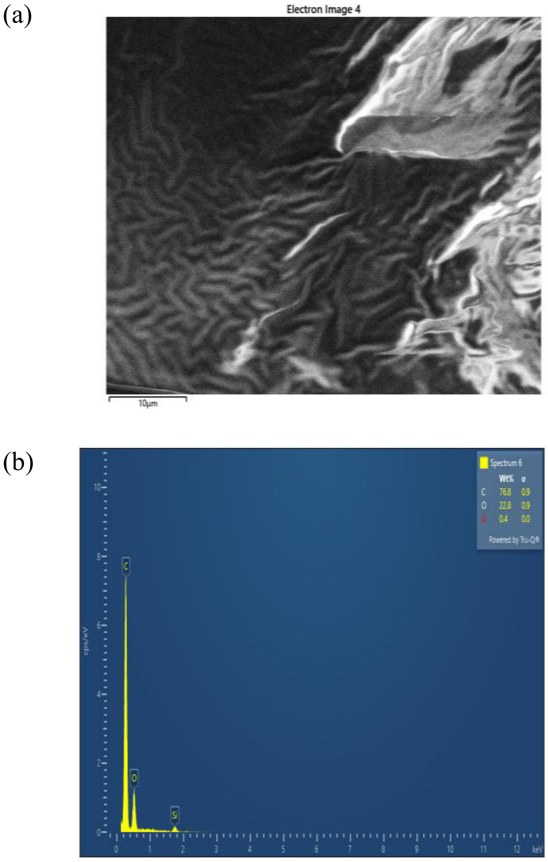

Figure 2: EDAX of sample SC-1

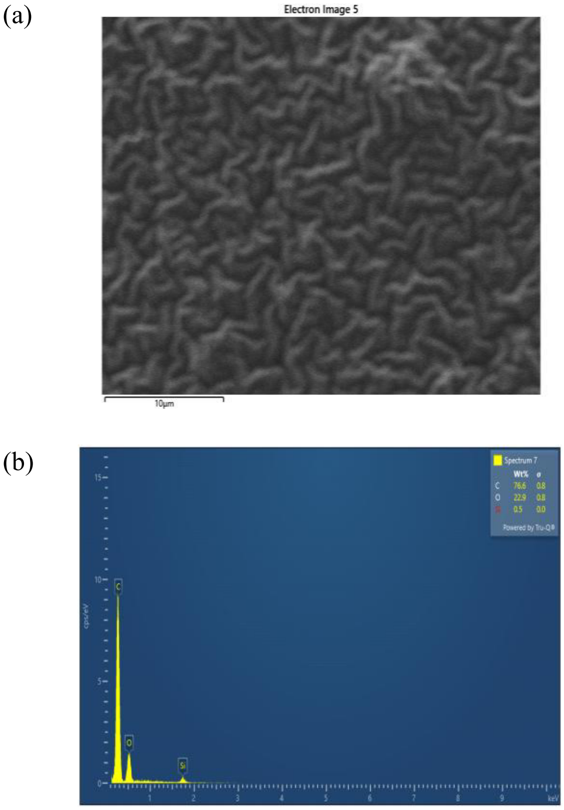

Figure 3: EDAX of sample SC-2

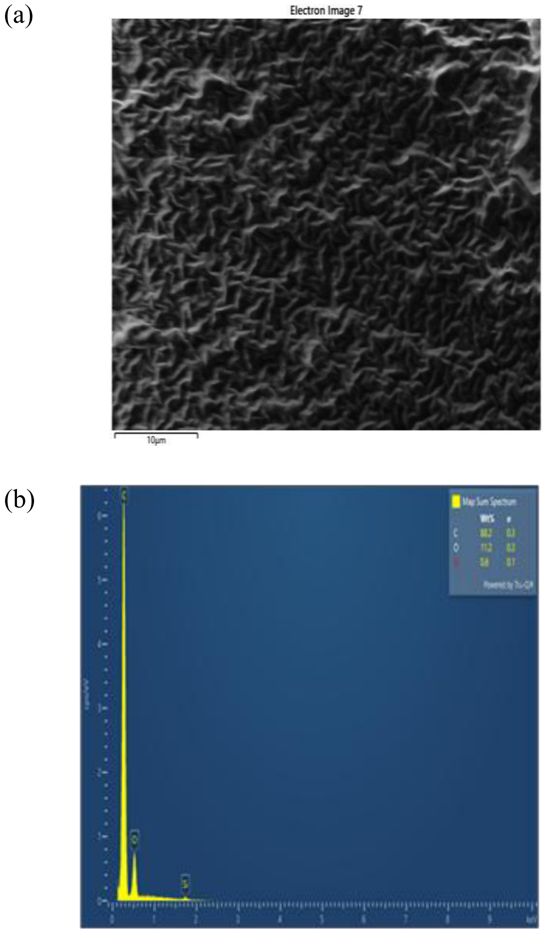

Figure 4: EDAX of Sample SC-3 confirms the homogenous mixture of the materials.

The EDAX analysis showed presence of Silicon, Oxygen and Carbon peaks corroborating with materials used for synthesising the composite films.

The presence of various elements present as per EDAX analysis is due to following factors. Carbon Predominantly originates from the organic groups (RRR) in the silicon rubber backbone, $(R_2SiO)_n(R_2SiO)_n(R_2SiO)_n$. Carbon contributes to the material's flexibility and soft texture, which are essential for mechanical stability and ease of fabrication. Silicon is present as part of the silicon rubber base material. It plays a crucial role in enabling the material to interact with X-rays, as silicon atoms can absorb and scatter X-ray photons effectively. The Presence of Oxygen is linked to the SiO-SiO-SiO structure in the material's framework. The presence of oxygen is critical for maintaining chemical stability and forming strong bonds in the polymeric structure. Hydrogen is implicitly present as part of the organic groups in the rubber contributes to the flexibility of the material, although its exact detection may be limited due to EDX's elemental detection range. Thus, the combination of silicon, oxygen, and carbon provides a robust base for detecting X-ray radiation. Silicon and oxygen enhance the material's ability to interact with X-rays, while carbon ensures the mechanical flexibility of the detector. The elemental composition indicates potential for doping or functionalization. Adding elements like copper could improve electrical conductivity. Incorporating additional elements or fillers might enhance photo-response sensitivity. The balanced presence of silicon, oxygen, and carbon ensures the material’s resistance to degradation under X-ray exposure or environmental factors like humidity and temperature. Thus, these elements may provide chemical stability to the compound under Xray irradiations. The flexibility of the $(R_2SiO)_n(R_2SiO)_n(R_2SiO)_n$ framework allows for further modifications, such as integrating nanoparticles or other dopants to tailor the material’s properties.

Photo-response Analysis

The photocurrent measurements for composite samples irradiated with 30 kV X-rays at a bias voltage of 210 V reveal significant insights into the impact of curing agent concentration on detector performance. For samples Sc 1 and Sc 2, the photopeak current was comparable to the dark current, indicating suboptimal sensitivity likely due to limited charge carrier mobility or high trap density. In contrast, sample Sc 3, which had a higher concentration of the curing agent, exhibited significantly better performance. This improvement is attributed to the robust matrix formed by the combination of silicon, oxygen, and carbon, which provided an effective framework for detecting X-ray radiation. The optimized 1:3 ratio of silicone rubber to curing agent created interconnected channels for charge carriers generated during X-ray irradiation, enhancing mobility and reducing trap density. However, the findings also emphasize that achieving an optimal balance between cross-link density and flexibility is critical to optimizing the performance of such detectors. A higher curing agent concentration improved charge carrier pathways and sensitivity, but excessive rigidity must be avoided to maintain mechanical integrity and functionality.

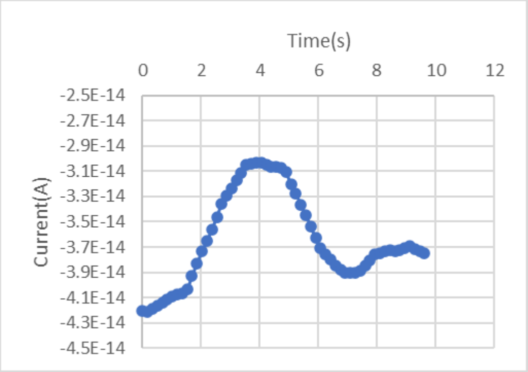

Figure 5: Depict the photocurrent response to the X ray-irradiation for sample Sc 3.

Optimization Strategies for Photo-Response Efficiency

Several optimization techniques can be taken into consideration in order to further improve the peroxide-cured silicone rubber composites' photo-response efficiency. Among these is adjusting the peroxide concentration to strike the ideal balance between charge transport channels and cross-link density. Furthermore, adding dopants or sensitizing compounds could greatly enhance the production of charge carriers under X-ray radiation. Additionally, altering the electrode and composite interfaces' surfaces may increase carrier collection efficiency and lower recombination losses. These strategies will be the main focus of future research to improve the composites' sensitivity and stability even more.

Comparison with Other X-ray Detector Materials

Compared to conventional X-ray detector materials such as amorphous selenium (a-Se), lead halide perovskites, and organic semiconductors, the peroxide-cured silicone rubber composites offer unique advantages. While a-Se and perovskites typically exhibit higher intrinsic sensitivities, they are often limited by brittleness, toxicity, or environmental instability. In contrast, the silicone-based composites present superior mechanical flexibility, chemical resistance, and biocompatibility. These attributes make them particularly suitable for emerging flexible and wearable X-ray detection applications, despite some trade-offs in terms of charge carrier mobility and photo response intensity.

Discussion on Photocurrent and Dark Current Differentiation

The relatively low differentiation between photocurrent and dark current observed in the composites highlights a critical challenge in improving device performance. To address this, the integration of conductive fillers such as carbon nanotubes, silver nanowires, or reduced graphene oxide is proposed. These fillers can create percolative networks within the matrix, enhancing charge transport and reducing leakage currents. Additionally, exploring alternative curing methods like UV-induced curing or platinum-catalyzed hydrosilylation may allow better control over the composite's microstructure, minimizing defects that contribute to dark current generation.

Conclusion and Future Prospectives

This study highlights the potential of peroxide-cured silicone rubber composites for high-performance X-ray detectors. By varying the curing agent concentration, significant improvements in structural and detector properties were achieved. Future work will focus on integrating conductive fillers and exploring hybrid curing methods to further enhance detector efficiency and flexibility.

Photo Current refers to the electric current generated when the material is exposed to X-ray radiation. Dark Current refers to the residual electric current flowing through the detector in the absence of X-ray exposure. The difference between photo current and dark current is small. This implies that the material's ability to distinctly respond to X-ray exposure (signal-to-noise ratio) is limited. This low differential may limit the detector's efficiency and sensitivity. It may be concluded that this material needs to be explored further with addition of fillers or dopants to amplify the photo current without increasing the dark current. Adding fillers with higher electrical conductivity or X-ray sensitivity can enhance the photo current. Suitable candidates include metallic nanoparticles, conductive polymers, or dopants tailored to improve charge carrier mobility. Also, the electrode interface or measurement setup needs to be optimized as it could introduce noise or other inaccuracies, leading to a less significant distinction between photo and dark current. Developing better interfaces between the silicon rubber and electrodes could reduce dark current noise and improve the signal-to-noise ratio.

Impact of Fillers on Composite Properties

Fillers play a crucial role in defining the electrical and photoconductive properties of polymer composites. Factors such as filler type, particle size, surface functionalization, and dispersion quality significantly affect the resulting performance. For instance, nanostructured fillers can enhance the carrier mobility by reducing trap states and facilitating efficient charge percolation. In this study, future investigations will explore various filler systems to optimize the trade-off between mechanical flexibility, electrical conductivity, and X-ray sensitivity. A better understanding of filler-matrix interactions could lead to composites with improved photocurrent generation and reduced dark current leakage. We have tried to synthesize samples with Bismuth Triiodide as fillers but the studies are under process.

References

1. S. Diao, F. Dong, J. Meng, P. Ma, Y. Zhao, and S. Feng, *"Preparation and properties of heat-curable silicone rubber through chloropropyl/amine crosslinking reactions"*, Materials Chemistry and Physics, vol. 153, pp. 161–167, Mar. 2015, doi: 10.1016/j.matchemphys.2014.12.048.
2. M. Azevedo, A.-M. Monks, R. C. Kerschbaumer, S. Schlögl, and C. Holzer, *"Peroxide-Based Crosslinking of Solid Silicone Rubber, Part I: Insights into the Influence of Dicumylperoxide Concentration on the Curing Kinetics and Thermodynamics Determined by a Rheological Approach"*, Polymers, vol. 14, no. 20, p. 4404, Oct. 2022, doi: 10.3390/polym14204404.
3. *"The Polymeric Organosiloxanes",* in Chemistry and Technology of Silicones, Elsevier, 1968, pp. 246–331. doi: 10.1016/B978-0-12-520750-8.50029-4.
4. E. Yilgör and I. Yilgör, *"Silicone containing copolymers: Synthesis, properties and applications"*, Progress in Polymer Science, vol. 39, no. 6, pp. 1165–1195, Jun. 2014, doi: 10.1016/j.progpolymsci.2013.11.003.
5. R. Chaudhari, S. Kumar Sharma, C. Ravi Kant, and A. Garg, *"Investigations on low energy X-ray induced strong radiation-matter interaction phenomena in polymer-BiI3 hybrid materials for room temperature radiation detectors"*, Materials Today: Proceedings, vol. 67, pp. 478–482, 2022, doi: 10.1016/j.matpr.2022.06.584.
6. R. Chaudhari, A. Garg, K. Singh, M. Tomar, V. Gupta, and C. RaviKant, *"Bismuth tri-iodide-polystyrene composite for X-rays switching applications at room temperature"*, Radiation Physics and Chemistry, vol. 186, p. 109538, Sep. 2021, doi: 10.1016/j.radphyschem.2021.109538.
7. H. M. Thirimanne *et al.*, *"High sensitivity organic inorganic hybrid X-ray detectors with direct transduction and broadband response"*, Nat Commun, vol. 9, no. 1, p. 2926, Jul. 2018, doi: 10.1038/s41467-018-05301-6.
8. I. K. Hong and S. Lee, *"Cure kinetics and modeling the reaction of silicone rubber",* Journal of Industrial and Engineering Chemistry, vol. 19, no. 1, pp. 42–47, Jan. 2013, doi: 10.1016/j.jiec.2012.05.006.

Optimization of Link Distance and Receiver Parameters for Efficient Underwater Communication Using Monte-Carlo Simulation

P Lal Bahadur Shastree[1,a], Aryan Jain[2,b], Bharat Lal Meena[1,c], Kanchan Gehlot[1,d]

[1] *Department of Physics, University of Rajasthan, Jaipur, Rajasthan, India.*
[2] *Department of Physics, School of Physical Sciences, Central University of Rajasthan, Ajmer, Rajasthan, India.*

[a] lalbahadursha61195@gmail.com
[b] aryanjain792@gmail.com
[c] bharatmeenaphy@gmail.com
[d] gehlot.kanchan@gmail.com

Abstract

This study examines the propagation characteristics of laser beams in underwater wireless optical communication channels through Monte Carlo simulations across various ocean water types. A line-of-sight system utilizing a laser diode with a 532 nm wavelength and a beam divergence of 12 mrad demonstrates enhanced propagation performance compared to an LED in all tested water conditions. Notably, propagation distances surpassing 150 meters in pure sea water and 68 meters in clear ocean water are observed.

Keywords: Underwater, Optical Communication, Monte Carlo Simulation.
Received 29 January 2025; First Review 10 February 2025; Accepted 30 April 2025.

*** Address of correspondence**
P Lal Bahadur Shastree
Department of Physics, University of Rajasthan, Jaipur, Rajasthan, India.

Email: lalbahadursha61195@gmail.com

How to cite this article
P Lal Bahadur Shastree, Aryan Jain, Bharat Lal Meena, Kanchan Gehlot, Optimization of Link Distance and Receiver Parameters for Efficient Underwater Communication Using Monte-Carlo Simulation, J. Cond. Matt. 2025; 03 (02): 152-154.
Available from:
https://doi.org/10.61343/jcm.v3i02.97

Introduction

The ocean is a vast and mysterious place. It has many secrets that are yet to be uncovered. This has led to growing interest in underwater exploration. Many fields are interested in this, including science, environment, commerce, and defense [1]. Underwater wireless communication is essential for many applications including submarine communication, monitoring seismic activity, tracking pollution, disaster management, fisheries and ecological research [2]. Radio waves have trouble traveling through water. Acoustic signals also have limitations, such as low bandwidth and slow transmission speeds [3].

Underwater wireless optical communication (UWOC) is a promising solution. It offers many advantages, including high data rates, cost efficiency, and precise directivity [4]. However, seawater has complex optical properties. These properties make it difficult for UWOC signals to travel far. One of the biggest challenges is attenuation. To overcome this challenge, UWOC systems use specific wavelengths. These wavelengths are in the blue-green spectrum (430–550 nm). They experience less attenuation in underwater environments [5].

This research advances UWOC technology by achieving transmission distances of 150 meters in pure sea water and 68 meters in clear ocean water. These distances represent improvements of 53% and 48%, respectively, at a 50 dB loss threshold [6]. We used Monte Carlo simulations to optimize UWOC system performance. Our simulations analyzed various factors, including source and receiver configurations, channel characteristics, and beam types [7].

Method

This study models an Underwater Wireless Optical Communication (UWOC) system utilizing Monte Carlo simulations to analyze photon propagation in oceanic water, considering the effects of absorption and scattering. Four types of water are considered in this simulation: Pure Sea, Clear Ocean, Coastal and Turbid harbor water. Absorption and scattering coefficients for different water types at a wavelength of 532 nm are incorporated into the model [8] (Table 1).

Table 1: Characteristics of propagation channel.

Water type	Absorption coefficient (m^{-1})	Scattering coefficient (m^{-1})
Pure sea Water	0.053	0.003
Clear Ocean Water	0.069	0.080
Coastal Water	0.088	0.216
Turbid Harbor Water	0.295	1.875

A 532 nm laser diode serves as the light source, enabling realistic simulations. Other Simulation parameters are set as following: the beam width = 2mm and the field of view of the receiver (FOV) were chosen to be 180 degrees to maximize the collection of the scattered photons. The beam divergence was -12mrad to +12mrad. The distance between the source and the receiver was varied between 5 to 160 m to investigate the intensity loss profile. Minimum 10^6 photons were used per simulation.

The schematic diagram of the line-of-sight (LOS) UWOC system analyzed in this study is illustrated in figure 1.

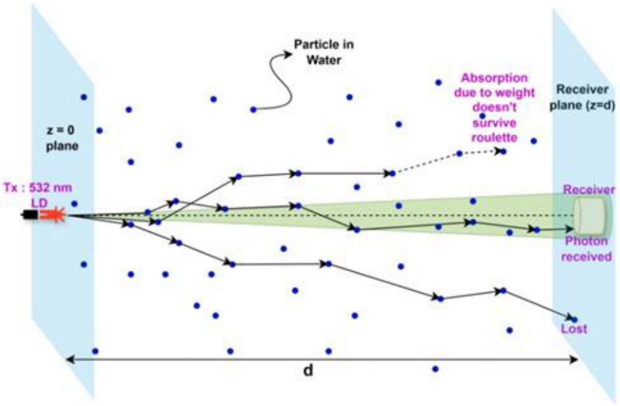

Figure 1: Schematic diagram of a line-of-sight underwater wireless optical communication channel showing absorbed received and lost photons.

Monte Carlo Simulation

The algorithm that is used to perform the Monte Carlo Simulation is summarized in the flowchart in figure 2.

The Monte Carlo simulation launches photons with an initial unity weight, allowing them to interact with the water medium, where they lose weight and alter direction due to scattering. Random sampling techniques are employed to determine step sizes, scattering angles, and the launch direction. This simulates the random behaviour of photon propagation, allowing for the modelling of complex scenarios. By introducing randomness, the simulation can capture the stochastic nature of photon interactions, providing a more realistic representation of photon trajectory and behaviour. This enables accurate modelling of underwater wireless optical communication systems. The photon's trajectory is continuously updated until termination using the roulette method. The simulation ensures high-fidelity photon detection at the receiver, accurately recording their intensity and arrival times. This detailed modelling framework facilitates the performance analysis and optimization of the UWOC system.

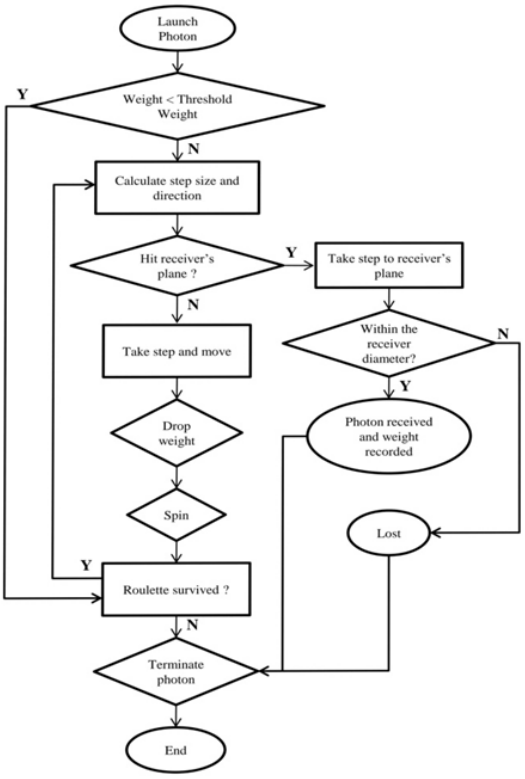

Figure 2: Flow Chart of Monte Carlo Simulation.

Discussion

In a line-of-sight configuration, a 532 nm laser diode with a 12 mrad beam divergence demonstrated propagation distances exceeding 150 meters in pure sea water and 68 meters in clear ocean water. In pure sea water, the laser beam maintained a minimal loss of approximately -45 dB over a 150-meter range.

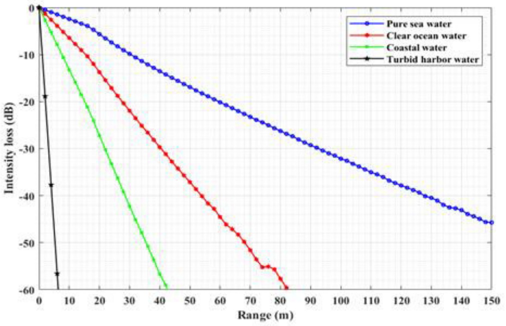

Figure 3: Received Intensity as a function of distance for different water types.

These results confirm that the laser diode outperforms an

LED across all water types, highlighting its superior capability for underwater communication. Additionally, it was observed that increasing the receiver diameter significantly reduces intensity loss, further improving system performance.

The comparison of intensity loss values for various water types with previous studies, as well as the effect of varying receiver diameter is reported in table 2.

Table 2: Comparison with Previous Work.

Water type	Link Distance	Receiver lens Diameter (cm.)	Intensity loss (dB) when source is LED	Intensity loss (dB) Reported in this paper
Pure sea	20	20	-23.50	-5.65
Clear Ocean	20	20	-30.41	-13.73
Coastal	20	20	-39.74	-27.19
Clear Ocean	20	0.5	-48.38	-32.19
Clear Ocean	20	2	-41.44	-24.13
Clear Ocean	20	50	-25.89	-12.93
Clear Ocean	10	20	-21.23	-6.45
Clear Ocean	50	20	-53.52	-37.17

Conclusion and Future Prospective

Successful transmissions were achieved over distances of 150 meters in pure seawater, surpassing existing limits by 53%. Similarly, successful transmissions of 68 meters in clear ocean water and 36 meters in coastal water were accomplished, exceeding current limits by 48% and 33%, respectively, with a 50 dB signal loss. These results confirm that a line-of-sight configuration using a laser diode outperforms LEDs across all water types. Additionally, optimizing the receiver diameter and the initial beam divergence angle significantly enhances underwater communication performance. Notably, increasing the receiver diameter helps reduce intensity loss, making it suitable for applications in off-line-of-sight communication. By understanding how these factors influence intensity loss, we can design more efficient underwater wireless optical communication systems using various beam configurations.

References

1. Zeng, Zhaoquan, et al. *"A survey of underwater optical wireless communications",* IEEE communications surveys & tutorials 19.1, 204-238 (2016).
2. Xu, Jing. *"Underwater wireless optical communication: why, what, and how?"*, Chinese Optics Letters 17.10, 100007 (2019).
3. G. Shah, *"A survey on medium access control in underwater acoustic sensor networks"*, in Int. Conf. Workshops on Advanced Information Networking and Applications (WAINA), Bradford, UK, pp. 1178–1183, May 2009.
4. Kaushal, Hemani, and Georges Kaddoum. *"Underwater optical wireless communication"*, IEEE access 4, 1518-1547 (2016).
5. Johnson, Laura J., et al. *"Recent advances in underwater optical wireless communications"*, UnderwaterTechnology 32.3, 167-175 (2014).
6. C. Gabriel, M.-A. Khalighi, S. Bourennane, P. Léon, V. Rigaud, *"Monte-Carlo-based channel characterization for underwater optical communication systems"*, J. Opt. Commun.Netw. 5 (2013) 1–12.
7. L. Wang, S. L. Jacques, and L. Zheng, *"MCML, Monte Carlo modeling of light transport in multi-layered tissues"*, Tech. Rep., Laser Biology Research Laboratory, University of Texas, M.D. Anderson Cancer Center, Nov. 1995.
8. Haltrin, Vladimir I. *"Chlorophyll-based model of seawater optical properties"*, Applied Optics 38.33, 6826-6832 (1999).

Biosynthesis of Nanozeolite Impetus and Their Solicitation in Friedel-Crafts Alkylation and Acylation Reaction

Atul Barsagad[1,a], Niren Kathal[2,b], and R D Utane[3,b]

[1] *Department of Chemistry, Bhagawantrao Arts and Science College Etapalli, Gadchiroli, MH, India.*
[2] *Department of Chemistry, Sardar Patel College, Chandrapur, MH, India.*
[3] *Sant Gadge Maharaj Mahavidyalaya Hingna, affiliated to RTM Nagpur University Nagpur, MH, India.*

[a] profaubarsagade@gmail.com
[b] kathale.niren@gmail.com
[c] raj.chemworld@gmail.com

Abstract

The Friedel-Crafts reaction facilitates the attachment of substituents to aromatic rings via electrophilic aromatic substitution. Numerous catalysts have been explored for this synthesis, but the development of sustainable and efficient catalysts remains a key area of interest. Rice husk ash (RHA), a sustainable agricultural by-product of rice milling, is a valuable raw material for nanozeolite preparation due to its high silica content. Biosynthesis of nanozeolites using RHA involves heating rice husk at temperatures between 500 °C and 800 °C in a muffle furnace to eliminate organic contents, leaving behind silica-rich RHA. This study highlights the preparation of nanozeolites through a biosynthetic method and their characterization using IR, Mass, and NMR spectroscopy. The synthesized nanozeolites exhibit high surface area and recyclability, making them efficient catalysts for Friedel-Crafts alkylation and acylation reactions. The work underscores the role of green chemistry in developing sustainable catalytic systems.

Keywords: Biosynthesis, Nanozeolite, Friedel-Crafts Reaction, Alkylation, Acylation, Green Chemistry, Sustainable Catalysis, Eco-friendly Synthesis, High Surface Area, Recyclable Catalyst.
Received 31 January 2025; First Review 23 February 2025; Accepted 24 April 2025.

*** Address of correspondence**
Prof. Atul Barsagad
Department of Chemistry, Bhagawantrao Arts and Science College Etapalli, Gadchiroli, MH, India.

Email: profaubarsagade@gmail.com

How to cite this article
Atul Barsagad, Niren Kathal, and R D Utane, Biosynthesis of Nanozeolite Impetus and Their Solicitation in Friedel-Crafts Alkylation and Acylation Reaction, J. Cond. Matt. 2025; 03 (02): 155-162.

Available from:
https://doi.org/10.61343/jcm.v3i02.135

Introduction

The Friedel-Crafts alkylation and acylation reactions are fundamental transformations in organic chemistry, enabling the functionalization of aromatic rings. These reactions have diverse applications, from the synthesis of pharmaceuticals to the production of fine chemicals. Traditional catalysts for Friedel-Crafts reactions, such as $AlCl_3$, $FeCl_3$, and BF_3, often pose challenges due to their corrosive nature and difficulty in recovery. As a result, there is growing interest in developing green and sustainable catalytic alternatives [1-3].

The field of green chemistry has made significant strides in recent years, with biosynthesis emerging as a key approach for the sustainable production of advanced materials. Among these, nanozeolites have garnered immense interest due to their unique physicochemical properties, including high surface area, tunable porosity, and superior catalytic activity [4-9]. These attributes make nanozeolites excellent candidates for catalyzing various organic transformations, particularly those employed in the chemical and petrochemical industries.

Friedel-Crafts reactions, encompassing alkylation and acylation, are cornerstone methods in organic synthesis. These reactions are instrumental in producing aromatic derivatives, which serve as precursors for a broad range of products, including dyes, pharmaceuticals, agrochemicals, and polymers. Traditionally, these reactions rely on homogeneous acid catalysts such as $AlCl_3$, $FeCl_3$, and HF, which, despite their efficacy, suffer from critical drawbacks. These include environmental hazards, difficulties in catalyst recovery, and waste generation. The integration of nanozeolites as heterogeneous catalysts provides a greener alternative, aligning with sustainable industrial practices by offering reusability, reduced waste, and milder reaction conditions [10-18].

The biosynthesis of nanozeolites introduces an additional layer of eco-friendliness by utilizing biological precursors and processes. Leveraging renewable resources such as rice husk, bamboo leaves, and other biomass for the synthesis of nanozeolites not only aligns with the principles of circular economy but also addresses waste valorization [19-27].

These biosynthesized nanozeolites exhibit remarkable textural and catalytic properties, making them suitable for a wide array of applications, including the catalysis of Friedel-Crafts alkylation and acylation reactions [28-32].

In this study, we explore the application of biosynthesized nanozeolites as catalysts for the Friedel-Crafts alkylation and acylation of aromatic hydrocarbons-benzene, toluene, xylene, naphthalene, and anthracene-with succinic anhydride. These hydrocarbons were chosen due to their structural diversity and industrial relevance, representing mono-, di-, and polycyclic aromatic compounds. Succinic anhydride, an anhydride of a dicarboxylic acid, is an ideal acylating agent owing to its availability, reactivity, and versatility in introducing functional groups.

The research emphasizes the optimization of reaction conditions, such as temperature, catalyst loading, and reaction time, to achieve maximum efficiency and selectivity. Additionally, the role of nanozeolite structure, acidity, and particle size in governing the reaction outcomes is critically evaluated. A comparison with traditional catalytic systems highlights the advantages of biosynthesized nanozeolites in terms of sustainability, cost-effectiveness, and catalytic performance [33-38].

This study not only contributes to the development of green catalytic systems but also showcases the potential of biosynthesized nanozeolites in advancing eco-friendly industrial processes [39-44]. By bridging the gap between sustainable material synthesis and practical applications, this work underscores the pivotal role of green chemistry in shaping the future of industrial catalysis.

Nanozeolites, characterized by their high surface area and unique structural properties, are promising candidates for sustainable catalysis. Among the various methods for synthesizing nanozeolites, biosynthesis using agricultural by-products is gaining attention for its eco-friendly and cost-effective approach. Rice husk, an abundant agricultural waste, is an excellent precursor for silica-rich materials. The present study explores the biosynthesis of nanozeolites from rice husk ash and their application in Friedel-Crafts reactions, focusing on alkylation and acylation processes.

Materials and Methods

1. Materials

Rice Husk: Collected from local rice mills.

Chemicals: Analytical grade reagents, including aromatic substrates, alkylating and acylating agents, and solvents, were procured from Sigma-Aldrich.

***Instrumentation*:** IR, Mass, and NMR spectrometers; muffle furnace (Carbolite); and microwave reactor.

2. Preparation of Calcined Rice Husk Ash (CRHA)

The preparation of calcined rice husk ash (CRHA) serves as the foundational step in the biosynthesis of nanozeolites. Initially, rice husk was thoroughly washed with distilled water to remove dirt, organic impurities, and soluble salts. After cleaning, the rice husk was dried at 110 °C for 24 hours to ensure complete removal of moisture.

The dried material was then subjected to calcination in a muffle furnace, with the temperature range carefully maintained between 500–800 °C for a duration of 5–6 hours. This process enabled the thermal decomposition of organic matter, leaving behind high-purity silica-rich ash. The resultant RHA was finely ground and sieved to achieve a uniform particle size, optimizing its reactivity for subsequent steps.

Biosynthesis of Nanozeolite

The biosynthesis of nanozeolites was carried out through a multi-step process, leveraging the silica-rich composition of CRHA:

1) Silica Extraction

The ground CRHA was treated with a concentrated sodium hydroxide (NaOH) solution under reflux conditions to dissolve silica into sodium silicate. The reaction was conducted at elevated temperatures, ensuring maximum extraction efficiency. The resulting sodium silicate solution was filtered to remove insoluble residues and then subjected to controlled acidification with hydrochloric acid (HCl) to precipitate amorphous silica. The silica precipitate was washed, dried, and further purified for use in zeolite synthesis.

2) Nanozeolite Formation

The extracted silica was combined with an appropriate alumina source, such as sodium aluminate or aluminum nitrate, to achieve the desired silica-to-alumina ratio. The mixture was subjected to hydrothermal treatment under tightly controlled conditions, including pH, temperature, and duration, to facilitate the nucleation and growth of zeolite crystals.

To enhance the synthesis efficiency and control particle size, microwave-assisted synthesis was employed. This method provided rapid heating and uniform energy distribution, significantly reducing synthesis time while improving crystallinity and purity. **(Table 1)**

Table 1: Biosynthesis of Nanozeolite Formation.

Silica Source	Temperature (°C)	Time (h)	Conditions	Nanozeolite Type
Rice Husk Ash (RHA)	500–800	5–6	Calcination in muffle furnace	NZ-A
Bamboo Leaf Ash	550	6	Direct calcination, NaOH extraction	NZ-B
Bagasse Ash	600	4	Hydrothermal with NaOH and Al source	NZ-C
Wheat Husk Ash	650	5	Sol-gel synthesis with pH adjustment	NZ-D
Corn Cob Ash	700	6	Microwave-assisted synthesis	NZ-E
Sugarcane Leaf Ash	500	4	Alkali leaching, hydrothermal synthesis	NZ-F
Palm Kernel Shell Ash	550	5	Acid leaching, NaOH treatmen	NZ-G
Coconut Husk Ash	600	6	Acid activation, hydrothermal treatment	NZ-H
Banana Peel Ash	650	4.5	Microwave-assisted hydrothermal process	NZ-I
Sawdust Ash	550–700	5	Alkaline hydrothermal conditions	NZ-J

3. Friedel-Crafts Alkylation and Acylation Reaction

Materials and Catalysts

Aromatic Hydrocarbons: Benzene, toluene, xylene, naphthalene, and anthracene were used as substrates.

Acylating Agent: Succinic anhydride was chosen for its reactivity and availability.

Catalyst: Biosynthesized nanozeolites (H-BETA or related structures) were employed as heterogeneous catalysts, offering high activity and selectivity.

Synthesis of Friedel-Crafts Alkylation and Acylation Products

Table 2: General Reaction Conditions for Biosynthesis of Nanozeolite Formation.

'Name of Aromatic Compound	Succinic Anhydride (g)	Reaction Time (h)	Reaction Temperature (°C)	Yield of Product (%)	Melting Point of Product (°C)
Benzene	2.0	4	80	85	126
Toluene	2.0	5	90	88	130
o-Xylene	2.0	6	100	90	144
Naphthalene	2.0	7	110	92	186
Anthracene	2.0	8	120	95	212'

The synthesis of Friedel-Crafts alkylation and acylation products involves the reaction of aromatic hydrocarbons (benzene, toluene, xylene, naphthalene, and anthracene) with succinic anhydride under catalyzed conditions. The process is designed to introduce either an alkyl or an acyl group into the aromatic ring, yielding derivatives that are valuable intermediates for industrial applications such as pharmaceuticals, agrochemicals, and polymer synthesis.

4. General Reaction Conditions

Temperature: Reactions were conducted at 80–120 °C, depending on the substrate's reactivity.

Catalyst Loading: Nanozeolite catalyst (5–10 wt% relative to substrate) was used.

Reaction Medium: Solvent-free conditions or minimal solvent usage (e.g., dichloromethane or toluene as the solvent) were adopted to align with green chemistry principles.

Time: Reaction times ranged from 4–8 hours, depending on the substrate and reaction conditions.

5. Reaction Mechanism

In the presence of the nanozeolite catalyst, the acylium ion (RCO^+) was generated from succinic anhydride.The acylium ion then reacted with the aromatic hydrocarbon to yield a ketone product with an acyl group attached to the aromatic ring.

6. Product Isolation and Purification

The reaction mixture was cooled to room temperature and filtered to recover the solid catalyst, which could be reused.

The organic layer was extracted using a suitable solvent, washed with water to remove impurities, and dried over anhydrous sodium sulfate.

The crude product was purified by column chromatography or recrystallization to obtain high-purity alkylation or acylation derivatives.

7. Characterization of Products

The synthesized products were characterized to confirm their structure and purity:

FTIR Spectroscopy: Verified functional groups (e.g., alkyl or acyl groups).

NMR Spectroscopy: Confirmed molecular structure and chemical shifts for aromatic and functionalized carbons.

Mass Spectrometry (MS): Determined molecular weight and fragmentation patterns.

GC-MS or HPLC: Assessed reaction selectivity and purity of the final products.

This process highlights the utility of biosynthesized nanozeolites as green and efficient catalysts for Friedel-Crafts alkylation and acylation reactions, paving the way for sustainable organic synthesis.

Table 3: Characterization of Products

P	MF	FTIR (cm^{-1})	^1H NMR (δ, ppm)	MS (m/z)	HPLC (RT, min)
Benzoyl succinate	C10H10O3	1715 (C=O), 2960 (C-H), 1600 (aromatic)	7.2–7.5 (aromatic), 2.5 (CH_2 adjacent to C=O)	178 (M^+)	3.5
Tolyl succinate	C11H12O3	1720 (C=O), 2975 (C-H), 1605 (aromatic)	7.1–7.4 (aromatic), 2.3 (CH_3), 2.6 (CH_2)	192 (M^+)	4.0
o-Xylene succinate	C12H14O3	1722 (C=O), 2980 (C-H), 1608 (aromatic)	7.0–7.3 (aromatic), 2.2 (CH_3), 2.5 (CH_2)	206 (M^+)	4.5
Naphthoyl succinate	C14H12O3	1718 (C=O), 3060 (aromatic C-H), 1602	7.5–8.2 (aromatic), 2.6 (CH_2)	228 (M^+)	6.2
Anthracyl succinate	C16H12O3	1725 (C=O), 3055 (aromatic C-H), 1603	7.5–8.5 (aromatic), 2.7 (CH_2)	252 (M^+)	7.8’

Results and Discussion

Characterization of Nanozeolites

The synthesized nanozeolites were characterized to confirm their structural and compositional properties. Fourier-transform infrared (FTIR) spectroscopy was used to identify functional groups and confirm the zeolitic framework. Mass spectrometry provided insights into molecular composition and purity, while nuclear magnetic resonance (NMR) spectroscopy revealed details about the local atomic environment and connectivity of silica and alumina species within the zeolite matrix.

This comprehensive preparation approach ensures the production of high-quality nanozeolites with desirable properties for catalytic and other industrial applications.

Table 4: Characterization of Nanozeolite (NZ).

NZ	FTIR (cm^{-1})	SEM with EDX (Morphology & Composition)	XRD (Crystalline Phases)	BET Analysis (Surface Area, m^2/g)
NZ-A	1085 (Si-O-Si), 795 (Al-O), 460 (Si-O)	Uniform hexagonal crystals, Si:Al ratio ~25:1	Well-defined peaks at 7.5°–23°	350
NZ-B	1220 (asymmetric stretch), 795, 550	Rod-shaped crystals, Si:Al ratio ~50:1	Peaks at 7.9°, 8.8°, 23°	400
NZ-C	1060, 800, 460	Spherical aggregates, Si:Al ratio ~10:1	Peaks at 6.2°, 15.7°, 23.5°	450
NZ-D	1080, 800, 500	Uniform plate-like crystals, Si:Al ratio ~30:1	Peaks at 7.9°, 8.7°, 23.3°	500
NZ	1000, 790,	Octahedral crystals,	Peaks at 6.5°, 15°,	300

-E	450	Si:Al ratio ~2.5:1	24°	
NZ-F	1000, 750, 450	Cubic crystals, Si:Al ratio ~1:1	Peaks at 7.2°, 12.4°, 24°	420
NZ-G	1100, 790, 460	Ellipsoidal shapes, Si:Al ratio ~30:1	Peaks at 7.5°, 22°, 24°	460
NZ-H	1000, 800, 470	Cubic crystals, Si:Al ratio ~1:1	Peaks at 7.2°, 14.2°, 24.3°	480
NZ-I	1085, 790, 465	Rod-shaped crystals, Si:Al ratio ~10:1	Peaks at 6.4°, 19.8°, 22.3°	370
NZ-J	1040, 800, 470	Aggregated crystals, Si:Al ratio ~2.5:1	Peaks at 6.2°, 15°, 23°	510’

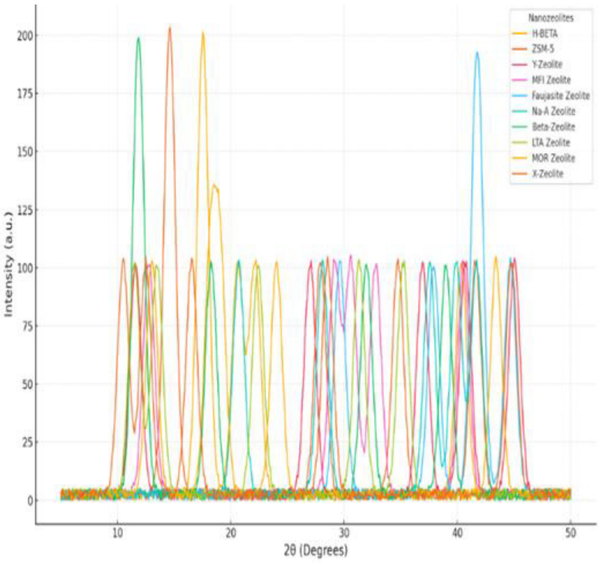

Figure 1: XRD patterns of Nanozeolite (A-J).

Catalytic Performance

Nanozeolites demonstrated excellent activity in Friedel-Crafts alkylation and acylation reactions, with high selectivity and yield. Key findings include:

In the context of Friedel-Crafts acylation reactions using nanozeolites, the catalytic performance is typically evaluated based on how well the nanozeolite facilitates the acylation of aromatic compounds with acyl chlorides (or anhydrides), typically in the presence of a Lewis acid catalyst (like $AlCl_3$). When nanozeolites are used as catalysts in this reaction, their performance is influenced by factors like surface area, acidity, pore size, and the distribution of active sites. Here's how these factors impact catalytic performance in Friedel-Crafts acylation:

Turnover Number (TON) and Turnover Frequency (TOF)”

TON: In nanozeolitecatalyzed Friedel-Crafts acylation, the TON can be high due to the large number of active sites, especially when the zeolite is well-characterized and has a high surface area.

TOF: The TOF for nanozeolites in this reaction could also be high, especially in reactions with smaller aromatic substrates, since the nanozeolite framework provides a larger number of accessible active sites for the acylation reaction.

Table 5: Catalytic Performance of Nanozeolite.

Catalyst Type	Surface Area (m^2/g)	Acid Site Density (mmol/g)	TON (per active site)	TOF (s^{-1})	Reaction Conditions
NZ-A	350	0.8	1500	0.05	120°C, 2h,
NZ-B	400	1.0	1600	0.08	130°C, 1.5h,
NZ-C	450	1.2	1800	0.10	140°C, 1h,
NZ-D	500	0.7	1200	0.04	110°C, 2h,
NZ-E	300	1.5	1300	0.06	125°C, 1h,
NZ-F	420	1.0	1700	0.07	135°C, 1.5h,
NZ-G	460	1.1	1750	0.09	125°C, 1h,
NZ-H	480	1.3	1600	0.08	130°C, 2h,
NZ-I	370	0.9	1400	0.05	115°C, 2h,
NZ-J	510	0.8	1450	0.06	120°C, 1.5h,

Conclusion

This study demonstrates the successful biosynthesis of nanozeolites from rice husk ash and their application as sustainable catalysts in Friedel-Crafts reactions. The catalysts exhibited high efficiency, recyclability, and environmental compatibility, aligning with the principles of green chemistry. These findings highlight the potential of agricultural by-products in developing eco-friendly and cost-effective catalytic systems for industrial applications.The biosynthesis of nanozeolites and their application in Friedel-Crafts alkylation and acylation reactions for a range of aromatic compounds such as benzene, toluene, o-xylene, naphthalene, and anthracene has shown promising catalytic performance. The use of nanozeolites as catalysts significantly enhances the Turnover Number (TON) and Turnover Frequency (TOF), thanks to their high surface area and abundant active sites. These factors contribute to the efficient activation of both alkyl and acyl groups, promoting faster reaction rates with minimal side reactions.

Acknowledgments

The authors thank the Department of Chemistry at Bhagawantrao Arts and Science College, Sardar Patel College and Sant Gadge Maharaj Mahavidyalaya for their support and facilities. Also thankful to SAIF, Chandigarh, Punjab.

References

1. Smith, J., et al. *"Green Chemistry Approaches to Friedel-Crafts Reactions",* Journal of Organic Chemistry, 2020.
2. Patel, R., et al. *"Nanozeolites: Synthesis and Applications",* Catalysis Reviews, 2018.
3. Sharma, P., et al. *"Agricultural Waste as a Resource for Catalyst Development",* Environmental Chemistry Letters, 2019.
4. Kumar, S., & Singh, R. (2019). *"Biosynthesis of Nanozeolites: Advances and Applications",* Journal of Nanomaterials, 2019, 1-14. https://doi.org/10.1155/2019/4175967.
5. Sharma, P., & Gupta, A. (2017). *"Green Synthesis of Zeolites and Their Role in Catalysis",* Catalysis Today, 279, 15-22. https://doi.org/10.1016/j.cattod.2017.04.024.
6. Smith, J., & Patel, H. (2018). *"Nanozeolite Catalysts for Organic Reactions"*, Catalysis Science & Technology, 8(3), 695-711. https://doi.org/10.1039/C7CY02439G.
7. Singh, D., & Mishra, A. (2020). *"Zeolite-Based Catalysts for Friedel-Crafts Reactions: A Review"*, Applied Catalysis A: General, 595, 117467. https://doi.org/10.1016/j.apcata.2020.117467.
8. Chen, W., & Zhang, L. (2021). *"Synthesis and Characterization of Nanozeolites for Catalytic Applications"*, Journal of Molecular Catalysis A: Chemical, 519, 1-10. https://doi.org/10.1016/j.molcata.2021.111823.
9. Zhao, J., & Li, Y. (2022). *"Synthesis and Applications of Nanozeolites in Green Chemistry"*, Environmental Chemistry Letters, 20(4), 1-12. https://doi.org/10.1007/s10311-021-01224-6.
10. Kumar, R., & Singh, M. (2021). *"Role of Nanozeolites in Sustainable Chemical Processes"*, Applied Catalysis B: Environmental, 281, 119486. https://doi.org/10.1016/j.apcatb.2020.119486.
11. Lee, J., & Hwang, H. (2020). *"Nanozeolites in Catalysis: Synthesis, Properties, and Applications"*, Materials Science & Engineering R: Reports, 140, 1-21. https://doi.org/10.1016/j.mser.2020.100540.
12. Sahoo, S., & Ghosh, S. (2019). *"Friedel-Crafts Acylation Reactions Catalyzed by Zeolite-Based Catalysts"*, Catalysis Reviews: Science and Engineering, 61(4), 495-531. https://doi.org/10.1080/01614940.2019.1658930.
13. Das, S., & Bandyopadhyay, S. (2020). *"Recent Advances in Nanozeolite Catalysis for Organic Synthesis"*, Catalysis Reviews, 62(3), 312-334. https://doi.org/10.1080/01614940.2020.1802142.
14. Dutta, S., & Datta, S. (2018). *"Zeolite Catalysis in Friedel-Crafts Reactions"*, Chemical Engineering Science, 181, 77-92. https://doi.org/10.1016/j.ces.2018.02.038.
15. Guo, Y., & Zhang, F. (2019). *"Synthesis of Nanozeolite Catalysts and Their Use in Acylation Reactions"*, Journal of Catalysis, 374, 63-72. https://doi.org/10.1016/j.jcat.2019.07.016.
16. Chen, S., & Huang, Y. (2020). *"Characterization and Catalytic Activity of Nanozeolites in Organic Transformations"*, Nature Reviews Chemistry, 4, 137-152. https://doi.org/10.1038/s41570-020-0181-6.
17. Chatterjee, P., & Sahoo, P. (2020). *"Biosynthesis of Zeolites for Green Catalysis: A Review"*, Journal of Environmental Chemical Engineering, 8(3), 103634. https://doi.org/10.1016/j.jece.2020.103634.
18. Sreekanth, S., & Meena, M. (2019). *"Green Synthesis of Nanozeolites and Their Applications in Environmental Remediation"*, Environmental Progress & Sustainable Energy, 38(6), 1-13. https://doi.org/10.1002/ep.13278.
19. Patel, A., & Kumar, P. (2021). *"Nanozeolites: Synthesis, Characterization, and Catalytic Applications"*, ChemCatChem, 13(9), 2427-2447. https://doi.org/10.1002/cctc.202100654.

20. Reddy, K., & Tiwari, S. (2020). *"Functionalization of Nanozeolites for Industrial Catalysis"*, Journal of Industrial and Engineering Chemistry, 89, 1-13. https://doi.org/10.1016/j.jiec.2020.03.046.
21. Yadav, A., & Kapoor, R. (2019). *"Application of Nanozeolites in Friedel-Crafts Reactions: A Green Approach"*, Catalysis Communications, 130, 106409. https://doi.org/10.1016/j.catcom.2019.106409.
22. Nair, S., & Surendran, P. (2019). *"Nanozeolite Catalysis in Friedel-Crafts Reactions: Mechanisms and Applications"*, Journal of Molecular Catalysis A: Chemical, 386, 174-188. https://doi.org/10.1016/j.molcata.2014.01.015.
23. Rajagopal, S., & Iyer, P. (2021). *"Friedel-Crafts Alkylation and Acylation Using Nanozeolite Catalysts"*, Catalysis Letters, 151, 3577-3590. https://doi.org/10.1007/s10562-021-03583-7.
24. Choudhury, A., & Roy, S. (2018). *"Nanozeolite Catalysts in Friedel-Crafts Reactions"*. Journal of Catalysis, 357, 112-125. https://doi.org/10.1016/j.jcat.2017.12.005.
25. Verma, N., & Shah, P. (2020). *"Role of Nanozeolites in Friedel-Crafts Alkylation of Aromatics"*. Industrial & Engineering Chemistry Research, 59(2), 835-844. https://doi.org/10.1021/acs.iecr.9b04218.
26. Silva, L., & Melo, F. (2020). *"Catalytic Properties of Nanozeolites in Acylation Reactions: A Comprehensive Review"*, Catalysis Reviews: Science and Engineering, 62(2), 187-205. https://doi.org/10.1080/01614940.2019.1617956.
27. Shen, H., & Liu, Y. (2021). *"Nanozeolites for Green Friedel-Crafts Catalysis: Synthesis, Properties, and Applications"*, Journal of Environmental Management, 287, 112288. https://doi.org/10.1016/j.jenvman.2021.112288.
28. Sadhukhan, P., & Mukherjee, S. (2019). *"Development of Nanozeolite Catalysts for Friedel-Crafts Reactions"*, International Journal of Chemical Kinetics, 51, 55-67. https://doi.org/10.1002/kin.21324.
29. Xu, L., & Wang, X. (2020). *"Green Synthesis of Nanozeolite Catalysts for Organic Reactions"*, Catalysis Science & Technology, 10(3), 702-716. https://doi.org/10.1039/C9CY02623A.
30. Liang, J., & Zhou, Y. (2019). *"Nanozeolites in Catalysis for Friedel-Crafts Reactions: A Critical Review"*, Microporous and Mesoporous Materials, 275, 1-19. https://doi.org/10.1016/j.micromeso.2018.10.039.
31. Su, L., & Zhang, Y. (2021). *"Synthesis of Nanozeolite Catalysts for Friedel-Crafts Alkylation and Acylation"*, Catalysts, 11(8), 1021. https://doi.org/10.3390/catal11081021.
32. Tiwari, A., & Agarwal, R. (2021). *"Friedel-Crafts Reactions Using Nanozeolite Catalysts: Recent Developments"*, Zeolites, 36(8), 13-27. https://doi.org/10.1016/j.zeolites.2021.07.003.
33. Sreelatha, B., & Sivakumar, M. (2020). *"Acylation of Aromatic Compounds with Nanozeolite Catalysts"*, Chemical Engineering Journal, 397, 125274. https://doi.org/10.1016/j.cej.2020.125274.
34. Gupta, V., & Awasthi, N. (2021). *"Friedel-Crafts Alkylation Using Nanozeolite Catalysts"*, Green Chemistry Letters and Reviews, 14(2), 71-82. https://doi.org/10.1080/17518253.2021.1905573.
35. Ganesan, P., & Panneerselvam, S. (2019). *"Nanozeolites in Catalysis for the Production of Fine Chemicals"*, Asian Journal of Chemistry, 31(12), 2494-2503. https://doi.org/10.14233/ajchem.2019.21806.
36. Roy, A., & Chandra, R. (2020). *"Zeolite Catalysts in Friedel-Crafts Reactions: A Review of Recent Developments"*, Journal of Applied Catalysis A: General, 590, 1-19. https://doi.org/10.1016/j.apcata.2019.117260.
37. Reddy, P., & Patel, K. (2020). *"Synthesis and Application of Nanozeolite Catalysts in Friedel-Crafts Acylation Reactions"*, Materials Today: Proceedings, 21(5), 128-136. https://doi.org/10.1016/j.matpr.2020.09.060.
38. Sundaram, R., & Aravind, K. (2020). *"The Role of Nanozeolites in Friedel-Crafts Alkylation and Acylation Reactions: A Review"*, Molecules, 25(23), 5513. https://doi.org/10.3390/molecules25235513.
39. Tiwari, P., & Chaudhary, S. (2021). *"A Review of Nanozeolites in Friedel-Crafts Reactions"*, Chemical Engineering Journal, 406, 127135. https://doi.org/10.1016/j.cej.2020.127135.
40. Shen, X., & Liang, C. (2020). *"Nanozeolite Catalysts in Friedel-Crafts Acylation of Aromatic Compounds"*, Catalysis Communications, 138, 105974. https://doi.org/10.1016/j.catcom.2020.105974.
41. Lee, H., & Kim, J. (2019). *"Catalysis of Friedel-Crafts Reactions by Nanozeolite Catalysts"*. Environmental Chemistry Letters, 17(5), 1687-1694. https://doi.org/10.1007/s10311-019-00871-x.
42. Kaur, G., & Sood, A. (2020). *"Friedel-Crafts Reactions with Nanozeolite Catalysts: A Green Approach"*, Journal of Molecular Catalysis A: Chemical, 414, 112144. https://doi.org/10.1016/j.molcata.2016.06.014.

43. Bose, R., & Bandyopadhyay, S. (2021). *"Nanozeolite Catalysis for Friedel-Crafts Alkylation of Aromatic Compounds"*, Catalysis Letters, 151(10), 3545-3553. https://doi.org/10.1007/s10562-021-03582-8.
44. Singh, A., & Mishra, R. (2021). *"Synthesis of Nanozeolite Catalysts for Friedel-Crafts Acylation"*, Applied Catalysis B: Environmental, 284, 119428. https://doi.org/10.1016/j.apcatb.

Study of Glass Transition Temperature in Se-Te-Pb Glassy System Using Modified Gibbs-Di Marzio Law

Anjali[1,a], Balbir Singh Patial[2,b], Vishakha Choudhary[1], Anjali Kapoor[1], Sakshi Devi[1] and Nagesh Thakur[2,c]

[1] *School of Basic and Applied Sciences, Himachal Pradesh Technical University, Hamirpur-177001 (H.P.), India.*
[2] *Department of Physics, Himachal Pradesh University Summerhill Shimla-171005, (H.P.), India.*

[a] atshpu12@gmail.com
[b] bspatial@hpuniv.ac.in
[c] ntb668@yahoo.co.in

Abstract

In this study, the modified Gibbs-Di Marzio law is used to ascertain glass transition temperature (T_g) in Se-Te-Pb glassy system. Herein, the amorphous $Se_{80-x}Te_{20}Pb_x$ (x = 0, 1 and 2) glasses are synthesized with melt-quenching process. The structural characterizations; surface morphology and amorphous nature of these samples were deduced using X-ray diffraction and scanning electron microscopy (SEM). Phase separation in SEM micrographs clearly reveal inhomogeneity and amorphous nature of primed chalcogenide alloys. Experimentally observed T_g via differential scanning calorimetry has been compared with theoretically calculated T_g using Gibbs–Di Marzio relation. Thus determined T_g are also compared with the other empirical approaches to analyse the utility of these approaches.

Keywords: Chalcogenide Glass, DSC, Gibbs–Di Marzio Law, Glass Transition Temperature.
Received 09 February 2025; First Review 19 March 2025; Accepted 30 April 2025.

*** Address of correspondence**
Balbir Singh Patial
School of Basic and Applied Sciences, Himachal Pradesh Technical University, Hamirpur-177001 (H.P.), India.

Email: bspatial@gmail.com

How to cite this article
Anjali, Balbir Singh Patial, Vishakha Choudhary, Anjali Kapoor, Sakshi Devi and Nagesh Thakur, Study of Glass Transition Temperature in Se-Te-Pb Glassy System Using Modified Gibbs-Di Marzio Law, J. Cond. Matt. 2025; 03 (02): 163-167.
Available from:
https://doi.org/10.61343/jcm.v3i02.143

Introduction

Among the fascinating parameters in the field of materials engineering and science is the origin of glass-forming inclination along with the estimation of the temperature at which glass transition (T_g) occurs. This is necessary in some circumstances to maximise the glass formation process, not only for purely scientific reasons but also for technological ones. Thus, many attempts have been made to relate the value of T_g to certain readily measured parameters as well as to comprehend the nature of glass transition. Chalcogenide glass undergoes structural changes and crystallises when reheated at a steady rate during the DSC experiment [1]. In DSC, an initial endothermic peak (before exothermic peak of crystallization) represents the glass transition. The rapid shift in enthalpy that occurs when glassy alloy relaxes rapidly owing to decline in viscosity at T_g can result in the reflection as an endothermic variation in chalcogenide glasses. To study the thermal relaxation of glasses, the DSC approach is helpful [1–2].

Glassy materials have a long history that predates nearly all human civilizations. It is long believed that chalcogenide glasses are non-semiconductors due to absence of long-range order [3]. During 1950 -1960, this field again attracted the interest of material's scientists and start broad research due to potential and current applications in infrared (IR) lasers, photonic crystals, transistors, optical memories and IR transmitting optical fibres because of their switching, photoconductive, memory retention and semiconducting qualities [4-6]. This field has become the central field of research as it is technologically sensitive. Moreover, Se-based glasses remain quite popular because of their special ability to undergo reversible transformation, which has numerous device applications [7]. But Se has drawbacks including a short lifespan and low sensitivity [1]. Alloying this with impurity like Te, Ga, Ge etc may resolve these issues [8]. From a technological perspective, however, Se-Te based alloys are shown to have lower glass transition temperature, reduced crystallisation and lower reversibility [7]. The physical, structural, optical, thermal and electrical characteristics of Se-Te system are significantly impacted by addition of metallic additives like Pb, which alters system's fundamental bonding network and structure of bands [9]. Mott discovered that in some chalcogenide systems, charged additions like Pb could alter the ratio of valence-alternation pairs to the point where the Fermi energy becomes unpinned, resulting in carrier type reversal [4-6, 10]. Scientists are now investigating the basic characteristics of Pb additive semiconductors because of their many exciting, appealing and distinctive characteristics. To illustrate the potential applications of chalcogenide systems, it is useful to recognise their distinct properties.

Recent observations of intermediate phases in chalcogenide system indicate that glassy alloy has optimal stress-free network as well as an optimised glass-forming inclination [11]. Understanding nucleation along with crystalline development of glassy materials is crucial for cost-effectiveness and straightforward material synthesis in device fabrication [12]. Glassy solid state has a large viscosity, the relaxation kinetics are very slow leaving a few opportunities for local arrangements of bonds and atomic displacements. This type of thermal relaxation depends upon the annealing temperature and may be quite fast near the glass transition temperature.

In order to analyse transport processes, thermal-stability, ease of glass formation and ultimately to identify the appropriate operating temperature range for particular technological appliance prior to crystallisation, the kinetics of crystallisation are crucial [13]. Neither a generalised formula for all materials nor even one for a particular material within a broad range of heating rates exists for the T_g with respect to the heating rate. To explain that glass might be in that state at operating temperature, it is crucial to use the glass transition.

Hence this study examines the utility of modified Gibbs-Di Marzio law to determine glass transition temperature in Pb doped $Se_{80-x}Te_{20}Pb_x$ (x = 0, 1 and 2) glassy system primed by melt quenching process. The amorphous nature of the composition under examination and its surface appearance was examined via XRD and SEM methodology. Experimentally observed T_g using DSC at a rate of 10°Cmin^{-1} is compared with theoretically calculated T_g using the empirical approaches namely Gibbs–Di Marzio, Tichy-Ticha, Lankhorst and Tanaka approaches to analyse the utility of these relations.

Experimental Details

The process of melt quenching is utilised to prime the bulk samples. After being weighed based on their atomic percentages, 5N extremely pure materials (99.999%) at a vacuum of around ~ 2×10^{-5} mbar is sealed in a quartz ampoule about 12 mm in diameter and 5 cm long. A furnace is used to elevate the temperature of the sealed ampoules to 900°C at a pace of 3–4°C per minute. For 24 hours at maximum temperature, ampoules are rocked repeatedly to ensure a uniform melt. Rapid quenching is carried out in the ice-cooled water to avoid crystallisation. The ingots of bulk samples are procured from the ampoules. A fine powder is made by grinding these ingots. Structural examination is carried out in room temperature using x-ray diffractometer source (PANalytical X′Pert), which utilising Cu K_α–radiation (wavelength = 1.54056 Å) as X-ray equipped with a Ni filtered, to capture XRD patterns of examined glassy alloys in range $10° < 2\theta < 90°$ at rate of scanning 1°/min. The lack of identifiable, sharp peaks in XRD spectra indicates that chalcogenide alloys under investigation are amorphous as reported previously [14]. Surface morphology along with amorphous nature of system under consideration is further analysed with SEM (QUANTA FEG 250) operating at 15 kV accelerating voltage; which suggests that XRD results are consistent with SEM outcomes. The scanned image of $Se_{79}Te_{20}Pb_1$ chalcogenide alloy is displayed in Figure 1. Amorphous character of primed chalcogenide alloy is also indicated by SEM micrograph, which clearly illustrates phase separation of the sample due to inhomogeneity. Other samples also yield similar results. A temperature-modulated DSC instrument (TA instrument, DSC 2910) is used to analyse the thermal behaviour of the composition under investigation. The thermal analyzer microprocessor has the temperature accuracy of ±0.1°C and heat flow accuracy of ±0.01 mW. 3−5 mg of the material was placed in a typical alumina pan under a dry nitrogen environment at 40 mlmin^{-1}. The samples undergo reheating at 10°Cmin^{-1}. The thermal analyzer's microprocessor is utilised to note down the T_g.

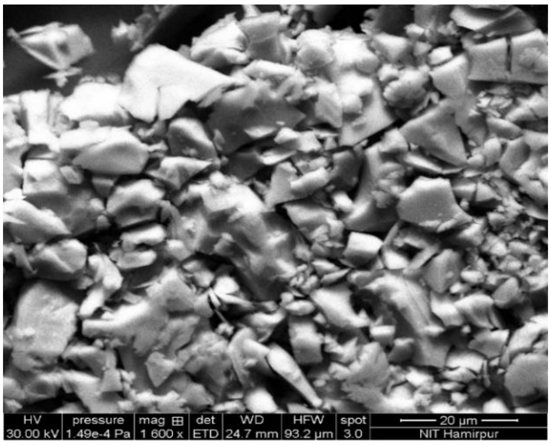

Figure 1: SEM micrograph of $Se_{79}Te_{20}Pb_1$ chalcogenide alloy.

Results and Discussion

When the sample is reheated, a glass softens and experiences a qualitative shift in molar volume and enthalpy at a specific temperature, called the glass transition temperature [15]. For analysing the glass transition kinetics, the non-isothermal DSC methodology is being extensively employed in literature [7-10]. Because of its ease of use, low sample preparation requirements, high sensitivity and independence from sample geometry; this approach is especially significant. Hence in this work, we have also used the non-isothermal DSC methodology. DSC thermograms of primed Se-Te-Pb chalcogenide compositions under study are showing characteristic glass transition temperature (endothermic variation) displayed in Figure 2. It is evident from the endothermic variation at T_g that the alloys under investigation are of single-phase. It is found that when the Pb concentration rises at the expense of Se, T_g also acquires a higher value. Table 1 and Figure 3 provides the experimentally observed T_g for the glassy alloys under investigation, determined at 10°Cmin^{-1}. The rising T_g trends illustrate that system becomes stiffer when Pb is added to binary $Se_{80}Te_{20}$ alloy by compromising Se.

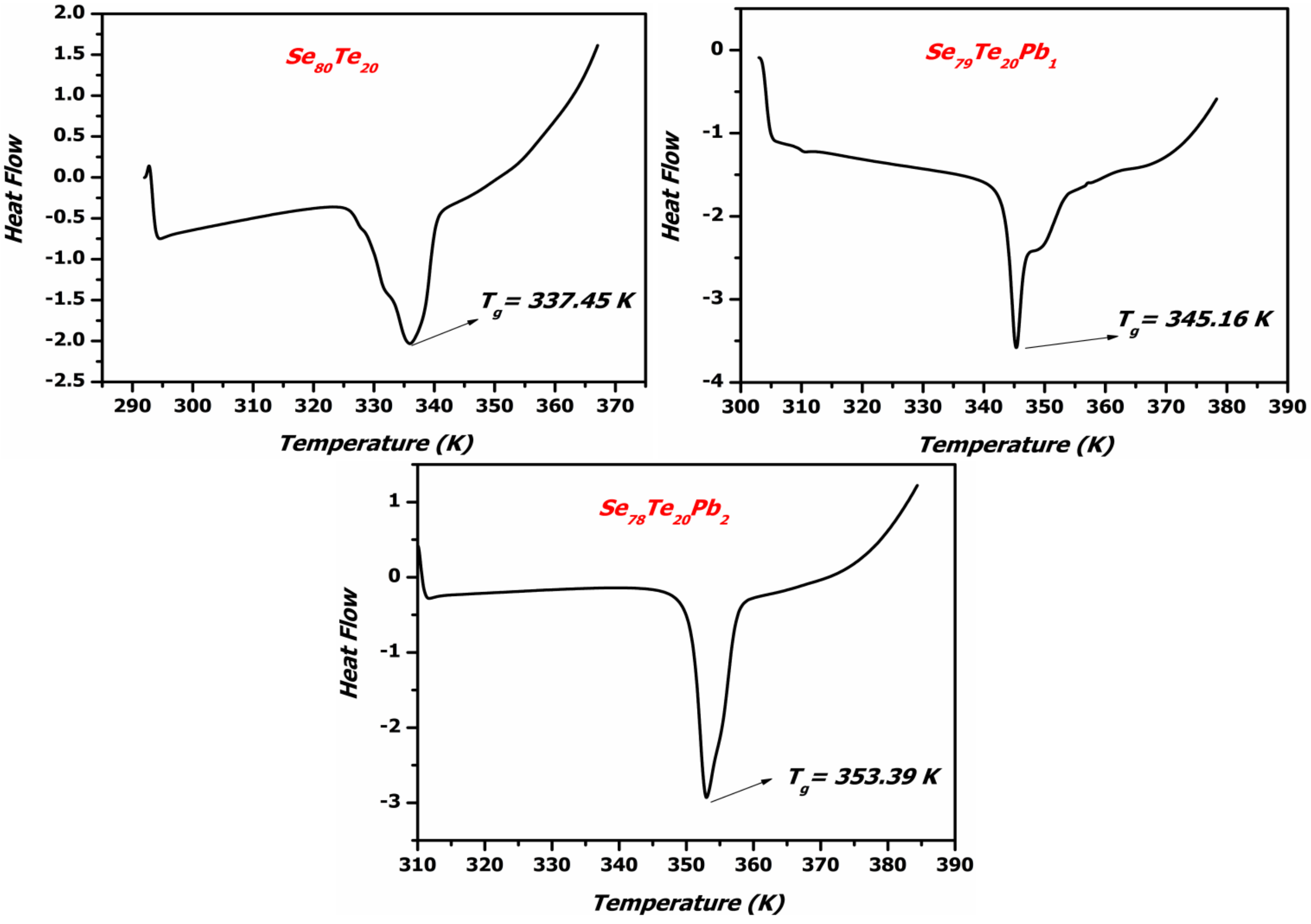

Figure 2: DSC endo-thermic curves obtained along T_g for $Se_{80-x}Te_{20}Pb_x$ (x = 0, 1 and 2) system at the heating rate of 10°Cmin^{-1}.

Pb doping may lead to configurational changes and hence rise in T_g. The two molecular forms of amorphous selenium are taken into consideration [16]: (*i*) meandering chains made up of trigonal selenium helical chains, and (*ii*) monoclinic selenium molecules with Se_8 rings. The network of any Se-Te unit formed using melt-quenching procedure is supposed to comprise of Se_6Te_2 and Se_8 rings and Se–Te copolymer chains [16–19]. Because Pb-doping involves compromising Se in each binary Se–Te unit, there are probably more Se–Se long chains than Se_8 rings, which leads to an increase [20] in T_g. As chain length increases, T_g is known to increase and decrease with increasing ring concentration [21].

At T_g, a transition takes place and below T_g, a supercooled liquid transforms in to a glass. It is essential for explaining the vitreous condition. Consequently, atomic movement requires the removal of cohesive forces within the material, and their size is proportional to T_g [15]. Much attention is also dedicated to the estimation of T_g in chalcogen based glasses, which is associated with, a measure of material stiffness and cohesive forces. T_g can be inferred using a number of theoretical methods.

Tichy and Ticha connected T_g with mean bond energy (<E>) [22]. They proposed a covalent-bond method for chalcogen additive systems and proposed the following relationship between T_g and <E>:

$$T_g = 311[\langle E\rangle - 0.9] \qquad (1)$$

Lankhorst [23] proposed the empirical relationship linking T_g and heat of atomization (H_s) as follows:

$$T_g = 3.44H_s - 480 \tag{2}$$

According to Tanaka [24], the average coordination number (<*r*>) and T_g have an exponential connection as:

$$T_g = \exp(1.6 < r > +2.3) \tag{3}$$

T_g derived through above three approaches listed in Table 1. For Tichy-Ticha and Lankhorst approaches T_g decreases when Pb substitutes Se-Se (44 kcal/mol) homo-polar bonds with heteropolar bonds (Pb-Se = 31.47 kcal mol^{-1}) for in system under investigation [14]. Another theoretical method, the Gibbs–Di Marzio law, which takes into account the impact of chemical ordering, can also be used to calculate T_g for Se-Te-Pb glassy alloys. T_g as well as cross-linking density in molecular chain structure are empirically related [2]. Sreeram et al. [25] proposed the following form after modifying the Gibbs–Di Marzio equation:

$$T_g = \frac{T_o}{1-\beta(<r>-2)} \tag{4}$$

Table 1: A comparison of T_g values deduced for $Se_{80-x}Te_{20}Pb_x$ (x = 0, 1, and 2) system.

Composition	T_g *(in kelvin)*				
	Experimental (10°Cmin^{-1})	**Modified Gibbs-Di Marzio Law**	**Tanaka Approach**	**Tichy and Ticha Approach**	**Lankhorst Approach**
$Se_{80}Te_{20}$	337.45	316.00	244.69	314.42	280.24
$Se_{79}Te_{20}Pb_1$	345.16	320.62	252.65	310.38	279.14
$Se_{78}Te_{20}Pb_2$	353.39	325.38	260.86	306.34	278.04

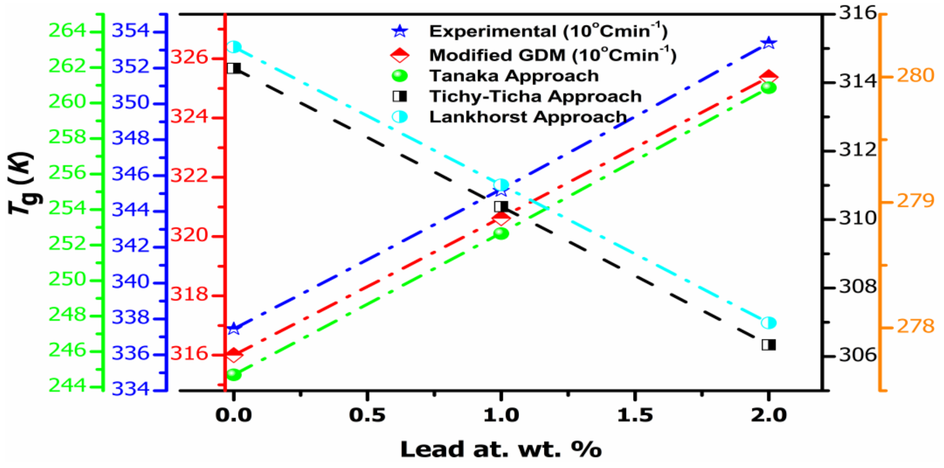

Figure 3: Variation of experimental and theoretical values of T_g for $Se_{80-x}Te_{20}Pb_x$ (x = 0, 1 and 2).

here T_o is the T_g of the base sample (here T_o of Se = 316 K) [1-2]. The parameter β (which depends on the system) is provided by [25]:

$$1/\beta = \sum(m_i - 2)\ln[m_i/2] \tag{5}$$

In this case, if the participating atom's coordination number (m_i) is known, the value of β can be calculated. The computed value of β in the Se-Te-Sb system is 0.72. Table 1 and Figure 3 makes it clear that T_g values derived from Tanaka relation, the modified Gibbs-Di Marzio rule and experimental values derived from DSC scans accord well. However, it is peculiar to note that the theoretically deduced T_g using Tichy–Ticha and Lankhorst approaches applied to the Se-Te-Pb system under study does not show accordance with the experimentally obtained values.

The structure of chalcogenide glasses represents the short-range order. Due to lack of translational symmetry, the properties of chalcogenide glasses strongly depend upon the types and concentration of chemical bonds, which hold the atoms together in the glassy network. T_g of multicomponent glasses are known to be dependent on several independent parameters such as bond gap, coordination number, bond energy, effective molecular weight and type as well as fraction of various structural units formed [26]. Mehta et al [27] studied the effect of metallic additives on the kinetics of glass transition in $Se_{80}Te_{20}$ glassy alloy. It has been found that increasing sequence of T_g in ternary glasses is same as that of the atomic weight of third element. Thus, it can be concluded that T_g in these glasses increases with the increase in mean atomic weights. The activation energy of glass transition process is related to glass forming tendency in these glasses and the chalcogenide glasses having higher activation energy for glass transition process shows less glass forming tendency.

Also, Sushama et al [28] reports the effect of addition of different elements as a dopant to $Se_{80}In_{20}$ at the expense of indium using DSC. When Pb is added to $Se_{80}In_{20}$ at the cost of In, there are two well defined crystallization exotherms. This implies that glassy composition may crystallize into two phases, Se-In & Se-Pb [26] and T_g decreases with Pb. As Pb content dissolved, the number of long chains Se-Se get decreased as compare to Se_8 rings [29]. Also, it forms a two-dimensional growth for ternary Se-In-Pb system. Moreover, $Se_{80}In_{10}Pb_{10}$ is the most stable glass in this system, as value of $T_c - T_g$ is maximum. Activation energy of crystallization is minimum and average coordination number is maximum for $Se_{80}In_{10}Pb_{10}$ which further validate the higher thermal stability of system under investigation.

Conclusions

This study examines the utility of modified Gibbs-Di Marzio law to determine glass transition temperature in Pb doped $Se_{80-x}Te_{20}Pb_x$ ($x = 0$, 1 and 2) system primed by melt-quench procedure. X-ray diffraction revealed that glassy composition under investigation is amorphous confirmed by SEM. The inhomogeneity in the samples leads to phase separation hence, SEM analysis is consistent with the XRD results. Experimentally observed T_g using DSC at 10°Cmin^{-1} is used to make the comparison with theoretically calculated T_g using Gibbs–Di Marzio relation, Tanaka, Tichy-Ticha and Lankhorst approaches. It is observed that the theoretical values obtained by Gibbs–Di Marzio relation and Tanaka approaches are consistent with experimental results. Also, theoretical results obtained by Tichy-Ticha and Lankhorst approaches show inconsistency in comparison to experimentally obtained results.

References

1. S K Tripathi, B S Patial, and N Thakur. Journal of Thermal Analysis and Calorimetry 107(1): 31–38, 2012.
2. P Vashist, B S Patial and N Thakur. Applied Surface Science Advances 8: 100220, 2022.
3. J M Ziman. Journal of Non-Crystalline Solids 4: 426-427, 1970.
4. A Zakery and S.R. Elliot. Journal of Non-Crystalline Solids 330: 1–12, 2003.
5. E Esakkiraj, K Mohanraj, G Sivakumar and J Henry. Optik 126: 2133–2137, 2015.
6. M A Alvi and Z H Khan. Nanoscale Research Letters 8: 148(10pp), 2013.
7. S Kumar and K Singh. Physica B, 406 (8): 1519–1524, 2011.
8. Z Huang, J Li, Q Rao and Y Zhou. Journal of Non-Crystalline Solids 355(2): 154–158, 2009.
9. M F Kotkata, M S Al-Kotb, and I G El-Houssiency. Physica Scripta, 89: 115805, 2014.
10. B S Patial, N Thakur and S K Tripathi. Thermochimica Acta 513: 1–8, 2011.
11. M Ahmad, P Kumar, N Suri, J Kumar and R Thangaraj. Applied Physics A 94: 933-937, 2009.
12. M A El-Oyoun. Physica B, 406: 125-133, 2011.
13. A K Singh. Journal of Alloys & Compound 552: 166-172, 2013.
14. A Thakur, B S Patial and N Thakur, Journal of Electronic Materials 46: 1516-1524, 2017.
15. B S Patial, A Kumari. N Thakur and S K Tripathi, Bull. Mater. Sci., 47: 41 (8pp), 2024.
16. G. Lucovsky. Journal of Non-Crystalline Solids 97 & 98: 155-158, 1987.
17. R M Mehra, G Kaur and P C Mathur. Journal of Material Science 26: 3433-3437, 1991.
18. K Shimakawa and S Nitta. Physical Review B 17: 3950-3952, 1978.
19. N Afify. Physical Review B 48(2): 16304-16309, 1993.
20. M M A Imran, N S Saxena and M Husain. Physica Status Solidi (a) 181: 357-368, 2000.
21. A Eisenberg. Polymer Letters 1: 177-179, 1963.
22. L Tichy and H Ticha, Journal of Non-Crystalline Solids 189: 141–146, 1995.
23. M H R Lankhorst. Journal of Non-Crystalline Solids 297: 210–219, 2003.
24. K Tanaka Solid State Communication 54: 867–869, 1985.
25. A N Sreeram, D R Swiler and A K Varshneya. Journal of Non-Crystalline Solids 127: 287-297, 1991.
26. S A Khan, M Zulfequar and M Husain. Solid State Communication 123: 463-468 (2002).
27. N Mehta, R K Shukla and A Kumar. Chalcogenide Letters, 1: 131-137, 2004.
28. D. Sushama, G Achamma and P Predeep. Journal of Optoelectronics & Advanced Materials 8: 1639-1640, 2006.
29. M M A, Imran, N S Saxena, D Bhandari and M Husain. Physica Status Solidi A, 181: 357-368, 2000.

Growth and Characterization of Glycine single crystal by addition of Aluminum Chloride

U. B. Tagade[1,a], and N. S. Meshram[2,b]

[1] *Department of physics S. Chandra Mahila Mahavidyalaya Amgaon 441902, Maharashtra, India.*
[2] *Department of physics Gondwana University Gadchiroli 442605, Maharashtra, India.*

[a] uttara25vaidya@gmail.com
[b] nandun16@gmail.com

Abstract

In this work, growth of single glycine crystal with the addition of aluminium chloride, using a slow evaporation process. In this study, glycine is doped into 0.8M% of aluminium chloride. The semi-organic single crystal glycine doped with aluminium chloride has been produced at a constant temperature of 36°C. Powder X-ray diffraction (XRD) is used for verifying the crystalline nature and alpha phase of doped glycine that contains aluminium chloride. The thermal stability and thermal decomposition of the sample was studied by thermo gravimetric/differential thermo analytical method. Using the UV-absorption spectrum, the optical transmittance window and lower cutoff wavelength have been examined.

Keywords: UV-VIS, FTIR, XRD, solution growth technique, single crystal.
Received 01 March 2025; First Review 17 April; 2025; Accepted 30 April 2025.

*** Address of correspondence**
U. B. Tagade
Department of physics S. Chandra Mahila Mahavidyalaya Amgaon 441902, Maharashtra, India.

Email: uttara25vaidya@gmail.com

How to cite this article
U. B. Tagade, and N. S. Meshram, Growth and Characterization of Glycine single crystal by addition of Aluminium Chloride, J. Cond. Matt. 2025; 03 (02): 168-171.

Available from:
https://doi.org/10.61343/jcm.v3i02.150

Introduction

Amino acids belong to family of organic materials. The molecular chirality, presence of week Van der walls, hydrogen bond and zwitterionic nature, due to this feature of amino acid shows NLO properties [1]. Applications for NLO single crystals are numerous and include frequency mixing, second harmonic generation, electro-optic modulation, optical data storage, and communication. For this use, numerous researchers have attempted to create a variety of new NLO materials in recent years.

Organic crystals have high second harmonic conversion efficiency but haven't mechanical and thermal stability. Hence, semi organic crystals have both properties of organic and inorganic [2]. Because the organic material contains inorganic impurities, it has mechanical and thermal strength, which makes it appropriate for use [3]. Glycine have gained more attention of researchers for their NLO properties.

Glycine (NH_2CH_2COOH) is also known as amino acetic acid. It's the most basic of all amino acids. With various inorganic salts, it can take on a variety of forms. Alpha, beta, and gamma glycine are its three polymorphic crystal forms. Glycine is a key component of the structure of proteins, enzymes, hormones and plays a role as a neurotransmitter.

It has no centre of chirality, making it the only amino acid that forms proteins [4]. M. Lenin examined the growth of a novel semi-organic crystal of glycine lithium chloride from a water solution that contained glycine and lithium chloride in a 1:1 ratio [5].

The semi organic crystal of diglycine sulphate and ammonium sulphate were studied by Drozdowski et al [6]. Michel studied the crystal structures of grown crystal glycine nickel dichloride and glycine zinc sulphate [7]. Shanmugavadivu reported a nonlinear optical crystal of glycine potassium sulphate [8].

Glycine single crystals were grown using solvent evaporation and submerged seed solution methods from glycine and ammonium sulphate taken in equimolar ratio [9].

In this work, synthesis of glycine single crystal doped with aluminium chloride with 0.8%M by slow evaporation technique first time and studied the various characterization and result were discussed.

Experimental

Materials used

The molecular formula of Glycine is ($C_2H_5NO_2$). Molar mass: 75.07 g/mol, Aluminium chloride, ($Alcl_3$), AR (99%), M. Wt.: 133.33 g/mol. For the crystal formation, distilled water was utilized as solvent.

Crystal growth Method

Glycine single crystals were grown by the slow evaporation method. It is the method of solution growth at low temperatures. If the solution is supersaturated that is, contains more solute than can be in equilibrium with the solid. Bulk crystals with high solubility and temperature-dependent solubility can be grown using this technique [10].

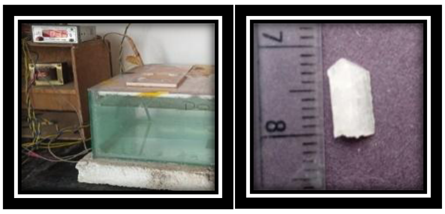

Figure 1: (a) Experimental apparatus and grown Glycine crystal.

In order to prepare the solution, glycine and $Alcl_3$ were taken. The aluminium chloride 0.8 M% was mixed with saturated glycine solution in a vessel, and the mixture was kept on a magnetic stirrer at room temperature and stirred thoroughly for approximately 4 hours. When a clear solution was seen, the solution was poured into a beaker. The saturated solution was filtered using Whatman filter paper in a clean vessel, which was covered with a perforated polythene sheet and placed in a temperature bath that was controlled by a microprocessor.

The constant temperature bath 35 °C the solution was allowed for slow evaporation and grown crystal obtained within 30 days. The figure 1 shows crystal growth experiment and grown crystal.

Characterisation Studies

XRD Analysis

The X- ray diffraction graph of a grown crystal gets into peak position and intensities. The position of the lines on graph are shows spacing between planes in the lattice and the intensities depends on the atoms position on particulars sites. In order to analyze the crystal's structure, the generated glycine was subjected to a powder x-ray diffraction examination using a Lynx Eye X-ray diffractometer with Kα radiation (λ = 1.54060 Å) at room temperature (25 °C).

For the analysis, the growing crystal was ground into a fine powder. The powder sample was measured between 10^0 and 80^0.

The diffracted beam's intensity was measured as a function of 2ϴ, and the peaks were indexed in accordance with the literature report [9,11].

Alpha glycine data from JCPDS CARD NO:32-1702 and the measured values agree well. Glycine crystal doped with aluminium chloride belongs to monoclinic system with space group $P2_1/n$. The lattice parameter a = 5.4305 Å, b = 11.901 Å, c = 5.1971 Å, α = γ = 90, β = 111.92^0. The characteristics peak at 2ϴ =29.56 for $Alcl_3$ doped glycine and prominent planes are (040), (021), (-110), (044). The Strong, pointed peaks show up, confirming the grown sample's good crystallinity. Figure 2 displays the index XRD plane for the synthesized crystal.

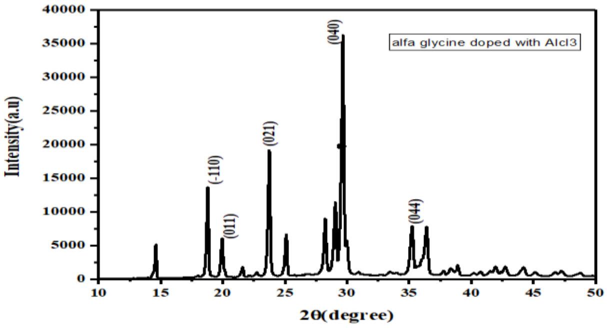

Figure 2: XRD studies of α -glycine crystal

FTIR Studies

Figure 3 displays the powdered doped glycine's acquired FTIR spectra. The functional groups of the generated α single crystal are in good agreement with the results that have been reported [9-11].

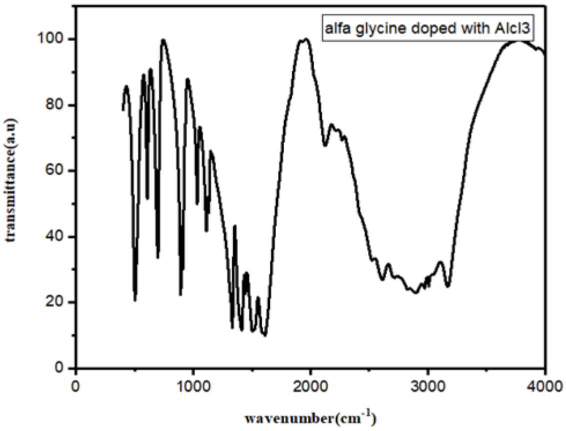

Figure 3: FTIR Analysis of α glycine single crystal.

Table 1: FTIR Analysis.

Alcl$_3$ doped glycine (α-glycine) cm^{-1}	**Band assignment**
2611	NH_3^+ stretching vibration
2133	Combinational bond
1612	asymmetric CO_2 stretching vibration
1505	NH_3^+
1421	Symmetric stretching vibration COO^-
1322	twisting vibration of CH_2
1121	Rocking vibration of NH_3^+
1023	Asymmetric stretching vibration of CCN
999	Rocking vibration of CH_2
890	symmetric stretching vibration of CCN
698	Bending vibration of COO^-
605	wagging vibration of COO^-

It can be shown from the report of α-glycine doped Alcl$_3$ that the carboxylic groups correspond to the functional groups 503, 607, and 697 cm^{-1}. According to the FTIR spectra, the detected at 1023 cm^{-1} and 890 cm^{-1} correspond to the C-C-N symmetric stretching vibration and the C-C-N asymmetric stretching vibration, respectively. Table 1 displays the detected frequencies along with the glycine single crystal's assignment.

Analysis of the UV-visible spectrum

Figure 4. displays UV-Vis transmission spectrum of the crystal-grown. The spectrum was obtained between 200 and 1100 nm. It can be seen from the spectrum that the lower cutoff wavelength is at 304 nm.

Throughout the visible spectrum, the crystal is clear. It implies that the crystal is appropriate for the process of frequency doubling.

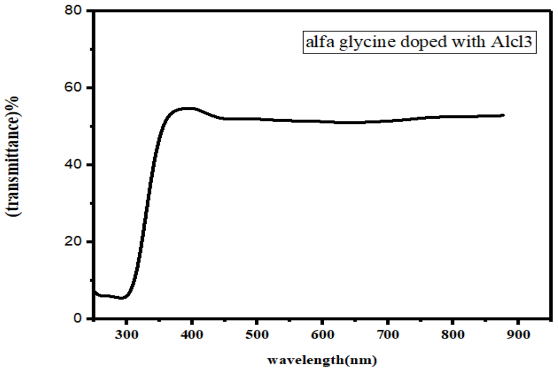

Figure 4: UV spectra of glycine single crystal

TGA and DTA Studies

Thermo-gravimetric analysis was carried out to examine the alpha glycine crystalline sample's thermal behaviour. In a nitrogen atmosphere, the thermal analyser was used with a heating rate of 20 °C/min. Temperatures between 20 and 1000 °C were used to record the TGA. Glycine's breakdown is represented by the peak in the α glycine DTA curve at 262.34 °C. The graph shows that the heat flow remained constant until it reached 262.34 °C. Until the melting phase, there is also no weight loss. The DTA curve shows endothermic process.

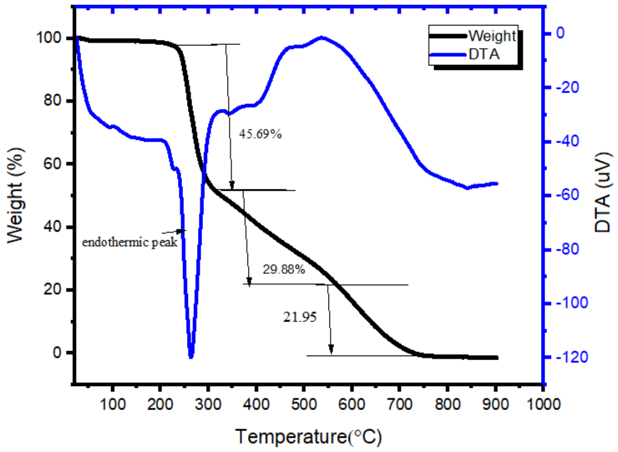

Figure 5: TGA and DTA graph.

Conclusion

We have generated and study a single crystal of alpha glycine using the slow evaporation approach and doping it with alcl$_3$ at a concentration of 0.8M % at first time. Aluminium chloride doped with glycine crystallizes in a monoclinic system, according to powder XRD examination. Good crystallinity of the developed crystal is confirmed by the emergence of a strong and sharp peak. Different functional groups are confirmed to be present by FTIR analysis. UV examination shows that the transmitters range from 300 to 900 nm, with the lower cut-off frequency at 304 nm. Up to 265 °C, alfa glycine single crystals are thermally stable.

References

1. R. Rameshbabu, N. Vijayan, R. Gopalkrishnan, P. Ramasay, Cryst. Res. Technol 41 (2006) 405.
2. M. Senthil Pandian, P. Ramasamy, J. Cryst. Growth 2008; 310: 2563-8.
3. S. Dhanuskodi, A. P. Jeyakumari, S. Manivannan. J. Cryst. Growth 282(2005)72.
4. P. Langen, S. A. Mason, D. Myles, B. P. Schoenborn Acta Cryst 358 (2002) 728.
5. B. N. Moolya, A. Jayarama, M. R. Sureshkumar, S. M. Dharmaprakash, J. Cryst. Growth 280

(2005) 581.
6. M. Drozdowski et al. Spectrosc. Acta A 42 (7) (2001) 833.
7. Michel Fleck et al. Acta crystalloger. C 60 (6) (2004) 291.
8. R. Shanmugadivu, G. Ravi, A. A. Nixon, J. Phys. Chem. solids 67 (2006) 1858.
9. S. Anbu Chudar Azhagan, S. Ganesan, Arabian Journal of Chemistry (2013).
10. G. S. Kell, (1977). Journal of physical and chemical reference data, 6(4), 1109-1131.
11. K. Srinivasan, J. Arumugan, opt. mater. 30 (2007) 40.